University of Nottingham
UK | CHINA | MALAYSIA

Engineering and Physical Sciences Research Council

Multi-Electron Charge Carriers for Next-Generation Flow Batteries

Catherine Lowri Peake

School of Chemistry, University of Nottingham

A thesis submitted for the degree of Doctor of Philosophy

2022

Acknowledgements

I would like to thank my supervisors Dr Darren Walsh and Dr Graham Newton, for the opportunity to undertake this research and for their valuable advice and support over the last four years. Their infectious positivity has not only helped me to stay motivated throughout my research but has also equipped me with an ethos that I'll carry into my future career.

I would like to thank Dr Alexander Kibler for his patience and enthusiasm in discussing my latest flow battery conundrum. Thank you for the mentorship in the synthesis of hybrid polyoxometalates when I first started my PhD and for your unwavering reassurance that I'm on the right track. I would like to extend my thanks to members of the NAMI group, past and present. I am fortunate to have worked with such a talented and friendly group of people. A special thanks is dedicated to Sean Goodwin, Daniel Smith, Neelam Mughal, Jack Jordan, Lisa Hampson, Matthew Bird and Heather Damien for their support and friendship over the years. It has been a great pleasure.

I would like to thank the EPSRC for funding and the CDT in Sustainable Chemistry for giving me the opportunity to undertake this research and to travel to international conferences to present these findings.

I would like to acknowledge our collaborators from the University of Leeds, Dr Thomas Chamberlain and Dr Xiangyi Chen. Xiangyi synthesised the fullerene-ferrocene charge carriers and conducted much of their physical characterisation. Thank you to Toby Maccormack for continuing the fullerene-ferrocene flow battery testing with such enthusiasm and care. I would also like to thank Dr Stephen Davies for completing the spectroelectrochemical analysis reported in this thesis.

Finally, I would like to sincerely thank my family and friends for their continued support throughout these four years. Thank you to Michelle Tindall for your willingness to listen to every details of my PhD journey with such patience. I would like to thank my partner Matt for reminding me to celebrate every success and for helping me to recognise the achievements I have made.

Abstract

The necessity to meet the ever-growing demand for energy while simultaneously reducing carbon emissions, requires a shift towards renewable sources of electricity. The intermittent nature of these sources has fuelled a demand for low-cost and reliable grid-scale energy storage. Redox flow batteries (RFBs) offer a promising solution due to their long cycle life and scalability. However, widespread commercial uptake of RFBs requires a reduction in cost and increase in energy density compared to the archetypal all-vanadium system. Increasing the volumetric energy density of RFBs requires the development of charge carriers with high solubility and the ability to undergo multi-electron redox processes.

The rich electrochemistry of polyoxometalates (POMs) and fullerenes make them particularly promising charge carriers for high energy density batteries. We demonstrate how functionalisation of these species can enhance their solubility and redox properties to further increase the energy density of RFBs. Furthermore, we focus on their application in nonaqueous electrolytes where the wide window of electrochemical stability allows for high voltages to be achieved. This thesis encompasses the design, synthesis, and characterisation of functionalised multi-electron charge carriers, and investigation of their performance in nonaqueous RFBs.

Chapter 2 discusses the theory behind electrochemical energy storage devices and the assessment metrics used for quantifying the performance of RFBs. We highlight the challenges of chemical compatibility of battery components with nonaqueous solvents and present best practice for testing of nonaqueous electrolytes in laboratory-scale RFBs.

In chapter 3 we seek to enhance the solubility of POMs in nonaqueous solvent through organic-inorganic hybridisation. We describe the synthesis and electrochemical analysis of the hybridised POM, $TBA_3[PW_{11}O_{39}(SiC_6H_5)_2O]$, PW_{11}-SiPh. Organofunctionalisation of the phosphotungstate Keggin-type POM with phenyl siloxane groups, increases its saturation concentration in acetonitrile by two orders of magnitude over that of the parent compound. The stability of PW_{11}-SiPh is investigated in several symmetric RFBs, and the system demonstrates high coulombic

efficiency (98%), voltage efficiency (89%), and energy efficiency (87%) during redox cycling. We show that capacity fade due to oxidation state imbalance and asymmetric membrane crossover can be counteracted by reduction or redistribution of electrolytes respectively. However, when cycling within a wide potential window such that PW_{11}-SiPh is reduced by four electrons per molecule, its stability appears to be diminished and rapid capacity fade is observed.

In chapter 4 we explore the application of PW_{11}-SiPh as charge carrier in the negative electrolyte of an asymmetric RFB. The battery uses the nitroxide radical 2,2,6,6-tetramethylpiperidinyloxyl (TEMPO) as the charge carrier in the positive electrolyte allowing for a larger cell voltage and theoretical energy density to be achieved compared to the symmetric system with PW_{11}-SiPh alone. Stable cycling was achieved for >400 hours with cell voltage of 1.6 V and coulombic efficiency of 95% (when PW_{11}-SiPh was reduced by three electrons upon charge). However, capacity fade due to membrane crossover was realised with this battery, as indicted by the presence of PW_{11}-SiPh in the positive electrolyte. Furthermore, the stability of the RFB was dramatically reduced when PW_{11}-SiPh was reduced by four electrons, indicating significant degradation of the hybrid POM under these conditions.

In chapter 5, the multi-electron redox process of fullerene and the positive redox potential of ferrocene were coupled to generate a bifunctional charge carrier termed $C_{60}Fc$. A symmetric $C_{60}Fc$ RFB exhibited an impressive coulombic efficiency (96%), voltage efficiency (77%), and energy efficiency (74%) over 100 cycles (150 hours). However, capacity fade of 0.3% per cycle was observed and ascribed to charge carrier degradation. A series of $C_{60}Fc$ charge carriers were synthesised in which the organic functionality surrounding the pyrrolidine ring linking the fullerene and ferrocene groups was modified. $C_{60}Fc$ charge carriers featuring a hexyl chain on the pyrrolidine linker group were found to have increased solubility in dichlorobenzene and therefore increased theoretical energy density in the resulting RFB. An unexpected consequence of the organic modification to $C_{60}Fc$ was its increased propensity to transport across the separator. RFBs with the hexyl substituent demonstrated significant asymmetric membrane crossover. The detrimental effect of asymmetric crossover on capacity retention was found to be preventable by polarity switching.

Declaration

I declare that all experimental work, analysis, writing, and figures presented in this thesis were conducted/prepared by myself unless specifically indicated. Many of the ideas behind the research presented in this thesis were conceptualised in collaboration with my supervisors Dr Darren Walsh and Dr Graham Newton. Dr Alexander Kibler is a co-author on publication (1), of which chapter 3 is based. Chapter 5 is based on a project conducted in collaboration with Dr Thomas Chamberlain, Xiangyi Chen and Toby Maccormack.

Publications

The following articles have been published as a result of the work undertaken during the course of this PhD program:

(1) C. L. Peake, A. J. Kibler, G. N. Newton and D. A. Walsh, Organic–Inorganic Hybrid Polyoxotungstates As Configurable Charge Carriers for High Energy Redox Flow Batteries, *ACS Appl. Energy Mater.,* 2021, **4**, 8765–8773.

(2) J. M. Cameron, C. Holc, A. J. Kibler, C. L. Peake, D. A. Walsh, G. N. Newton and L. R. Johnson, Molecular redox species for next-generation batteries, *Chem. Soc. Rev.*, 2021, **50**, 5863–5883.

(3) C. L. Peake, G. N. Newton, D. A. Walsh, Charge Carriers for Next-Generation Redox Flow Batteries in *Redox Chemistry - From Molecules to Energy Storage*, P. O. Fontaine, IntechOpen, Online, 2022.

Abbreviations

ASR	Area specific resistance
AQ	Anthraquinone
CAES	Compressed air energy storage
CE	Coulombic efficiency
CEM	Cation exchange membrane
CV	Cyclic voltammetry/voltammogram
DCM	Dichloromethane
DMF	Dimethylformamide
DPV	Differential pulse voltammetry
EE	Energy efficiency
EES	Electrochemical energy storage
EIS	Electrochemical impedance spectroscopy
E_v	Volumetric energy density
Fc	Ferrocene
IVCT	Intervalence charge transfer
LIB	Lithium-ion battery
LUMO	Lowest unoccupied molecular orbital
MALDI-TOF	Matrix assisted laser desorption/ionisation-time of flight
NMR	Nuclear magnetic resonance
OCP	Open circuit potential
oDCB	Ortho-dichlorobenzene
PTFE	Poly(tetrafluoroethylene)
POM	Polyoxometalate
POV	Polyoxovanadate
RFB	Redox flow battery
SEM	Scanning electron microscopy
SHE	Standard hydrogen electrode
SOC	State of charge
TBA	Tetra-n-butylammonium
Tf	Trifluoromethanesulfonate
TRIOL	tridentate tris(hydroxymethyl)methane ligand
V_{cell}	Cell voltage
VE	Voltage efficiency
VRFB	All-vanadium redox flow battery

Table of Content

Chapter 1: Introduction 1

1.1. Energy Storage Technologies 1

1.2. Redox Flow Batteries 7

1.3. Charge Carriers for Next-Generation RFBs 10

1.3.1 Organic charge carriers 13

1.3.2 Organometallic charge carriers 16

1.3.3 Polyoxometalates charge carriers 18

1.4. Conclusions 29

1.5. Thesis Aims 30

1.6. References 31

Chapter 2: Redox Flow Battery Theory and Method Development 36

2.1. Introduction 36

2.2. Experimental 36

2.2.1 Membrane conductivity testing 36

2.2.2 Membrane selectivity testing 37

2.3. Theory 37

2.4. Method Development 42

2.4.1 Cell design 42

2.4.2 Membranes 45

2.5. Conclusions 51

2.6. References 51

Chapter 3: Hybrid Polyoxometalates for Symmetric Nonaqueous Redox Flow Batteries 53

3.1. Introduction 53

3.2. Experimental 56

3.2.1 General experimental methods 56

3.2.2 Synthesis of PW_{11}-SiPh 56

3.2.3 Saturation concentration analysis 56

3.2.4 Cyclic voltammetry 57

3.2.5 Bulk electrolysis 57

3.2.6 Redox flow battery 57

3.3. Results and Discussion 58

3.3.1 Solubility of charge carriers 59

3.3.2 Electrochemical analysis 61
3.3.3 Flow battery performance 67
3.4. Conclusions 81
3.5. References 83
Chapter 4: Hybrid Polyoxometalates for Asymmetric Nonaqueous Redox Flow Batteries 85
4.1. Introduction 85
4.2. Experimental 88
4.2.1 General experimental methods 88
4.2.2 Cyclic voltammetry 88
4.2.3 Electrochemical impedance spectroscopy 88
4.2.4 Redox flow battery 88
4.3. Results and Discussion 89
4.3.1 Electrochemical characterisation of TEMPO 89
4.3.2 Electrochemical characterisation of PW_{11}-SiPh 93
4.3.3 PW_{11}-SiPh |TEMPO 93
4.4. Conclusions 105
4.5. References 107
Chapter 5: Fullerene-Ferrocene Charge Carriers for Symmetric Nonaqueous Redox Flow Batteries 109
5.1. Introduction 109
5.2. Experimental 113
5.2.1 General experimental methods 113
5.2.2 Synthesis of C_{60}Fc charge carriers 113
5.2.3 Cyclic voltammetry 116
5.2.4 Electrochemical impedance spectroscopy 116
5.2.5 Redox flow battery 116
5.2.6 Electrolyte extraction 117
5.3. Results and Discussion 118
5.3.1 Solubility of charge carriers 118
5.3.2 Electrochemical analysis of C_{60}Fc charge carriers 120
5.3.3 Flow battery performance of C_{60}Fc charge carriers 130
5.4. Conclusions 148
5.5. References 150
Chapter 6: Conclusions and Outlook 153

6.1. References 156
Appendix A: Supplementary Analysis of Fullerene-Ferrocene Charge Carriers 157
A.1. Electrochemical analysis of $C_{60}Fc2$ 158
A.2. Electrochemical analysis of $C_{60}Fc3$ 161
A.3. Flow battery performance of $C_{60}Fc2$ and $C_{60}Fc3$ 164

Chapter 1: Introduction

1.1. Energy Storage Technologies

Global energy consumption is forecast to increase by 23% between 2015 and 2040 with 50% of the demand due to development in India and China alone.[1] Access to cheap and reliable electrical energy is paramount to maintain high standards of living and for social and economic growth in developing countries. At present approximately two thirds of global electricity is generated by combustion of fossil fuels which releases copious amount of CO_2.[1] The increased concentration of CO_2 and other greenhouse gases in the atmosphere has led to an increase in the Earth's average surface temperature.[2] Temperatures are forecast to continue rising[2] with destructive consequences for humanity and the natural environment.

A quarter of global CO_2 emissions originate from the production of electricity[1] and therefore decarbonisation of the electricity sector is of utmost importance to curb the rising temperatures. Numerous countries are committing to carbon reduction policies such as the USA's pledge to achieve a carbon-free electricity sector by 2035.[3] Consequently, the adoption of low-carbon renewable sources is increasing rapidly and becoming more economically competitive with fossil fuel sources.[4,5] Power generation and distribution infrastructures, known as electrical grids, operate on an instantaneous balance between supply and demand. While renewable sources such as solar and wind have favourable green credentials, their electricity generation is dependent on the season, time of day and weather (e.g. cloud coverage and wind speed). A greater dependence on intermittent sources can threaten the balance between supply and demand which is necessary for stable electrical grid infrastructures.[6]

Grid-scale energy storage facilities are essential to the integration of intermittent renewable sources on electrical grids. Their primary service is in load levelling, where electricity is stored when supply is ample and demand is low, and is released when demand increases. Energy storage technologies provide a range of other grid-services which can be broadly classified into two categories; power quality services (short duration), which include voltage and frequency regulation, and energy management

services (long duration) such as load levelling and load following.[7] Ultimately, the integration of energy storage technologies onto the grid enables efficient deployment of electricity generation resources which can provide performance, safety, sustainability and economic benefits. By far the most widely adopted energy storage technology for grid-scale applications is pumped hydroelectric storage (98% of global capacity),[8] followed by compressed air energy storage (CAES), flywheel energy storage, thermal energy storage and electrochemical energy storage (EES) such as batteries, supercapacitors and fuel cell-electrolysers. Figure 1.1 provides an overview of energy storage technologies currently in use or under development for grid-scale applications, comparing their power ratings and discharge time at rated power.[9] An overview of established and developing grid-scale energy storage technologies is provided, followed by a detailed examination of EES technologies.

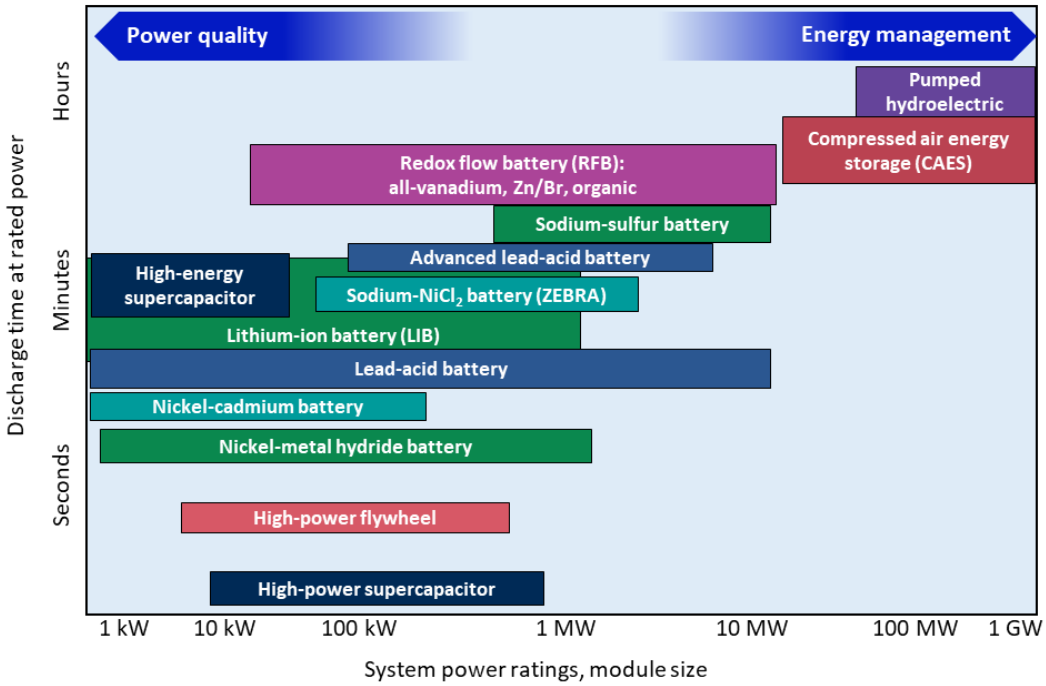

Figure 1.1. A comparison of discharge time and power rating (absolute value) for various energy storage technologies. Figure was adapted from reference 9 (EPRI).

Pumped hydroelectric storage facilities store electrical energy by pumping water from a reservoir at low to high altitude. Electricity is generated on demand by releasing water from the high altitude reservoir to drive turbines and power generators. The rapid response time (seconds-minutes), long cycle/calendar life

(>50,000 cycles/25+ years)[7], and low maintenance costs makes pumped hydro a benchmark for future grid-scale storage technologies in terms of efficiency, economics and safety.[10] The primary disadvantage is its geographical limitations due to the requirement of two water reservoirs at different altitudes.

The second most utilised grid-scale energy storage technology is CAES, in which air is pumped into a chamber (often an underground cavern or disused mine) to high pressure (typically ~70 bar). Electrical energy is regenerated as compressed air is released to power an expansion turbine driving a generator.[8] Start-up time is in the order of 10 minutes and power output of 300 MW for 2 hours is typical. Again, this storage method is geographically limited due to the need for a suitable location to store pressurised gas.[8] The roundtrip efficiency of 45-60% and poor economic viability of CAES are also limiting for widespread adoption.

Flywheel energy storage operates by converting electrical energy to rotational kinetic energy. Rotors are spun at high speeds and electricity is extracted by deceleration of the flywheel.[8] It is a high power, low capacity technology suitable for niche applications. Strong containment vessels are necessary due to the potential for explosion upon material failure. Consequently, the cost of flywheels are an order of magnitude more expensive than batteries.[8] Thermal energy storage encompasses a wide range of technologies, including concentrated solar thermal power plants which use materials such as molten salts to store solar heat during the day, and use the heat to power steam turbine generators on demand.

The fundamental principle of EES is the conversion of chemical energy stored in the bonds of molecules to electrical energy, and vice versa. Importantly, the redox reactions in the electrochemical cell are separated in space and connected by an electrical circuit. Batteries can be categorised as primary (non-rechargeable) or secondary (rechargeable) systems and only the latter are suitable for energy storage purposes where recurrent charge and discharge is a requirement. Several battery technologies are suitable for grid-scale energy storage, including nickel-metal hydride, lead-acid, sodium-sulfur batteries, lithium-ion batteries (LIBs), and redox flow batteries (RFBs). While the energy storage capacities of batteries do not rival

that of pumped hydroelectric storage, they offer a scalable and geographically independent solution with a fast response times of milliseconds-seconds.[7]

Lead-acid batteries were first developed by Gaston Planté in 1859 and now have a well-established worldwide market within the automotive sector and as standby power for the utility industry.[11,12] They are constructed of a high surface area lead negative electrode and lead dioxide positive electrode which are divided by a porous separator and immersed in an aqueous electrolyte containing sulfuric acid. Upon discharge, Pb at the negative electrode is oxidised to Pb^{2+} and further reacts with SO_4^{2-} from the aqueous electrolyte to generate $PbSO_4$ crystals on the electrode surface (figure 1.2a). Simultaneously, PbO_2 (Pb^{4+}) at the positive electrode is reduced to Pb^{2+}. Further reaction with H^+ and SO_4^{2-} from the supporting electrolyte generates H_2O and $PbSO_4$ crystals at the electrode surface. The overall discharge reaction in a lead-acid battery is:

$$PbO_2 + Pb + 2H_2SO_4 \rightarrow 2PbSO_4 + 2H_2O$$

Importantly, the reactions are reversible, meaning the battery is rechargeable. Lead-acid batteries provide a cost-effective solution for many energy storage requirements, however, their energy and power density fall well below that of LIBs. Several technical challenges reduce the performance and therefore commercial viability of lead-acid batteries for grid-scale applications. Deposition of $PbSO_4$ on the negative electrode becomes irreversible at high charge rates, leading to a relatively limited cycle life. In addition, charging at high current densities induces hydrogen evolution at the negative electrode and therefore reduced efficiency.

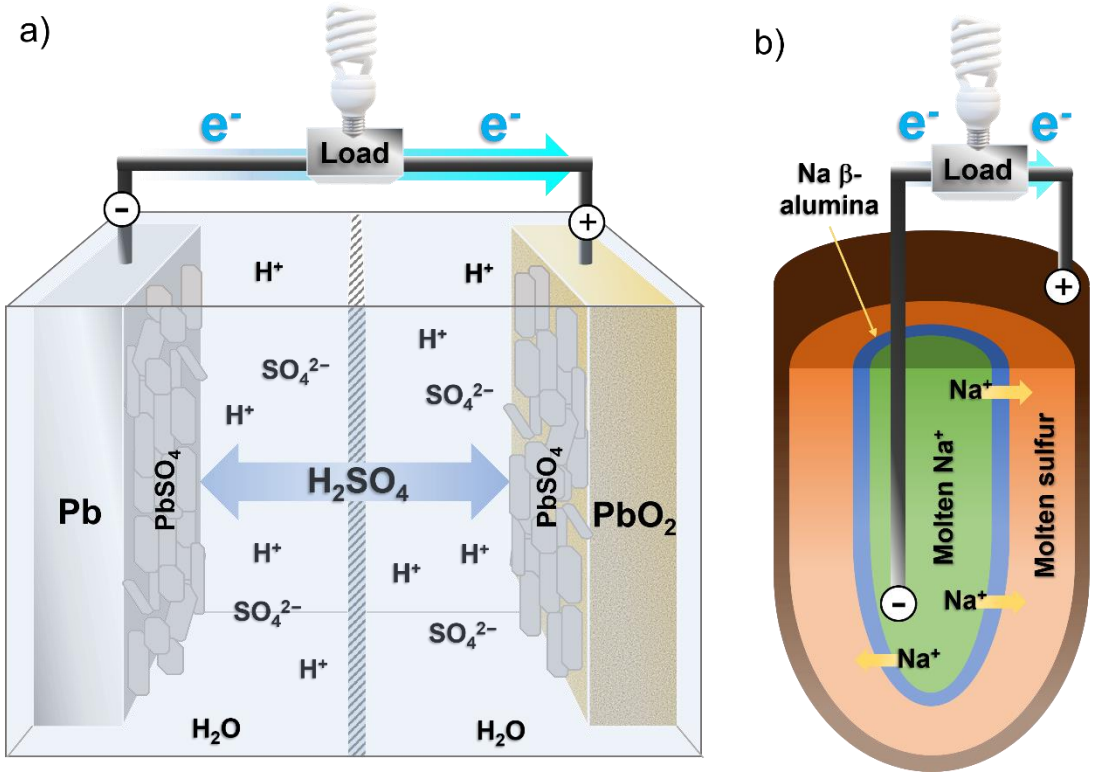

Figure 1.2. a) Schematic of a single lead-acid cell under discharge conditions. Pb negative electrode is oxidised while the PbO_2 positive electrode is reduced. $PbSO_4$ crystals are formed on both electrode surfaces upon discharge. b) Sodium-sulfur battery under discharge conditions. Molten Na at the negative electrode is oxidised to Na^+ and is transported through a β-alumina ceramic separator. The molten S positive electrode is reduced upon contact with Na^+ to Na_2S_5 and other sodium polysulfides.

Sodium-sulfur batteries were first developed in the 1960s and are composed of a molten sodium negative electrode and molten sulfur positive electrode separated by a solid β-alumina Na^+-conducting electrolyte.[10] During discharge, Na at the negative electrode is oxidised to Na^+ (figure 1.2b). Na^+ moves through the ceramic separator where it reacts on contact with sulfur at the positive electrode to produce Na_2S_5 and other sodium polysulfides.[11] The reverse reactions occur upon charge. The sodium-sulfur battery operates at 300 °C and is currently being demonstrated commercially primarily in Japan.[10,13] However, the safety of sodium-sulfur batteries is of concern due to the risk of sodium fires in the event of a membrane rupture.[14] Sodium-$NiCl_2$ batteries, nicknamed ZEBRA, are also based on the high ionic conductivity of β-alumina ceramics, and both battery types have moderate commercial interest.

Since their commercialisation by Sony in 1991, LIBs have transformed portable electronics, are the battery of choice for electric vehicles and have been integrated into electric grid infrastructures. John Goodenough, Stanley Whittingham and Akira Yoshino were jointly awarded the 2019 Noble Prize in Chemistry for their contributions towards the revolutionising technology.[15] LIBs are constructed from two lithium-intercalating electrodes, usually $Li_x(TM)O_2$ (TM = transition metal, typically Co or Ni) and graphite, divided by a porous separator immersed in nonaqueous electrolyte. Upon charge, Li-ions move from the $Li_x(TM)O_2$ material in the positive electrode (typically termed cathode) to the negative electrode (termed anode) to form lithiated graphite (LiC_6). Upon discharge, the Li-ion movement is reversed, which accounts for the expression 'rocking-chair battery' used to describe LIBs.

The low molecular weight and redox potential of Li (−3.04 V *vs.* the standard hydrogen electrode (SHE))[14], give LIBs a practical volumetric energy density, E_v, of 200-300 Wh L^{-1}.[16] The demand for LIBs for portable electronics and the automotive industry has seen a dramatic increase in their scale of manufacture. Consequently, the cost of the LIB has significantly reduced over the past decade and was estimated at \$156 kWh^{-1} in 2020.[17] The established manufacturing routes and low cost of the LIB make it the most widely adopted EES technology for grid-scale applications. The largest EES grid storage device to date is a 200 MWh LIB constructed in Southern Australia in 2017 by Tesla, Inc.[18]

The global interest in LIBs for portable devices, vehicles and grid storage is likely to place significant pressure on the world's supply of lithium.[19] Lithium is classified as having 'limited availability with future risk to supply' according to the Chemical Innovation Knowledge Transfer Network.[20] A more pressing challenge is to meet the demand for cobalt, which is commonly used in the positive electrode of LIBs, due to the questionable stability of its supply chain.[21] The demand for more sustainable and higher E_v batteries has seen the field of 'beyond LIBs' emerge in recent decades.[22] This includes the development of high-E_v devices, such as lithium-air (also termed Li-O_2) and lithium-sulfur batteries, and technologies that avoid lithium entirely in favour of more abundant elements such as sodium-ion and magnesium-ion batteries.[10] The

primary application of these next-generation batteries is not for grid-scale energy storage and therefore they are not discussed further.

1.2. Redox Flow Batteries

RFBs differ from conventional batteries in that redox-active molecules, termed charge carriers, are dissolved into electrolyte and are stored in reservoirs external to the electrochemical cell. The charge carrier-containing electrolyte is pumped through electrodes in the electrochemical cell to charge and discharge the battery. Upon charge, energy is stored as the positive electrolyte (also termed catholyte or posolyte) is oxidised and the negative electrolyte (also termed anolyte or negolyte) is simultaneously reduced. Upon discharge, energy is released as the redox reactions are reversed. The cell voltage (V_{cell}) is dictated by the difference in redox potential between the reactions at the positive and negative electrodes. The electrolytes are

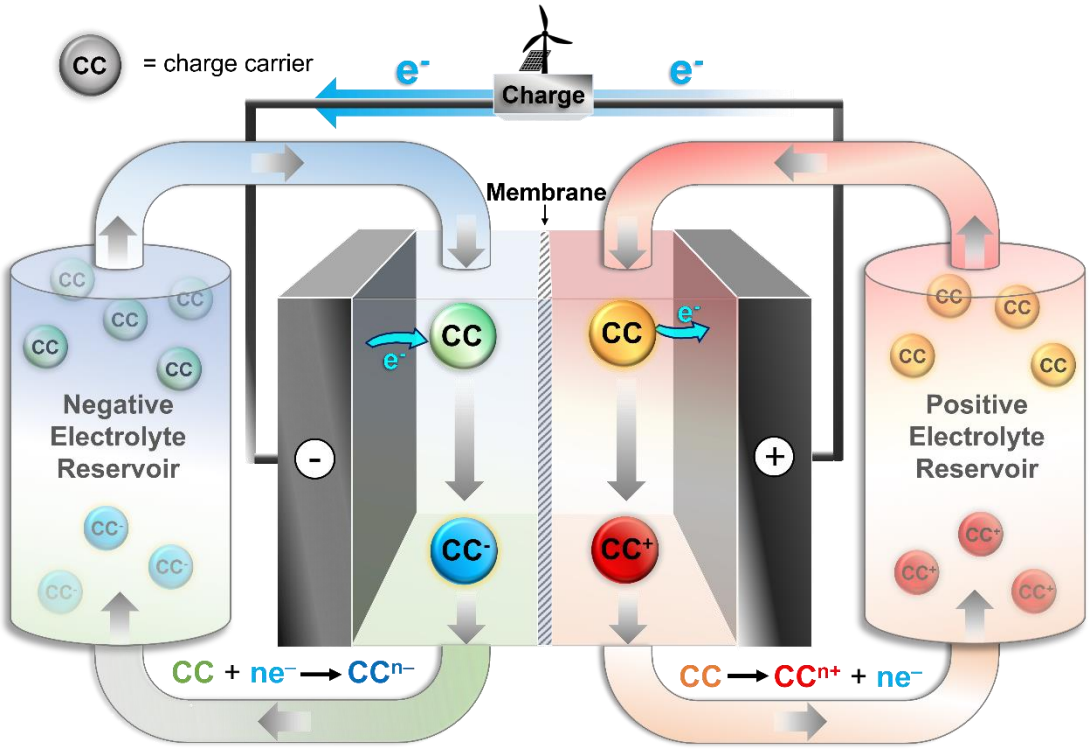

Figure 1.3. Schematic of a RFB under charge conditions. Electrolytes are stored in reservoirs and are pumped through the electrochemical cell to charge and discharge the battery. Upon charge the charge carriers in the positive electrolyte are oxidised while those in the negative electrolyte are reduced. The polarity is reversed to allow the opposite redox reactions to occur upon discharge. Reproduced from reference 16 with permission from the Royal Society of Chemistry.

separated in the cell by a membrane or separator, which allows transfer of charge-balancing counterions but prevents crossover of charge carriers to the opposite half-cell, thus preventing self-discharge. Figure 1.3 shows a schematic of a generic RFB under charge conditions.

The distinctive design of RFBs allows decoupling of energy and power, and therefore facile scale-up to high capacities.[23] Capacity can be enhanced by simply increasing the volume of electrolyte in the reservoirs, without the need to modify the electrochemical cell, while power is determined by the cell design (e.g. electrode surface area etc). Furthermore, in contrast to conventional batteries such as the LIB, RFBs avoid the intercalation and deintercalation of redox-active molecules between the electrolyte and solid electrode material. Instead, redox reactions occur via solution phase charge carriers at the electrode surface. This underpins the long operational lifetimes of RFBs (15-20 years), making them particularly suited to grid-scale energy storage applications.

Historically, RFBs have relied on ionic charge carriers such as iron, chromium, zinc, and cerium, dissolved in aqueous electrolytes.[24] The earliest investigations were conducted by the National Aeronautics and Space Administration (NASA) in the 1970s. Their most notable development was the iron-chromium RFB which used Fe^{2+}/Fe^{3+} and Cr^{2+}/Cr^{3+} as charge carriers in the positive and negative electrolyte respectively.[25] Scale-up and commercialisation of the system were hindered by several technical challenges including the slow electron transfer kinetics of Cr^{2+}/Cr^{3+}.[24]

Today, the most commercially advanced RFB system is the all-vanadium RFB (VRFB) developed by Skyllas–Kazacos and co-workers in the late 1980s.[26,27] It is an example of a symmetric RFB as the same charge carrier in different oxidation states is use in both the positive and negative electrolyte. Upon charge, VO^{2+} (V^{4+}) is oxidised to VO_2^+ (V^{5+}) at the positive electrode while V^{3+} is reduced to V^{2+} at the negative electrode. One electron is transferred in the charge and discharge reactions and the average V_{cell} is 1.3 V (dictated by the difference in redox potential between the two reactions). Vanitec lists 33 companies manufacturing VRFBs[28] and several plants have been

installed worldwide.[23] The largest EES plant in the world is forecast to be a 200 MW/800 MWh VRFB and is under construction by Rongke Power of China.[23]

Despite their advantages for grid-scale energy storage, commercial uptake of the VRFB is dwarfed by that of LIBs due to several drawbacks. Firstly, the cost of the VRFB was estimated at \$500 kWh^{-1} in 2014,[29] which far exceeds the target of \$100 kWh^{-1} set by the USA Department of Energy,[30] and the ever decreasing cost of LIBs.[17] The high capital cost is largely attributed to the ion exchange membrane and vanadium sulfate charge carriers. The price of vanadium ore is closely linked to the steel industry and has fluctuated significantly over recent decades, destabilising the supply chain.

Table 1.1. Key parameters of some established RFB systems. Table is adapted from reference 32. C_{active} is the concentration of charge carrier in the electrolyte.

RFB system	C_{active} (M)	V_{cell} (V)	Stability	Key drawbacks	Element price (0.1 \$ Kg^{-1})
VRFB	3	1.3	>10,000 cycles -5-50 ℃	High chemical cost	V: 2.7
Fe/Cr	1.25	1.18	30-100 cycles	Slow kinetics, H_2 evolution	Fe: 0.02 Cr: 0.28
Fe/V	1.5	1.02	>100 cycles 0-50 ℃	High chemical cost	Fe: 0.02 V: 2.7
Zn/Br	4	1.76	>300 cycles	Zinc dendrite formation	Zn: 0.18 Br: 0.15
Polysulfide /Br	2.6	~1.5	50 cycles	Br_2 crossover, S precipitation	S: 0.01 Br: 0.15
Organic RFB	up to 4	up to 4	Variable 700 cycles	Under development	Variable

Secondly, the E_v of the VRFB is an order of magnitude lower than LIBs.[16] The limited solubility of vanadium sulfate in aqueous solution (2-3 M) and the V_{cell} of 1.3 V limits the E_v to 25-35 Wh L^{-1}.[31] Table 1.1 shows a summary of established and developing

RFB systems and their key parameters. A reoccurring drawback of established RFB systems is their high cost and/or low E_v.

The optimisation of the VRFB remains an active area of research and development in academia and more recently in industry. Research is focused on reducing cost, increasing E_v and optimisation of performance.[31] A parallel strategy to develop more commercially competitive RFBs has been to design and investigate alternative charge carriers. The so called next-generation RFBs deviate from the use of simple metal ion charge carriers in aqueous electrolyte, in favour of designer redox-active molecules with superior properties.

1.3. Charge Carriers for Next-Generation RFBs

In designing novel charge carriers for RFBs, there are several variables to consider. While lower E_v is generally more tolerable for stationary rather than portable applications, there is a demand to enhance RFB E_v to cut cost, reduce space requirements and access new markets. E_v is a measure of the energy output per unit volume of total electrolyte and is defined in Eq. 1.1;

$$E_v = \frac{n\,F\,V_{cell}\,C_{active}}{V_+ + V_-} \tag{1.1}$$

where n (unitless) is the number of electrons transferred per molecule in the charge/discharge redox reaction, V_{cell} (V) is the average cell voltage, C_{active} (mol L^{-1}) is the concentration of charge carrier in the electrolyte, F (C mol^{-1}) is the Faraday constant, and $V_+ + V_-$ (unitless) accounts for the volumes of the positive and negative electrolyte respectively. It is conventional to report E_v in units of Wh L^{-1} and therefore a division by 3600 is required to alter the time constant from seconds to hours.

It is desirable to design charge carriers with high solubility and multi-electron redox process at extreme potentials to maximise C_{active}, n and V_{cell} respectively. An optimised charge carrier would have redox potentials at extremely high potentials for the positive electrolyte, low potentials for the negative electrolyte and at both high and low potential for symmetric systems. Furthermore, fast electron transfer kinetics and high stability of the charge carrier are crucial to achieve high power density and long cycle and calendar life. It is also important that charge carriers are

cost-effective, sustainable, environmentally benign and that, where possible, their synthesis is from abundant materials. In this regard, charge carriers underpin the E_v and performance of RFBs, and strongly influences the overall cost and sustainability too.

Historically, RFBs have been based on aqueous electrolytes which are limited to a maximum V_{cell} of *ca.* 2.0 V, beyond which, electrolysis of water occurs. Nonaqueous electrolytes, those based on organic solvents and ionic liquids, have been explored due to their larger window of electrochemical stability (often >4 V).[33] This opens the opportunity to develop high V_{cell} batteries, which directly correlates to the achievable E_v of the RFB. The alternative solubilising properties of nonaqueous electrolytes enhances the diversity of applicable charge carriers beyond hydrophilic molecules alone. In addition, nonaqueous electrolytes could facilitate RFB operation outside the temperature window of 0 to 100 °C offered by aqueous electrolytes. For example, a RFB containing a porphyrin-based charge carrier in dichloromethane solvent, showed excellent performance within the temperature range of 20 to −40 °C.[34] However, nonaqueous electrolytes are not without their disadvantages. Their properties vary depending on the specific solvent but nonaqueous electrolytes are generally more ionically resistive, costly, hazardous and less sustainable compared to aqueous electrolytes.[33] In addition, commercial membranes and separators are primarily designed for aqueous electrolytes and their performance in nonaqueous systems is often compromised.[35,36] In this respect, it is necessary for the performance benefits of nonaqueous RFBs to outweigh their disadvantages, to render them commercially viable.

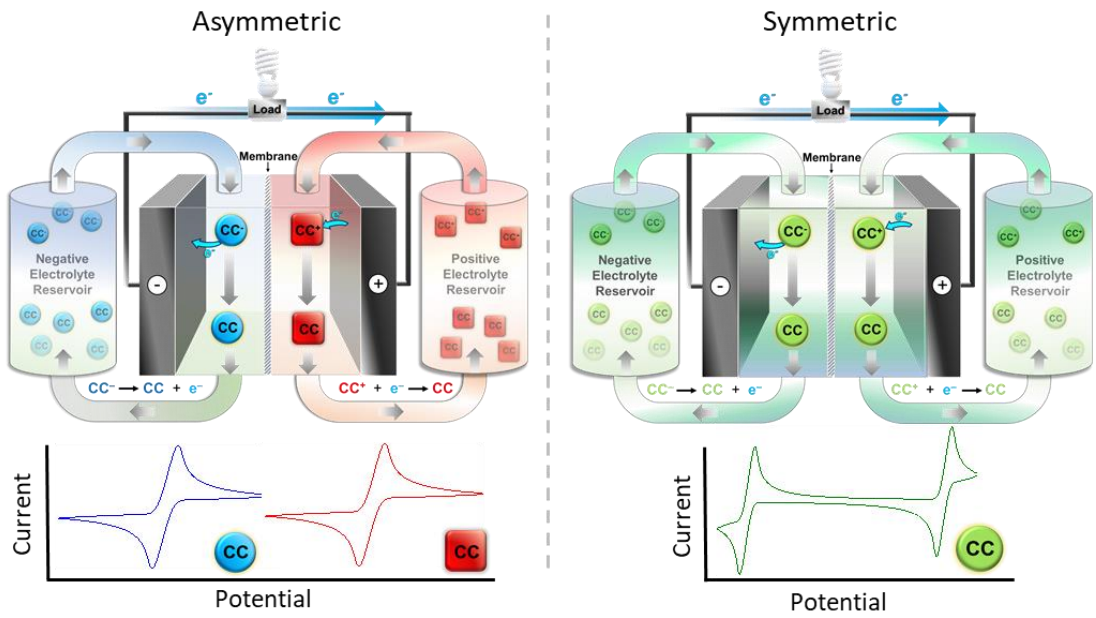

Figure 1.4. Schematic representation of asymmetric and symmetric RFBs and CV of their respective charge carriers.

As previously noted, RFBs can be categorised into asymmetric and symmetric systems and figure 1.4 shows a schematic of their working principles. Asymmetric RFBs are those which use a different charge carrier in the positive and negative electrolyte. The design allows the greatest flexibility in choice of charge carrier and for the properties of the positive and negative electrolyte to be tuned independently of each other. This often results in asymmetric RFBs having enhanced V_{cell} and E_v. However, in the event of membrane crossover, significant and irreversible capacity fade is typical in asymmetric RFBs.

An effective strategy to minimise the detrimental effects of membrane crossover is to design symmetric systems in which a single charge carrier is used in both the positive and negative electrolyte. Symmetric RFBs require a single charge carrier with reversible redox processes at both high and low potentials. In this regard, an active area of research has been the development of multi-electron charge carriers with reversible redox processes at both high and low potentials that can be used in symmetric RFBs.

While symmetric RFBs have less flexibility in the design of charge carriers, their advantage is that capacity loss due to membrane crossover can be regenerated. The advantage of symmetric RFBs in minimising the detrimental effects of membrane

crossover is elegantly demonstrated by the VRFB.[37] In the event of membrane crossover, vanadium ions that cross to the opposite half-cell can be reduced/oxidised to match the oxidation state of the surrounding charge carriers, and can partake in the subsequent charge-discharge cycles. While this reduces the coulombic efficiency (CE) of a given cycle, net movement of charge carriers in both directions, does not lead to permanent capacity fade. However, it is possible for the VRFB to become imbalanced due asymmetric membrane crossover or by parasitic reactions such as hydrogen evolution at the negative electrode. The symmetric nature of the battery means that capacity can be regenerated to a large extent, by simply mixing the positive and negative electrolytes and redistributing between reservoirs.[38]

Here, we categorise charge carriers based on their molecular structure and highlight some of the most notable advancements in the development of next-generation charge carriers for RFBs.

1.3.1 Organic charge carriers

Charge carriers composed of Earth abundant elements such as carbon, hydrogen, oxygen and nitrogen have the potential to be more cost effective and sustainable alternatives to metals.[39] The structural diversity and tunability of organic molecules

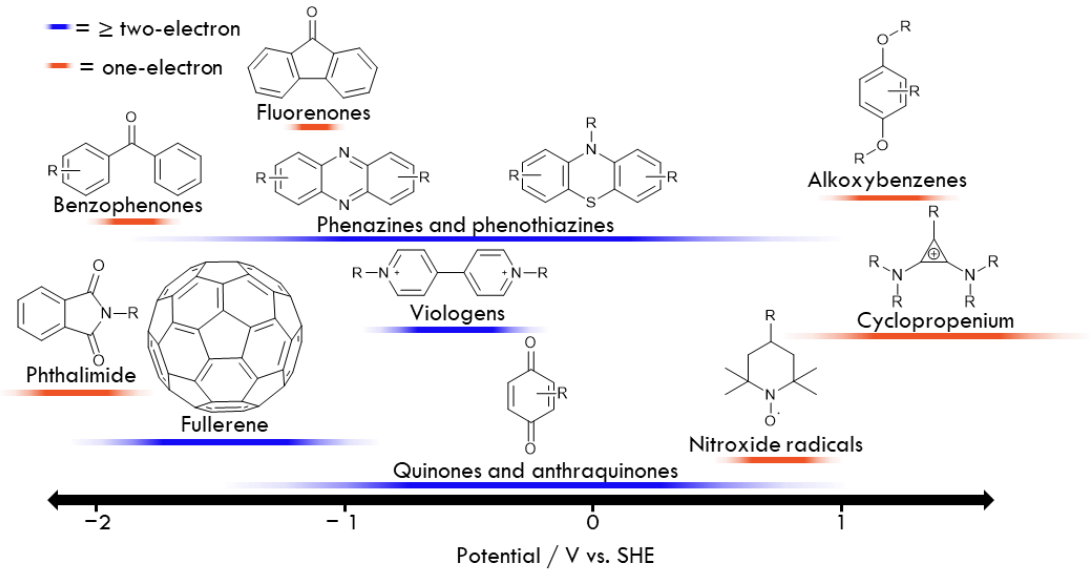

Figure 1.5. Schematic showing the structure of organic charge carriers investigated for RFBs and the potential region in which they are redox-active. Orange bars indicate species that undergo one-electron redox reactions while those with blue bars are multi-electron charge carriers.

allows for optimisation of their solubility, stability, and redox properties such as redox potential and electron transfer kinetics. A brief introduction to the various classifications of organic charge carriers is provided along with some of the most noteworthy applications in RFBs. Figure 1.5 shows the structure of some organic charge carriers investigated for RFBs and the potential region in which they are redox-active.

Carbonyls, molecules containing a carbon oxygen double bond, can be reduced by one-electron in the presence of small cations such as H^+ and Li^+, which stabilise the resulting negative charge on the oxygen. Carbonyls such as quinones, anthraquinones (AQs), fluorenones and benzophenones, feature a conjugated aromatic structure which stabilises the reduced state through delocalisation of the negative charge. This stabilisation enhances the electrochemical reversibility of the redox reaction, making them effective charge carriers for RFBs. Quinones and AQs contain two carbonyl groups per molecule enabling their reduction by two electrons. Aziz and co-workers are particularly active in this area of research having developed a catalogue of water-soluble quinone and AQ-based charge carriers and optimised their solubility, stability and redox properties.[40–43]

While radical molecules (those bearing an unpaired electron) are generally considered highly reactive, they can be stabilised through steric and/or resonance effects, making them promising charge carriers for RFBs. The field of radical-based charge carriers (or those which generate radicals upon charge) can be sub-categorised by their functional groups, namely nitroxide radicals, heteroaromatic-based species such as viologens, phenazines and phthalimides, alkoxybenzene-based species and cyclopropeniums (CPs).

The high stability of the 2,2,6,6-tetramethylpiperidinyloxyl (TEMPO) radical (structure shown in figure 1.5 where R=H) is due to delocalisation of the unpaired electron across the nitrogen-oxygen bond. The four methyl groups adjacent to the nitroxide radical contribute to its stability due to the steric hinderance they provide. Consequently, TEMPO undergoes a reversible one-electron oxidation to an oxoammonium cation ($TEMPO^+$) at the relatively high redox potential of 0.33 V *vs.*

$Ag^+|Ag$[44] and has been investigated as positive electrolyte charge carrier in several asymmetric RFBs.[45–48]

A series of substituted CP species have been designed, synthesised and tested by Sanford and co-workers and were found to exhibit remarkably high redox potentials and stability in nonaqueous electrolyte.[49–53] Initial investigations focused on the tris(dialkyl)amino-substituted CP cations[49] and later a joint computational and synthetic strategy was employed leading to the development of a butylthioether-substituted CP. The butylthioether-substituted CP undergoes a reversible oxidation at +1.40 V *vs.* ferrocenium/ferrocene ($Fc^+|Fc$), a 480 mV positive shift compared to the earlier anologue.[51] N-alkylphthalimide was employed as the charge carrier in the negative electrolyte to demonstrate an all-organic nonaqueous RFB with a remarkable V_{cell} of 3.2 V. CPs remain one of the few organic charge carriers with redox potentials at such extreme positive potentials.

The π-conjugated cage structure of fullerene gives it uniquely rich electrochemical properties compared to other organic redox-active molecules. It can be reversibly reduced by up to six electrons at negative redox potentials, making it a desirable charge carrier for the negative electrolyte in RFBs.[54] Without molecular modification, fullerene is nonpolar and unable to partake in hydrogen bonding, meaning its solubility in many solvents is poor.[55] Consequently, fullerene was first investigated as a bifunctional molecule where Fc groups were covalently grafted to a C_{60} fullerene cage ($C_{60}Fc$).[56] The functionalisation significantly enhanced the solubility of fullerene in ortho-dichlorobenzene (oDCB) from 0.037 M to 0.12 M for $C_{60}Fc$.[57] The Fc groups served as the redox centre for the positive electrolyte, while the multi-electron redox processes of fullerene were accessed in the negative electrolyte. To balance the redox processes of fullerene, multiple Fc moieties (between 1-4 equivalents) were grafted to C_{60}.The redox process of the positive and negative electrolyte were separated by approximately 1.3 V and 1.8 V for the first and second reduction of C_{60} respectively, giving an average V_{cell} of 1.64 V.

Figure 1.6 shows the structure of the $C_{60}Fc$ bifunctional charge carriers, and the redox reactions occurring in the positive and negative electrolytes upon charge in the RFB.

The performance of $C_{60}Fc$ charge carriers were investigated by galvanostatic cycling in coin cells. The coin cells were successfully cycled for 100 charge-discharge cycles but experienced considerable capacity fade. Considering the rich electrochemistry and plentiful opportunities for functionalisation of fullerene, there is great scope for development of new fullerene-based charge carriers in the future.

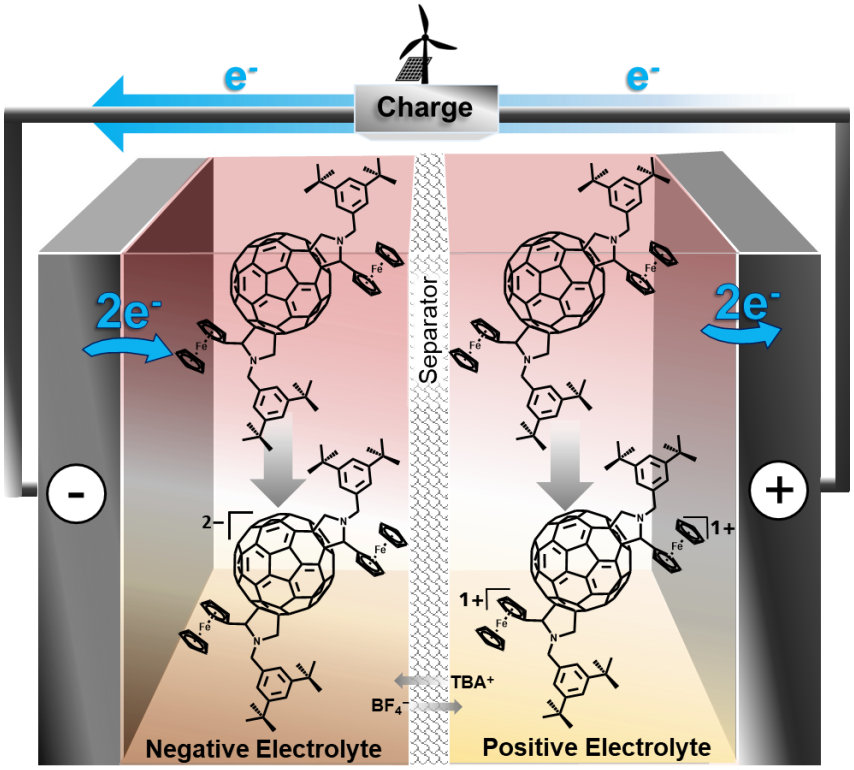

Figure 1.6. Schematic showing the redox reactions of $C_{60}Fc$ bis-adduct (two Fc equivalents per C_{60}) in a symmetric nonaqueous RFB. Upon charge, $C_{60}Fc$ in the positive electrolyte undergoes a two-electron oxidation centred at the two Fc moieties. Simultaneously, $C_{60}Fc$ in the negative electrolyte is reduced by two electrons at the fullerene core. The reverse reactions occur upon discharge.

1.3.2 Organometallic charge carriers

Metal coordination complexes are promising candidates for nonaqueous RFBs as they are often stable over multiple oxidation states and their properties are highly tuneable.[58] The first metal coordination complex to be investigated as a charge carrier for nonaqueous RFBs was the ruthenium bipyridine (bpy) complex, $[Ru(bpy)_3]^{2+}$ in the 1980s.[59] Bpy ligands not only solubilise the metallic cation, they also provide additional redox activity to the molecule. In a symmetric system the

Ru^{2+}/Ru^{3+} transition was targeted in the positive electrolyte while the bpy-centred reduction was targeted in the negative electrolyte. The redox processes were separated by 2.6 V, allowing for a high V_{cell}, but poor CE and voltage efficiency (VE) were observed upon cycling. Within the last decade a range of metal-ligand combinations have been investigated to include nickel, cobalt, iron, vanadium, and chromium metal centres and acetylacetonate, terpyridine and dithiolene ligands to name a few.[58] Ligand design can have a remarkable impact on the charge carrier solubility, stability and redox properties and is therefore a key research focus for optimisation of metal coordination complexes.

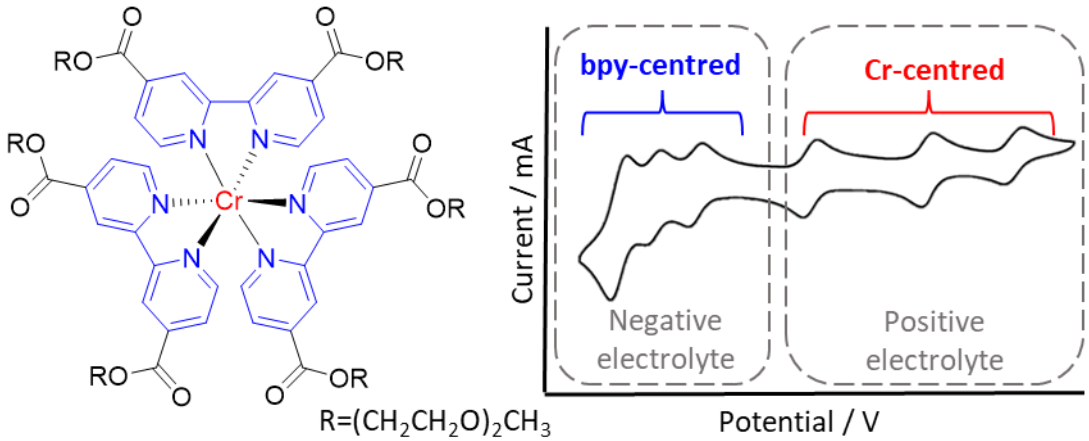

Figure 1.7. Structure and CV of functionalised $[Cr(bpy)_3]^{3+}$ coordination complex investigated for symmetric nonaqueous RFBs. Figure was adapted with permission from reference 60. Copyright © 2015, American Chemical Society.

The chromium-centred bpy coordination complex, $[Cr(bpy)_3]^{3+}$ is of particular note due to the six one-electron reversible redox processes observed over a 2 V window.[60] Figure 1.7 shows the structure and cyclic voltammogram (CV) of $[Cr(bpy)_3]^{3+}$. The three most positive redox couples were attributed to the Cr^{3+}/Cr^{2+}, Cr^{2+}/Cr^{1+} and Cr^{1+}/Cr transitions, while the three most negative redox processes were ascribed to reduction of the three bpy ligands. The authors sought to enhance solubility in acetonitrile through ester-functionalisation of the bpy ligands. The complex functionalised with the most polar and flexible R group, (2-(2-methoxyethoxy)ethyl), showed the most promising redox properties and solubility and was selected for battery testing. Galvanostatic cycling in a H-cell showed poor cycling stability when charged by three electrons but relatively stable performance when charged by two.

The saturation concentration of both the neutral and 3+ complexes was tested and as anticipated the solubility was dramatically reduced in the neutral form. Despite the promising multi-electron redox properties of $[Cr(bpy)_3]^{3+}$, the poor solubility of the neutral complex (0.21 M in acetonitrile) and inadequate stability upon cycling, meant that the E_v of the system was limited to 10.2 Wh L^{-1}.

1.3.3 Polyoxometalates charge carriers

Polyoxometalates (POMs) are a class of discrete metal-oxide nano clusters composed of early transition metals bound by bridging and terminal oxo-ligands. They represent an emerging and promising class of charge carriers for RFBs due to their ability to reversibly store multiple electrons per molecule.[61–63] We present an introduction to this important class of molecules before reviewing the literature precedent in the context of RFBs.

1.3.3.a Introduction to polyoxometalates

The vast structural diversity, excellent stability and rich electrochemistry of POMs has seen their application is diverse fields such as photo- and electrocatalysis,[64] medicine,[65] magnetism,[66] and energy conversion and storage technologies.[62] They are composed of metal oxide polyhedra of the general formula $[MO_y]$, where y=4-7, which cluster via corner, edge and/or face-sharing oxygen ligands. The metal centre, M, is termed the addenda atom and is typically an early transition metal such as V, Nb, Ta, Mo or W in its highest oxidation state (d^0 or d^1). POMs can broadly be classified into two categories; isopolyoxometalates, represented by the general formula $[M_mO_y]^{n-}$, and heteropolyoxometalates, of the general formula $[X_xM_mO_y]^{n-}$, which contain a heteroatom centre, X, usually a main group element such P, S, Si, or As.

POMs are synthesised through self-assembly in aqueous acidic conditions as seen in figure 1.8. Their synthesis is facilitated by the protonation of $[MO_y]^{n-}$ which forms labile water ligands. The increased Lewis acidity of the metal centre and lability of the water ligands facilitate a polycondensation reaction of the metal oxoanions.[61] For the synthesis of heteropolyoxometalates, a salt of the heteroanion is added for the metal oxide polyhedra to condense around. Typically, a source of counter cations is added

to balance the negative charge of the polyanion and facilitate precipitation and isolation of the product. The formation of discrete POM clusters rather than extended metal-oxide matrixes is explained by the stabilising thermodynamic trans-effect of the terminal oxo-ligands. The short and highly polarised terminal M=O bond weakens and lengthens the M-O bond at the opposite side (trans) of the polyhedron. This displaces the metal centre towards the terminal oxygen, thereby reducing its basicity and preventing further protonation and condensation reactions from proceeding.[67] The reaction is highly sensitive to pH, temperature, solvent, and ratio of starting materials and can be tuned to yield the desired structure.

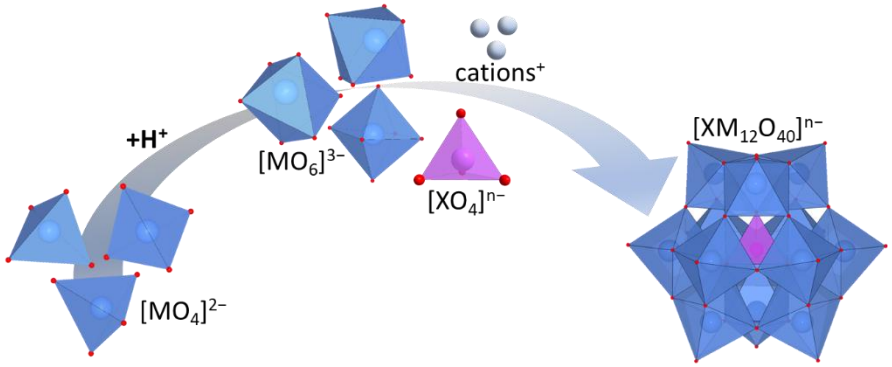

Figure 1.8. Schematic of a generic acid mediated polycondensation reaction of metal oxoanions into POMs. Colour code; blue polyhedra = $[MO_y]^{n-}$, magenta polyhedra = $[XO_4]^{n-}$, grey spheres = cations, red spheres = oxygen.

The structural diversity of POMs is almost infinite but several structural geometries are frequently observed, namely Lindqvist, Keggin and Wells-Dawson structures (figure 1.9). The Lindqvist structure is an isopolyoxometalate composed of six edge-sharing octahedral $[MO_6]$ units and has the general formula of $[M_6O_{19}]^{n-}$. The Keggin structure has the formula $[XM_{12}O_{40}]^{n-}$ and is regarded as one of the most stable and well-studied POM structures. The crystallographic structure of $H_3[PW_{12}O_{40}]$ was first solved in 1933 by J. F. Keggin.[68] The Wells-Dawson structure contains two heteroatom centres and has the general formula $[X_2M_{18}O_{62}]^{n-}$. The removal of one or more metal oxide polyhedra from the POM structure, results in a defective structure known as lacunary POMs. They are synthesised either by controlled decomposition of the parents POM (addition of base) or through 'bottom up' reactions under precise pH control.[69] The vacant site(s) have unshared bridging oxygen atoms allowing for

covalent grafting of anchoring groups or metal cations. Figure 1.9c and e show the structures of the mono lacunary Keggin and Wells-Dawson respectively.

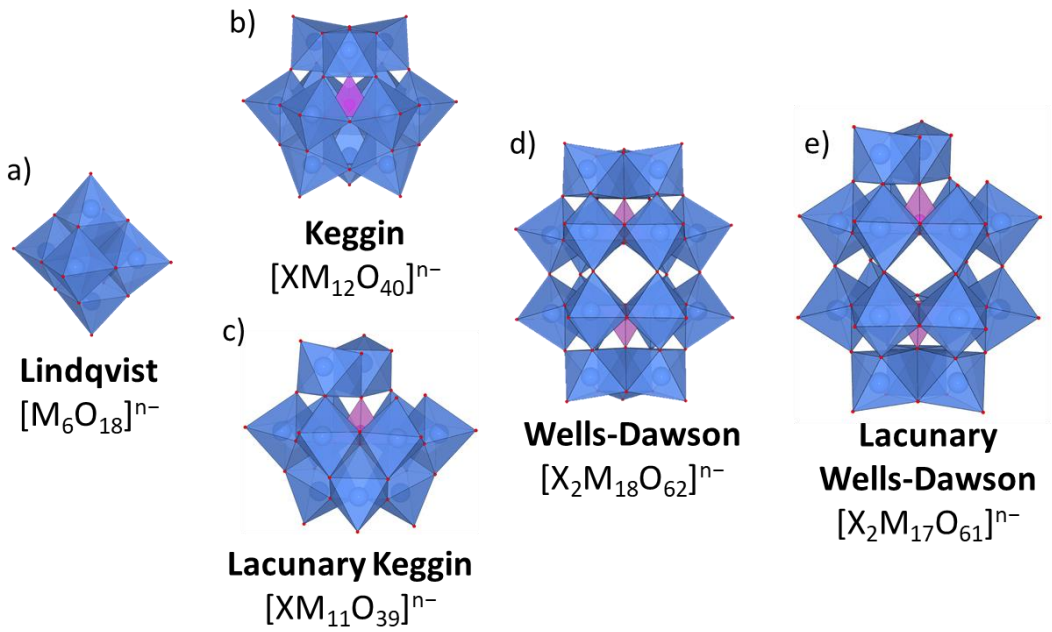

Figure 1.9. Generic structure and formula for the three most frequently reported POM geometries; a) Lindqvist, b) Keggin and d) Wells-Dawson and the mono lacunary structures of c) Keggin and e) Wells-Dawson. Colour code; blue polyhedra = $[MO_y]^{n-}$, magenta polyhedra = $[XO_4]^{n-}$, red spheres = oxygen.

POMs are composed of a framework of highly oxidised transition metals, enabling them to undergo rapid and often multi-electron redox processes. Upon reduction, electrons are accepted into non-bonding orbitals meaning that reduced POMs retain the structure of the parent compound.[70] A characteristic blue colour is observed upon reduction of POMs giving them the name 'heteropoly blues'. The intense blue colour was first observed in reduced molybdates and is the result of rapid electron transfer between the metal centres within the POM core known as intervalence charge-transfer (IVCT).[70] In highly symmetrical POMs such as the Lindqvist and Keggin structures, a large degree of electron delocalisation is observed between the identical addenda atoms. A characteristic absorption signal can be observed in the low energy visible and infrared absorption spectra which provides a valuable diagnostic tool in monitoring the reduced states of POMs.[71]

1.3.3.b Introduction to hybrid polyoxometalates

The interaction of POM clusters with inorganic or organic substituents to create hybrid POMs, often results in a molecular species with modified properties or additional functionality. Hybridisation can be achieved through a range of methodologies. Inorganic hybrid POMs are those with transition metals or f-block metals integrated into the POM structure (see figure 1.10a). They are typically synthesised through post-synthetic addition of the metal centre to a lacunary POM.[69]

Organic-inorganic hybrid POMs can be classified into two categories based on the nature of the interaction of the organic component and inorganic POM core. Class I hybrids are those where the organic and inorganic component are not bound covalently and are instead interacting through hydrogen, electrostatic, or van der Waals interactions. The archetypal class I hybrid is the electrostatic interaction of anionic POM clusters with cationic salts (see figure 1.10b). They can be accessed easily through salt metathesis reactions and can have a profound effect on the solubility, electrochemical properties and even the supramolecular structure of the POM.[72] However, the weak interaction between the inorganic core and organic moiety leave the material prone to dissociation (especially in solution phase) and further ion metathesis.

Class II hybrids have organic substituents covalently grafted to the inorganic core of the POM (see figure 1.10c).[73] The covalent linkage gives a robust connection between the inorganic and organic moieties and superior control over the geographic location of the components with respect to one another. The organic moiety is generally bound to the POM core via an anchoring group which greatly influences the degree of functionalisation, overall charge and redox properties of the final product.[74] The archetypal anchoring groups are organosilicates, organogermanates, organotin, organophosphonates, tripodal alcohols such as 1,1,1-tris(hydroxymethyl)alkanes (TRIOL) and N-containing organics such as imido.[74] Anchoring groups are typically grafted to the POM core via oxygen groups in the vacant site(s) of lacunary POMs. Importantly, the addition of an electron withdrawing group or electron donating group to the POM, has the effect of shifting the redox potential of the resulting hybrid POM to more positive or negative potentials respectively.

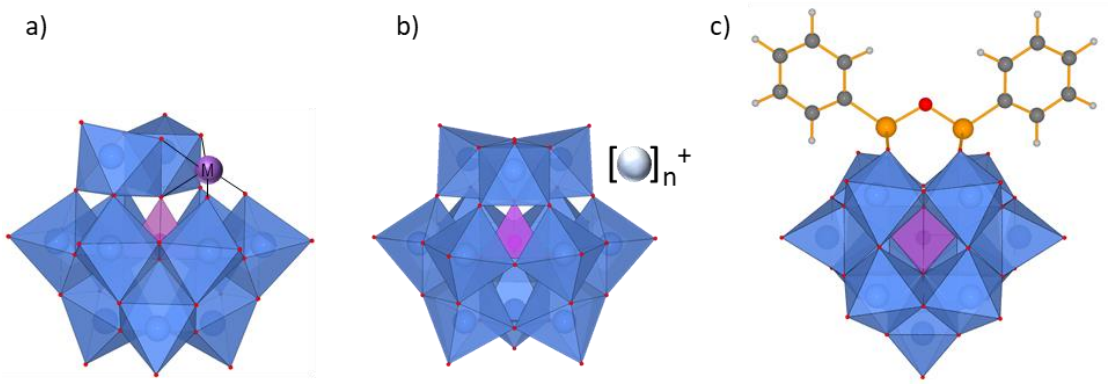

Figure 1.10. Polyhedral and ball and stick representations of three hybrid POM structures. a) Inorganic hybrid POM (metal substitution), b) class I organic-inorganic hybrid POM (non-covalent bond) and c) class II organic-inorganic hybrid POM (covalent bond). Colour code; blue polyhedra = $[MO_y]^{n-}$, magenta polyhedra = $[XO_4]^{n-}$, red spheres = oxygen, purple sphere = transition or f-block metal and grey sphere = organic cation.

1.3.3.c Polyoxometalate charge carriers

The earliest work on POM-based charge carriers for RFBs was conducted by Anderson and co-workers, who used the tri-vanadium substituted silicotungstate Keggin, $K_6H[SiV_3W_9O_{40}]$ (SiV_3W_9), in a symmetric aqueous system.[75] The POM undergoes a three-electron reduction centred at the vanadium metals and a further two, two-electron reduction processes centred at the tungsten metals. The vanadium-centred redox processes were separated from those of the tungsten by 0.8 V allowing for the application of SiV_3W_9 in a symmetric system. Prior to galvanostatic cycling, the charge carrier was reduced to $[SiV_3W_9O_{40}]^{13-}$ by bulk electrolysis to generate the fully charged negative electrolyte. Galvanostatic cycling in a 5 cm^2 RFB showed CE of >95% and modest capacity fade of 0.02% per cycle over 100 cycles. Following 100 cycles, the electrolyte solution was recovered and used in a fresh cell with a new membrane. Full performance was restored suggesting that any capacity losses observed were not the result of POM degradation. Given the saturation concentration of SiV_3W_9 in water of 0.45 M, the three-electron redox reaction upon charge and discharge and V_{cell} of approximately 0.8 V, the theoretical E_v was calculated to be 14.5 Wh L^{-1}. While the E_v is half that of the VRFB, this publication pioneered a new class of charge carrier with stable multi-electron redox processes. Anderson and colleagues investigated several more mixed addenda POMs, including tri-vanadium substituted Keggin and Wells-Dawson phosphotunsgstates,[76] $K_6[PV_3W_9O_{40}]$ and $K_8H[P_2V_3W_{15}O_{62}]$, the Lindqvist

ion, $Li_4[V_2W_4O_{19}]$, and the iron-containing silicotungstate dimer, $K_4Na_7[SiFe_3W_9(OH)_3O_{34})_2(OH)_3]$.[77]

Lu and Xiang extended the library of POM-based charge carriers to include the cobalt-centred tungstic acid, $H_6[CoW_{12}O_{40}]$ (CoW_{12}).[78] Similarly to SiV_3W_9, the tungsten-centred redox processes of the POM were targeted in the negative electrolyte (two, two-electron reduction processes), while in this case, the one-electron oxidation of the central cobalt atom from 2+ to 3+ was targeted in the positive electrolyte. The separation of the cobalt- and tungsten-centred redox processes allowed for a larger V_{cell} of 1.24 V (0.8 V for SiV_3W_9). However, the positive electrolyte required four equivalents of CoW_{12} to balance the four-electron redox process occurring in the negative electrolyte. The laboratory-scale flow battery achieved CE >98% and good capacity retention over 30 cycles. Given the saturation concentration of CoW_{12} in water of 0.8 M, the theoretical E_v was calculated to be 13.3 Wh L^{-1} (accounting for necessary balance of POM equivalents in the positive and negative electrolyte).

Stimming and colleagues sought to maximise the rich electrochemistry of POMs by designing an asymmetric RFB with different POM-based charge carriers in the positive and negative electrolyte.[79] They investigated an asymmetric aqueous RFB using $[PV_{14}O_{42}]^{9-}$ (PV_{14}) and $[SiW_{12}O_{40}]^{4-}$ (SiW_{12}) as charge carriers for the positive and negative electrolyte respectively. PV_{14} is reversibly reduced by seven electrons in a single process at a relatively positive redox potential of 0.60 V *vs.* SHE. CV of SiW_{12} has two reversible one-electron reduction processes with redox potentials of 0.01 V and −0.21 V *vs.* SHE. SiW_{12} can be reduced by a further two-electrons but only the first two one-electron redox couples are accessible without significant hydrogen evolution. Consequently, a flow cell was assembled with two equivalents of SiW_{12} (n=2) to balance the multi-electron redox process of PV_{14} (n=4). Prior to galvanostatic cycling, PV_{14} was reduced by the addition of hydrazine to attain the discharged positive electrolyte. With an average V_{cell} of approximately 0.8 V and limited solubility of PV_{14} (demonstrated at 0.3 M), the theoretical E_v was calculated to be 13 Wh L^{-1}. Successful charge-discharge cycling was demonstrated in a 25 cm^2 flow cell and later upscaled to a 1400 cm^2 system, which remained stable over a 3 month period.[80] This provided a rare example of a next-generation RFB systems being tested at scale for

extended periods of time. Capacity fade was attributed to the reoxidation of reduced POMs from trace oxygen which could be avoided with an airtight setup.

A step change in E_v came from the work of Cronin and co-workers where $Li_6[P_2W_{18}O_{40}]$ (P_2W_{18}) was reversibly reduced by 18 electrons in aqueous acidic conditions (see figure 1.11).[81] The authors found that the electrochemical properties of P_2W_{18} was highly dependent on pH and concentration and that reversible reduction by 18 electrons was only achievable at concentrations >100 mM under acidic conditions. Paired with HBr/Br_2 positive electrolyte, the asymmetric RFB demonstrated a V_{cell} of 1.25 V equating to a practical E_v of 225 Wh L^{-1}. Extrapolated to the saturation concentration of P_2W_{18} in water of 1.9 M, and assuming equivalent concentrations are achievable in the presence of supporting electrolyte, the authors calculate a theoretical E_v of >1000 Wh L^{-1}. It should be noted that while the saturation concentration of HBr/Br_2 is reported in the literature to be very high,[82] the authors appear not to account for the volume of positive electrolyte in the E_v calculations.

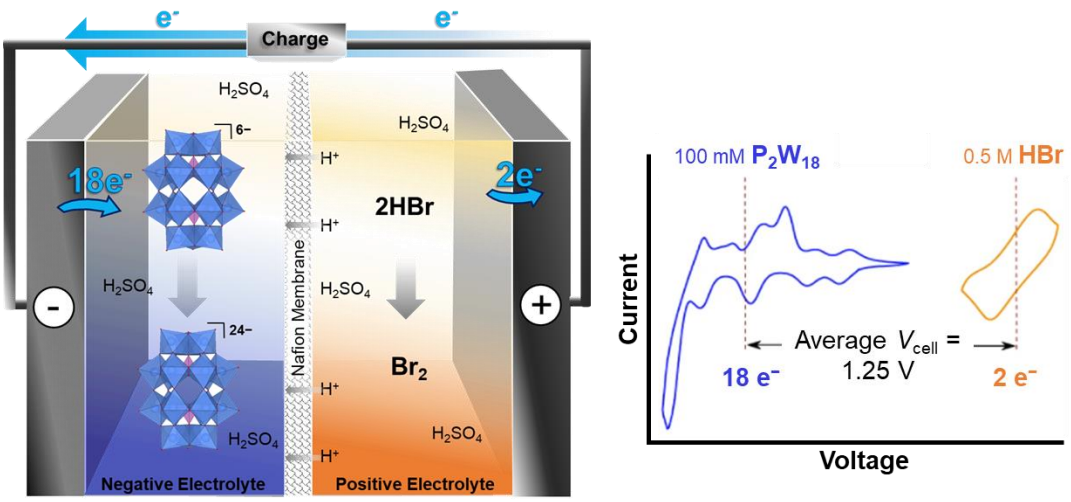

Figure 1.11. Schematic of an aqueous asymmetric RFB with P_2W_{18} negative electrolyte and HBr positive electrolyte. Upon charge P_2W_{18} undergoes an 18 electrons proton coupled reduction, while 2HBr is oxidised to Br_2. The concentration of HBr is 18 times that of P_2W_{18} in order to balance the redox reaction. The CV of each charge carrier is shown on the right. Adapted with permission from Nature Chemistry, copyright 2018, reference 81.

Under aqueous conditions, only some of the multi-electron redox processes of POMs can be accessed without the risk of parasitic reactions such as hydrogen evolution upon charge. The wide window of electrochemical stability offered by nonaqueous

solvent is thought to allow access to more redox processes of the POM and thereby enhance the E_v of the resulting RFB. However, without targeted modification, the solubility of POMs in nonaqueous solvent is limited. In an effort to enhance the solubility of SiV_3W_9 in nonaqueous solvent, Anderson and co-workers conducted metathesis of the potassium counter cations to tetrabutylammonium (TBA).[75] The TBA analogue of SiV_3W_9 was soluble in acetonitrile, propylene carbonate and methanol, but the redox processes became electrochemically irreversible in propylene carbonate, and was not explored further.

Barteau and colleagues were the first to report the application of POMs as charge carriers in nonaqueous RFBs.[83] They investigated the lithium salt of the Keggin phosphomolybdate, $Li_3[PMo_{12}O_{40}]$ (PMo_{12}), in acetonitrile with lithium trifluoromethanesulfonate (LiTf) supporting electrolyte. PMo_{12} undergoes two, one-electron quasi-reversible reductions centred at −0.21 V and −0.57 V *vs.* $Ag^+|Ag$. For application in a symmetric system, the PMo_{12} electrolyte was first electrochemically reduced by one-electron to generate the discharged positive and negative electrolyte. Galvanostatic cycling was conducted with a one-electron redox reaction upon charge and discharge. As stated by the authors, this system does not exploit the full capabilities of POMs as multi-electron charge carriers nor the wide window of electrochemical stability provided by the nonaqueous solvents. CE of 68% was achieved, which was substantially lower than that achieved for aqueous POM-based RFBs. The low CE was attributed to crossover of the POM through the membrane, a common cause of inefficiency in nonaqueous RFBs.[35] The saturation concentration of PMo_{12} in acetonitrile is relatively high at 0.8 M, but with only a one-electron redox reaction and V_{cell} of 0.35 V, the theoretical E_v was calculated to be 3.8 Wh L^{-1}.

While PMo_{12} can be reversibly reduced by two electrons in acetonitrile, in dimethylformamide (DMF), PMo_{12} can be reduced by an additional two electrons, enhancing the number of electrons transferred in the charge/discharge redox reaction to two and increasing V_{cell} to 0.45 V.[84] The saturation concentration of PMo_{12} in DMF was reported to be 1.2 M, enhancing the theoretical E_v to 14.5 Wh L^{-1}. Barteau and co-workers later expanded the investigation to include an asymmetric RFB with PMo_{12} and P_2W_{18} as charge carriers in the positive and negative electrolyte

respectively.[84] The systems had a V_{cell} of 1.3 V and the number of electrons transferred upon charge/discharge increased to four, thereby further enhancing E_v.

The first example of significant molecular engineering of POMs to enhance solubility in nonaqueous solvent came from Matson and co-workers who investigated polyoxovanadate (POV) alkoxide clusters of the general formula $V_6O_5(OR)_{12}$ (where R = CH_3, C_2H_5).[85] These materials display four one-electron redox couples over a potential range of 2 V, enabling their application in a symmetric system with two-electron transfer upon charge and discharge. Upon charge the POV undergoes a two-electron reduction at the negative electrode concurrently with a two-electron oxidation at the positive electrode. The research was extended to investigate alternative organic functionalisation of the POV surface (see figure 1.12). Introduction of a TRIOL ligand, increased solubility in acetonitrile to 0.6 M and the charge carriers cycling stability was retained.[86] In a separate study the solubility of POVs was increased by replacing several surface alkoxy groups with ethers, R=$C_2H_4OCH_3$, $C_2H_4OC_2H_5$.[87] Clusters with a mixture of alkoxide and ether groups showed an impressive solubility of 1.2 M in 0.1 M [TBA][PF_6] in acetonitrile. While the increased solubility in organic solvent and multi-electron redox chemistry is promising for enhanced E_v, preliminary testing of the alkoxide-ether functionalised POVs in a laboratory-scale RFB showed steady capacity fade. CV of electrolytes following 30 cycles in a RFB indicated partial degradation of the POV clusters.

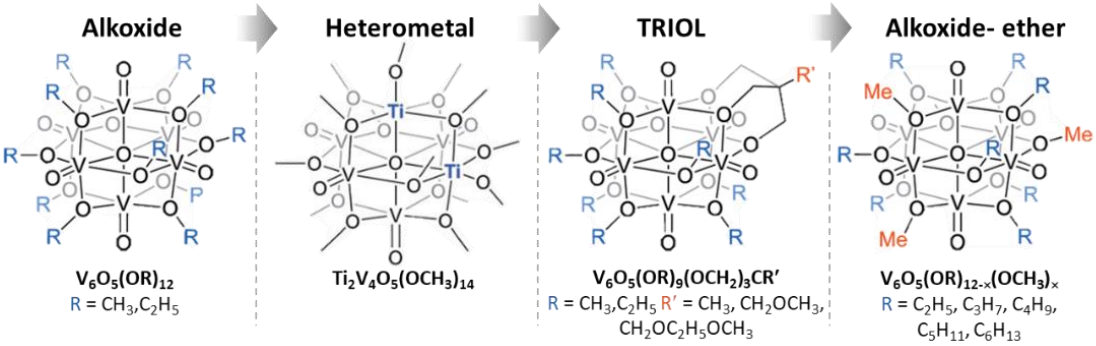

Figure 1.12. Summary of functionalised POV charge carriers investigated by Matson and colleagues for symmetric nonaqueous RFBs. Structures were adapted from references 85-87.

Yan and colleagues explored the use of a sulfur-templated Wells-Dawson POM, $TBA_4[S_2W_{18}O_{62}]$ (S_2W_{18}), as charge carrier in both symmetric and asymmetric

nonaqueous RFBs.[88] In the asymmetric system benzophenone was chosen as the charge carrier for the negative electrolyte (structure shown in figure 1.5). Benzophenone undergoes a reversible one-electron reduction with a redox potential of −1.75 V *vs.* $Ag^+|Ag$, while S_2W_{18} can be reversible reduced by one electron, a second electron, then two electrons with redox potentials of 0.23, −0.15 and −0.49 V *vs.* $Ag^+|Ag$. In the asymmetric RFB, four equivalents of benzophenone (n=1) were used to balance the four-electron redox process of S_2W_{18} (n=4). Although not stated by the authors, reduction of S_2W_{18} to generate discharged positive electrolyte (or reduction of benzophenone to generate charged negative electrolyte) would have been necessary prior to galvanostatic cycling. The flow cell cycled successfully with V_{cell} of 1.54 V. Based on the saturation concentration of S_2W_{18} in acetonitrile of 0.11 M, the theoretical E_v was calculated to be 9.4 Wh L^{-1}.

Table 1.2 lists POM-based charge carriers investigated in both aqueous and nonaqueous RFBs. The theoretical E_v of the RFBs were calculated based on Eq. 1.1. The theoretical E_v does not consider the stability and solubility of the charge carrier in each oxidation state, and therefore does not reflect the practical E_v of each system.

Table 1.2. A summary of POM-based charge carriers investigated for RFBs. Theoretical E_v was calculated based on the saturation concentration of the POM in the given electrolytes, and the V_{cell} and *n* value of the resulting RFBs. V_{cell} was estimated based on the CV of the charge carriers. *projected value from authors.

Positive (C_{active} /M)	**Negative** (C_{active} /M)	**Electrolyte**	V_{cell} / V	***n* (pos./neg.)**	**Theoretical E_v / Wh L^{-1}**	**Realised E_v / Wh L^{-1}**	**Ref.**
SiV_3W_9 (0.45)		Aqueous, H_2SO_4	0.8	3/3	14.5	0.6	[75]
CoW_{12} (0.8)		Aqueous, H_2SO_4	1.24	1/4	13.3	13.3	[78]
PV_{14} (0.3)	SiW_{12} (0.88)	Aqueous, LiCl	0.8	4/2	13	4.3	[79,80]
HBr/Br_2 (-)	PW_{18} (1.9)	Aqueous, H_2SO_4	1.25	1/18	1000*	225*	[81]
PMo_{12} (0.8)		Acetonitrile, LiTf	0.35	1/1	4	0.05	[83]
PMo_{12} (0.8)		DMF, LiTf	0.45	2/2	14.5	1.2	[84]
PMo_{12} (0.8)	PW_{18} (-)	DMF, LiTf	1.3	4/4	-	-	[84]
$V_6O_7(OC_2H_5)_{12}$ (0.05)		Acetonitrile, TBA PF_6	1.12	2/2	1.5	0.3	[85]
$V_5TiO_6(OCH_3)_{14}$ (0.51)		Acetonitrile, TBA PF_6	2.30	1/1	15.8	0.2	[89]
$V_6O_7(OC_2H_5)_9(TRIS^{R'})$ R′= $CH_2OC_2H_4OCH_3$ (0.59)		Acetonitrile, TBA PF_6	1.09	2/2	17.1	0.3	[86]
$V_6O_7(OR)_{12}$ R=alkoxy/ether (1.17)		Acetonitrile, TBA PF_6	*ca.* 0.99	2/2	30.9	0.03	[87]
S_2W_{18} (0.11)	Benzophenone	Acetonitrile, TBA PF_6	1.54	4/1	9.4	8.3	[88]

1.4. Conclusions

RFBs are ideally suited to grid-scale energy storage application due to their unparalleled calendar and cycle life and ease of scale up compared to conventional batteries. These advantages incentivise research and development of RFBs which is currently ongoing. The commercial uptake of VRFBs is increasing but the challenges of high cost and low E_v have prompted research into next-generation RFBs.

Here, we present an overview of charge carriers for next-generation RFBs and highlight multi-electron charge carriers such as POMs and fullerenes as some of the most promising classes. POMs undergo multi-electron redox processes spanning a broad potential range, making them promising charge carriers for symmetric system and for high-E_v RFBs. Since the first investigation of POMs as charge carriers in 2013, several types of POM have been studied. Many aspects of the POM chemistry have been explored including various addenda metals, heteroatoms, geometries, counter cations, and hybridisation methodologies. However, given the diversity of this class of charge carrier, the field of POM-based RFBs is still in its infancy.

The narrow window of electrochemical stability of aqueous electrolyte, prevents access to all the redox processes of POMs without the onset of parasitic reactions. The wider window of electrochemical stability of nonaqueous electrolytes, allows access to more redox processes of POMs and therefore has the potential to enable high V_{cell} and E_v RFBs. To date, very few examples of POM-based charge carriers in nonaqueous electrolyte have been investigated. Matson and colleagues were able to enhance the solubility of POVs through organofunctionalisation with alkoxy, ethoxy and TRIOL groups. POVs represent a fraction of the POM diversity and therefore there is great scope to expand on this concept and explore other organic-inorganic hybrid POMs.

Fullerenes represent another class of multi-electron charge carrier with promising credentials for RFBs. A major drawback of fullerene is its poor solubility in many solvents. However, functionalisation is known to enhance solubility and similarly to POMs, the functionalisation strategies of fullerenes are almost infinite. Thus far, very

few variants have been investigated for RFBs and there is great opportunity for development here.

1.5. Thesis Aims

The work presented in this thesis aimed to address the challenge of low E_v RFBs in order to enhance their viability as commercial energy storage devices. An initial research objective was to design and synthesise charge carriers with multi-electron redox processes and high solubility in nonaqueous solvent to yield energy dense electrolytes. A secondary objective was to investigate the potential of such redox species as charge carriers for RFBs by means of electrochemical characterisation and analysis of their performance in low concentration laboratory-scale RFBs.

Two different categories of multi-electron charge carriers were explored; POMs and fullerenes. There are very few investigations of POM-based charge carriers in nonaqueous electrolyte reported in the literature, in part due to the unfavourable solubility of POMs in organic solvent. This work set out to enhance the solubility of POMs in nonaqueous solvent through grafting of an organic moiety to the inorganic POM core. Furthermore, this work aimed to investigate the performance of these so called organic-inorganic hybrid POMs in nonaqueous RFBs for the first time. The multi-electron redox properties of POMs, allowed for their investigation in symmetric and asymmetric RFBs, enabling the exploration of systems with high theoretical E_v.

This research also set out to better understand the potential of functionalised fullerene species as charge carriers for nonaqueous RFBs. Specifically, a key research objective was to enhance the solubility of a previously reported C_{60}Fc bifunctional charge carrier through organic modification. Furthermore, this work aimed to investigate this class of charge carrier in a laboratory-scale RFB for the first time, thereby allowing a detailed understanding of the molecules strengths and limitations for application in RFBs.

1.6. References

1 T. M. Gür, *Energy Environ. Sci.*, 2018, **11**, 2696–2767.

2 R. Neukom, L. A. Barboza, M. P. Erb, F. Shi, J. Emile-Geay, M. N. Evans, J. Franke, D. S. Kaufman, L. Lücke, K. Rehfeld, A. Schurer, F. Zhu, S. Brönnimann, G. J. Hakim, B. J. Henley, F. C. Ljungqvist, N. McKay, V. Valler and L. von Gunten, *Nat. Geosci.*, 2019, **12**, 643–649.

3 J. R. Biden, Executive order on tackling the climate crisis at home and abroad, https://www.whitehouse.gov/briefing-room/presidential-actions/2021/01/27/executive-order-on-tackling-the-climate-crisis-at-home-and-abroad/, accessed January 2022.

4 International Energy Agency, WEO 2017 - Executive Summary - English version, 2017.

5 DOE-EIS International Energy Outlook 2021, Washington, 2021.

6 K. Engeland, M. Borga, J. D. Creutin, B. François, M. H. Ramos and J. P. Vidal, *Renew. Sustain. Energy Rev.*, 2017, **79**, 600–617.

7 A. Castillo and D. F. Gayme, *Energy Convers. Manag.*, 2014, **87**, 885–894.

8 J. Andrews and N. Jelley, Energy Science, Oxford University Press, second., 2013.

9 EPRI, Electricity energy storage technology options: a white paper primer on applications, costs, and benefits, Palo Alto, CA, 2010.

10 D. Larcher and J. M. Tarascon, *Nat. Chem.*, 2015, **7**, 19–29.

11 J. Cho, S. Jeong and Y. Kim, *Prog. Energy Combust. Sci.*, 2015, **48**, 84–101.

12 G. J. May, A. Davidson and B. Monahov, *J. Energy Storage*, 2018, **15**, 145–157.

13 Z. Yang, J. Zhang, M. C. W. Kintner-Meyer, X. Lu, D. Choi, J. P. Lemmon and J. Liu, *Chem. Rev.*, 2011, **111**, 3577–3613.

14 B. Dunn, H. Kamath and J.-M. Tarascon, *Science*, 2011, **334**, 928–935.

15 The Nobel Prize, The Nobel Prize in Chemistry 2019, https://www.nobelprize.org/prizes/chemistry/2019/summary/, accessed June 2022.

16 J. M. Cameron, C. Holc, A. J. Kibler, C. L. Peake, D. A. Walsh, G. N. Newton and L. R. Johnson, *Chem. Soc. Rev.*, 2021, **50**, 5863–5883.

17 L. Trahey, F. R. Brushett, N. P. Balsara, G. Ceder, L. Cheng, Y. M. Chiang, N. T. Hahn, B. J. Ingram, S. D. Minteer, J. S. Moore, K. T. Mueller, L. F. Nazar, K. A. Persson, D. J. Siegel, K. Xu, K. R. Zavadil, V. Srinivasan and G. W. Crabtree, *Proc. Natl. Acad. Sci. U. S. A.*, 2020, **117**, 12550–12557.

18 BBC, Tesla mega-battery in Australia activated, http://www.bbc.co.uk/news/world-australia-42190358, accessed June 2022.

19 A. Mahmoudzadeh Andwari, A. Pesiridis, S. Rajoo, R. Martinez-Botas and V. Esfahanian, *Renew. Sustain. Energy Rev.*, 2017, **78**, 414–430.

20 AmericanChemicalSociety, Endangered Elements - American Chemical Society, https://www.acs.org/content/acs/en/greenchemistry/research-innovation/endangered-elements.html, accessed March 2022.

21 G. N. Newton, L. R. Johnson, D. A. Walsh, B. J. Hwang and H. Han, *ACS Sustain. Chem. Eng.,* 2021, **9**, 6507–6509.

22 A. Luntz, *J. Phys. Chem. Lett.*, 2015, **6**, 300–301.

23 E. Sánchez-Díez, E. Ventosa, M. Guarnieri, A. Trovò, C. Flox, R. Marcilla, F. Soavi, P. Mazur, E. Aranzabe and R. Ferret, *J. Power Sources*, 2021, **481**, 228804.

24 P. Leung, X. Li, C. Ponce De León, L. Berlouis, C. T. J. Low and F. C. Walsh, *RSC Adv.*, 2012, **2**, 10125–10156.

25 L. Thaller, in Terestrial Energy Systems Conference, Orlando, Florida, US, 1979.

26 S. Roe, C. Menictas and M. Skyllas-Kazacos, *J. Electrochem. Soc.*, 2016, **163**, A5023–A5028.

27 P. Zhao, H. Zhang, H. Zhou, J. Chen, S. Gao and B. Yi, *J. Power Sources*, 2006, **162**, 1416–1420.

28 Vanitec, Vanadium Redox Flow Battery Companies, http://www.vanitec.org/vanadium-redox-flow-battery-vrfb-companies, accessed November 2021.

29 R. Dmello, J. D. Milshtein, F. R. Brushett and K. C. Smith, *J. Power Sources*, 2016, **330**, 261–272.

30 GRIDS: Grid-Scale Rampable Intermittent Dispatchable Storage, USA, 2010.

31 K. Lourenssen, J. Williams, F. Ahmadpour, R. Clemmer and S. Tasnim, *J. Energy Storage*, 2019, **25**, 100844.

32 X. Wei, W. Pan, W. Duan, A. Hollas, Z. Yang, B. Li, Z. Nie, J. Liu, D. Reed, W. Wang and V. L. Sprenkle, *ACS Energy Lett.*, 2017, **2**, 2187–2204.

33 K. Gong, Q. Fang, S. Gu, S. F. Y. Li and Y. Yan, *Energy Environ. Sci.*, 2015, **8**, 3515–3530.

34 T. Ma, Z. Pan, L. Miao, C. Chen, M. Han, Z. Shang and J. Chen, *Angew. Chemie*, 2018, **130**, 3212–3216.

35 J. Yuan, Z. Z. Pan, Y. Jin, Q. Qiu, C. Zhang, Y. Zhao and Y. Li, *J. Power Sources*, 2021, **500**, 229983.

36 Z. Liang, N. H. Attanayake, K. V. Greco, B. J. Neyhouse, J. L. Barton, A. P. Kaur, W. L. Eubanks, F. R. Brushett, J. Landon and S. A. Odom, *ACS Appl. Energy Mater.*, 2021, **4**, 5443–5451.

37 M. Skyllas-Kazacos, M. Rychcik, R. G. Robins, A. G. Fane and M. A. Green, *J. Electrochem. Soc.*, 1986, **133**, 1057–1058.

38 N. Roznyatovskaya, T. Herr, M. Küttinger, M. Fühl, J. Noack, K. Pinkwart and J. Tübke, *J. Power Sources*, 2016, **302**, 79–83.

39 B. Yang, L. Hoober-Burkhardt, F. Wang, G. K. Surya Prakash and S. R. Narayanan, *J. Electrochem. Soc.*, 2014, **161**, A1371–A1380.

40 B. Huskinson, M. P. Marshak, C. Suh, S. Er, M. R. Gerhardt, C. J. Galvin, X. Chen, A. Aspuru-Guzik, R. G. Gordon and M. J. Aziz, *Nature*, 2014, **505**, 195–198.

41 K. Lin, Q. Chen, M. R. Gerhardt, L. Tong, S. B. Kim, L. Eisenach, A. W. Valle, D. Hardee, R. G. Gordon, M. J. Aziz and M. P. Marshak, *Science*, 2015, **349**, 1529–1532.

42 M. Wu, Y. Jing, A. A. Wong, E. M. Fell, S. Jin, Z. Tang, R. G. Gordon and M. J. Aziz, *Chem*, 2020, **6**, 1432–1442.

43 Y. Jing, M. Wu, A. A. Wong, E. M. Fell, S. Jin, D. A. Pollack, E. F. Kerr, R. G. Gordon and M. J. Aziz, *Green Chem.*, 2020, **22**, 6084–6092.

44 Y. Zhao, J. Zhang, G. Agarwal, Z. Yu, R. E. Corman, Y. Wang, L. A. Robertson, Z. Shi, H. A. Doan, R. H. Ewoldt, I. A. Shkrob, R. S. Assary, L. Cheng, V. Srinivasan, S. J. Babinec and L. Zhang, *J. Mater. Chem. A*, 2021, **9**, 16769–16775.

45 Z. Li, S. Li, S. Liu, K. Huang, D. Fang, F. Wang and S. Peng, *Electrochem. Solid-State Lett.*, 2011, **14**, A171–A173.

46 X. Wei, W. Xu, M. Vijayakumar, L. Cosimbescu, T. Liu, V. Sprenkle and W. Wang, *Adv. Mater.*, 2014, **26**, 7649–7653.

47 B. Ok, W. Na, T. H. Kwon, Y. W. Kwon, S. Cho, S. M. Hong, A. S. Lee, J. H. Lee and C. M. Koo, *J. Ind. Eng. Chem.*, 2019, **80**, 545–550.

48 X. Yu, W. A. Yu and A. Manthiram, *ACS Appl. Mater. Interfaces*, 2020, **12**, 48654–48661.

49 C. S. Sevov, S. K. Samaroo and M. S. Sanford, *Adv. Energy Mater.*, 2017, **7**, 1602027.

50 S. G. Robinson, Y. Yan, K. H. Hendriks, M. S. Sanford and M. S. Sigman, *J. Am. Chem. Soc.*, 2019, **141**, 10171–10176.

51 Y. Yan, S. G. Robinson, M. S. Sigman and M. S. Sanford, *J. Am. Chem. Soc.*, 2019, **141**, 15301–15306.

52 Y. Yan, T. P. Vaid and M. S. Sanford, *J. Am. Chem. Soc.*, 2020, **142**, 17564–17571.

53 Y. Yan, D. B. Vogt, T. P. Vaid, M. S. Sigman and M. Sanford, *Angew. Chemie Int. Ed.*, 2021, **60**, 2–9.

54 L. Echegoyen and L. E. Echegoyen, *Acc. Chem. Res.*, 1998, **31**, 593–601.

55 N. Sivaraman, R. Dhamodaran, I. Kaliappan, T. G. Srinivasan, P. R. V. Rao and C. K. Mathews, *J. Org. Chem.*, 1992, **57**, 6077–6079.

56 J. Friedl, M. A. Lebedeva, K. Porfyrakis, U. Stimming and T. W. Chamberlain, *J. Am. Chem. Soc.*, 2018, **140**, 401–405.

57 R. S. Ruoff, D. S. Tse, R. Malhotra and D. C. Lorents, *J. Phys. Chem.*, 1993, **97**, 3379–3383.

58 R. W. Hogue and K. E. Toghill, *Curr. Opin. Electrochem.*, 2019, **18**, 37–45.

59 Y. Matsuda, K. Tanaka, M. Okada, Y. Takasu, M. Morita and T. Matsumura-Inoue, *J. Appl. Electrochem.*, 1988, **18**, 909–914.

60 P. J. Cabrera, X. Yang, J. A. Suttil, K. L. Hawthorne, R. E. M. Brooner, M. S. Sanford and L. T. Thompson, *J. Phys. Chem. C*, 2015, **119**, 15882–15889.

61 J. J. Borrás-Almenar, E. Coronado, A. Müller and M. Pope, Polyoxometallate Molecular Science, Tenerife, Spain, 1st edn., 2004.

62 Q. Li, L. Zhang, J. Dai, H. Tang, Q. Li, H. Xue and H. Pang, *Chem. Eng. J.*, 2018, **351**, 441–461.

63 T. Ueda, *ChemElectroChem*, 2018, **5**, 823–838.

64 S. S. Wang and G. Y. Yang, *Chem. Rev*., 2015, **115**, 4893–4962.

65 J. T. Rhule, C. L. Hill, D. A. Judd and R. F. Schinazi, *Chem. Rev.*, 1998, **98**, 327–357.

66 J. M. Clemente-Juan, E. Coronado and A. Gaita-Ariñoa, *Chem. Soc. Rev.*, 2012, **41**, 7464–7478.

67 L. C. W. Baker and D. C. Glick, *Chem. Rev.*, 1998, **98**, 3–49.

68 J. F. Keggin, *Proc. R. Soc. London*, 1934, **144**, 75–100.

69 A. Patel, N. Narkhede, S. Singh and S. Pathan, *Catal. Rev.,* 2016, **58**, 337–370.

70 N. I. Gumerova and A. Rompel, *Nat. Rev. Chem.*, 2018, **2**, 0112.

71 G. M. Varga, E. Papaconstantinou and M. T. Pope, *Inorg. Chem.*, 1970, **9**, 662–667.

72 A. Misra, K. Kozma, C. Streb and M. Nyman, *Angew. Chemie - Int. Ed.*, 2020, **59**, 596–612.

73 S. Berardi, M. Carraro, A. Sartorel, G. Modugno and M. Bonchio, Isr. *J. Chem.*, 2011, **51**, 259–274.

74 A. J. Kibler and G. N. Newton, *Polyhedron*, 2018, **154**, 1–20.

75 H. D. Pratt, N. S. Hudak, X. Fang and T. M. Anderson, *J. Power Sources*, 2013, **236**, 259–264.

76 H. D. Pratt and T. M. Anderson, *Dalt. Trans.*, 2013, **42**, 15650–15655.

77 H. D. Pratt, W. R. Pratt, X. Fang, N. S. Hudak and T. M. Anderson, *Electrochim. Acta*, 2014, **138**, 210–214.

78 Y. Liu, S. Lu, H. Wang, C. Yang, X. Su and Y. Xiang, *Adv. Energy Mater.*, 2017, **7**, 1601224.

79 J. Friedl, M. V Holland-Cunz, F. Cording, F. L. Pfanschilling, C. Wills, W. McFarlane, B. Schricker, R. Fleck, H. Wolfschmidt and U. Stimming, *Energy Environ. Sci.*, 2018, **11**, 3010–3018.

80 J. Friedl, F. L. Pfanschilling, M. V. Holland-Cunz, R. Fleck, B. Schricker, H. Wolfschmidt and U. Stimming, *Clean Energy*, 2019, **3**, 278–287.

81 J. J. Chen, M. D. Symes and L. Cronin, *Nat. Chem.*, 2018, **10**, 1042–1047.

82 M. Küttinger, J. K. Wlodarczyk, D. Daubner, P. Fischer and J. Tübke, *RSC Adv.*, 2021, **11**, 5218–5229.

83 J. J. J. Chen and M. A. Barteau, *J. Energy Storage*, 2017, **13**, 255–261.

84 Y. Cao, J. J. J. Chen and M. A. Barteau, *J. Energy Chem.*, 2020, **50**, 115–124.

85 L. E. Vangelder, A. M. Kosswattaarachchi, P. L. Forrestel, T. R. Cook and E. M. Matson, *Chem. Sci.*, 2018, **9**, 1692–1699.

86 L. E. VanGelder, B. E. Petel, O. Nachtigall, G. Martinez, W. W. Brennessel and E. M. Matson, *ChemSusChem*, 2018, **11**, 4139–4149.

87 L. E. Vangelder, H. D. Pratt, T. M. Anderson and E. M. Matson, *Chem. Commun.,* 2019, **55**, 12247–12250.

88 Z. F. Chen, Y. L. Yang, C. Zhang, S. Q. Liu and J. Yan, *J. Energy Storage*, 2021, **35**, 102281.

89 L. E. VanGelder and E. M. Matson, *J. Mater. Chem. A*, 2018, **6**, 13874–13882.

Chapter 2: Redox Flow Battery Theory and Method Development

Research outlined in this chapter has been published in the following scientific article: C. L. Peake, A. J. Kibler, G. N. Newton and D. A. Walsh, Organic–Inorganic Hybrid Polyoxotungstates As Configurable Charge Carriers for High Energy Redox Flow Batteries, ACS Appl. Energy Mater., 2021, 4, 8765–8773.

2.1. Introduction

This chapter seeks to provide some theoretical background to RFBs and the metrics that are used to describe their performance throughout this thesis. Consistency in testing methods and assessment metrics are necessary for the comparison of RFBs and evaluation of their potential for practical applications.

The second half of this chapter provides details of the laboratory-scale H-cell and flow cell apparatus used to test the performance of charge carriers. The engineering behind industrial RFBs is complex and arguably more so than with conventional batteries (those with solid active materials). Each battery component must be suitable for the given chemistry and assembled such that the system is leak tight. The performance of a RFB is highly dependent of the flow cell design and therefore construction of laboratory-scale RFBs is non-trivial. Furthermore, testing of nonaqueous rather that water-based electrolytes provides additional complexity. A detailed discussion of the laboratory-scale RFB components is provided and consideration of their chemical compatibility with nonaqueous electrolytes. The components of the RFB discussed include flow frames, gaskets, tubing, and membranes/separators for nonaqueous electrolytes.

2.2. Experimental

2.2.1 Membrane conductivity testing

Investigations were carried out in the laboratory atmosphere at room temperature, using a CHI 760c potentiostat. Membranes were soaked in a solution of 0.1 M [TBA][PF_6] in acetonitrile for a minimum of 16 hours before conductivity testing. The pre-soaked membrane was cut to 1 cm^2 and sandwiched between Pt plate electrodes. Electrodes were cleaned in a butane flame before use. Polytetrafluoroethylene (PTFE) gaskets and steel plates were clamped either side of

the electrodes to hold the assembly together. Potentiostatic electrochemical impedance spectroscopy (EIS) was conducted over the frequency range of 100 kHz to 100 mHz at AC amplitude of 5 mV.

2.2.2 Membrane selectivity testing

A glass membrane-separated H-cell (Pine Research) was assembled in a N_2 filled glove box. The membrane was allowed to soak in 0.1 M [TBA][PF_6] in acetonitrile for a minimum of 16 hours before the crossover experiment began. The electrolyte was removed from one side of the H-cell and replaced with 1 mM of $TBA_3[PW_{12}O_{40}]$ (PW_{12}) in 0.1 M [TBA][PF_6] in acetonitrile. A UV-visible absorption spectroscopy dip probe was placed in the electrolyte reservoir containing 0.1 M [TBA][PF_6] in acetonitrile, and absorbance measurement were captured periodically over a 24 hour period. The electrolyte containing PW_{12} was stirred at 100 rpm throughout the experiment.

2.3. Theory

The fundamental principle of EES is the conversion of chemical energy stored in the bonds of molecules to electrical energy, and vice versa. Importantly, the redox reactions in the electrochemical cell are separated in space and connected by an electrical circuit. Upon charge, a thermodynamically unfavourable reaction is facilitated by an applied electrical current. In the case of RFBs, this entails the reduction of the negative electrolyte and oxidation of the positive electrolyte. Upon discharge, electricity is released as the thermodynamically favourable reaction proceeds (oxidation of negative electrolyte and reduction of positive electrolyte).

The theoretical V_{cell} of a battery is defined by the difference in formal potential between the redox processes of the charge carriers in the positive and negative electrolyte. Under open-circuit conditions, V_{cell} is related to the Gibbs free energy change by Eq. 2.1;

$$\Delta G = -nV_{cell}F \tag{2.1}$$

where ΔG is the Gibbs free energy change in J and all other terms have been previously defined. V_{cell} is related to the compositions of the electrolytes via the Nernst equation;

$$V_{cell} = V^{o}{}_{cell} - \frac{RT}{nF} ln \frac{[ox]}{[red]} \quad (2.2)$$

where $V^{o}{}_{cell}$ is the standard cell potential in V, R is the gas constant (8.314 J K^{-1} mol^{-1}), T is temperature in K, [ox] and [red] are the concentrations of oxidised and reduced species respectively and all other terms have been previously defined.

During battery operation (active charging or discharging), the practical V_{cell} deviates from that of the theoretical value due to irreversible losses within the cell (often termed polarisation). There are three sources of losses which are termed the activation overpotential, ohmic overpotential and mass transport overpotential. Figure 2.1 is a generalised polarisation curve for RFBs. It demonstrates the influence of increasing current density on V_{cell} at a given state of charge (SOC) and highlights the source of overpotential that dominate in each region.

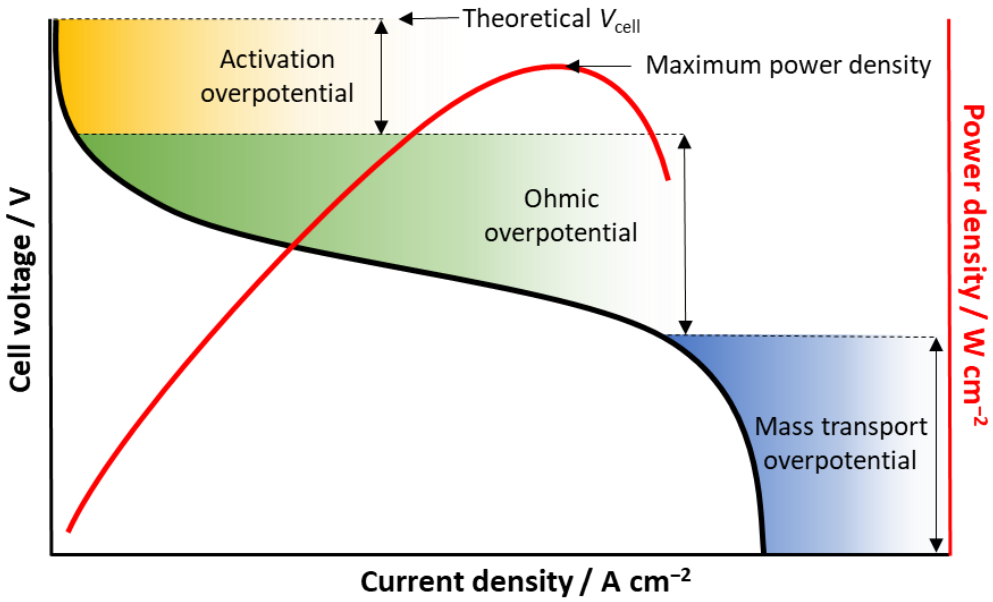

Figure 2.1. Generalised polarisation curve for a RFB, showing V_{cell} as a function of current density and the dominant overpotential in each region. A generalised power density curve is overlaid (red) indicating the current density at which the maximum power density is achieved. Figure inspired by reference 1.

At very low current densities, polarisation is minimal (VE is at its highest) and the activation overpotential is the major contributor to reduced V_{cell}. The activation overpotential is associated with the kinetics of the electron transfer reaction of the charge carrier. This is a property inherent to the charge carrier but can be tuned

through molecular design and through modification of the electrode surface (for example, pre-treatment or addition of catalytic sites).[1] Ohmic losses arise from the electronic resistance of the electrolyte solution, membrane, electrode, and current collectors. In line with ohms law, voltage losses due to the cell resistance increase with increasing current density and therefore ohmic resistance is the primary contributor in the middle region. At very high current densities, mass transport of charge carrier to the electrode surface becomes insufficient to fulfil the demanded current, and therefore the concentration overpotential dominates. Upon charge, the concentration of charge carrier in the discharged state is low at high SOC and therefore concentration overpotentials become more prominent. The same phenomenon is observed at very low SOC upon discharge. While VE decreases with increasing current density, high currents are necessary to achieve high power density. Consequently, the optimal power density is observed at an intermediary current density. This is evident from the power density curve shown in red in figure 2.1.

Table 2.1 lists the key assessment metrics and their equations used for quantifying the performance of RFBs. As seen in Eq. 1.1, the theoretical capacity, Q_{theory}, of a battery can be calculated based on the number of electrons transferred per charge carrier, n, the number of moles of charge carrier (calculated based on the concentration, C_{active}, and volume of charge carrier-containing electrolyte, V_+/V_-) and F. Conversion from the SI units of coulomb (C) to milliampere hour (mA h) is conventional as it allows for easy calculation of the time required to charge or discharge the cell at a given current density.

The battery capacity may be reported as an absolute value or normalised based on Q_{theory} or Q_{charge} of a specified cycle number. In this case the value may be displayed as a percentage. Reporting of capacity as a function of Q_{theory} is known as the electrochemical yield.

The time required to charge the cell at a given current (or current required to charge in a given time) can be calculated using Eq. 2.3;

$$Q = I\,t \tag{2.3}$$

where *I* is the applied current in mA and *t* is time in h. It is conventional to report the performance of a battery at a given current density, where the current is normalised to the geometric surface area of the electrode. Alternatively current can be normalise based on the duration of charge. The so called C-rate is defined in Eq. 2.7. Cycling at a rate of 1C indicates that the charge or discharge cycle occurs in one hour.

Table 2.1. Performance metrics for RFBs. *I* is current (mA), A is the geometric surface area of the electrode (cm^2), $Q_{theory/charge/discharge}$ is the theoretical/charge/discharge capacity (mA h), $V_{discharge/charge/cell}$ is the average voltage upon discharge/charge/or of the cell (V), *n* is the number of electrons transferred per charge carrier, *F* is the Faraday constant (96485 C mol^{-1}), C_{active} is the concentration of charge carrier (mol L^{-1}) and $V_{+/-}$ is the volume of positive/negative electrolyte (L).

Eq.	Metric	Definition	Units
2.4	Capacity, *Q*	$Q = \frac{n\,F\,C_{active}\,V_{+/-}}{3600} \times 1000$	mA h
2.5	Electrochemical yield	$Electrochemical\ yield\ = \frac{Q_{charge}}{Q_{theory}}$	%
2.6	Current density	$Current\ density\ = \frac{I}{A}$	mA cm^{-2}
2.7	C-rate	$Crate = \frac{I}{Q_{theory}}$	h^{-1}
2.8	Power density	$Power\ density = \frac{(I \times V_{cell})}{A}$	W cm^{-2}
2.9	Coulombic efficiency, CE	$CE = \frac{Q_{discharge}}{Q_{charge}}$	%
2.10	Voltage efficiency, VE	$VE\ = \frac{\int V_{discharge}}{\int V_{charge}}$	%
2.11	Energy efficiency, EE	$EE\ = \frac{\int Q_{discharge} V_{discharge}\,dt}{\int Q_{charge} V_{charge}\,dt}$ $EE = CE \times VE$	%

The rate of capacity fade is a quantitative analysis of the battery cycling stability. It is reported as a percentage per cycle or per day and the total number of cycles or duration of cycling should be reported along with the decay rate.[2,3] There are several

mechanism that most commonly underpin capacity fade in RFBs. These include cell leakage, parasitic reactions, charge carrier degradation, precipitation, crossover and self-discharge.[4] There are techniques for concluding which source of capacity fade is dominant, several of which are used in this thesis. For example, observing the effect of pausing the galvanostatic cycling (in the charge and discharged states) on the capacity fade can provide a wealth of information on the cause of capacity fade.[3]

CE is a measure of discharge capacity divided by charge capacity and is an assessment of the reversibility of a given charge-discharge cycle. Often, CE less than 100% is observed concurrently with capacity fade. Mechanisms such as charge carrier decomposition, crossover or precipitation are most likely in this case. It is also possible to have CE losses independently to capacity fade. Mechanism that reduce CE but do not impact capacity retention, include charge carrier self-discharge or parasitic reactions of the battery (for example, solvent electrolysis where the by-products are not damaging to the cell chemistry). Poor CE at low current densities is associated with a greater degree of membrane crossover. Conversely, poor CE at high current densities is more likely associated with parasitic side reactions such as the HER in aqueous RFBs.

VE is a measure of the average discharge voltage over the average charge voltage. VE losses are attributed to overpotentials highlighted in the polarisation curve above and generally VE decreases with increasing current density.[1] VE can be maximised by using low resistance battery components to include the membrane, electrolyte, electrodes and current collectors. The use of electrodes with good electroactivity and high surface area is also beneficial to maximise VE.

EE, also referred to as the round trip efficiency, is the accumulative effect of CE and VE and is a measure of the RFB overall efficiency. It can be calculated from the discharge energy divided by charge energy as seen in Eq. 2.11. The cycling conditions greatly influence the performance of a RFB and it is therefore important to compare the performance of batteries under equivalent conditions where possible.

2.4. Method Development

2.4.1 Cell design

2.4.1.a H-cell

Due to the complexity of flow cell assemblies, it is commonplace to conduct initial investigations of novel charge carriers in static systems such as H-cells. In a typical H-cell assembly, electrolyte is contained in glass reservoirs and separated by a membrane/separator. To ensure a leak tight system, O-rings are placed either side of the membrane and the two reservoirs are secured together with a pinch clamp. Figure 2.2 shows a schematic and photograph of an H-cell (Pine Research, USA) being used for galvanostatic cycling of nonaqueous electrolytes. In this experiment, electrodes are inserted into the electrolyte and mass transport of charge carriers to the electrode is enhanced by stirring the electrolytes. H-cells can be also modified for experiments such as bulk electrolysis, and membrane conductivity and selectivity testing.

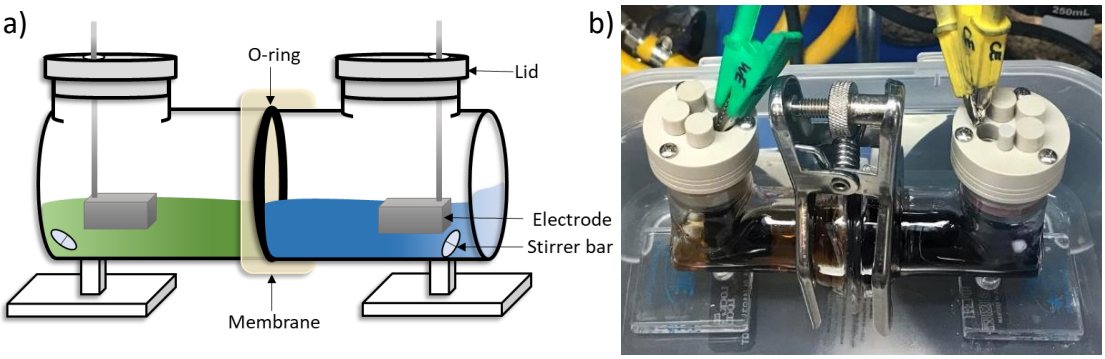

Figure 2.2. a) Schematic and b) photograph of a glass membrane-separated H-cell assembly.

Cell assemblies for aqueous electrolytes commonly use O-rings composed of compressible polymers such as nitrile rubber or Viton®. When in contact with some organic solvents (including acetonitrile), the synthetic rubbers absorb solvent and swell, which leads to leakage of the cell. PTFE is chemically resistant to most organic solvents but the rigid nature of PTFE means that it is incompressible and therefore makes a poor O-ring material. An elegant solution to this is to use specialised O-rings that have a compressible rubber core and PTFE coating, which provide both compressibility and chemical stability.

2.4.1.b Flow cell

Testing of electrolytes in an assembly that more closely resembles industrial RFBs requires the use of flow cells. Figure 2.3 shows a schematic of a typical laboratory-scale flow battery. The cell is assembled by sandwiching its components together and securing in place with bolts. The cell it typically assembled symmetrically around a central membrane/separator in the following layout (from outside towards the centre); end plate (red), current collector (gold), flow field, gasket, flow frame, electrode, second gasket and membrane/separator. Electrolyte is stored in sealed reservoirs (not shown) and is pumped through the electrochemical cell via tubing. Components of the flow cell which interface with battery electrolyte must withstand chemical degradation. Components of the flow cell which contact the electrolyte include flow frames, gaskets, tubing, reservoirs, electrode, and membrane.

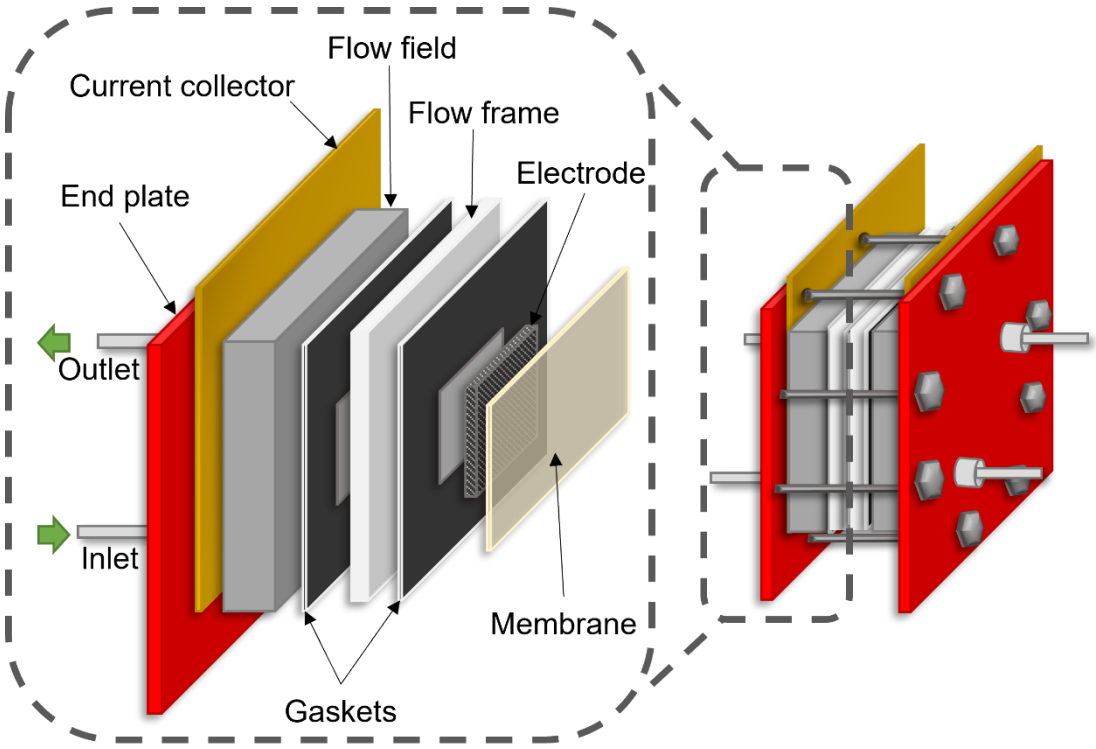

Figure 2.3. Schematic of a typical laboratory-scale RFB used for assessing the performance of charge carriers. Battery components include the membrane/separator, electrodes, gaskets, flow frames, flow fields, current collectors, end plates, tubing*, pump*, and electrolyte reservoirs*. * not pictured in schematic.

Cell assemblies for aqueous electrolytes commonly use gaskets and O-rings composed of ethylene propylene diene monomer (EPDM) or compressible polymers

such as nitrile rubber and Viton®. As discussed above, these synthetic rubbers often have poor chemical compatibility with organic solvents such as acetonitrile. For testing of nonaqueous electrolytes, the use of PTFE gaskets is recommended. PTFE has high chemical stability towards many organic solvents but is less compressible compared to EPDM and requires a higher torque strength when sealing the cell.

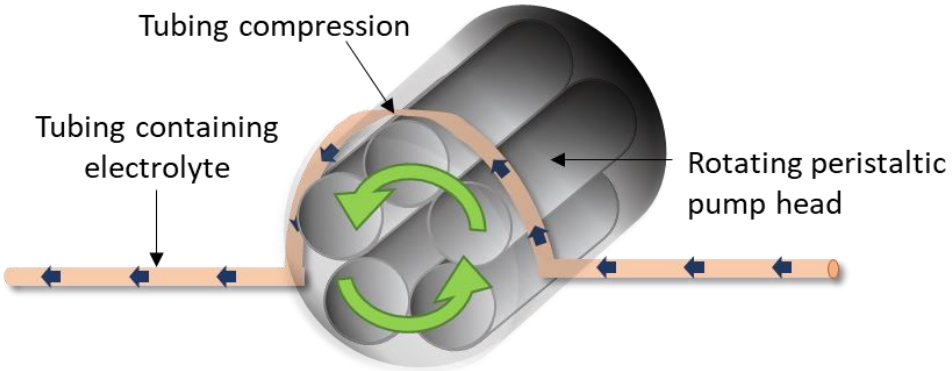

Figure 2.4. Schematic of a peristaltic pump used for pumping electrolyte through tubing between the reservoirs and electrochemical cell.

The most common method to pump electrolyte through the flow cell in laboratory-scale devices is via a peristaltic pump. The pump operates by compressing flexible tubing between rollers in a rotational fashion, as depicted in figure 2.4. While many polymeric flexible tubing will support aqueous electrolytes, organic solvents such as acetonitrile and *N*,*N*'-dimethylformamide (DMF) can induce unwanted degradation processes of the polymer. Consequently common tubing material such as Tygon® and Neoprene® are unsuitable for nonaqueous electrolytes and chemical compatibility databases must be consulted to find suitable materials. While PTFE has good chemical compatibility with most organic solvents it is not flexible and requires the use of a specialised pump head. C-Flex® Ultra was found to be compatible with acetonitrile-based electrolytes while, Viton was the preferred material for dichlorobenzene. The physical durability of tubing should be considered in addition to its chemical compatibility with the electrolyte. While Viton is chemically compatible with dichlorobenzene, the area of the tubing which contacts the peristaltic pump head is prone to cracking and requires replacing after approximately 150 hours (depending of flow rate).

Figure 2.5 shows the flow cell assembly (Scribner, USA) used for testing of charge carriers in chapters 3 to 5. The figure shows aluminium end plates, gold-plated copper current collectors with O-rings, graphite flow fields with interdigitated flow pattern, PTFE flow frames, inlet/outlet tubing with Swagelok fittings, gaskets, washers and bolts.

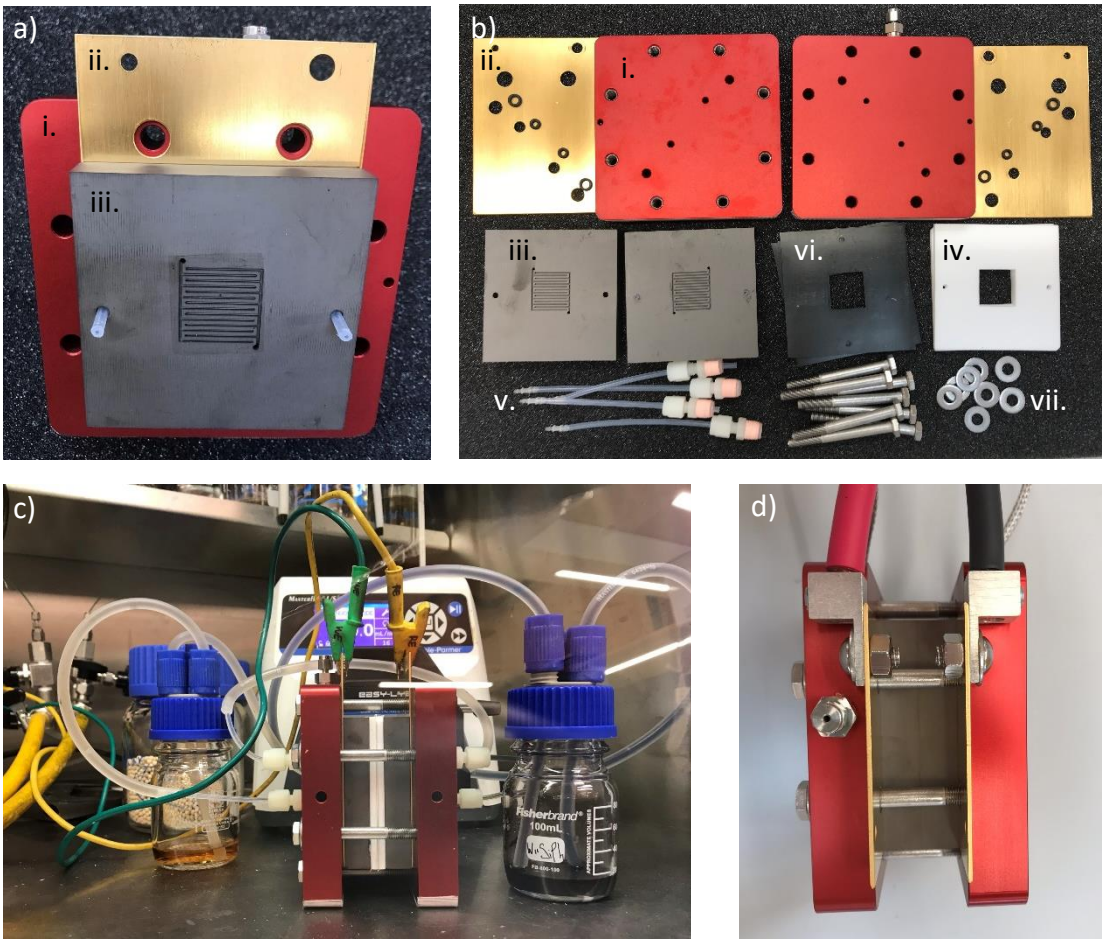

Figure 2.5. Redox flow battery assembly. i. aluminium end plates, ii. gold-plated copper current collectors with O-rings, iii. graphite flow fields with interdigitated flow pattern, iv. PTFE flow frames, v. inlet/outlet tubing with Swagelok fittings, vi. gaskets, vii. washers and bolts.

2.4.2 Membranes

The purpose of membrane/separators in RFBs is to allow the transport of charge-balancing supporting electrolyte while preventing crossover of charge carriers. An ideal membrane would have the following properties;[5,6]

- High ionic conductivity
- High selectivity

- High mechanical stability (to include resistance to swelling)
- High chemical stability
- Low cost

High ionic conductivity is key to reduce the ohmic resistance across the flow battery, and thereby reduce overpotentials and enable high current densities to be achieved. High ionic selectivity is necessary to avoid transport of charge carriers to the opposite half-cell, termed membrane crossover, which can lead to reduced CE and capacity fade. In the case of symmetric RFBs, capacity fade can often be recovered through electrolyte rebalancing whereas in asymmetric RFBs the effect is permanent. High mechanical stability of the membrane is necessary to enable the battery to perform well across its lifetime (typically 15-20 years). In addition, the membrane must be stable to the oxidative and reductive potentials applied when charging and discharging the RFB.

There are several types of membrane and separator which are commonly used in RFBs. Generally they fall into one of two categories; first, ion exchange membranes such as cation exchange membranes (CEMs), anion exchange membranes (AEMs) and dense ceramics. CEMs and AEMs are typically constructed of organic polymers with ionic functionalisation that allows the exclusive transport of cations or anions while preventing the passing of the oppositely charged ions. The second category is porous separators. They are made from organic polymers and achieve ionic selectivity based on a size exclusion effect. Small molecules such as the ions of the supporting electrolyte will pass freely through the separator pores while molecules larger than the pose size (charge carriers) will be prevented from crossing over.

There are many membranes suitable for application in aqueous RFBs but much fewer for nonaqueous RFBs. Here, the most common types of membranes/separators are introduced with emphasis on their performance with nonaqueous electrolytes.

2.4.2.a Membranes for nonaqueous RFBs

CEMs such as the proton exchange membrane Nafion, are widely used in aqueous RFBs such as the VRFB. For application in nonaqueous RFBs, the membrane requires pre-treating in a solution of supporting electrolyte to allow for exchange of the H^+-form to that of the supporting electrolyte cation e.g. Li^+ or TBA^+. Ion exchange

membranes typically have better ionic selectivity than porous separators and crossover of small organic charge carriers occurs over the timescale of several days.[7] However, CEMs often exhibit low ionic conductivity, poor chemical stability and extensive swelling and are therefore unsuitable for application in nonaqueous RFBs. Similar challenges are observed when using AEMs such as AMI-7001 for application in nonaqueous RFBs. Low ionic conductivity results in large overpotentials and poor VE which limits the feasible current densities and therefore power density of the RFB.[8]

There are several examples of dense ion-conducting ceramic having been applied as membranes in RFB to include the Na^+-conduction Na-β-Al_2O_3[9] and Li^+-conduction NASICON-type $Li_{1+x+3z}Al_xTi_{2-x}Si_{3z}P_{3-z}O_{12}$.[10] As with CEMs and AEMs, they exhibit good ionic selectivity, but their low ionic conductivity greatly limits the achievable current density.

Daramic and Celgard are two commonly employed commercial porous separators used in nonaqueous RFBs. They generally achieve higher ionic conductivity and chemical and mechanical stability than ion exchange membranes but are limited by their low ionic selectivity. Crossover of small organic charge carriers typically occurs within hours.[7] Membrane thickness and pore size have significant influence on ionic conductivity and selectivity. Ionic conductivity can be improved by reducing membrane thickness and increasing pore size. However, this has a detrimental effect on ionic selectivity. This leads to somewhat of a trade off in RFB performance. While smaller pore size leads to improved ionic selectivity, it should be noted that pore size of Daramic and Celgard separators are typically in the range of 25-150 nm which far exceeds the molecular diameter of most charge carriers.

Several research groups have sought to develop membranes with improved performance for nonaqueous RFBs. Introducing crosslinking groups into the membrane structure, result in reduced swelling, as demonstrated in both ion exchange membranes and porous separators.[5] Porous separators with pore size <2 nm, often termed polymers of intrinsic microporosity (PIMs)[11] have been developed and investigated for nonaqueous RFBs, and show improved ionic selectivity.[12,13] PIMs

allow for high ionic selectivity for even small organic molecules which are the most promising charge carriers for nonaqueous RFBs. However, they are still under development and are not commercially available at present.

2.4.2.b Membrane conductivity

Ionic conductivity of a membrane/separator can be measure using EIS in a H-cell or conductivity cell assembly. The membrane resistivity, R (Ω) is determined from the high frequency intercept of Re(Z) on the Nyquist plot and can be used to calculate the membrane conductivity, σ (S cm^{-1}) using Eq. 2.12;

$$\sigma = \frac{l}{A \times R} \tag{2.12}$$

where l is the membrane thickness (cm) and A is the membrane area (cm^2). The ionic conductivity of several membranes/separators were assessed in a conductivity cell (pictured in figure 2.6) where electrolyte-soaked membranes were sandwiched between platinum electrodes and clamped in place with PTFE gaskets and steel plates. Membranes/separators were soaked in a solution of 0.1 M [TBA][PF_6] in acetonitrile for a minimum of 16 hours before testing.

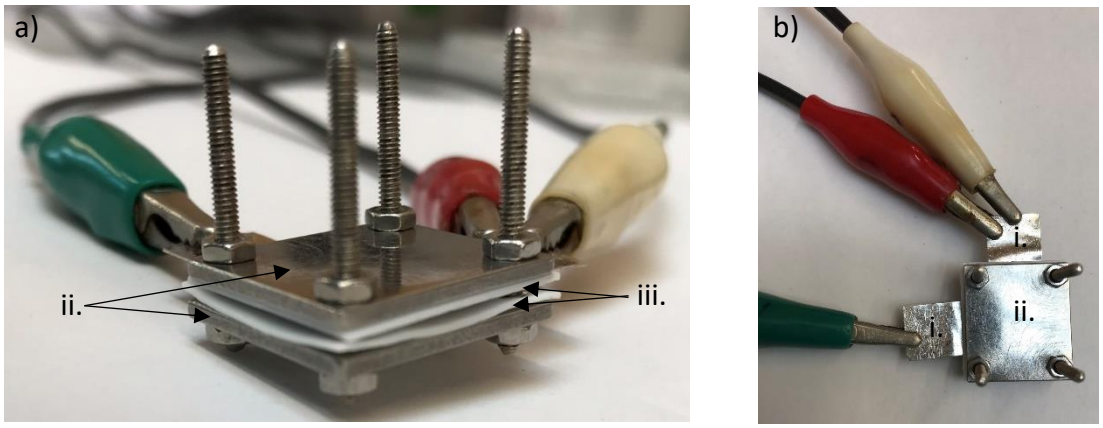

Figure 2.6. Conductivity testing cell pictured from a) the side and b) above. i. Pt plate electrodes, ii. steel plates and iii. PTFE gaskets.

The results indicate that AMI-7001 has the poorest ionic conductivity (5 μS cm^{-1}) of the three membranes tested, while the porous separator Celgard is most conductive.

Table 2.2. Conductivity of membranes for nonaqueous RFB applications. *data was obtained from the literature[14] from measurements in 0.5 M tetraethylammonium tetrafluoroborate ([TEA][BF_4]) in acetonitrile.

Membrane	Type	Thickness (l) / μm	Conductivity in acetonitrile-based electrolyte (σ) / μS cm^{-1}
AMI-7001	AEM	450	5
F-930-RFD	CEM	30	750
Celgard 2500	Porous separator	25	8100*
FAP-450	AEM	50	5000*

2.4.2.c Membrane selectivity

Movement of solvated molecules across the membrane is primarily motivated by diffusion (concentration gradient driven) and migration (electric field driven). Concentration gradient driven crossover is minimised in symmetric RFBs and in the asymmetric RFBs in which the positive and negative electrolytes have been premixed.[7] However, when charge carriers change oxidation state upon charge, a concentration gradient is established inducing crossover by diffusion. Electroosmotic drag can also contribute to ion and solvent transport across membranes.[15] Additionally, a pressure differential across the membrane can promote transfer of electrolyte across the cell. This can occur due to several factors to include the formation of a blockage by precipitation.

The selectivity of three membranes/separators to PW_{12} in an acetonitrile based electrolyte were investigated in a H-cell assembly. An electrolyte consisting of 1 mM PW_{12} in 0.1 M [TBA][PF_6] in acetonitrile was placed in one reservoir, while an electrolyte containing 0.1 M [TBA][PF_6] in acetonitrile was placed in a second reservoir divided by a chosen membrane/separator. A UV-visible absorption spectroscopy dip probe was placed in the electrolyte reservoir containing 0.1 M [TBA][PF_6] in acetonitrile, and absorbance measurement were captured periodically over a 24 hour period to measure the ingress of PW_{12}.

As seen in figure 2.7, the anion exchange membrane AMI-7001 was shown to have the best selectivity of the three membrane/separator tested. After 24 hours, crossover of PW_{12} through the membrane to the opposite half-cell was approximately 20% compared to Celgard and FAP-450. We observed a correlation between high selectivity and poor conductivity.

Odom and colleagues compare the performance of ion exchange membranes and porous separators in nonaqueous RFBs with small organic charge carriers (phenothiazine and viologen derivatives).[15] Similarly to our findings, they observe that the porous separator has good ionic conductivity but poor selectivity while the ion exchange membrane exhibits poor ionic conductivity but improved selectivity.

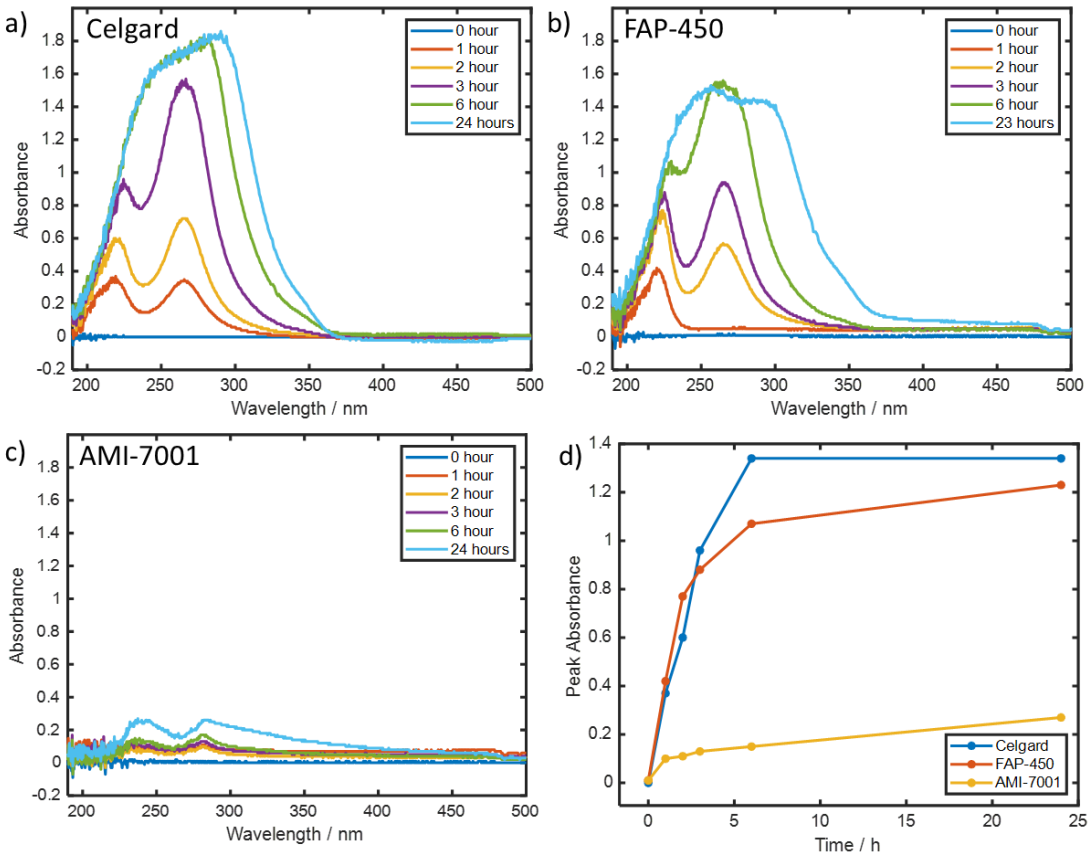

Figure 2.7. Results of membrane selectivity testing in a H-cell with 1 mM of PW_{12} in 0.1 M $[TBA][PF_6]$ in acetonitrile. a-c) Overlay of UV-visible absorption spectra of opposite H-cell reservoir at time intervals for Celgard, FAP-450 and AMI-7001 respectively. d) Peak absorbance at wavelength of 220-230 nm with time for each membrane/separator.

2.5. Conclusions

This chapter provides some theory behind RFBs and the key assessment metrics used for quantification of their performance. The laboratory-scale RFBs used for testing of charge carriers in chapter 3 to 5 is introduced. The main components of the RFB are explained and best practice for modification of RFBs for testing of nonaqueous electrolytes is provided. The rubber and polymeric materials conventionally used for gaskets and tubing are not chemically compatible with acetonitrile based electrolytes. We recommend the use of PTFE based flow frames and gaskets and C-flex ULTRA flexible tubing for use with acetonitrile.

Furthermore, the challenge of acquiring highly conductive and selective membranes for nonaqueous RFBs was presented. Some scoping experiment of commercially available membranes show similar trends to those observed in the literature. A general pay off of conductivity verses selectivity is observed. The porous separator, Celgard shows the greatest conductivity but poor selectivity towards PW_{12}, while the opposite is true for the AEM AMI-7001. These trends will help guide the choice of membrane for the next-generation RFBs investigated in this thesis.

2.6. References

1 M. Skyllas-Kazacos, C. Menictas and T. Lim, Electricity Transmission, Distribution and Storage Systems, Woodhead Publishing Limited, 2013, pp. 398–441.

2 Y. Yao, J. Lei, Y. Shi, F. Ai and Y. C. Lu, *Nat. Energy*, 2021, **6**, 582–588.

3 M.-A. Goulet and M. J. Aziz, *J. Electrochem. Soc.*, 2018, **165**, A1466–A1477.

4 C. G. Armstrong, R. W. Hogue and K. E. Toghill, *J. Electroanal. Chem.*, 2020, **872**, 114241.

5 J. Yuan, Z. Z. Pan, Y. Jin, Q. Qiu, C. Zhang, Y. Zhao and Y. Li, *J. Power Sources*, 2021, **500**, 229983.

6 S. H. Shin, S. H. Yun and S. H. Moon, *RSC Adv.*, 2013, **3**, 9095–9116.

7 Z. Liang, N. H. Attanayake, K. V Greco, B. J. Neyhouse, J. L. Barton, A. P. Kaur, W. L. Eubanks, F. R. Brushett, J. Landon and S. A. Odom, *ACS Appl. Energy Mater.*, 2021, **4**, 5443–5451.

8 Z. F. Chen, Y. L. Yang, C. Zhang, S. Q. Liu and J. Yan, *J. Energy Storage*, 2021, **35**, 102281.

9 G. Muthuraman, L. Boyeol and M. Il-Shik, *J. Electrochem. Soc.*, 2018, **165**, A1920–A1924.

10 Y. Ding, Y. Zhao, Y. Li, J. B. Goodenough and G. Yu, *Energy Environ. Sci.*, 2017, **10**, 491–497.

11 N. B. McKeown and P. M. Budd, *Macromolecules*, 2010, **43**, 5163–5176.

12 S. E. Doris, A. L. Ward, A. Baskin, P. D. Frischmann, N. Gavvalapalli, E. Chénard, C. S. Sevov, D. Prendergast, J. S. Moore and B. A. Helms, *Angew. Chemie Int. Ed.*, 2017, **56**, 1595–1599.

13 S. on Tung, S. L. Fisher, N. A. Kotov and L. T. Thompson, *Nat. Commun.*, 2018, **9**, 4193.

14 N. S. Hudak, L. J. Small, H. D. Pratt and T. M. Anderson, *J. Electrochem. Soc.*, 2015, **162**, A2188–A2194.

15 Z. Liang, N. H. Attanayake, K. V. Greco, B. J. Neyhouse, J. L. Barton, A. P. Kaur, W. L. Eubanks, F. R. Brushett, J. Landon and S. A. Odom, *ACS Appl. Energy Mater.*, 2021, **4**, 5443–5451.

Chapter 3: Hybrid Polyoxometalates for Symmetric Nonaqueous Redox Flow Batteries

3.1. Introduction

The rich electrochemistry of POMs make them promising charge carriers for high E_v RFBs. Their multi-electron redox properties also allow for their application in symmetric RFBs, where the same charge carrier is applied in both the positive and negative electrolyte. As seen for the VRFB, symmetric systems have the advantage that electrolytes can be regenerated to regain lost capacity in the event of membrane crossover.[1] An introduction to POMs and their application in symmetric[2–8] and asymmetric RFBs[9–14] was provided in chapter 1.

Aqueous RFBs are limited to a maximum V_{cell} of *ca.* 2.0 V, beyond which, electrolysis of water occurs. Stimming and co-workers investigated SiW_{12} as charge carrier for the negative electrolyte of an aqueous asymmetric RFB.[9] Only the first two redox processes of SiW_{12} were accessible without the onset of the hydrogen evolution reaction.[9] The third redox process (a two-electron redox event) was inaccessible in the aqueous electrolyte, thereby limiting the RFB capacity and E_v. Nonaqueous electrolytes comprising of organic solvents or ionic liquids offer a wider window of electrochemical stability. They allow access to the redox process of POMs at highly negative potentials and thereby facilitate higher V_{cell} and E_v batteries.[15,16]

Barteau and co-workers demonstrated the first nonaqueous POM-based RFB with PMo_{12} in acetonitrile[4] and later in DMF.[8] The solubility of PMo_{12} in acetonitrile with Li^+ counter cations was remarkably high at 1 M, but was compromised upon addition of lithium-based supporting electrolyte.[8] The highly charged inorganic clusters generally demonstrate higher solubility in polar solvents such as water, and poorer solubility in organic solvents. Without targeted modification, the solubility of POMs in nonaqueous solvents is limited. Matson and co-workers demonstrated the use of POV nanoclusters of the general formula $[V_6O_7(OR)_{12}]$, where R = organic moiety, as the charge carriers in symmetric nonaqueous RFBs.[17] In an effort to enhance solubility and cycling stability, several variations of organic moiety were explored to include alkoxides,[17] ethers,[7] TRIOL derivatives[5] and mixed systems.[7] An impressive

saturation concentration of 1.2 M in acetonitrile was reported for a mixed alkoxide/ether-functionalised POV.[18] The neutral clusters demonstrated four one-electron redox processes spanning *ca.* 2 V, allowing for their application in symmetric systems.

We seek to expand on the concept of organofunctionalisation of POMs, to develop a new class of multi-electron charge carriers with high solubility in organic solvent, namely organic-inorganic hybrid POMs. Hybrid POMs have already been used in catalysis, energy materials and life sciences,[20] and can be further functionalised to yield novel soft materials.[21–26] We hypothesised that introduction of an organic moiety to the POM core would enhance solute-solvent interaction and therefore solubility in organic solvents, while maintaining the rich electrochemistry of the POM. Furthermore, the choice of POM counter cation greatly influences the molecules solubility and TBA salts are known to a have amongst the highest solubility in acetonitrile.[27]

Organic-inorganic hybrid POMs are a diverse class of redox-active species with excellent scope for tuning of the properties. A wealth of knowledge has been accumulated through decades of computational and experimental studies of POMs, and can inform the design of hybrid POMs to achieve specific properties. Targeted selection of the POM core (addenda metal, heteroatom and geometry), counter cation, anchoring group (P, Si, Ge or Sn), and organic moiety can yield POMs with particular redox and solubility properties.

Our primary aim was to identify POMs with rich redox properties and high solubility in nonaqueous solvent. A secondary objective was to identify POMs with highly negative redox potentials. Although not relevant for application in a symmetric system (as studied in chapter 3), charge carriers with highly negative redox potentials enable high V_{cell} RFBs when applied in the negative electrolyte of asymmetric systems (see chapter 4). Increasing the electronegativity of the POM addenda atom decreases the redox potential of the resulting POM. The high electronegativity of tungsten means that polyoxotungstates generally have the most negative redox potentials of POMs.[28] Furthermore, the anchoring group of hybrid POMs plays an important role in governing the electronic properties of the resulting molecule[19], and allows for

tuning of the charge carrier redox potentials. Siloxane was identified as an appropriate anchoring group due to its electron donating nature, which is known to shifts the redox potential of POMs negatively.[19]

A screening study was conducted in which the saturation concentration in acetonitrile of a range of polyoxotungstate structures were investigated. A rudimentary visual inspection was used to identify the most promising candidates to pursue for further study. A range of organic-inorganic hybrid polyoxotungstates were screened and $TBA_3[PW_{11}O_{39}(SiC_6H_5)_2O]$, denoted PW_{11}-SiPh, emerged as a particularly promising candidate for further study.

3.2. Experimental

3.2.1 General experimental methods

Electrochemical investigations were carried out in a N_2-filled glove box (MBraun, Garching, Germany; <0.1 ppm H_2O; <0.1 ppm O_2) at room temperature, using a Bio-Logic SP-300 potentiostat/galvanostat (Seyssinet-Parizet, France) run using EC-Lab software. Glassware and equipment were dried in a vacuum oven at 60 °C for 16 hours prior to use. [TBA][PF_6] (≥ 99.0%, Sigma Aldrich) was dried at 60 °C under vacuum for a minimum of 1 day before being transferred to the glove box. Acetonitrile was degassed by several cycles of freezing under Ar, evacuation and thawing, before being dried over 4 Å molecular sieves (Sigma-Aldrich). The dryness of electrolytes was verified by Karl-Fischer titration (METTLER TOLEDO).

^{1}H NMR spectra were recorded using a Bruker BioSpin GmbH 400 MHz nuclear magnetic resonance spectrometer and referenced to the residual ^{1}H solvent signals. UV-visible spectroscopy of electrolytes was performed using an Agilent Cary UV-visible NIR spectrometer (Santa Clara, USA).

3.2.2 Synthesis of PW_{11}-SiPh

The synthesis of PW_{11}-SiPh was carried out using literature precedent.[25,29] Trichlorophenylsilane (0.44 mL, 2.7 mmol) was added to a solution of $[TBA]_4H_3[PW_{11}O_{39}]$, PW_{11} (5.0 g, 1.4 mmol) in acetonitrile (60 mL) under inert atmosphere. The solution was stirred at room temperature in the absence of light for 15 hours and then evaporated to dryness. The crude product was dissolved in a minimum volume of acetonitrile and precipitated by the addition of water. The product was isolated by centrifugation and washed with 1:1 volume ratio of diethyl ether : ethanol, to yield a pale-yellow powder (yield - 2.9 g, 57%). ^{1}H NMR (DMSO-d_6, 400 MH, ppm): δ = 7.77 (m, 4.1H, CHAr), 7.51 (m, 6H, CHAr), 3.17 (m, 27.6H, NCH_2), 1.58 (m, 28.6H, CH_2), 1.32 (m, 29.3H, CH_2), 0.95 (t, J=7.3Hz, 43H, CH_2CH_3). ^{31}P{H} NMR (DMSO-d_6, 162 MHz, ppm): δ = −13.58.

3.2.3 Saturation concentration analysis

The saturation concentration of PW_{11}-SiPh and PW_{12} in anhydrous acetonitrile was investigated spectroscopically. A saturated solution of POM in anhydrous acetonitrile

was prepared by adding the analyte stepwise with stirring until the solid no longer dissolved. The solution was filtered through cotton wool and diluted to a concentration in which its UV-visible absorbance intensity was below 1. The sample concentration was determined using the Beer-Lambert Law and back calculated to determine the concentration of the saturated solution. Peak absorption in the range of 265-267 nm was compared to a pre-prepared five-point calibration to determine the concentration of PW_{11}-SiPh. The molar absorption coefficient, ε, was calculated using the Beer-Lambert law to be 42284 M^{-1} cm^{-1}.

3.2.4 Cyclic voltammetry

CV was carried out using a three-electrode cell, containing a 3 mm diameter glassy carbon working electrode (WE) (0.071 cm^2 surface area) and Pt wire counter electrode (CE) (>0.16 cm^2 surface area). The potential was referenced to a Ag wire quasi reference electrode (QRE) with ferrocenium|ferrocene (Fc^+|Fc) internal standard or Ag^+|Ag nonaqueous reference electrode (RE) containing 10 mM $AgNO_3$ in 0.1 M [TBA][PF_6] in acetonitrile. The glassy carbon WE and Ag wire QRE were polished using aqueous alumina slurries of decreasing particle size (1 µm, 0.3 µm and 0.05 µm), and rinsed thoroughly with deionised water. The Pt wire CE was cleaned in a butane flame prior to use. CV was iR compensated at 85% using the ZIR tool included within the EC-Lab software.

3.2.5 Bulk electrolysis

Bulk electrolysis of electrolyte solutions was carried out in a purpose-built bulk electrolysis cell (BASi, Lafayette, USA) in a N_2-filled glove box. The cell contained a high surface area reticulated vitreous carbon working electrode, Ag^+|Ag nonaqueous RE, and Pt gauze CE positioned behind a glass frit in 0.1 M [TBA][PF_6] in acetonitrile. The solution was stirred using a Teflon-coated stirrer bar. Constant-potential chronocoulometry was used to electrolyse the solution and UV-visible spectroscopy was used to monitor the oxidation state of the electrolyte.

3.2.6 Redox flow battery

Flowing charge-discharge experiments were carried out in a N_2-filled glove box with 5 cm^2 membrane surface area RFB assembly (Scribner, Southern Pines, USA).

Graphite felt electrodes (0.6 cm thickness, SGL carbon, Wiesbaden, Germany) were sandwiched between interdigitated graphite flow fields with PTFE flow frames and gaskets. A cation-exchange membrane (Fumasep F-930-RFD, Fumatech, Bietigheim-Bissingen, Germany) was used to separate the two half cells. Electrolytes comprised 10 mM PW_{11}-SiPh in 0.5 M [TBA][PF_6] in acetonitrile were reduced to the desired oxidation state by bulk electrolysis. 15 cm^3 of electrolyte was placed in each reservoir. A dual-channel peristaltic pump (Masterflex L/S, Vernon Hills, USA) was used to pump electrolytes through the cell at a flow rate of 5 mL min^{-1} using C-flex ULTRA tubing (Masterflex, Vernon Hills, USA). ±1 mA charge/discharge currents were used to test the cell performance.

3.3. Results and Discussion

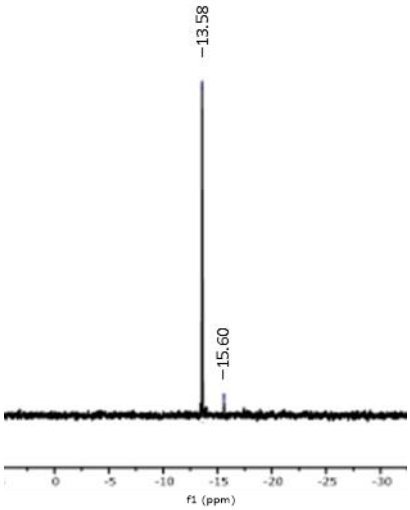

Figure 3.1. ^{31}P NMR spectrum of PW_{11}-SiPh in DMSO-d_6 (162 MHz). Reprinted with permission from reference 42. Copyright 2021 American Chemical Society.

Figure 3.1 shows the ^{31}P NMR of PW_{11}-SiPh. A single phosphorus environment is observed for PW_{11}-SiPh at −13.58 ppm. A secondary peak is observer at −15.60 ppm and is attributed to a minor PW_{12} impurity. Figure 3.2 shows the ^{1}H NMR spectra of PW_{11}-SiPh. Peaks have been assigned to proton environments on the PW_{11}-SiPh structure and have been labelled and colour coded for clarity. The integration of peaks in the ^{1}H NMR indicated a slight excess of TBA cations (additional ~0.5 equivalents). The discrepancy in TBA equivalents is due to the PW_{12} impurity. The impurity is not thought to significantly affect the electrochemical analysis.

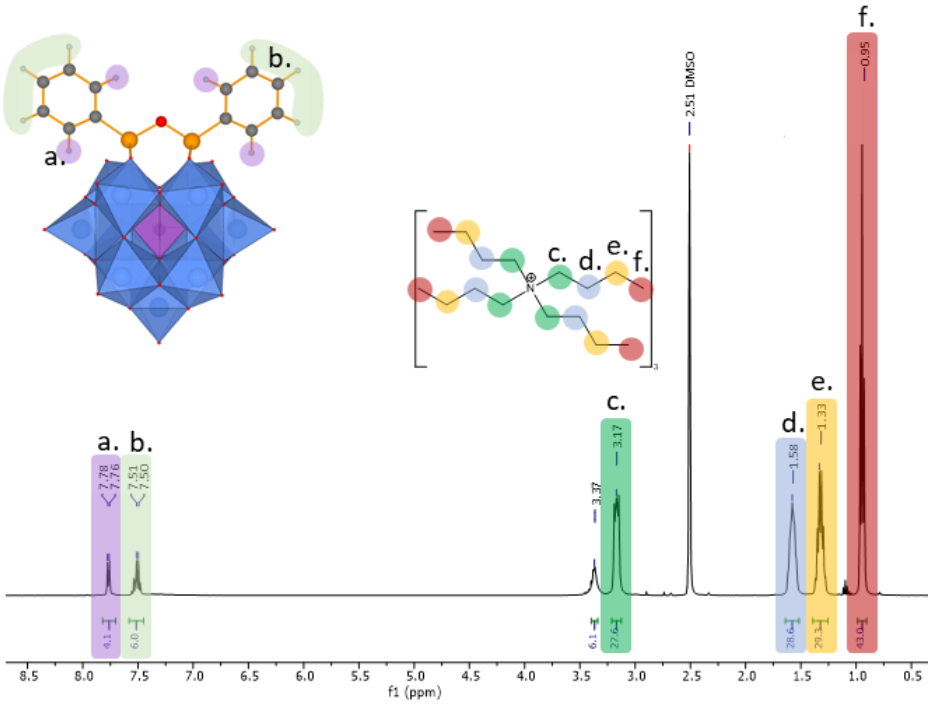

Figure 3.2. ^{1}H NMR spectrum of PW_{11}-SiPh in DMSO-d_6 (400 MHz). The proton environments a-f have been labelled and colour coded for clarity. Reprinted with permission from reference 42. Copyright 2021 American Chemical Society.

3.3.1 Solubility of charge carriers

The saturation concentration of PW_{11}-SiPh in acetonitrile was compared to that of the non-hybridised analogue, PW_{12} to directly compare the influence of organofunctionalisation of POMs on their solubility in organic solvent. Saturated solutions of PW_{11}-SiPh and PW_{12} in anhydrous acetonitrile were prepared and diluted to a concentration detectable by UV-visible absorption spectroscopy. Concentrations were determined using a pre-prepared calibration and back calculated to determine the saturation concentration of each POM. Figure 3.3 shows the calibration curve and absorbance spectra for PW_{11}-SiPh within the concentration range of 0-20 μM. The saturation concentration of the hybrid PW_{11}-SiPh in acetonitrile was calculated to be 600 mM. Conversely, the saturation concentration of PW_{12} was calculated to be <1 mM. The organic-inorganic hybridisation resulted in two orders of magnitude increase in solubility compared to the non-hybridised analogue.

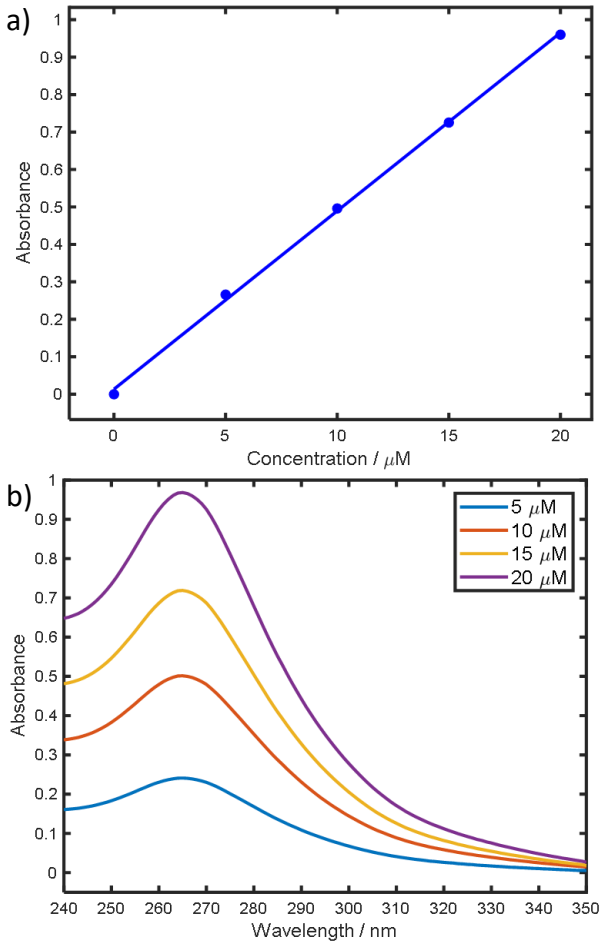

Figure 3.3. a) Beer Lambert plot of absorbance at 265-267 nm versus concentration for PW_{11}-SiPh in acetonitrile. b) Absorbance spectra of PW_{11}-SiPh in acetonitrile at concentrations of 5, 10, 15 and 20 µM. Reprinted with permission from reference 42. Copyright 2021 American Chemical Society.

The counter cations for both PW_{12} and PW_{11}-SiPh are TBA and the charge of the POM anion was 3–. The discrepancy in solubility is attributed to the increased solvent-solute interaction of PW_{11}-SiPh compared to PW_{12}. The phenyl ring of PW_{11}-SiPh breaks the spherical symmetry of the POM preventing ordered packing of the molecules, and therefore increases the solvent-solute interaction.

While there are some examples of POM solubility >0.6 M in nonaqueous solvents,[8,18] organic-inorganic hybridisation is a solubility-enhancing technique that is applicable to a wide range of POM structures.[19] The flexibility in selection of POM metal-oxide core (elemental composition and size), covalent linker and organic moiety, provides a powerful technique for tailoring properties of multi-electron charge carriers for RFBs.

3.3.2 Electrochemical analysis

Figure 3.4 shows a CV of PW_{11}-SiPh dissolved in acetonitrile containing 0.1 M [TBA][PF_6] as electrolyte, recorded using a polished glassy carbon WE and a scan rate, v, of 100 mV s^{-1}. Four reduction processes (labelled I - IV, from positive to negative potentials) are observed and correspond to four one-electron processes as seen in Eq. 3.1 - 3.4. The corresponding oxidation process are labelled I' - IV'. The redox couples accessed during the voltammetric experiment are as follows:

$$\text{I/I':} \quad [PW_{11}\text{-SiPh}]^{3-} + e^- \rightleftharpoons [PW_{11}\text{-SiPh}]^{4-} \tag{3.1}$$

$$\text{II/II':} \quad [PW_{11}\text{-SiPh}]^{4-} + e^- \rightleftharpoons [PW_{11}\text{-SiPh}]^{5-} \tag{3.2}$$

$$\text{III/III':} \quad [PW_{11}\text{-SiPh}]^{5-} + e^- \rightleftharpoons [PW_{11}\text{-SiPh}]^{6-} \tag{3.3}$$

$$\text{IV/IV':} \quad [PW_{11}\text{-SiPh}]^{6-} + e^- \rightleftharpoons [PW_{11}\text{-SiPh}]^{7-} \tag{3.4}$$

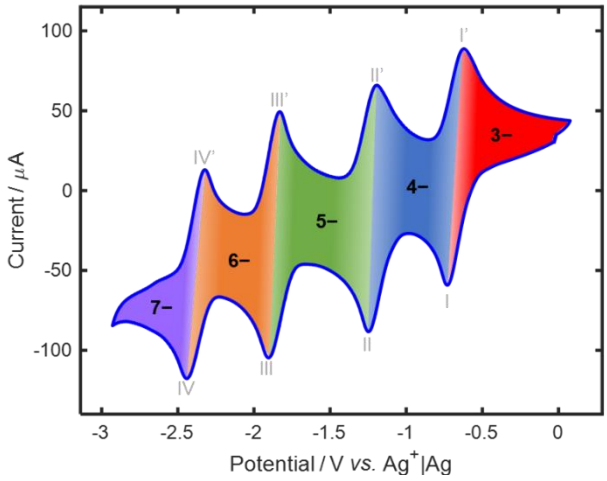

Figure 3.4. CV of 5 mM PW_{11}-SiPh in 0.1 M [TBA][PF_6] in acetonitrile recorded using a glassy carbon WE (0.071 cm^2), Pt wire CE, and $Ag^+|Ag$ RE at v of 100 mV s^{-1}. Roman numerals denote the redox processes defined in Eq. 3.1 – 3.4. Coloured areas denote the approximate regions of potential stability of PW_{11}-SiPh in various oxidation states (3– to 7– anion). Reprinted with permission from reference 42. Copyright 2021 American Chemical Society.

The mid-point potential between the anodic and cathodic peak potentials, E_{mid}, peak-to-peak separation, ΔE_p, and ratio of anodic to cathodic peak currents, $i_{p,a}/i_{p,c}$, of each redox couple are provided in table 3.1. These data are in good agreement with the values found in the literature.[25] $i_{p,a}/i_{p,c}$ is close to unity for each redox couple, as expected for an electrochemically-reversible redox couple. However, ΔE_p for

processes I/I', III/III' and IV/IV' is greater than the value of 57 mV expected for the electrochemically-reversible transfer of a single electron. Moreover, ΔE_p increased as v increased, indicating that each redox process was electrochemically quasi-reversible.

Table 3.1. E_{mid}, ΔE_p, and $i_{p,a}/i_{p,c}$ determined from CV of PW_{11}-SiPh recorded at 100 mV s^{-1}. All potentials are reported *vs.* that of an $Ag^+|Ag$. $E_{mid} = (E_c + E_a)/2$, where E_c = cathodic peak potential and E_a = anodic peak potential

Process	E_{mid} / V	ΔE_p / mV	$i_{p,a}/i_{p,c}$
I/I'	−0.66	106	0.96
II/II'	−1.18	58	1.12
III/III'	−1.81	70	0.97
IV/IV'	−2.31	122	1.00

Fast mass transport and electron transfer of charge carriers is key to enabling high power density RFBs. We determined the diffusion coefficient, *D*, and heterogeneous electron transfer rate constant, k^0, of PW_{11}-SiPh by investigating the effect of v on the voltammetric response (see figure 3.5). At v > 50 mV s^{-1}, the plot of $i_{p,c}$ *vs.* $v^{1/2}$ for process I deviated from linearity, so the gradient in the region 10 mV $s^{-1} < v <$ 50 mV s^{-1} was used in conjunction with Eq. 3.5 to estimate *D*: [30]

$$i_p = 2.69\times10^5\, n^{3/2}\, D^{1/2}\, C\, A\, v^{1/2} \qquad (3.5)$$

where *A* is surface area of the electrode (0.071 cm^2), *C* is the bulk concentration (5 mM), and *n* is the number of electrons transferred (1). Our analysis reveals that, despite its relatively large size, *D* of PW_{11}-SiPh = 1.4 × 10^{-5} cm^2 s^{-1}. The organic functionality of PW_{11}-SiPh allows for application of diffusion ordered NMR spectroscopy (DOSY NMR) to calculate *D* in acetonitrile. The aromatic signals decay similarly with a *D* of 1.2 × 10^{-5} cm^2 s^{-1}, which corresponds well with that determined electrochemically. The value of *D* calculated by DOSY NMR is an order of magnitude greater than functionalised POVs investigated by Matson and colleagues (~1.5 × 10^{-6}

cm^2 s^{-1})[31] and of vanadium sulfate in aqueous electrolyte[32] and vanadium acetylacetonate in acetonitrile.[33]

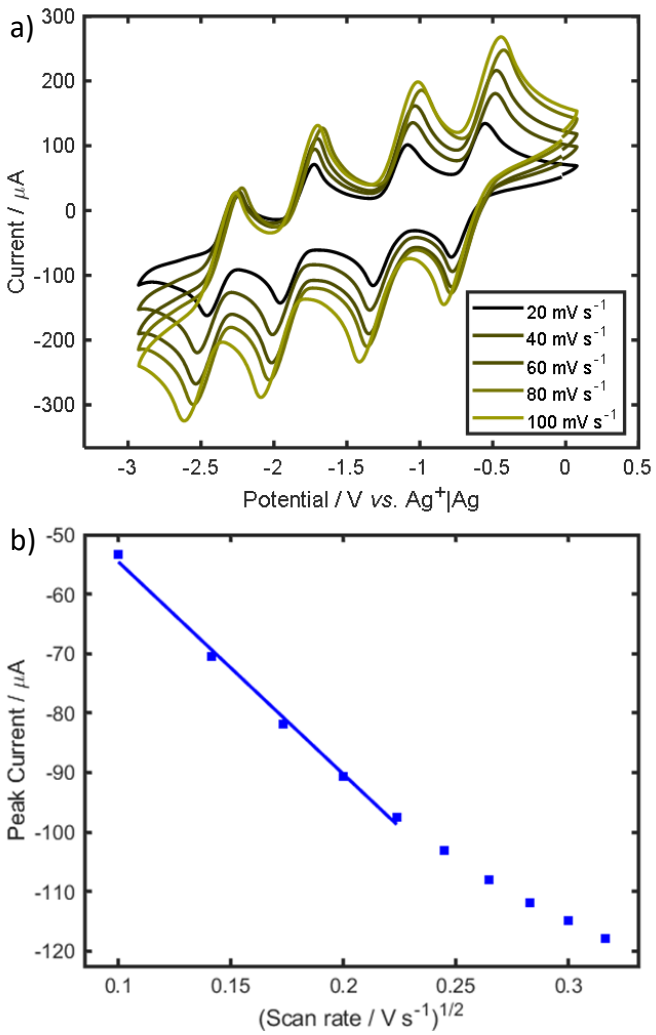

Figure 3.5. a) CV of 5 mM PW_{11}-SiPh in 0.1 M [TBA][PF_6] in acetonitrile at a glassy carbon WE (0.071 cm^2), with Pt wire CE, referenced to $Ag^+|Ag$. Recorded at v ranging from 20 - 100 mV s^{-1}. b) Peak current versus square root of scan rate for the first reduction of PW_{11}-SiPh (process I/I'). Reprinted with permission from reference 42. Copyright 2021 American Chemical Society.

The Nicholson method was used to estimate k^0 for PW_{11}-SiPh.[34] ΔE_p of the first redox couple of PW_{11}-SiPh was determined within the range 100 < v < 500 mV s^{-1}. The corresponding dimensionless transfer parameter, Ψ, was obtained from table 1 of reference 34. A more practical method of determining Ψ from ΔE_p is by using Eq. 3.6 from reference 35. k^0 was extracted from the gradient of the plot of Ψ *vs.* $[\pi DnF/RT]^{-1/2}$, and in conjunction with Eq. 3.7 (see figure 3.6).

$$\Psi = \frac{(-0.6288+0.0021\,\Delta E_p)}{(1-0.017\,\Delta E_p)} \tag{3.6}$$

$$\Psi = k^0 \left[\frac{\pi D\,\mathrm{F}}{\mathrm{R}T}\right]^{-1/2} \upsilon^{-1/2} \tag{3.7}$$

where R is the ideal gas constant and T is the absolute temperature. Using this analysis and the D value attained from DOSY NMR, k^0 was estimated at 2.5×10^{-2} cm s^{-1}, which is higher than that of the VO_2^+/VO^{2+} and V^{3+}/V^{2+} couples used in the VRFB (~10^{-5} cm s^{-1}).[32]

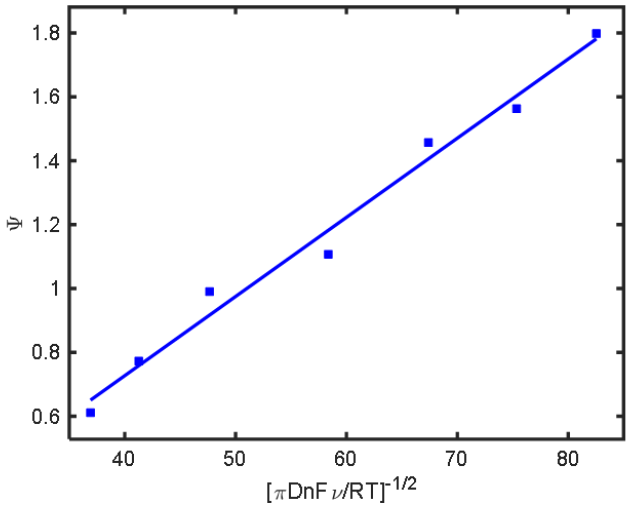

Figure 3.6. Transfer parameter, Ψ *vs.* $[\pi \mathrm{DnF}/\mathrm{RT}]^{-1/2}$ for the first redox couple of PW_{11}-SiPh**.** Data was attained from the iR compensated CV of 1 mM PW_{11}-SiPh in 0.1 M [TBA][PF_6] in acetonitrile over the υ range of 100 - 500 mV s^{-1}. Reprinted with permission from reference 42. Copyright 2021 American Chemical Society.

Repetitive CV cycling was used as an initial assessment of electrochemical stability of PW_{11}-SiPh. As seen in figure 3.7, after 300 cycles in the potential range of −3.0 to 0 V, the CV shape remained unchanged. This indicates that PW_{11}-SiPh would be stable towards repetitive charge and discharge cycling in a RFB.

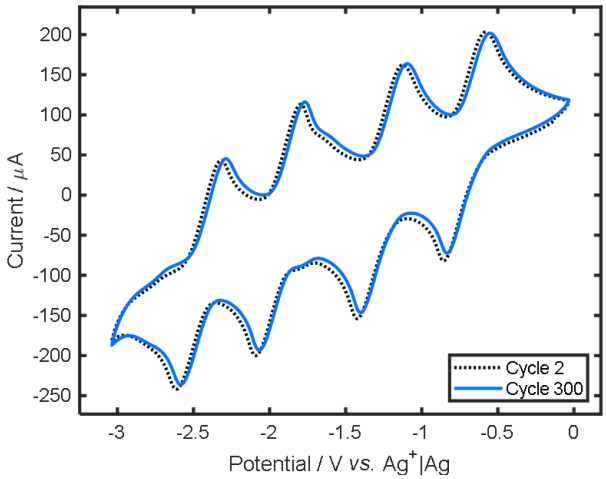

Figure 3.7. CV of 5 mM PW_{11}-SiPh in 0.1 M [TBA][PF_6] in acetonitrile at a glassy carbon WE (0.071 cm^2), with Pt wire CE referenced to $Ag^+|Ag$, recorded at v of 0.5 V s^{-1}. Cycle 2 (black dashed) and cycle 300 (blue) are displayed. Reprinted with permission from reference 42. Copyright 2021 American Chemical Society.

Spectroelectrochemical analysis was conducted on the PW_{11}-SiPh electrolyte to determine its UV-visible absorption response at various states of charge. The electrolyte was electrolysed in a three-electrode cell and in situ UV-visible absorption spectroscopy was conducted. The electrolyte was consecutively reduced by one electron to a total of three electrons, before being reoxidised. The potentials used for reduction were determined from CV of the electrolyte. Oxidised electrolyte shows no absorbance in the visible region. Upon reduction by one electron to the 4– anion, an absorbance band is observed in the visible region with peak absorbance at 730 nm. The wavelength of the peak absorbance closely corresponds to that observed in the literature for similar siloxane hybridised phosphotungstate Keggin POMs.[29] Reduction by a second electron to the 5– anion, results in a more intense absorption in the visible region and a shift in the peak absorbance to 620 nm. Reduction by a third electron to the 6– anion, increases the intensity further and peak absorbance is observed at 635 nm. The observed signal is characteristic of the $W^V \rightarrow W^{VI}$ IVCT expected for reduced phosphotungstate Keggins.[36]

Reoxidation from the 5– electrolyte back to the 4– and 3– electrolyte, was entirely reversible and the spectra observed upon reoxidation were identical to those observed upon reduction. However, the same cannot be said for the 6– reduced

state. The absorbance spectrum of the 3– electrolyte generated by reoxidation of the 6– electrolyte, was not identical to the initial sample. This indicates instability of the three-electron reduced state of PW_{11}-SiPh.

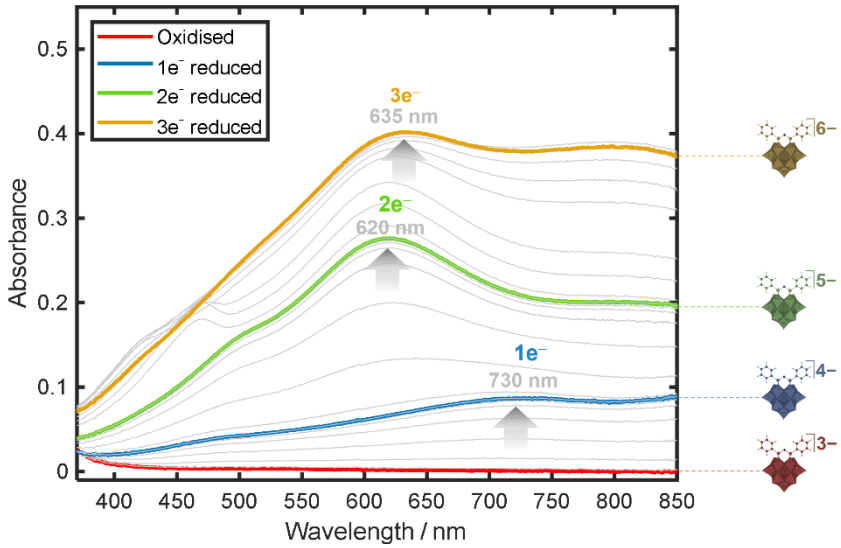

Figure 3.8. Time resolved UV-visible absorption spectra showing the electrochemical reduction of PW_{11}-SiPh in 0.1 M [TBA][PF_6] in acetonitrile. Target potentials for one-,two-, and three-electron reduced states were determined from CV. Reprinted with permission from reference 42. Copyright 2021 American Chemical Society.

Comparison of the CV of PW_{11}-SiPh to that of the non-hybridised analogue PW_{12}, revealed an 80 mV negative shift in onset potential of the first reduction after hybridisation, in line with observations made in the literature.[29] This is attributed to the electron-donating nature of the siloxane group and reiterates the ability of hybridisation to influence the energy level of the lowest unoccupied molecular orbital (LUMO) in addition to the POM solubility.[37] While this molecular tuning does not have a direct benefit to symmetric systems, a negative shift in the onset potential of the first reduction, will enhance the V_{cell} when applied as a negative electrolyte in an asymmetric system (see chapter 4).

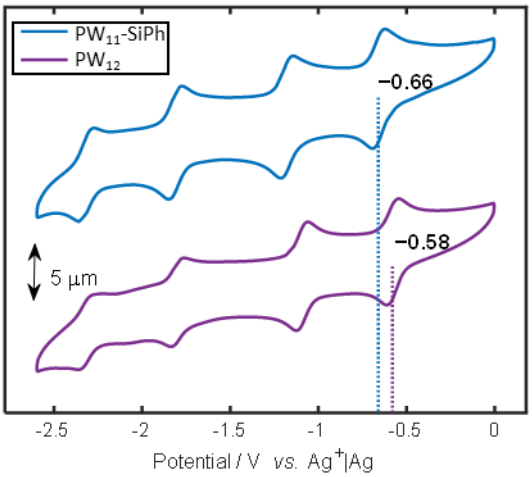

Figure 3.9. CV of 0.25 mM PW_{12} and PW_{11}-SiPh in 0.1 M [TBA][PF_6] in acetonitrile, both recorded at a glassy carbon WE (0.071 cm^2), with Pt wire CE, referenced to $Ag^+|Ag$, and recorded at v of 100 mV s^{-1}. Reprinted with permission from reference 42. Copyright 2021 American Chemical Society.

3.3.3 Flow battery performance

PW_{11}-SiPh was tested as charge carrier in several different symmetric RFBs. Testing in a symmetric system is beneficial for two reasons; (1) it reduces the complexity of the system allowing for the investigation of PW_{11}-SiPh performance in isolation from a second charge carrier, (2) in the event of membrane crossover, charge carriers which migrate to the opposite side can be recharged in the subsequent charge cycle, preventing permanent capacity loss. Here we present charge-discharge cycling results of several symmetric RFBs. The first RFB is termed Flow1 and exploits PW_{11}-SiPh in its 3−, 4−, and 5− states (oxidised, one- and two-electron reduced). The second cell is termed Flow2 and exploits PW_{11}-SiPh in its 3−, 4−, 5−, 6−, and 7− states (oxidised to four-electron reduced).

3.3.3.a Flow 1

An electrolyte consisting of 10 mM PW_{11}-SiPh in 0.5 M [TBA][PF_6] in acetonitrile was electrochemically pre-reduced by one electron per POM, from an open circuit potential (OCP) of −0.05 to −0.95 V *vs.* $Ag^+|Ag$. 15 mL of the one-electron reduced electrolyte was added to each reservoirs in the RFB. Galvanostatic cycling was conducted within the potential window of 0 to 1.2 V at a current density of 0.2 mA cm^{-2} (C-rate of 0.25 based on the theoretical capacity of 4.02 mA h). Given the

saturation concentration of 0.6 M, average V_{cell} of 0.6 V and one-electron redox reaction, the theoretical E_v of Flow1 was calculated to be 4.8 Wh L^{-1}.

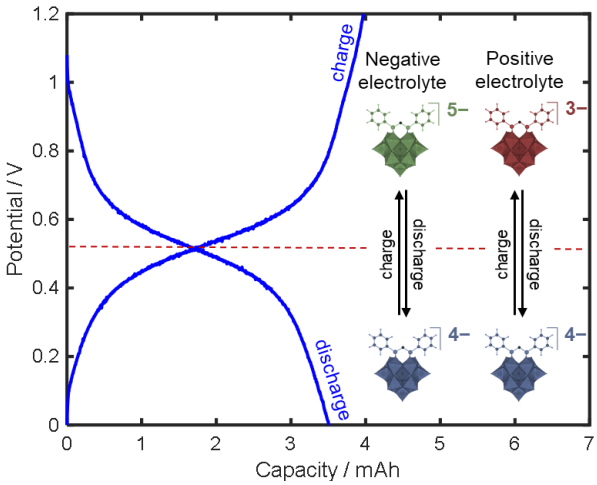

Figure 3.10. Overlayed charge and discharge profile from cycle 1 of Flow1 (symmetric PW_{11}-SiPh RFB). Current density of 0.2 mA cm^{-2}, voltage window of 0 to 1.2 V, and flow rate of 5 mL min^{-1}. Reprinted with permission from reference 42. Copyright 2021 American Chemical Society.

Upon charge, the one-electron reduced electrolyte (4– state) is oxidised to 3– in the positive electrolyte and is simultaneously reduced to 5– state in the negative electrolyte. The redox reactions are reversed upon discharge. The charge/discharge reactions at the positive and negative electrolyte correspond to those in Eq. 3.1 and 3.2 respectively (processes I/I' and II/II'). A single charge plateau is observed upon charge at a potential of 0.55 V which closely corresponds to the value expected from the difference in the E_{mid} of processes I/I' and II/II' (Table 3.1). A single discharge plateau is observed upon discharge at a potential of 0.55 V. Figure 3.10 shows the charge and discharge profiles for cycle 1 overlayed and a schematic of the redox reactions of PW_{11}-SiPh in the positive and negative electrolyte.

The charge and discharge plateaus remained at a consistent potential and shape over the course of 75 cycles and >440 hours (18 days). The RFB exhibited an average CE of 98% over 75 cycles (orange), demonstrating that electron transfer to and from the hybrid POM was reversible. The RFB also displayed consistently high EE (purple) and VE (green), averaging 87% and 89% respectively over the 75 cycles.

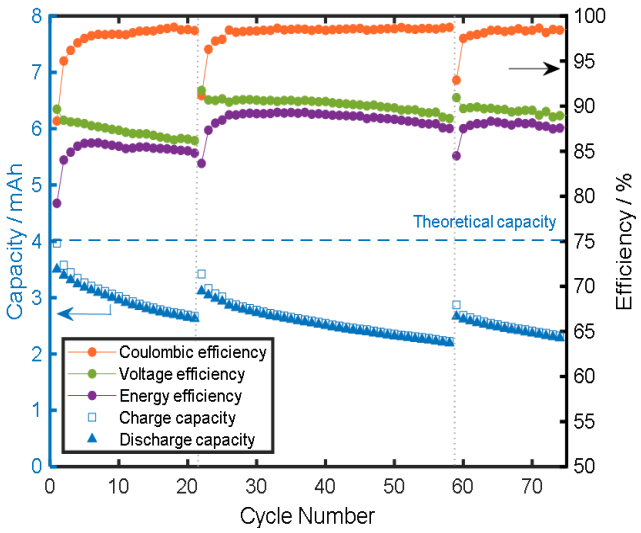

Figure 3.11. Charge capacity, discharge capacity, CE, VE and EE *vs.* cycle number for the galvanostatic cycling of (symmetric PW_{11}-SiPh RFB). Current density of 0.2 mA cm^{-2}, voltage window of 0 to 1.2 V, flow rate of 5 mL min^{-1}. Grey dotted lines indicate electrolyte regeneration. Reprinted with permission from reference 42. Copyright 2021 American Chemical Society.

The initial charge cycle achieved an electrochemical yield of 99%. However, the electrochemical yield decreased by 24% over the course of the initial 10 cycles. The capacity fade was significant for the initial cycle and quickly stabilised to an average drop of 1.6% per cycle over 20 cycles (figure 3.11). There are several physical and chemical factors that could contribute to the observed capacity loss, including degradation, precipitation or oxidation of PW_{11}-SiPh, asymmetric membrane crossover (preferential in one direction), electrolyte leakage, or unwanted side reactions. Several studies have offered experimental methodologies to determine the source of capacity fade in novel RFB systems.[38,39] No electrolyte leakage or charge carrier precipitation was observed during the cycling experiment and therefore these causes were dismissed. To determine the cause of capacity fade, several experimental observations were made at intervals throughout the 440 hours of charge-discharge cycling. Grey dotted lines at cycle 21 and cycle 59 highlighted on figure 3.11, indicate points at which the RFB was analysed and/or altered.

Following 21 cycles (140 hours of cycling), discharged electrolytes were removed from the cell and were analysed by CV. A seen in figure 3.12, the CV of positive and negative electrolyte pre cycling and following 21 cycles were broadly similar, indicating that degradation of PW_{11}-SiPh was not the primary cause of capacity fade. While CV analysis alone cannot rule out the presence of redox-inactive degradation products, it does indicate that the redox chemistry of PW_{11}-SiPh remains stable to cycling between the oxidised and two-electron reduced states.

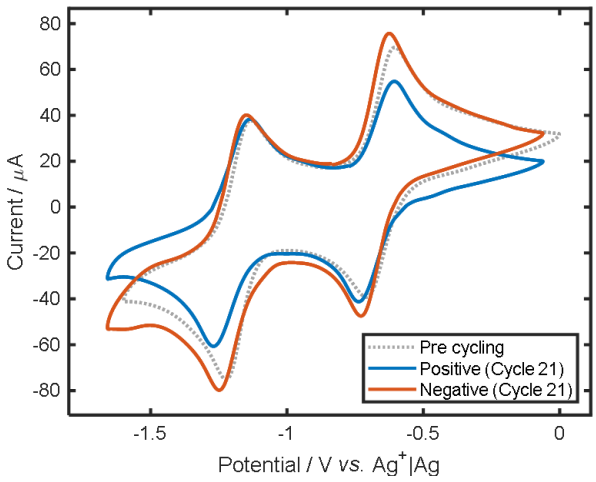

Figure 3.12. CV of positive (blue) and negative(orange) electrolyte after 21 cycles in Flow1 and electrolyte pre cycling (grey dotted). CVs were recorded using a glassy carbon WE (0.071 cm^2), Pt wire CE, and $Ag^+|Ag$ RE, at v of 50 mV s^{-1}. Reprinted with permission from reference 42. Copyright 2021 American Chemical Society.

The OCP of discharged positive and negative electrolytes were measured in a three-electrode cell. We observed a positive shift in OCP of discharged electrolytes post cycling compared to pre cycling (post electrolysis). The OCP increased from −0.95 V (pre cycling) to −0.74 V and −0.80 V (post 21 cycles) for the positive and negative electrolyte, respectively, indicating that the electrolytes had undergone a net oxidation over the course of cycling. Despite being assembled in a N_2-filled glove box, we hypothesised that trace amounts of O_2 in the solvent and atmosphere are responsible for the oxidation of the POM. This net oxidation of electrolytes upon charge-discharge cycling causes a reduction in the concentration of charge carrier in an oxidation state available to undergo charge, and therefore capacity fade occurs.

In a separate experiment, the reduction potential of O_2 at a glassy carbon WE was measured and compared to that of PW_{11}-SiPh. A solution of 0.1 M [TBA][PF_6] was purged with oxygen for 10 minutes before being analysed by CV in a three-electrode cell. Figure 3.13 shows an overlay of the CV of saturated O_2 (orange) and 5 mM PW_{11}-SiPh (blue). The reduction peak observed for saturated O_2 at –1.4 V (labelled a) is due to the one-electron reduction of O_2 to $O_2^{\bullet-}$ (superoxide).[40] Under aprotic conditions the electrochemical reduction of O_2 is quasi-reversible. The corresponding one-electron oxidation of O_2^- to O_2 is observed and labelled b. The reduction of oxygen occurs at a potential equal to or more positive than the 2nd, 3rd and 4th reduction of PW_{11}-SiPh. This indicated that the reduction of O_2 can be expected in the presence of reduced PW_{11}-SiPh. This supports our hypothesis that trace oxygen in the solvent is responsible for the net oxidation of charge carriers and therefore capacity losses in the RFB.

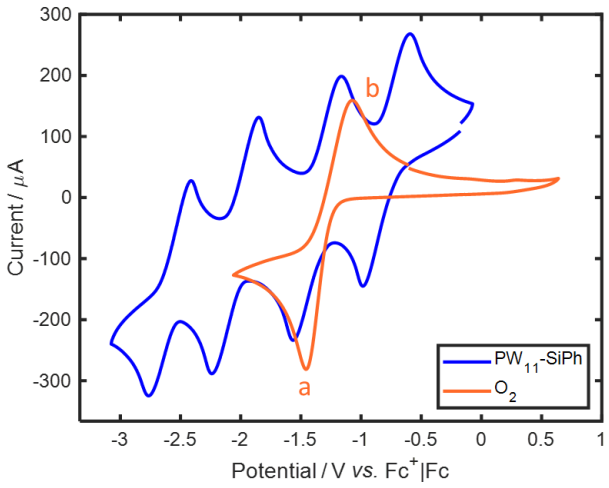

Figure 3.13. CV of 5 mM PW_{11}-SiPh in 0.1 M [TBA][PF_6] in acetonitrile (blue) and O_2 saturated 0.1 M [TBA][PF_6] in acetonitrile (orange), both recorded at a glassy carbon WE (0.071 cm^2), with Pt wire CE and $Fc^+|Fc$ internal reference, recorded at v of 100 mV s^{-1}. Reprinted with permission from reference 42. Copyright 2021 American Chemical Society.

Stimming and co-workers observed a similar phenomenon in an aqueous POM-based RFBs, in which $[PV_{14}O_{42}]^{9-}$ in the positive electrolyte underwent a net oxidation by residual O_2 in the system.[41] Stimming and colleagues were able to demonstrate regeneration of lost capacity through injection of the chemical reductant, hydrazine. In a similar vein, we were able to regain lost capacity through electrochemical re-

reduction of electrolytes. Electrolytes were removed from the battery and re-reduced to the target potential of −0.95 V (via bulk electrolysis) before being returned to their respective reservoirs without alteration to the membrane or electrodes. The RFB with regenerated electrolyte (cycle 22 onwards, figure 3.11) regained lost capacity, with the electrochemical yield returning to 86%. Due to the scale of these experiments, small volumes of liquid lost in the transfer of electrolyte between the RFB and bulk electrolysis assemblies, account for the incomplete capacity regain. These results indicate that the primary cause of capacity fade is electrolyte imbalance and not structural degradation of the POM.

Following 58 cycles (350 hours), the RFB cycling was paused and the volume in each electrolyte reservoir was measured. A discrepancy in electrolyte volume in the positive and negative electrolyte reservoirs was observed, with a larger volume measured in the negative electrolyte reservoir. This was attributed to asymmetric membrane crossover which causes an imbalance of charge carrier equivalents on each side of the battery and is a secondary cause of capacity fade in this system. To counter this effect, the discharged positive and negative electrolytes were removed from the RFB and mixed together before being equally redistributed to the electrolyte reservoirs without altering the RFB assembly. The RFB with rebalanced electrolytes (cycle 59 onwards) showed some regeneration of lost capacity.

Barteau and colleagues reported good selectivity of an aramid nanofiber membrane in POM-based nonaqueous RFBs which separates electrolytes based on size-exclusion,[4] offering a possible route to solving this source of capacity fade in our system.

3.3.3.b Flow 1 Alternating Polarity

To assess the impact of asymmetric membrane crossover more closely, a second Flow1 experiment was assembled under the same conditions, but the potential thresholds were alternated between 0 and 1.2 V and 0 and −1.2 V for a given cycle. This has the effect of alternating which reservoir is the acting positive and negative electrolyte, thereby minimising the concentration imbalance caused by asymmetric membrane crossover. Over the course of 17 cycles, the alternating cell showed a capacity fade of approximately 0.8 % per cycle (see figure 3.14). In contrast, the

standard cell exhibited a capacity loss of approximately 1.8 % per cycle over 17 cycles. The improved capacity retention demonstrated by the RFB with alternating polarity suggests that crossover is a significant source of capacity loss under standard conditions. It is clear that cycling with alternating polarity did not completely eliminate capacity fade from the cell. The capacity fade of 0.8% per cycle observed in the alternating polarity RFB is primarily attributed to oxidation of electrolytes by trace O_2.

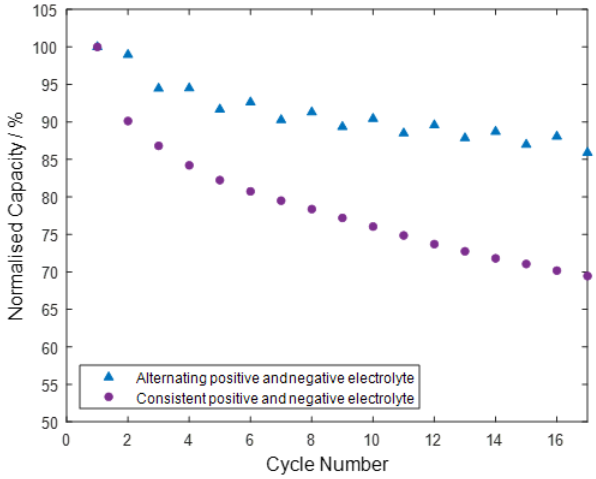

Figure 3.14. Comparison of Flow1 with consistent polarity (purple circles) and alternating polarity (blue triangles). Capacity was normalised to cycle 1 charge capacity. All other conditions were kept consistent. Reprinted with permission from reference 42. Copyright 2021 American Chemical Society.

3.3.3.c Flow 2

A second RFB was designed to investigate whether all five accessible states of PW_{11}-SiPh (3− to 7− anions) could be exploited. This strategy has the potential to increase the number of electrons transferred per molecule from one to two and to enhance V_{cell}. Given the saturation concentration of 0.6 M, theoretical average V_{cell} of 1.1 V and two-electron redox reaction, the theoretical E_v of Flow2 was calculated to be 17.7 Wh L^{-1}.

An electrolyte consisting of 10 mM PW_{11}-SiPh in 0.5 M [TBA][PF_6] in acetonitrile was prepared and pre-reduced by two electrons per molecule, by bulk electrolysis from an OCP of −0.05 to −1.45 V *vs.* $Ag^+|Ag$. 15 mL of the two-electron reduced electrolyte was added to each reservoir of the RFB. Galvanostatic cycling was conducted within

the potential window of 0 to 2.0 V at a current density of 0.2 mA cm^{-2} (C-rate of 0.125 based on the theoretical capacity of 8.04 mA h).

The proposed charge reactions are the two-electron oxidation from 5– to 3– (processes II′ and I′) in the positive electrolyte and concurrent two-electron reduction from 5– to 7– (processes III and IV) in the negative electrolyte. Upon charging the cell, two charge plateaus were observed at potentials of 0.6 V and 1.6 V (figure 3.15a). These values closely correspond to those expected from the difference in E_{mid} of the redox process in the positive and negative electrolyte (see table 3.1). Two plateaus are observed upon discharge; the first is a sloping plateau between 1.8 and 1.0 V and the second is more defined plateau at 0.6 V.

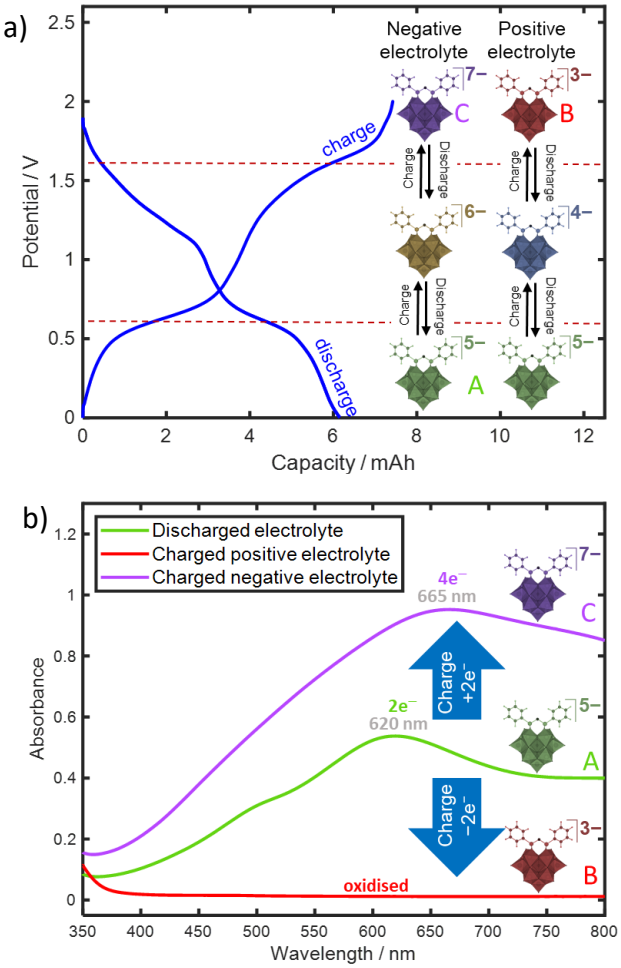

Figure 3.15. Galvanostatic cycling of Flow2 (symmetric PW_{11}-SiPh RFB). Current density of 0.2 mA cm^{-2}, voltage window of 0 to 2.0 V, and flow rate of 5 mL min^{-1}. a) Overlay of the charge and discharge profiles of cycle 1 and b) UV-visible absorbance spectra of charged and discharged electrolytes. Reprinted with permission from reference 42. Copyright 2021 American Chemical Society.

The effects of charging and discharging the cell on the states of the charge carriers were examined using UV-visible absorption spectroscopy. Electrolytes were sampled from the reservoirs of the RFB when charged and discharged and diluted in acetonitrile by a factor of 100 for analysis. Figure 3.15b shows the overlayed spectra of discharged electrolyte (pre cycling and post bulk electrolysis) and charged positive and negative electrolyte. The broad absorbance maxima at 620 nm and the shoulder peak at 500 nm observed for electrolyte in the discharged state (green trace) is characteristic of the $W^{V} \rightarrow W^{VI}$ IVCT expected for a two-electron reduced phosphotungstate Keggin[36] and confirms that 5– charged anion is the dominant state. Spectroelectrochemical analysis of PW_{11}-SiPh shown in figure 3.8 supports this

observation. The charged positive electrolyte (red trace) is a colourless solution and shows negligible absorbance in the visible region. This confirms that the positive electrolyte was fully oxidised to 3– upon charge. A broad and intense peak with an absorbance maximum at 665 nm is observed in the spectrum of the charged negative electrolyte (purple trace). While spectroelectrochemical analysis was not extended to the four-electron reduced state, the increase in absorbance and shift in maxima beyond that observed for the 6– state (635 nm) is consistent with the presence of some 7– state in solution. The extent of reduction to the 7– state cannot be confirmed and a mixed solution of 6– and 7– states is plausible.

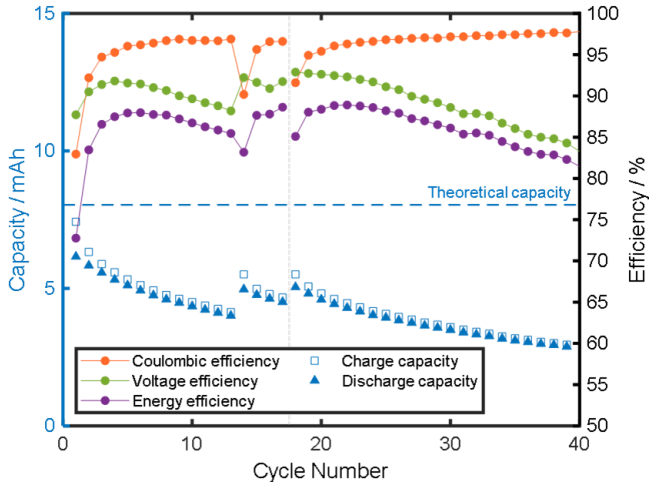

Figure 3.16. Charge capacity, discharge capacity, CE, VE and EE *vs.* cycle number for the galvanostatic cycling of Flow2 (symmetric PW_{11}-SiPh RFB). Current density of 0.2 mA cm^{-2}, voltage window of 0 to 2.0 V, and flow rate of 5 mL min^{-1}. Reprinted with permission from reference 42. Copyright 2021 American Chemical Society.

Figure 3.16 shows the charge and discharge capacities and efficiency of cycling for the initial 40 cycles of Flow2. Once stabilised, high CE was achieved averaging >97% over the course of 92 cycles. A general decrease in VE and EE was observed with cycling but remained relatively high, averaging 79% and 77 % respectively over the course of 92 cycles. The initial charge cycle achieved an electrochemical yield of 92%, which then decreased by 36% over the course of the first 10 cycles. A capacity fade of 3.6% per cycle was observed for Flow2 over the course of 12 cycles. Over the equivalent number of cycles, Flow 1 showed a capacity fade of 2.2 % per cycle. As

seen in figure 3.17, the capacity fade for Flow2 (green) is greater than for Flow1 (purple) with respect to the number of cycles and the duration of cycling.

Figure 3.18 shows the change in the shape of the charge and discharge profiles over the course of cycling. After 10 cycles the charge and discharge plateaus at 0.6 V remained consistent but the second charge and discharge plateaus at 1.6 V were no longer observed and instead occurred at a voltage of 1.2 V. Upon charge, a colour change from blue to colourless in the positive electrolyte is observed. This is indicative of oxidation to the fully charged 3– anion and was confirmed by UV-visible absorption spectroscopy. The redox potential for the 4– to 3– transition (process I/I′) is known to occur at a potential of –0.66 V (see table 3.1). Given that the second charge plateau occurs at a potential of ~1.2 V, we can deduce that the redox reaction occurring in the negative electrolyte was the 5– to 6– transition (process III/III′) as its E_{mid} is –1.81 V. The loss of the 6– to 7– transition in the negative electrolyte indicates substantial instability of the 7– state of PW_{11}-SiPh.

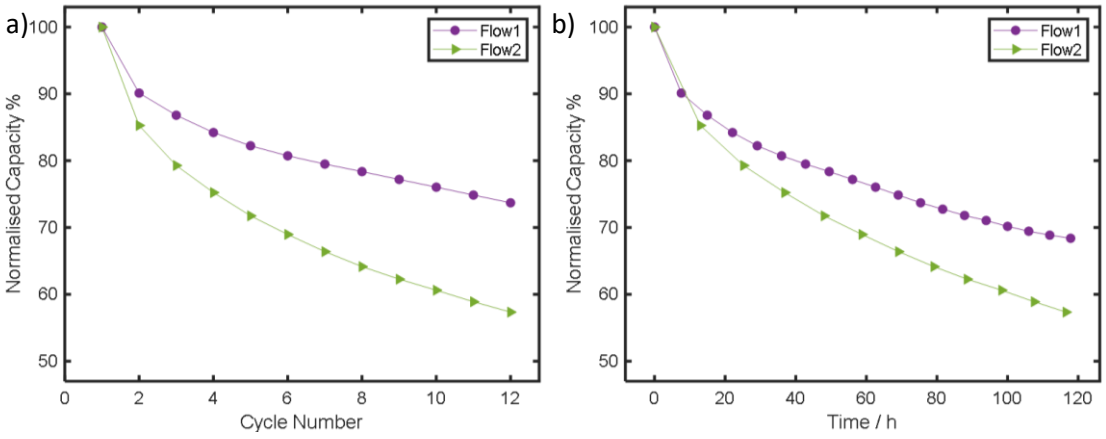

Figure 3.17. A comparison of normalised charge capacity for Flow1 and Flow2 verses a) cycle number and b) time. Note that an equivalent current density of 0.2 mA cm^{-2} was used in both cases. Reprinted with permission from reference 42. Copyright 2021 American Chemical Society.

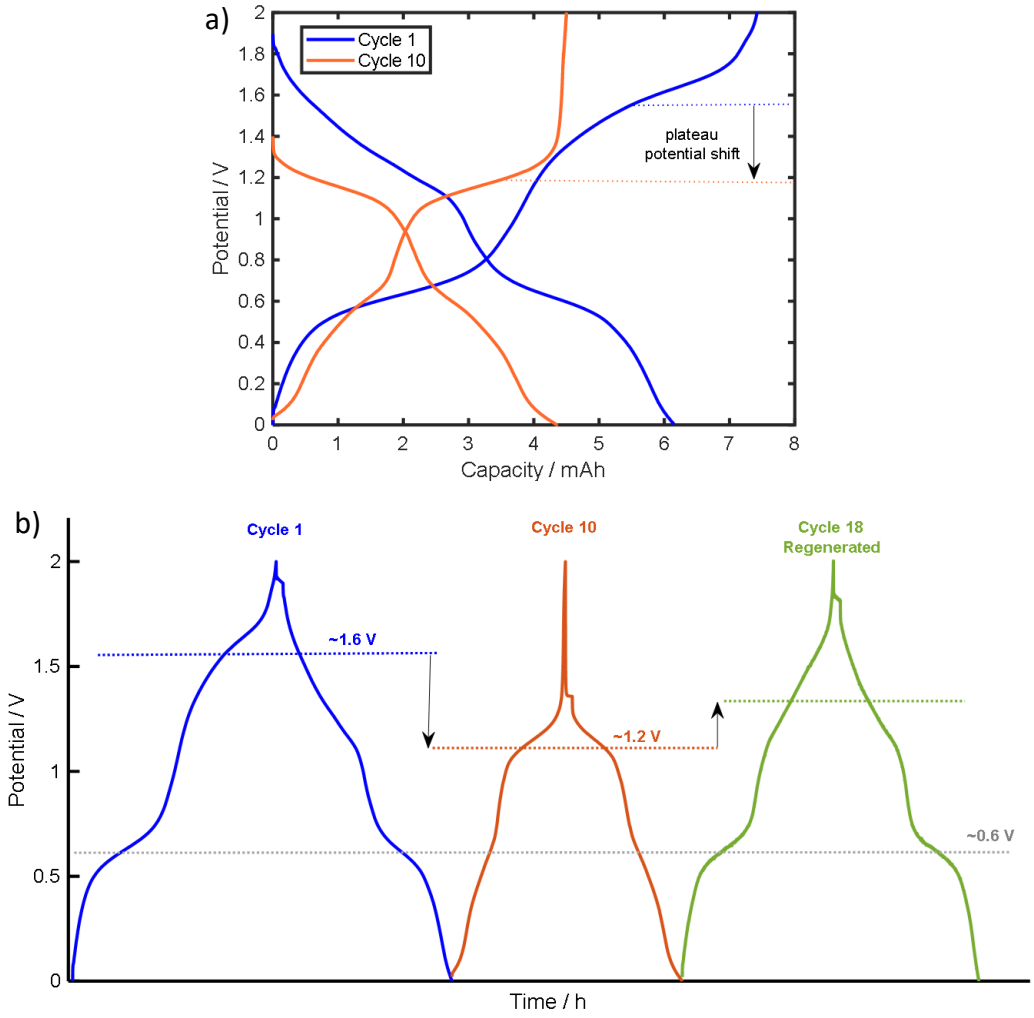

Figure 3.18. Charge and discharge cycles of Flow2 (symmetric PW_{11}-SiPh RFB). a) Overlay of cycle 1 (blue) and 10 (orange) and b) comparison of cycle 1 (blue), 10 (orange) and 18 (green). Current density of 0.2 mA cm^{-2}, voltage window of 0 to 2.0 V, flow rate of 5 mL min^{-1}. Reprinted with permission from reference 42. Copyright 2021 American Chemical Society.

The OCP of discharged electrolyte following cycling was measured in a three-electrode cell. As for Flow1, the OCP measurements indicated that both electrolytes had undergone a net oxidation over the course of cycling in the RFB. The OCP of the positive and negative electrolyte, following 17 cycles had increased from −1.45 V to −1.07 V and −1.08 V, respectively. The electrolytes were regenerated by bulk electrolysis to a target potential of −1.45 V and returned to the reservoirs without alteration to the RFB assembly. An increase in capacity is observed for cycle 18 with the regenerated electrolyte (as seen in figure 3.16). In additions, regeneration of electrolytes by bulk reduction results in a partial recovery of the charge and discharge plateau at 1.6 V (see figure 3.18). This indicates that the instability of PW_{11}-SiPh in

the 7− state is reversable. The instability is primarily due to reoxidation of the POM by trace O_2 as opposed to a permanent structural instability. The higher rate of capacity fade observed for Flow2 compared to Flow1 could be explained by the increased driving force for oxidation of 7− anion compared to the 5− anion.

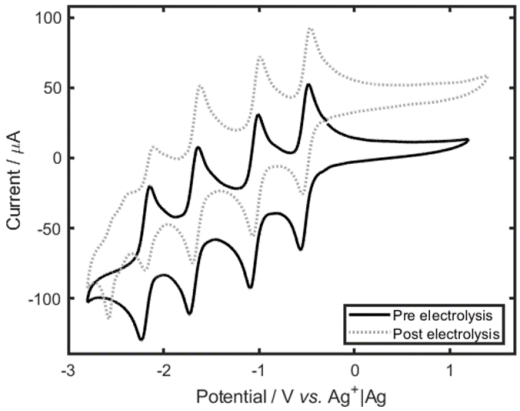

Figure 3.19. CV of 10 mM PW_{11}-SiPh in 0.5 M [TBA][PF_6] in acetonitrile, both recorded at a glassy carbon WE (0.071 cm^2), with Pt wire CE and $Ag^+|Ag$ RE, recorded at v of 100 mV s^{-1}. Black line is oxidised electrolyte pre-electrolysis and dotted grey line is electrolyte following electrolysis to two-electron reduced state (5− anion). Reprinted with permission from reference 42. Copyright 2021 American Chemical Society.

Figure 3.19 shows the CV of the PW_{11}-SiPh electrolyte before and after bulk electrolysis to the 5− anion. Following bulk electrolysis the current response for processes IV/IV' decreased in magnitude in comparison to the sample pre electrolysis. In addition, an irreversible reduction peak appeared at −2.57 V *vs.* $Ag^+|Ag$. Bulk electrolysis of the electrolyte was carried out in a purpose built cell with high surface area carbon WE, $Ag^+|Ag$ RE and a Pt gauze CE separated from the bulk by a glass frit. Upon reduction at the WE, a solution of 0.5 M [TBA][PF_6] is oxidised at the CE. The by-products generated at the CE contaminate the PW_{11}-SiPh electrolyte and are thought to contribute towards the altered CV response observed following reduction.

CV of electrolytes were recorded at intervals in the Flow2 RFB cycling experiment. Figure 3.20 shows the CV of electrolyte pre cycling (and post bulk electrolysis) and after 17 and 92 cycles in Flow2 (following discharge). The concentration of PW_{11}-SiPh can be expected to increase over the course of cycling due to the evaporation of the

acetonitrile solvent. Therefore, an increase in current magnitude can be expected in the CV response for the electrolytes sampled later in the RFB cycling experiment. Both the positive and negative electrolytes retain their rich electrochemistry throughout the RFB cycling experiment. However, some alterations to the CV response are observed which indicate some instability of PW_{11}-SiPh when cycled to the 6– and 7– states. The CV of the positive electrolyte following RFB cycling (blue lines) shows that the one-electron redox process III/III' had split into two peaks. The CV of the negative electrolyte following RFB cycling (orange and yellow lines) showed the splitting of process IV/IV' into two distinct redox couples each with comparatively low peak currents.

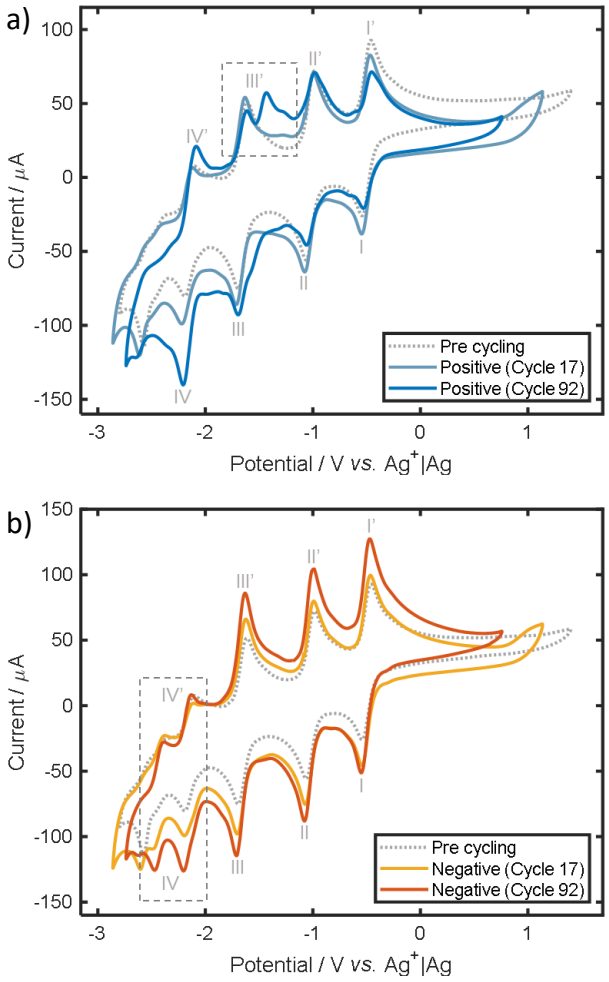

Figure 3.20. CV of a) positive and b) negative electrolyte after 17 cycles (185 h) and 92 cycles (610 h) in Flow2. The dotted line is the response obtained pre cycling and post bulk electrolysis. CV was recorded at a glassy carbon WE (0.071 cm^2), with Pt wire CE and $Ag^+|Ag$ RE, at ν of 50 mV s^{-1}. Reprinted with permission from reference 42. Copyright 2021 American Chemical Society.

3.4. Conclusions

An organic-inorganic hybridised polyoxotungstate has been presented as a charge carrier for nonaqueous RFBs for the first time. The Keggin siloxane hybrid POM, PW_{11}-SiPh investigated in this study is more soluble than its non-hybridised analogue by two orders of magnitude. The CV of PW_{11}-SiPh shows its four quasi-reversible redox process across a 2 V window. The multiple oxidation states of PW_{11}-SiPh (3– to 7– anions) allow for its application in symmetric RFBs where the same charge carrier is used in the positive and negative electrolyte. We investigated the performance of

PW_{11}-SiPh in a low V_{cell} RFB termed Flow1 (accessing the 3− to 5− anions), and later expanded the study to a high V_{cell} RFB termed Flow2 (accessing the 3− to 7− anions).

The symmetric RFBs were cycled for 75 cycles (>440 hours) with high CE, but capacity fade was observed upon cycling. The capacity fade was attributed to oxidation of the POMs by trace O_2 contamination in the system and asymmetric membrane crossover, resulting in a concentration imbalance between the electrolytes. These causes of capacity fade could be reversed to an extent through re-reduction of the electrolytes via bulk electrolysis or mixing of the electrolytes.

Given the saturation concentration of 0.6 M, average V_{cell} of 1.1 V and two-electron redox reaction, the theoretical E_v of Flow2 was calculated to be 17.7 Wh L^{-1}. However, Flow2 showed faster capacity fade compared to Flow1. This was in part attributed to the stronger driving force for reoxidation of the fully charge negative electrolyte in Flow 2 (7− anion) compared to Flow1 (5− anion). However, an additional cause of capacity fade was identified in Flow2. CV of electrolyte before and after bulk electrolysis showed instability of PW_{11}-SiPh in its highly reduced states. Future work will focus on stabilising such highly reduced forms of the POM and identifying improved methods of performing bulk electrolysis to synthesise the 5– anion.

The ability of PW_{11}-SiPh to reversibly exchange up to four electrons at highly negative potentials is advantageous for use as negative electrolyte in asymmetric RFBs. Coupled with a charge carrier with high positive redox potentials, PW_{11}-SiPh has the potential to generate a high V_{cell} and high E_v RFB. Moreover, such an approach could lessen the impact of O_2 ingress on capacity retention. The negative electrolyte in the symmetric systems investigated here is held at reduced states when charged and discharged, therefore significantly increasing its propensity to lose capacity via oxidation. As the negative electrolyte in an asymmetric system, PW_{11}-SiPh could be reduced upon charge and reoxidised to the air-stable 3– state when fully discharged, potentially combating this source of capacity fade. The performance of PW_{11}-SiPh as a negative electrolyte in an asymmetric RFB is investigated in chapter 4.

3.5. References

1 K. Lourenssen, J. Williams, F. Ahmadpour, R. Clemmer and S. Tasnim, *J. Energy Storage*, 2019, **25**, 100844.

2 H. D. Pratt, N. S. Hudak, X. Fang and T. M. Anderson, *J. Power Sources*, 2013, **236**, 259–264.

3 Y. Liu, S. Lu, H. Wang, C. Yang, X. Su and Y. Xiang, *Adv. Energy Mater.*, 2017, **7**, 1601224.

4 J. J. J. Chen and M. A. Barteau, *J. Energy Storage*, 2017, **13**, 255–261.

5 L. E. VanGelder, B. E. Petel, O. Nachtigall, G. Martinez, W. W. Brennessel and E. M. Matson, *ChemSusChem*, 2018, **11**, 4139–4149.

6 L. E. VanGelder and E. M. Matson, *J. Mater. Chem. A*, 2018, **6**, 13874–13882.

7 L. E. Vangelder, H. D. Pratt, T. M. Anderson and E. M. Matson, *Chem. Commun.*, 2019, **55**, 12247–12250.

8 Y. Cao, J. J. J. Chen and M. A. Barteau, *J. Energy Chem.*, 2020, **50**, 115–124.

9 J. Friedl, M. V Holland-Cunz, F. Cording, F. L. Pfanschilling, C. Wills, W. McFarlane, B. Schricker, R. Fleck, H. Wolfschmidt and U. Stimming, *Energy Environ. Sci.*, 2018, **11**, 3010–3018.

10 Q. Li, L. Zhang, J. Dai, H. Tang, Q. Li, H. Xue and H. Pang, *Chem. Eng. J.*, 2018, **351**, 441–461.

11 J. J. Chen, M. D. Symes and L. Cronin, *Nat. Chem.*, 2018, **10**, 1042–1047.

12 J. Friedl, F. L. Pfanschilling, M. V. Holland-Cunz, R. Fleck, B. Schricker, H. Wolfschmidt and U. Stimming, *Clean Energy*, 2019, **3**, 278–287.

13 M. Skunik-Nuckowska, K. Węgrzyn, S. Dyjak, N. H. Wisińska and P. J. Kulesza, *Energy Storage Mater.*, 2019, **21**, 427–438.

14 Z. F. Chen, Y. L. Yang, C. Zhang, S. Q. Liu and J. Yan, *J. Energy Storage*, 2021, **35**, 102281.

15 A. Ejigu, P. A. Greatorex-Davies and D. A. Walsh, *Electrochem. commun.*, 2015, **54**, 55–59.

16 K. Gong, Q. Fang, S. Gu, S. Fong, Y. Li and Y. Yan, *Energy Environ. Sci.*, 2015, **8**, 3515–3530.

17 L. E. Vangelder, A. M. Kosswattaarachchi, P. L. Forrestel, T. R. Cook and E. M. Matson, *Chem. Sci.*, 2018, **9**, 1692–1699.

18 L. E. VanGelder, H. D. Pratt, T. M. Anderson and E. M. Matson, *Chem. Commun.*, 2019, **55**, 12247–12250.

19 A. J. Kibler and G. N. Newton, *Polyhedron*, 2018, **154**, 1–20.

20 Y. F. Song and R. Tsunashima, *Chem. Soc. Rev.*, 2012, **41**, 7384–7402.

21 D. J. Wales, Q. Cao, K. Kastner, E. Karjalainen, G. N. Newton and V. Sans, *Adv. Mater.*, 2018, **30**, 1800159.

22 E. Hampson, J. M. Cameron, S. Amin, J. Kyo, J. A. Watts, H. Oshio and G. N. Newton, *Angew. Chemie - Int. Ed.*, 2019, **58**, 18281–18285.

23 E. Hampson, J. M. Cameron, J. A. Watts and G. N. Newton, *Chem. Commun.*, 2020, **56**, 8237–8240.

24 S. Amin, J. M. Cameron, J. A. Watts, D. A. Walsh, V. Sans and G. N. Newton, *Mol. Syst. Des. Eng.*, 2019, **4**, 995–999.

25 A. J. Kibler, C. Martín, J. M. Cameron, A. Rogalska, J. Dupont, D. A. Walsh and G. N. Newton, *Eur. J. Inorg. Chem.*, 2019, 456–460.

26 M. Piot, B. Abécassis, D. Brouri, C. Troufflard, A. Proust and G. Izzet, *Proc. Natl. Acad. Sci. U. S. A.*, 2018, **115**, 8895–8900.

27 A. Misra, K. Kozma, C. Streb and M. Nyman, *Angew. Chemie - Int. Ed.*, 2020, **59**, 596–612.

28 I. K. Song and M. A. Barteau, *J. Mol. Catal. A Chem.*, 2004, **212**, 229–236.

29 D. Agustin, J. Dallery, C. Coelho, A. Proust and R. Thouvenot, *J. Organomet. Chem.*, 2007, **692**, 746–754.

30 R. Crompton and C. Banks, Understanding Voltammetry, World Scietific Publishing Europe Ltd., New Jersey, 3rd edn., 2018.

31 L. E. VanGelder, T. R. Cook and E. M. Matson, *Comments Inorg. Chem.*, 2019, **39**, 51–89.

32 E. Sum and M. Skyllas-Kazacos, *J. Power Sources*, 1985, **15**, 179–190.

33 Q. Liu, A. E. S. Sleightholme, A. A. Shinkle, Y. Li and L. T. Thompson, *Electrochem. commun.*, 2009, **11**, 2312–2315.

34 R. S. Nicholson, *Anal. Chem.*, 1965, **37**, 1351–1355.

35 I. Lavagnini, R. Antiochia and F. Magno, *Electroanalysis*, 2004, **16**, 505–506.

36 G. M. Varga, E. Papaconstantinou and M. T. Pope, *Inorg. Chem.*, 1970, **9**, 662–667.

37 M. Boujtita, J. Boixel, E. Blart, C. R. Mayer and F. Odobel, *Polyhedron*, 2008, **27**, 688–692.

38 M.-A. Goulet and M. J. Aziz, *J. Electrochem. Soc.*, 2018, **165**, A1466–A1477.

39 C. G. Armstrong, R. W. Hogue and K. E. Toghill, *J. Electroanal. Chem.*, 2020, **872**, 114241.

40 M. E. Peover and B. S. White, *Electrochim. Acta*, 1966, **11**, 1061–1067.

41 J. Friedl, M. V. Holland-Cunz, F. Cording, F. L. Pfanschilling, C. Wills, W. McFarlane, B. Schricker, R. Fleck, H. Wolfschmidt and U. Stimming, *Energy Environ. Sci.*, 2018, **11**, 3010–3018.

42 C. L. Peake, A. J. Kibler, G. N. Newton and D. A. Walsh, *ACS Appl. Energy Mater.*, 2021, **4**, 8765–8773.

Chapter 4: Hybrid Polyoxometalates for Asymmetric Nonaqueous Redox Flow Batteries

4.1. Introduction

The investigations of POMs as charge carriers in RFBs has primarily been conducted in symmetric systems, where the same POM in several oxidation states is used in both positive and negative electrolytes. While the symmetric design has the advantage that capacity loss can be regenerated in the event of crossover, the V_{cell} and number of electrons transferred per molecule upon charge and discharge, *n*, is limited. There are several examples of symmetric RFBs using POMs which have four accessible redox process.[1–6] In these systems, the POM is utilised as charge carrier across both electrolytes, meaning the maximum value of *n* for a given electrolyte is two. Introducing a second charge carrier to create an asymmetric system, vastly enhances the scope of possible charge carrier combinations and opens the opportunity for greater values of *n,* higher V_{cell} and therefore increased E_v.

Stimming and co-workers first investigated asymmetric RFBs using POM-based electrolytes.[7] They used PV_{14} and SiW_{12} as charge carriers for the positive and negative electrolyte respectively. However, despite the rich electrochemistry of SW_{12}, the narrow window of electrochemical stability offered by the aqueous electrolyte, limited the value of *n* to two in the negative electrolyte. A second asymmetric RFB using POM-based electrolytes was introduced by Yan and colleagues.[8] They demonstrated a nonaqueous RFB using the sulfate-templated Wells-Dawson POM, S_2W_{18} and benzophenone as the positive and negative electrolyte respectively. Benzophenone undergoes a reversible one-electron reduction with redox potential of −1.75 V *vs.* $Ag^+|Ag$, while S_2W_{18} can be reversibly reduced by one electron, a second electron, then two electrons with redox potentials of 0.23, −0.15 and −0.49 V *vs.* $Ag^+|Ag$. In this case, four equivalents of benzophenone were used to balance the four-electron redox process of S_2W_{18}. In this case the nonaqueous electrolyte and choice of charge carriers allowed for a high V_{cell} of 1.54 V and a theoretical E_v of 9.4 Wh L^{-1}.

The four one-electron redox couples of PW_{11}-SiPh allow for its application in symmetric RFBs, and this was examined in detail in chapter 3. The symmetric study allowed for a detailed investigation of PW_{11}-SiPh stability in its various oxidation states without risk of contamination from a secondary charge carrier. It also allowed for regeneration of electrolytes by mixing and redistribution following asymmetric membrane crossover. However, using PW_{11}-SiPh in a symmetric system enables a maximum of two electrons to be transferred upon charge and discharge (n=2), and therefore a limited theoretical E_v of 17.7 Wh L^{-1}. Application of PW_{11}-SiPh as negative electrolyte in an asymmetric system has the potential for a four-electron transfer (n=4), enhanced V_{cell} and therefore increased E_v. In this investigation we introduce TEMPO as charge carrier in the positive electrolyte, while using PW_{11}-SiPh in the negative electrolyte. To the best of our knowledge, this is the first example of a POM-based negative electrolyte in a nonaqueous asymmetric RFB.

TEMPO was selected as the charge carrier for the positive electrolyte due to its well-studied, stable, and reversible redox couple at the relatively high redox potential of 0.33 V *vs.* $Ag^+|Ag$.[9] TEMPO undergoes a one-electron oxidation to an oxoammonium cation ($TEMPO^+$) as shown in scheme 4.1. The high stability of the TEMPO radical is due to delocalisation of the unpaired electron across the nitrogen-oxygen bond.[10] The four methyl groups adjacent to the nitroxide radical contribute to the stability due to the steric hinderance they provide. In addition, the solubility of TEMPO in organic solvents is generally very high as demonstrated by Wang and colleagues who report the saturation concentration of TEMPO in mixed carbonate solvents to be 5.2 M.[11]

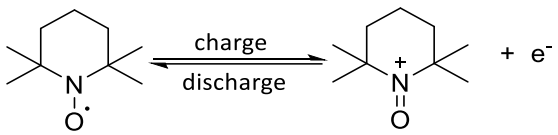

Scheme 4.1. Reversible one-electron oxidation of TEMPO nitroxide radical to the oxoammonium cation ($TEMPO^+$). As charge carrier in the positive electrolyte of a RFB, TEMPO is oxidised to $TEMPO^+$ upon charge and reduced upon discharge.

TEMPO has been applied as charge carrier in the positive electrolyte of several asymmetric RFB systems. They include a system with N-methylphthalimide negative electrolyte[12], and the hybrid RFB systems with lithium-graphite,[11] lithium,[13] and zinc[14] negative electrodes. The well-studied nature of TEMPO as charge carrier in positive electrolytes makes it an ideal candidate for testing in a novel asymmetric system with POM-based negative electrolyte.

4.2. Experimental

4.2.1 General experimental methods

Electrochemical investigations were carried out in a N_2-filled glove box (MBraun, Garching, Germany; <0.1 ppm H_2O; <0.1 ppm O_2) at room temperature, using a Bio-Logic SP-300 potentiostat/galvanostat (Seyssinet-Parizet, France) ran using EC-Lab software. Glassware and equipment were dried in a vacuum oven at 60 °C for 16 hours prior to use. [TBA][PF_6] (≥ 99.0%, Sigma Aldrich) was dried at 60 °C under vacuum for a minimum of 1 day before being transferred to the glove box. Acetonitrile solvent was degassed by sonication before being dried over 4 Å molecular sieves (Sigma-Aldrich). The dryness of electrolytes was verified by Karl-Fischer titration (METTLER TOLEDO). UV-visible absorption spectroscopy of electrolytes was performed using an Agilent Cary UV-visible NIR spectrometer (Santa Clara, USA).

4.2.2 Cyclic voltammetry

CV was carried out using a three-electrode cell, containing a 3 mm diameter glassy carbon working WE (0.071 cm^2 surface area) and Pt wire CE (>0.16 cm^2 surface area). The potential was referenced to a Ag wire QRE with Fc internal standard or $Ag^+|Ag$ nonaqueous RE containing 10 mM $AgNO_3$ in 0.1 M [TBA][PF_6] in acetonitrile. The glassy carbon WE was polished using aqueous alumina slurries of decreasing particle size (1 µm, 0.3 µm and 0.05 µm), and rinsed thoroughly with water. The Pt wire CE was cleaned in a butane flame prior to use. CVs were iR compensated at 85% using the ZIR tool included within the EC-Lab software.

4.2.3 Electrochemical impedance spectroscopy

EIS measurements were conducted over frequency range from 100 kHz to 100 mHz at AC amplitude of 10 mV.

4.2.4 Redox flow battery

Galvanostatic charge-discharge cycling experiments were carried out in a N_2-filled glove box with a 5 cm^2 membrane surface area assembly (Scribner, Southern Pines, USA). Graphite felt electrodes (0.6 cm thickness, SGL carbon, Wiesbaden, Germany) were sandwiched between interdigitated graphite flow fields with PTFE flow frames

and gaskets. An anion-exchange membrane AMI-7001 (Membranes International Inc. Ringwood, USA) was used to separate the two half cells. 0.5 M [TBA][PF_6] in acetonitrile was pumped through the RFB for a minimum of 16 hours prior to charge-discharge cycling in order to wet the electrodes and membrane. A negative electrolyte of 10 mM PW_{11}-SiPh in 0.5 M [TBA][PF_6] in acetonitrile was prepared. A positive electrolyte of 40 mM TEMPO in 0.5 M [TBA][PF_6] in acetonitrile was prepared. 20 mL of electrolyte was placed in each reservoir. A dual channel peristaltic pump (Masterflex L/S, Vernon Hills, USA) was used to pump electrolytes through the cell at a flow rate of 10 mL min^{-1} using C-flex ULTRA tubing (Masterflex, Vernon Hills, USA). Galvanostatic cycling was conducted within a defined potential window.

4.3. Results and Discussion

4.3.1 Electrochemical characterisation of TEMPO

Figure 4.1 shows the CV of TEMPO dissolved in acetonitrile containing 0.1 M [TBA][PF_6], recorded at a polished glassy carbon WE within the v range of 10 to 500 mV s^{-1}. An oxidation peak (labelled I) and corresponding reduction peak (labelled I') are observed with mid-point potential, E_{mid}, of 0.37 V *vs.* $Ag^+|Ag$, which is in good agreement with values found in the literature.[9] The redox couple is attributed to the one-electron oxidation of TEMPO to $TEMPO^+$ and its corresponding reduction back to TEMPO (see scheme 4.1). At v of 100 mV s^{-1}, the ratio of anodic to cathodic peak currents, $i_{p,a}/i_{p,c}$, was 0.98 which is close to unity as expected for an electrochemically reversible redox couple. The peak-to-peak separation, ΔE_p was 122 mV which is greater than the value of 59 mV expected for the electrically-reversible transfer of a single electron. Moreover, ΔE_p increased with increasing v, indicating that each redox process was electrochemically quasi-reversible.

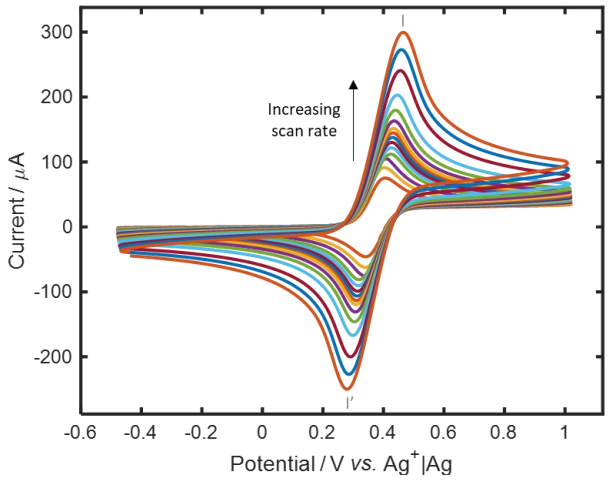

Figure 4.1. CV of 5 mM TEMPO in 0.1 M [TBA][PF_6] in acetonitrile at a glassy carbon WE (0.071 cm^2) with Pt wire CE and $Ag^+|Ag$ RE. Voltage was swept between −0.5 and 1 V at v of 10 to 500 mV s^{-1} with iR compensation applied.

Fast mass transport and electron transfer of charge carriers is key to enabling high power density RFBs.[15] We determined the diffusion coefficient, *D*, of TEMPO by investigating the effect of v on the voltametric response. At v > 200 mV s^{-1}, the plot of $i_{p,a}$ *vs.* $v^{1/2}$ deviated from linearity (see figure 4.2), so the gradient in the region 10 mV s^{-1} < v < 200 mV s^{-1} was used in conjunction with Eq. 3.5 from chapter 3 to estimate *D* (reversible Randles-Sevcik equation).[16] Our analysis reveals that *D* of TEMPO = 2.1 × 10^{-5} cm^2 s^{-1}. Several investigations have reported the diffusion coefficient of TEMPO in acetonitrile in the same order of magnitude (1.1 – 3.4 × 10^{-5} cm^2 s^{-1}).[10,12,17] The Nicholson method was used to calculate the heterogeneous electron transfer constant, k^0 of TEMPO. Our analysis reveals k^0 of 2.2 × 10^{-2} cm s^{-1} which aligns well with literature values (8.4 × 10^{-1} cm s^{-1} for TEMPO in 0.1 M [TBA][BF_4] in acetonitrile).[10] This value far exceeds k^0 for the VO_2^+/VO^{2+} and V^{3+}/V^{2+} couples used in the VRFB (~10^{-5} cm s^{-1}).[18] This analysis confirms that the redox properties of TEMPO in a solution of [TBA][PF_6] in acetonitrile is suitable for application in RFBs.

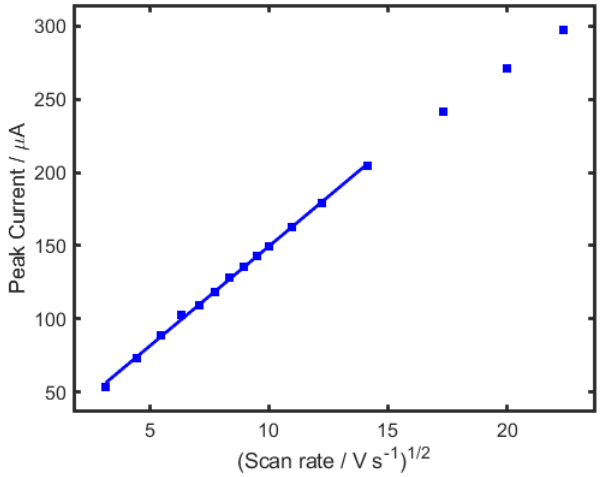

Figure 4.2. Peak current *vs.* $v^{1/2}$ for the oxidation of TEMPO (process I). Data was obtained from the first voltammetry sweep of 5 mM TEMPO in 0.1 M [TBA][PF_6] in acetonitrile over the $\boldsymbol{v}$ range of 10 to 200 mV s^{-1}.

A key drawback of asymmetric RFBs is the detrimental effects of membrane crossover on the battery capacity. The development of highly selective and conductive membranes and separators for nonaqueous RFBs is ongoing, and membranes crossover is common with the current commercially available offerings.[19] As discussed in chapter 2, crossover is generally driven by a concentration gradient, migration effects and/or electroosmotic drag. A concentration gradient is present across the PW_{11}-SiPh|TEMPO RFB and migration of the charged positive electrolyte, $TEMPO^+$, towards the negative electrode can be expected. With this knowledge, it is important to investigate the electrochemical behaviour of TEMPO at more negative potentials. In the event of TEMPO crossover to the opposite half-cell, the charge carrier will be exposed to highly reducing potentials (PW_{11}-SiPh is reduced within the potential window of −0.5 and −2.5 V *vs.* $Ag^+|Ag$).

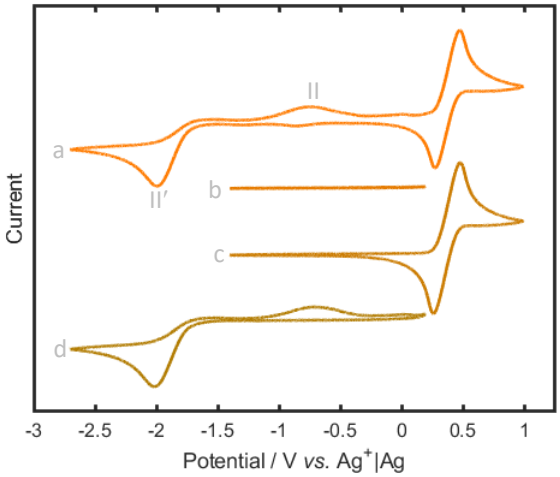

Figure 4.3. CV of 40 mM TEMPO in 0.1 M [TBA][PF_6] in acetonitrile at a glassy carbon WE (0.071 cm^2) with Pt wire CE, and $Ag^+|Ag$ RE, at v of 100 mV s^{-1} and with iR compensation. Voltage window was varied between a) −2.8 V to 1 V, b) −1.4 V to 0.2 V, c) −1.4 V to 1 V and d) −2.8 V to 0.2 V.

Figure 4.3 shows a series of voltammograms of TEMPO across various potential windows. Figure 4.3a shows the CV of TEMPO within the potential window of −2.8 V to 1.0 V *vs.* $Ag^+|Ag$. A cathodic peak is observed at −1.93 V (labelled II′) and is attributed to the one-electron reduction of TEMPO to an aminoxy anion ($TEMPO^-$). The anodic peak at −0.85 V (labelled II) is only observed when the potential is swept such that TEMPO is first reduced to $TEMPO^-$ i.e. to the potential of −2.8 V. This indicates that the anodic peak II is coupled to the cathodic peak II′. Maruyama *et al.* investigated the electrochemical reduction of TEMPO in organic solvents and ionic liquids and observed an irreversible reduction of TEMPO at −2.1 V *vs.* $Ag^+|Ag$ in dichlorobenzene.[20] $TEMPO^-$ is known to be highly unstable due to its fast chemical reaction with electrophiles such as protons (from solvent or other contaminants) to produce the hydroxylamine derivative (TEMPOH) as depicted in scheme 4.2.[21] The presence of some protons can be expected in the electrolyte despite the use of the aprotic solvent, due to minor water contamination. Consequently, the majority of $TEMPO^-$ is protonated to TEMPOH and a comparatively small current is observed for the reoxidation peak.

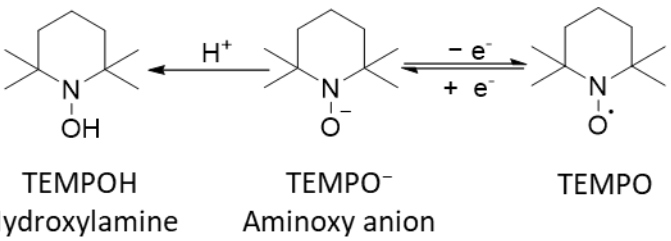

Scheme 4.2. One-electron reduction of TEMPO nitroxide radical to aminoxy anion ($TEMPO^-$), followed by protonation to an hydroxylamine (TEMPOH).

Izgorodina and colleagues sought to enhance the electrochemical reversibility of TEMPO reduction by stabilising $TEMPO^-$ with ionic liquids.[21] Two reversible one-electron redox couples of TEMPO would allow for its application as charge carrier in symmetric RFBs. However, for the application of TEMPO as positive electrolyte in an asymmetric system, as investigated here, the reduction of TEMPO is, at best inconsequential, and at worst detrimental to the battery performance. In an asymmetric RFB with stable charge carriers, complete membrane crossover would cause a 50% reduction in capacity as the concentration of positive and negative charge carriers are halved in their respective electrolytes. In contrast, when TEMPO crossover to the negative half-cell occurs, we can expect its degradation via irreversible reduction to $TEMPO^–$, ultimately leading to a >50% reduction in capacity.

4.3.2 Electrochemical characterisation of PW_{11}-SiPh

The detailed electrochemical characterisation of PW_{11}-SiPh was reported in chapter 3. The benefit of organic-inorganic hybridisation is twofold. First, the saturation concentration of PW_{11}-SiPh in acetonitrile is increased by two orders of magnitude compared to the non-hybridised parent compound PW_{12}. Secondly, the hybridisation negatively shifted the onset potential of the first reduction by 80 mV compared to that of the non-hybridised POM. This is attributed to the electron-donating nature of the siloxane linker.[22] This increases the difference in redox potential between PW_{11}-SiPh and TEMPO leading to a larger V_{cell} in the RFB.

4.3.3 PW_{11}-SiPh |TEMPO

A PW_{11}-SiPh|TEMPO RFB was assembled in a N_2-filled glove box. An electrolyte consisting of 0.5 M [TBA][PF_6] in acetonitrile was pumped through the assembled RFB in order to soak the membrane and electrodes prior to the addition of charge carriers.

An AMI-7001 anion exchange membrane was used to separate the half-cells and a flow rate of 10 mL min^{-1} was applied. AMI-7001 is composed of quaternary ammonium groups tethered to a polystyrene backbone and was supplied in the chlorinated form. Pre-soaking allows for exchange of Cl^- for PF_6^-, and should thereby enhance membrane conductivity in the chosen electrolyte.

After soaking for 16 hours, potentiostatic EIS was recorded across the assembled RFB to measure the resistance across the flow cell. Measurements were recorded within the frequency range of 100 kHz to 100 mHz. R_{ohm} is the sum of ohmic resistance within the cell and includes contributions from the electrolyte, membrane, graphite felt electrodes, and electrical leads between the cell and the potentiostat. R_{ohm} of the cell was measured to be 600 Ω, leading to an area specific resistance of 3 kΩ cm^2. This value far exceeds the target ASR for nonaqueous RFBs of 5 Ω cm^2, determined necessary for cost effective energy storage.[23] High ohmic resistance leads to large overpotentials and therefore low VE, and a limitation to the achievable power density of the RFB. In spite of this high ohmic resistance, AMI-7001 was selected due to its high selectivity which is known to prevents crossover of POMs and cations. Yan and co-workers reported <1% crossover of S_2W_{18} over three days in static cell permeability tests with acetonitrile-based electrolyte.[8]

4.3.3.a PW_{11}-SiPh |TEMPO performance

Following soaking of the membrane and electrodes, the blank electrolyte was removed and charge carrier-containing electrolytes were added. The negative electrolyte consisted of 20 mL of 10 mM PW_{11}-SiPh in 0.5 M [TBA][PF_6] in acetonitrile, while the positive electrolyte contained 20 mL of 40 mM TEMPO in 0.5 M [TBA][PF_6] in acetonitrile. The concentration of TEMPO (one-electron redox reaction) in the positive electrolyte was four times that of PW_{11}-SiPh in order to balance the four-electron redox reaction of PW_{11}-SiPh upon charge. Figure 4.4 shows the CV of PW_{11}-SiPh and TEMPO overlayed and illustrates the redox reactions targeted in the charge and discharge cycling of the PW_{11}-SiPh|TEMPO RFB.

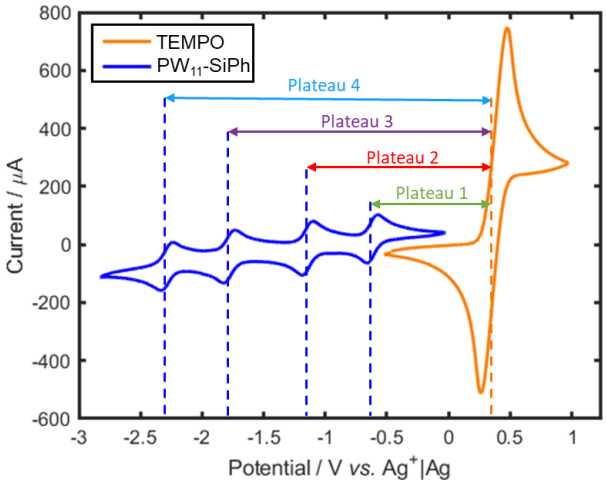

Figure 4.4. CV overlay of 40 mM TEMPO (orange) and 10 mM PW_{11}-SiPh (blue). Both CVs recorded in 0.5 M [TBA][PF_6] in acetonitrile at a glassy carbon WE (0.071 cm^2) with Pt wire CE and $Ag^+|Ag$ RE at v of 100 mV s^{-1}. Dashed lines indicate E_{mid} of each redox couple and the coloured arrows indicate the expected average voltage of charge/discharge plateaus in a PW_{11}-SiPh|TEMPO RFB.

Table 4.1. Expected charge and discharge reactions within the positive and negative electrolytes of the PW_{11}-SiPh|TEMPO RFB. The expected potential of plateaus have been calculated based on the E_{mid} from the CV of each charge carrier.

Plateau	Positive electrolyte rxn. (E_{mid} *vs.* $Ag^+|Ag$)	Negative electrolyte rxn. (E_{mid} *vs.* $Ag^+|Ag$)	Potential / V
1	$TEMPO \rightleftharpoons TEMPO^+ + e^-$ (0.37 V)	$PW_{11}\text{-}SiPh^{3-} + e^- \rightleftharpoons PW_{11}\text{-}SiPh^{4-}$ (-0.66 V)	1.03
2	$TEMPO \rightleftharpoons TEMPO^+ + e^-$ (0.37 V)	$PW_{11}\text{-}SiPh^{4-} + e^- \rightleftharpoons PW_{11}\text{-}SiPh^{5-}$ (-1.18 V)	1.55
3	$TEMPO \rightleftharpoons TEMPO^+ + e^-$ (0.37 V)	$PW_{11}\text{-}SiPh^{5-} + e^- \rightleftharpoons PW_{11}\text{-}SiPh^{6-}$ (-1.81 V)	2.18
4	$TEMPO \rightleftharpoons TEMPO^+ + e^-$ (0.37 V)	$PW_{11}\text{-}SiPh^{6-} + e^- \rightleftharpoons PW_{11}\text{-}SiPh^{7-}$ (-2.31 V)	2.68

In chapter 3 we concluded that PW_{11}-SiPh is less stable in its most reduced oxidation states. Consequently, the initial galvanostatic cycling tests were conducted within the potential window of 0 to 2.2 V to access only the first two redox process of PW_{11}-SiPh. The theoretical capacity was calculated to be 10.72 mA h, given the electrolyte composition and number of electrons transferred upon charge/discharge (n=2). The current density was limited to 0.2 mA cm^{-2} (absolute current of ±1 mA) which equates to a theoretical C-rate of approximately 1/10 C.

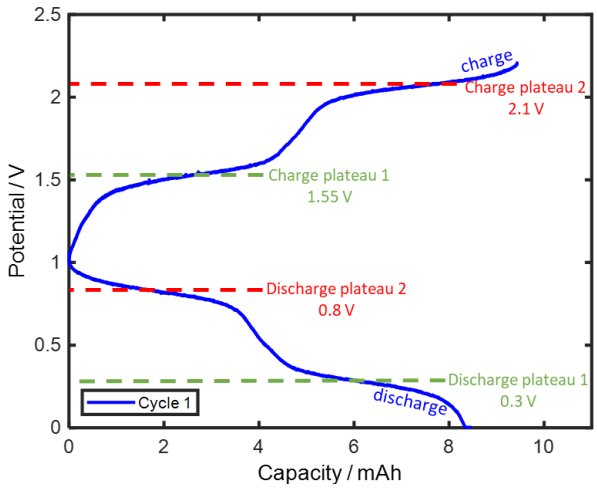

Figure 4.5. Galvanostatic charge-discharge analysis of a PW_{11}-SiPh|TEMPO RFB containing 40 mM TEMPO in the positive electrolyte and 10 mM PW_{11}-SiPh in the negative electrolyte. Half-cells were separated by anion exchange membrane AMI-7001, the voltage range was 0 to 2.2 V, current density was 0.2 mA cm^{-2} and flow rate was 10 mL min^{-1}. Charge and discharge profiles of cycle 1 are shown. Dashed lines indicate the average potential of each plateau.

Figure 4.5 shows the initial charge and discharge profiles for PW_{11}-SiPh|TEMPO RFB. Two charge plateaus were observed at potentials of 1.55 V (green) and 2.10 V (red). This correspond to the one-electron oxidation of TEMPO to $TEMPO^+$ in the positive electrolyte and simultaneous reduction of PW_{11}-SiPh from anion charges of 3– to 4– (plateau 1) and 4– to 5– (plateau 2) in the negative electrolyte. Two corresponding discharge plateaus were observed at 0.8 V (red) and 0.3 V (green). These correlate to the reverse reactions. The potential of each charge and discharge plateau is approximately 0.6 V higher and lower respectively than the values anticipated in table 4.1. This is in line with the expected overpotential given the cells ohmic

resistance of 600 Ω and current of ±1 mA. The large overpotentials observed are attributed to the high resistance of AMI-7001 anion exchange membrane in nonaqueous solvent. Despite the large overpotentials, the average voltage of the charge and discharge plateaus are in good agreement with the values predicted from the voltammetry as stated in table 4.1.

Interestingly, we observed a reduction in overpotentials over the course of cycling. Figure 4.6 shows the charge and discharge profiles of cycle 1 and cycle 8 overlayed. The overpotential is reduced from 0.6 V (cycle 1) to 0.3 V (cycle 8). The reduced overpotential indices increase conductivity across the RFB and is most likely linked to the membrane. We can speculate that exchange of the chlorinated form of AMI-7001 to the PF_6^- form was not complete within the pre-soaking period. Alternatively, it may indicate structure changes to the membrane such as pore enlargement, which increase conductivity but may also reduce selectivity.

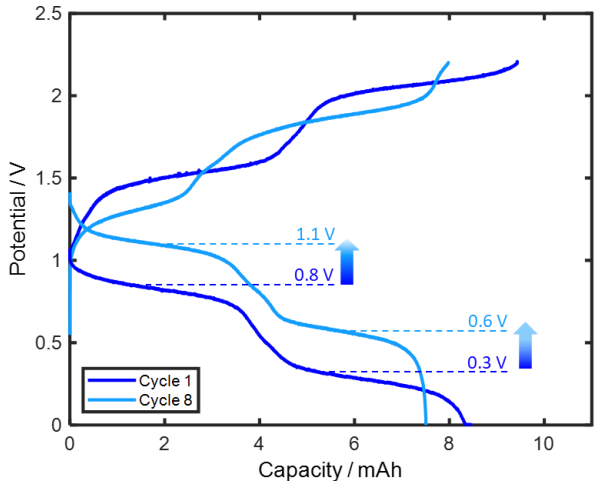

Figure 4.6. Galvanostatic charge-discharge analysis of a PW_{11}-SiPh|TEMPO RFB containing 40 mM TEMPO in the positive electrolyte and 10 mM PW_{11}-SiPh in the negative electrolyte. Half cells were separated by anion exchange membrane AMI-7001, the voltage range was 0 to 2.2 V, current density was 0.2 mA cm^{-2} and flow rate was 10 mL min^{-1}. Charge and discharge profiles of cycle 1 and 8 are overlayed. Dashed lines indicate the average potential of discharge plateaus and highlight the reduced overpotential following 8 cycles.

After 8 cycles, the upper potential threshold was increased to 2.7 V in order to access the third redox couple of PW_{11}-SiPh. In this instance, upon charge PW_{11}-SiPh is reduced from the anion charge of 3– to 4– (plateau 1), 4– to 5– (plateau 2) and then

5– to 6– (plateau 3). This increases the number of electrons transferred upon charge/discharge from two to three, resulting in an increased theoretical capacity of 16.08 mA h. Figure 4.7a shows the charge and discharge profiles of cycle 1 (blue) and cycle 9 (green). A third charge and discharge plateau (labelled C3 and D3 respectively) was observed when the potential window of cycling was increased to 0 to 2.7 V. Both plateaus occur at potentials corresponding to plateau 3 in table 4.1 when accounting for the overpotential of 0.3 V. Charge capacity of cycle 9 increased by 59% compared to cycle 8. This increase in capacity is roughly in line with the 50% increase in capacity anticipated based on increasing the number of electrons transferred per molecule from two to three. The average V_{cell} increased from 1.3 V for cycles 1-8 (n=2) to 1.6 V for cycles 9-20 (n=3).

The RFB was cycled successfully for 20 cycles (>400 hours) with average CE of 95%. Over the cause of the initial 8 cycles, VE increased due to the reduced overpotentials. The VE and EE stabilised at 70% and 67% respectively by cycle 20. The shape of the charge and discharge curves within a given potential window did not change over the course of cycling. However, as seen in figure 4.7b, capacity fade is observed upon cycling. Capacity fade averaged 2.2 % per cycle over the initial 8 cycles and 2.1% per cycle over the following 12 cycles. The cause of capacity fade was investigated by post cycling analysis of electrolytes and is discussed in section 4.3.3.b.

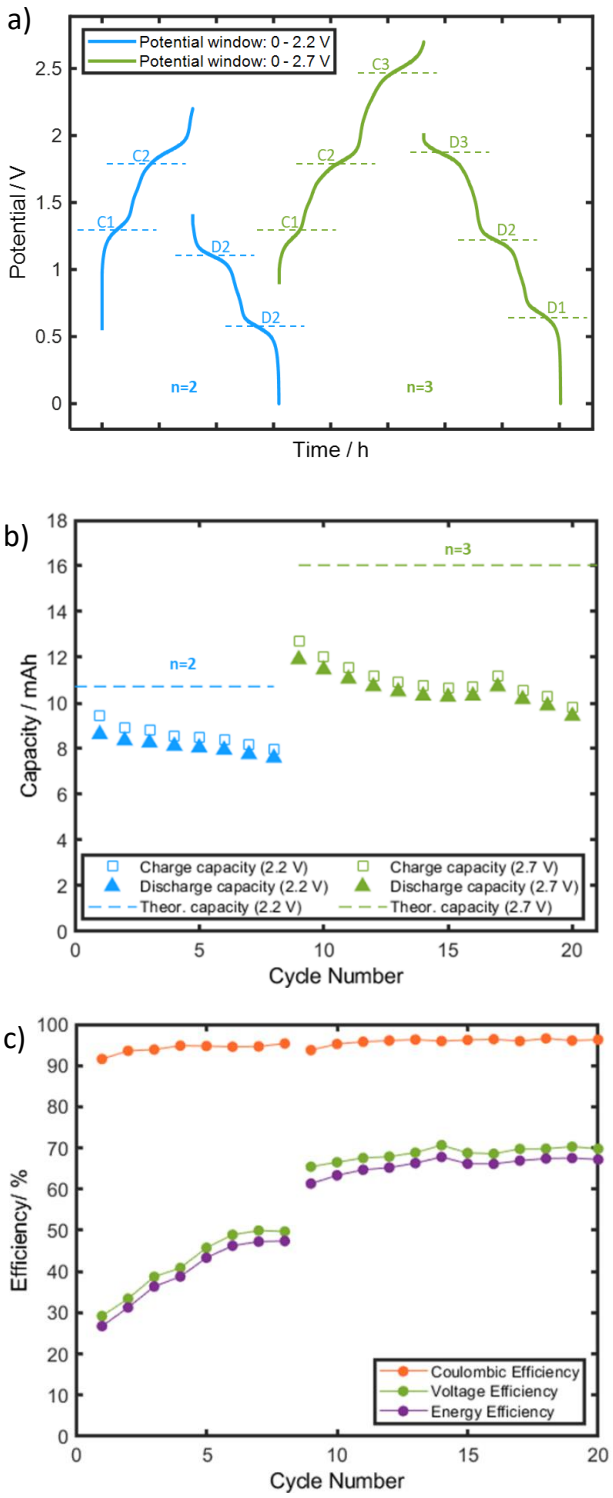

Figure 4.7. Galvanostatic charge-discharge analysis of a PW_{11}-SiPh|TEMPO RFB containing 40 mM TEMPO and 10 mM PW_{11}-SiPh, within the potential window of 0 to 2.2 V, then 0 to 2.7 V. Half-cells were separated by AMI-7001, current density was 0.2 mA cm^{-2} and flow rate was 10 mL min^{-1}. a) Charge and discharge profiles for cycles 8 (potential threshold of 0 to 2.2 V, *n*=2) and cycle 9 (potential threshold of 0 to 2.7 V, *n*=3), b) charge and discharge capacity for cycles 1-16 and c) CE, VE and EE for cycles 1 to 16.

In a separate RFB experiment with fresh electrolyte, galvanostatic cycling was conducted within the potential window of 0 to 3.5 V to access all four redox process of PW_{11}-SiPh. Given the increased number of electrons transferred upon charge/discharge to four, the theoretical capacity was calculated to be 21.44 mA h. The charging current density was increased to 0.3 mA cm^{-2} (absolute current of ±1.5 mA) which equates to a theoretical C-rate of 1/14 C. This theoretical C-rate more closely aligns with the values used in the previous battery.

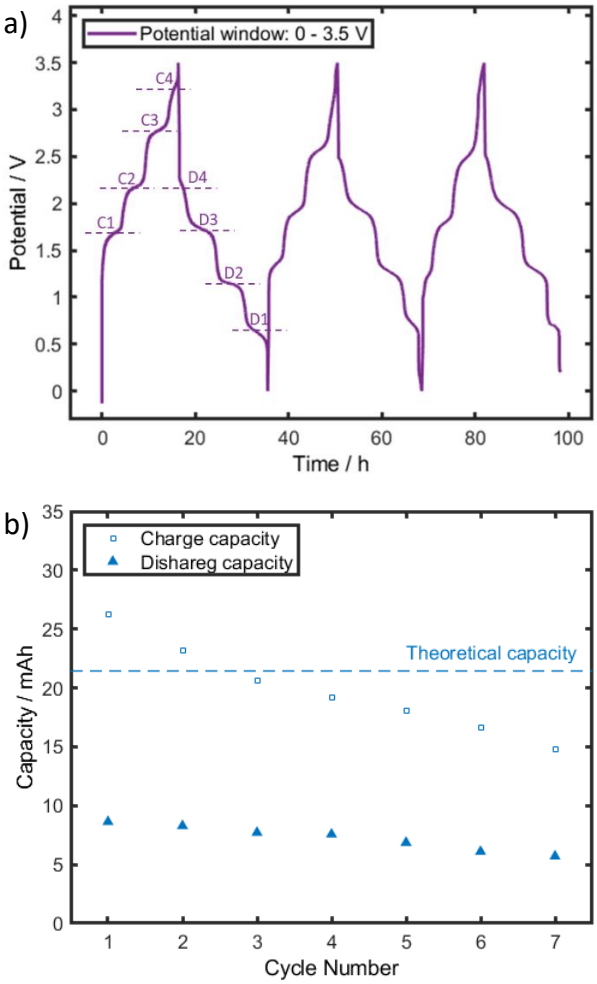

Figure 4.8. Galvanostatic charge-discharge analysis of a PW_{11}-SiPh|TEMPO RFB containing 40 mM TEMPO and 10 mM PW_{11}-SiPh, within the potential window of 0 to 3.5 V. Half-cells were separated by AMI-7001, current density was 0.3 mA cm^{-2} and flow rate was 10 mL min^{-1}. a) Charge and discharge profiles for cycles 1 to 3 and b) charge and discharge capacity for cycles 1 to 7.

Figure 4.8 shows the performance of the PW_{11}-SiPh|TEMPO RFB cycled within the potential window of 0 to 3.5 V. Four well-defined charge plateaus (labelled C1 to C4)

and discharge plateaus (labelled D1 to D4) are observed in the initial cycle. This indicates that PW_{11}-SiPh is successfully reduced by four electrons upon charge. The potential of the plateaus correlates well to the values anticipated from the voltammetry and stated in table 4.1 (accounting for overpotentials). However, C4 and D4 are not sustained in the following cycles. Only charge and discharge plateaus 1 to 3 are observed, which indicates instability of PW_{11}-SiPh when reduced to the 7– anion. This is in alignment with observations made in chapter 3 where the asymmetric PW_{11}-SiPh RFB termed Flow2 showed poor stability when the negative electrolyte was charged to the 7– anion.

As seen in figure 4.8b, the achieved discharge capacity are far lower than the charge capacity for a given cycle. The CE averages 37% and is substantially lower than the values for the PW_{11}-SiPh|TEMPO RFB which were limited to a narrower potential window (CE >90%). Our investigation of PW_{11}-SiPh in symmetric systems indicates that reduced PW_{11}-SiPh is sensitive to reoxidation with trace oxygen and water and that the increased driving force for reoxidation is greatest in its most reduced oxidation state (7– anion). This phenomenon could account for the reduced CE observed for the RFB when PW_{11}-SiPh is charged to the 7– anion compared to the RFB when PW_{11}-SiPh is charged to the 5– or 6– anions.

If the reduced CE was exclusively due to reoxidation of the 7– anion to 6– anion, we would expect a decrease in the capacity of plateau 4 only. However, the discharge profile of cycle 1 shows a reduction in capacity for each discharge plateau. In addition, figure 4.9 shows dark brown residue on the flow frame of the negative half-cell and on the side of the membrane which interfaced with the negative half-cell. The residue was stained onto the battery components and we were unable to sample the material for analysis. The residue is indicative of degradation products and was only observed when the RFB was cycled within the potential window of 0 to 3.5 V.

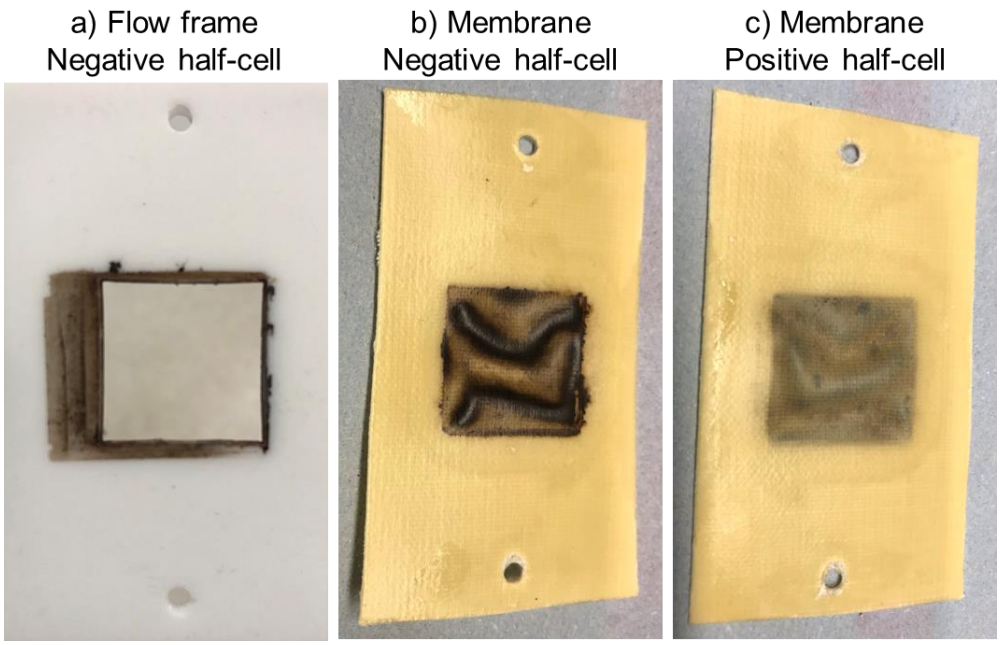

Figure 4.9. Images of a) flow frame from the negative half-cell, b) membrane interfacing the negative half-cell and c) membrane interfacing the positive half-cell, following galvanostatic cycling in a PW_{11}-SiPh|TEMPO RFB within the potential window of 0 to 3.5 V.

4.3.3.b PW_{11}-SiPh |TEMPO post cycling analysis

Post cycling analysis was conducted to investigate the cause of capacity fade in the PW_{11}-SiPh|TEMPO RFB when cycled within the potential window of 0 to 2.7 V. Electrolytes were analysed by CV and UV-visible absorption spectroscopy pre and post cycling. Figure 4.10 shows the CV of positive and negative electrolytes pre cycling and following 8 cycles (140 hours) and 20 cycles (>400 hours). A wide potential window was scanned in the voltammetry of the electrolytes in order to investigate the presence of charge carrier from the opposite half-cell. We observe minor redox couples at −0.6 V and −2.3 V (indicated by green arrows) in the CV of positive electrolyte following 20 cycles. The potential of the peaks correlate to the first and fourth redox couple of PW_{11}-SiPh and indicates that crossover of charge carriers to their opposite half-cell has occurred. The second and third redox couples of PW_{11}-SiPh are masked by the current of the TEMPO reduction peak.

A second observation is the decrease in current magnitude of the TEMPO redox couples with increasing number of charge-discharge cycles in the RFB. Due to the volatility of acetonitrile, the concentration of TEMPO would be expected to increase

somewhat as solvent evaporates from the electrolyte. However, the reduced current response in the voltammetry of the positive electrolyte indicates that the concentration of TEMPO in the electrolyte has reduced. This is likely as a result of TEMPO crossover to the negative electrolyte.

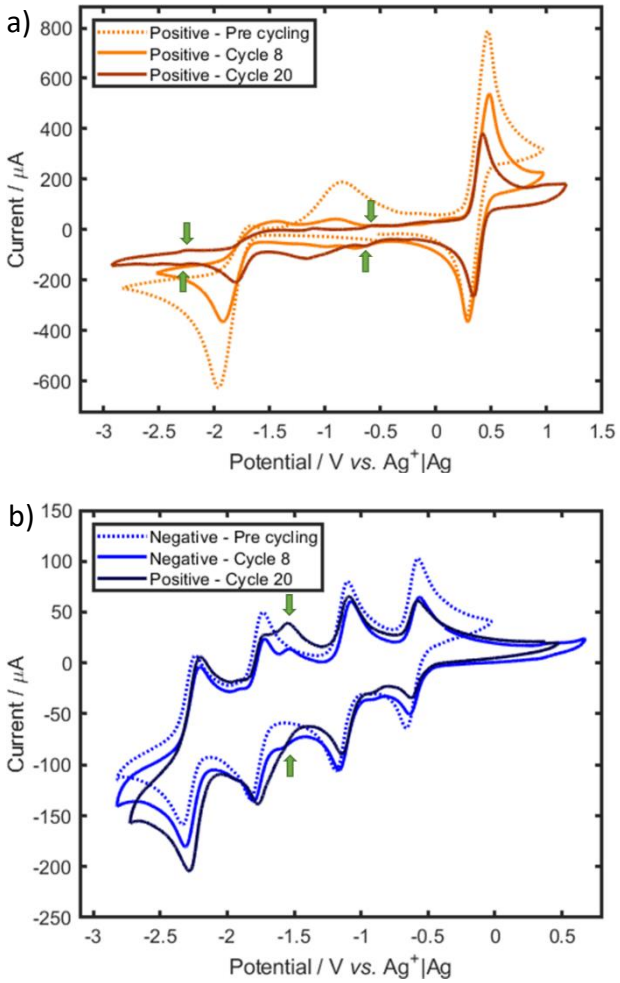

Figure 4.10. a) CV overlay of positive electrolyte pre cycling (dashed orange), and follow 8 (orange) and 20 (dark orange) cycles, b) CV overlay of negative electrolyte pre cycling (dashed blue), and follow 8 (blue) and 20 (navy) cycles. CVs were recorded at a glassy carbon WE (0.071 cm^2) with Pt wire CE and $Ag^+|Ag$ RE at $\boldsymbol{\nu}$ of 100 mV s^{-1}.

CV of the negative electrolyte indicates the rich electrochemistry of PW_{11}-SiPh is maintained following cycling in the RFB for >400 hours. The green arrows in figure 4.10b highlight the spliting of the third redox couple of PW_{11}-SiPh (termed process III/III' in chapter 3). The same changes were observed in the CV of PW_{11}-SiPh positive electrolyte post cycling in the symmetric RFB (chapter 3, figure 3.20b) and they indicate some instability of PW_{11}-SiPh. The one-electron redox couple of TEMPO to

$TEMPO^+$ (expected at 0.37 V) is not observed in the CV of the negative electrolyte. Given the irreversibility of TEMPO reduction, it is plausible that TEMPO which crossed over to the negative electrolyte is reduced to the aminoxy anion and decomposes to an electrochemically silent species.

UV-visible absorption spectroscopy was used to monitor the electrolytes over the course of cycling in the RFB. The spectra of TEMPO and PW_{11}-SiPh prior to galvanostatic cycling are shown in figure 4.11. TEMPO shows a dominant absorbance peak at 243 nm and a minor peak at 462 nm as indicated by the grey arrows. PW_{11}-SiPh shows a strong ligand-to-metal charge transfer (LMCT) band at 266 nm and a tail up to the solvent limit in the 200-230 nm region.

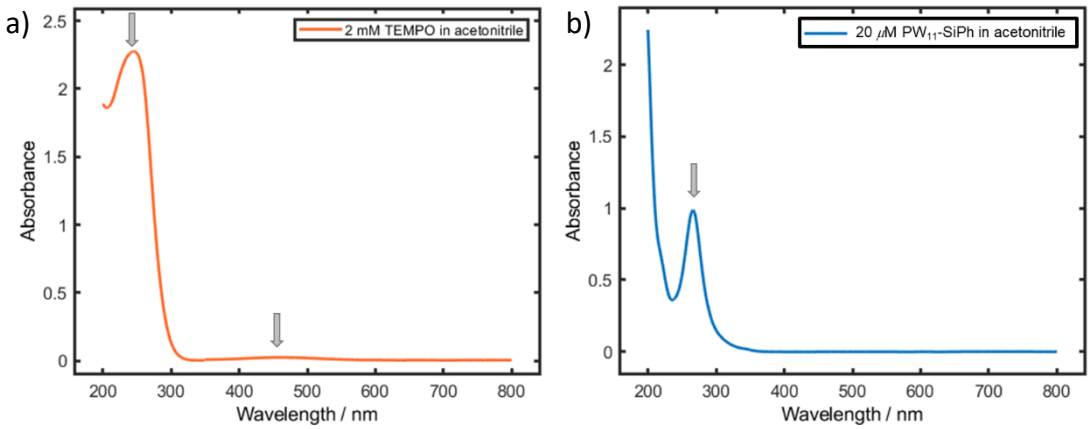

Figure 4.11. UV-visible absorption spectra of a) 2 mM TEMPO and b) 20 μM PW_{11}-SiPh. Spectra were recorded in acetonitrile prior to galvanostatic cycling in a RFB.

The positive electrolyte was sampled from the RFB before cycling and after 20 cycles and was diluted in acetonitrile by a factor of 100 for analysis by UV-visible absorption spectroscopy (figure 4.12). The spectrum for positive electrolyte post cycle 20 shows a shift in peak absorbance to 263 nm and increased absorbance in the 200-230 nm region. Given that the peak absorbance for $TEMPO^+$ occurs at 290 nm and 480 nm,[24] the presence of some charged positive electrolyte can be assumed. The increase in absorbance in the 200 to 230 nm region is thought to be due to the presence of PW_{11}-SiPh in the positive electrolyte.

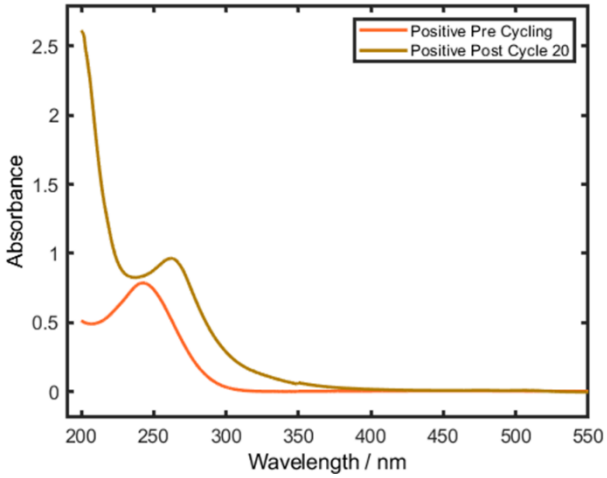

Figure 4.12. UV-visible absorption spectra of positive electrolyte pre cycling (orange) and following 20 cycles (yellow). Electrolyte was sampled in the discharged state. Electrolyte was diluted by a factor of 100.

It is evident from the CV and UV-visible absorption spectroscopy of spent electrolytes that crossover of TEMPO from the positive electrolyte to the opposite half-cell does occur and is likely the primary reason for capacity fade in the PW_{11}-SiPh RFB when the potential window is limited to 0 to 2.7 V.

4.4. Conclusions

We have investigated the application of POMs as negative electrolyte charge carriers in asymmetric nonaqueous RFBs for the first time. The organic-inorganic hybrid POM, PW_{11}-SiPh was selected as the charge carrier for the negative electrolyte due to its high saturation concentration in acetonitrile of 0.6 M and its rich electrochemistry at highly negative redox potentials. Paired with TEMPO as the charge carrier for the positive electrolyte, we have demonstrated high E_v and high V_{cell} RFBs.

The number of electrons transferred per molecules in the negative electrolyte can be controlled by adjusting the potential window of cycling. Limiting the potential window to allow for the reduction of PW_{11}-SiPh by two or three electrons per molecule, results in a theoretical E_v of 20.8 and 38.3 Wh L^{-1} respectively. In this instance, CE averages 95% and the shape of the charge and discharge curves remains stable over >400 hours. Capacity fade of 2.1 to 2.2% per cycle was observed and was attributed to crossover of charge carriers to the opposite half-cell. CV and UV-visible

absorption spectroscopy confirmed the presence of PW_{11}-SiPh in the positive electrolyte.

Table 4.2. Table outlining the theoretical $Q_{negative}$, V_{cell} and E_v of a PW_{11}-SiPh|TEMPO RFB with varying values of *n* for the negative electrolyte.

***n* (negative)**	**$Q_{negative}$ / mA h L^{-1}**	**V_{cell} / V**	**Theoretical E_v / Wh L^{-1}**
2	32.2	1.29	20.8
3	48.2	1.59	38.3
4	64.3	1.86	59.8

Extending the potential window of cycling to 0 to 3.5 V allowed for the reduction of PW_{11}-SiPh in the negative electrolyte by four electrons per molecules (*n*=4) upon charge. In this instance, the increased value of *n* and V_{cell} resulted in a theoretical E_v to 59.8 Wh L^{-1}. However, poor CE of 37% , inconsistency in the shape of the charge and discharge profiles, and the presence of decomposition product upon disassembly of the cell, indicated that PW_{11}-SiPh was unstable when reduced by four electrons in the RFB.

Future work should focus on the development of more selective and conductive membranes or separators for the PW_{11}-SiPh|TEMPO RFB. Polymers of intrinsic microporosity, those with pore size of <2 nm, show promising performance of nonaqueous RFBs.[25,26] PIMs allow for high ionic selectivity for even small organic molecules. This will minimise capacity fade due to membrane crossover and allow for operation of the RFB at higher current densities and at higher VE. Furthermore, the paring of PW_{11}-SiPh with a positive electrolyte charge carrier that is stable at negative redox potentials could minimise capacity fade further. TEMPO undergoes an irreversible reduction at a potential which PW_{11}-SiPh is redox active. In the event of membrane crossover of TEMPO to the negative half-cell, it is thought to degrade via an irreversible reduction process. Alternative redox-active species for consideration as charge carriers for the positive electrolyte include ferrocene and derivatives,[27,28] cyclopropenium and derivatives,[29,30] or dialkoxybenzenes.[31,32]

The advantage of using these hybrid materials as charge carriers in RFBs is their synthetic flexibility; the addenda atoms, heteroatoms, anchoring group, and organic moieties of these systems can all be readily tuned, offering numerous opportunities for optimisation of these novel charge carriers. Hybridisation can be applied to a broad range of POMs, which presents the opportunity to develop multi-electron charge carriers across a wide potential range. Future work could include the design of organic-inorganic hybrid POMs with highly positive redox potentials for use as charge carriers in the positive electrolyte. Paired with a PW_{11}-SiPh negative electrolyte, this strategy could achieve a nonaqueous asymmetric POM/POM RFB, where the number electrons transferred per molecule exceeds two.

4.5. References

1 H. D. Pratt, N. S. Hudak, X. Fang and T. M. Anderson, *J. Power Sources*, 2013, **236**, 259–264.

2 L. E. VanGelder and E. M. Matson, *J. Mater. Chem. A*, 2018, **6**, 13874–13882.

3 L. E. VanGelder, B. E. Petel, O. Nachtigall, G. Martinez, W. W. Brennessel and E. M. Matson, *ChemSusChem*, 2018, **11**, 4139–4149.

4 L. E. Vangelder, A. M. Kosswattaarachchi, P. L. Forrestel, T. R. Cook and E. M. Matson, *Chem. Sci.*, 2018, **9**, 1692–1699.

5 L. E. Vangelder, H. D. Pratt, T. M. Anderson and E. M. Matson, *Chem. Commun.*, 2019, **55**, 12247–12250.

6 Y. Cao, J. J. J. Chen and M. A. Barteau, *J. Energy Chem.*, 2020, **50**, 115–124.

7 J. Friedl, M. V Holland-Cunz, F. Cording, F. L. Pfanschilling, C. Wills, W. McFarlane, B. Schricker, R. Fleck, H. Wolfschmidt and U. Stimming, *Energy Environ. Sci.*, 2018, **11**, 3010–3018.

8 Z. F. Chen, Y. L. Yang, C. Zhang, S. Q. Liu and J. Yan, *J. Energy Storage*, 2021, **35**, 102281.

9 Y. Zhao, J. Zhang, G. Agarwal, Z. Yu, R. E. Corman, Y. Wang, L. A. Robertson, Z. Shi, H. A. Doan, R. H. Ewoldt, I. A. Shkrob, R. S. Assary, L. Cheng, V. Srinivasan, S. J. Babinec and L. Zhang*, J. Mater. Chem. A*, 2021, **9**, 16769–16775.

10 Y. Yonekuta, K. Oyaizu and H. Nishide, *Chem. Lett.*, 2007, **36**, 866–867.

11 X. Wei, W. Xu, M. Vijayakumar, L. Cosimbescu, T. Liu, V. Sprenkle and W. Wang, *Adv. Mater.*, 2014, **26**, 7649–7653.

12 Z. Li, S. Li, S. Liu, K. Huang, D. Fang, F. Wang and S. Peng, *Electrochem. Solid-State Lett.*, 2011, **14**, A171–A173.

13 B. Ok, W. Na, T. H. Kwon, Y. W. Kwon, S. Cho, S. M. Hong, A. S. Lee, J. H. Lee and C. M. Koo, *J. Ind. Eng. Chem.*, 2019, **80**, 545–550.

14 X. Yu, W. A. Yu and A. Manthiram, *ACS Appl. Mater. Interfaces*, 2020, **12**, 48654–48661.

15 H. Wang, S. Y. Sayed, E. J. Luber, B. C. Olsen, S. M. Shirurkar, S. Venkatakrishnan, U. M. Tefashe, A. K. Farquhar, E. S. Smotkin, R. L. McCreery and J. M. Buriak, *ACS Nano*, 2020, **14**, 2575–2584.

16 R. Crompton and C. Banks, Understanding Voltammetry, World Scietific Publishing Europe Ltd., New Jersey, 3rd edn., 2018.

17 A. M. Kosswattaarachchi and T. R. Cook, J. Electrochem. Soc., 2018, 165, A194–A200.

18 E. Sum and M. Skyllas-Kazacos, J. Power Sources, 1985, 15, 179–190.

19 J. Yuan, Z. Z. Pan, Y. Jin, Q. Qiu, C. Zhang, Y. Zhao and Y. Li, J. Power Sources, 2021, 500, 229983.

20 Y. Maruyama, K. Nagamine, A. Nomura, S. Iwasa and S. Tokito, Electrochemistry, 2020, 88, 34–38.

21 L. Wylie, T. Blesch, R. Freeman, K. Hatakeyama-Sato, K. Oyaizu, M. Yoshizawa-Fujita and E. I. Izgorodina, ACS Sustain. Chem. Eng., 2020, 8, 17988–17996.

22 M. Boujtita, J. Boixel, E. Blart, C. R. Mayer and F. Odobel, Polyhedron, 2008, 27, 688–692.

23 R. M. Darling, K. G. Gallagher, J. A. Kowalski, S. Ha and F. R. Brushett, Energy Environ. Sci., 2014, 7, 3459–3477.

24 T. P. P. Le and P. Opaprakasit, Appl. Spectrosc., 2021, 75, 325–335.

25 S. E. Doris, A. L. Ward, A. Baskin, P. D. Frischmann, N. Gavvalapalli, E. Chénard, C. S. Sevov, D. Prendergast, J. S. Moore and B. A. Helms, Angew. Chemie Int. Ed., 2017, 56, 1595–1599.

26 S. on Tung, S. L. Fisher, N. A. Kotov and L. T. Thompson, *Nat. Commun.*, 2018, **9**, 4193.

27 B. Hwang, M.-S. Park and K. Kim, *ChemSusChem*, 2015, **8**, 310–314.

28 H. S. Kim, T. Yoon, Y. Kim, S. Hwang, J. H. Ryu and S. M. Oh, *Electrochem. commun.*, 2016, **69**, 72–75.

29 Y. Yan, S. G. Robinson, M. S. Sigman and M. S. Sanford, *J. Am. Chem. Soc.*, 2019, **141**, 15301–15306.

30 K. H. Hendriks, S. G. Robinson, M. N. Braten, C. S. Sevov, B. A. Helms, M. S. Sigman, S. D. Minteer and M. S. Sanford, *ACS Cent. Sci.*, 2018, **4**, 189–196.

31 J. Huang, L. Cheng, R. S. Assary, P. Wang, Z. Xue, A. K. Burrell, L. A. Curtiss and L. Zhang, *Adv. Energy Mater.*, 2015, **5**, 1401782.

32 X. Wei, W. Xu, J. Huang, L. Zhang, E. Walter, C. Lawrence, M. Vijayakumar, W. A. Henderson, T. Liu, L. Cosimbescu, B. Li, V. Sprenkle and W. Wang, *Angew. Chemie Int. Ed.*, 2015, **54**, 8684–8687.

Chapter 5: Fullerene-Ferrocene Charge Carriers for Symmetric Nonaqueous Redox Flow Batteries

5.1. Introduction

An effective strategy to minimise the detrimental effects of membrane crossover is to design symmetric systems in which a single charge carrier is used in both the positive and negative electrolyte.[1] Symmetric RFBs require a single charge carrier with reversible redox processes at both high and low potentials. The advantage of symmetric RFBs is that capacity loss due to membrane crossover can be regenerated.

There are two primary strategies for designing charge carriers for symmetric RFBs. First, the use of redox-active molecules with multiple oxidation states. For example, the four stable oxidation states of vanadium allow for its application in the VRFB.[2] In addition, the multiple oxidation states of polyoxometalates also allow for their application as charge carriers in symmetric RFBs, as demonstrated in chapter 3.[3] While this is an effective strategy to minimise capacity loss due to membrane crossover, the properties of the charge carriers for the positive and negative electrolyte cannot be tuned independently of each other. This often results in symmetric RFBs having reduced V_{cell} compared to asymmetric systems.

A second strategy in the design of charge carriers for symmetric RFBs is to combine two redox-active groups into one bifunctional molecule. This allows for the selection of two redox-active groups which are targeted for the positive and negative electrolyte, and for their integration into a single molecule, thereby maximising V_{cell} while also achieving the advantages of symmetric systems. Importantly, the performance of the resulting bifunctional charge carrier should exceed the performance of an electrolyte consisting of a mixture of the two independent charge carriers. Given that the molecular masses of the two systems would be comparable, it is important to realise a benefit to the additional synthetic effort required for the bifunctional charge charrier (such as a solubility or stability enhancement).

Schubert and co-workers demonstrated a symmetric aqueous RFB with a bifunctional charge carrier consisting of TEMPO and phenazine moieties covalently grafted within

a single molecule.[4] Upon charge, a TEMPO-centred oxidation occurs in the positive electrolyte while a phenazine-centred reduction happens in the negative electrolyte. As shown in figure 5.1, the bifunctional charge carrier contains two TEMPO groups (red) per phenazine (blue) in order to balance its two-electron redox chemistry. Both redox groups were covalently bonded via a water-soluble triethylene glycol linker (black), yielding a single charge carrier with V_{cell} of 1.2 V and enhanced solubility in the aqueous electrolyte.

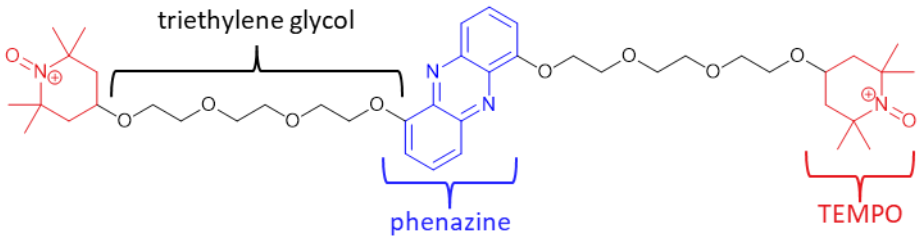

Figure 5.1. Structure of TEMPO-phenazine bifunctional charge carrier. The TEMPO moiety (red) is targeted in the positive half-cell and the phenazine group (blue) is targeted in the negative half-cell.

A second example of bifunctional charge carriers comes from the work of Chamberlain, Stimming and colleagues, in which Fc groups were covalently grafted to a C_{60} fullerene cage.[5] Figure 5.2 shows the structure of the fullerene-ferrocene charge carriers, termed C_{60}Fc, including the pyrrolidine moiety which links the redox-active groups. The Fc groups (red) served as the redox centre for the positive electrolyte, while the multi-electron redox processes of fullerene (blue) were utilised in the negative electrolyte. To balance the redox processes of fullerene, multiple Fc moieties (between 1 - 4 equivalents) were grafted to C_{60}. The redox process of the positive and negative electrolyte were separated by approximately 1.3 V and 1.8 V for the first and second reduction of C_{60} respectively. The functionalisation significantly enhanced the solubility of fullerene in ortho-dichlorobenzene (oDCB) from 0.037 M to 0.12 M for the tetra-adduct of C_{60}Fc.[6]

The performance of C_{60}Fc charge carriers were investigated by galvanostatic cycling in coin cells. Coin cells were assembled with carbon felt electrodes soaked in electrolyte (1 mM C_{60}Fc in 0.1 M tetrabutylammonium tetrafluoroborate ([TBA][BF_4]) in oDCB) sandwiched between glass fibre separators. Charge carriers were assessed

in symmetric and asymmetric configurations where indene-C_{60} bis-adduct was used as the charge carrier in the negative electrolyte.

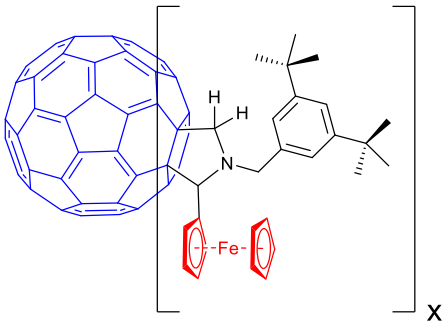

Figure 5.2. Structure of C_{60}Fc charge carrier, where x=1-4.

The coin cells were successfully cycled for 100 charge-discharge cycles but experienced considerable capacity fade which was attributed to three causes; (1) the low volume of electrolyte (~1 mL) in the coin cell assemblies meant that a significant proportion of capacity fade was attributed to electrolyte soaking into the absorbent glass fibre separator, (2) significant membrane crossover, which was alleviated by using the symmetric system rather than an analogous asymmetric system with indene-C_{60} bis-adduct negative electrolyte, (3) degradation of C_{60}Fc charge carriers, which was not explored in detail. In addition, the high ohmic resistance of the coin cells led to poor VE, even at low current densities of 0.1 mA cm^{-2}.

Given the average V_{cell} of 1.64 V and saturation concentration of C_{60}Fc charge carriers (reported at 0.12 M for the tetra-adduct), a theoretical E_v of 5.3 Wh L^{-1} was calculated. While the increase in saturation concentration upon functionalisation is impressive, the theoretical E_v of 5.3 Wh L^{-1} is significantly below that of commercial RFBs where the practical E_v for the VRFB is 25-35 Wh L^{-1}.[2] However, considering the rich electrochemistry and plentiful opportunities available through the functionalisation of fullerene, there is a large scope for development of new fullerene-based charge carriers.

C_{60} fullerene has a π-conjugated system composed of 60 sp_2-carbon atoms arranged into a spherical cage structure similar to a football. It was first discovered in 1985 and termed the buckminsterfullerene.[7] The unique structure enables C_{60} to be reversibly

reduced by up to 6 electrons[8] and for its surface to be functionalised in diverse ways thereby tuning redox properties, solubility and/or functionality. The rich and versatile chemistry of fullerene lead to the 1996 Nobel Prize in Chemistry being awarded to its discoverers, Curl, Kroto and Smalley.[9–11]

Fullerene and its derivatives have been applied in diverse fields including biomedicine,[12] photovoltaics,[13] catalysis[14] and more recently electrochemical energy storage.[15] It has been investigated as negative electrode material in several EES devices including LIBs, sodium-ion and magnesium-ion batteries.[15] Herein, we expand on the investigation of Chamberlain and colleagues who were the first to explore the application or fullerene and its derivatives as charge carrier in RFBs.

We sought to enhance the saturation concentration of C_{60}Fc bis-adducts in oDCB to increase the theoretical E_v beyond 5.3 Wh L^{-1}. A series of C_{60}Fc bis-adducts were prepared, with varying organic functionality surrounding the pyrrolidine ring in an aim to enhance solubility in oDCB. The three charge carriers were termed C_{60}Fc1, C_{60}Fc2 and C_{60}Fc3, and their structures are defined in figure 5.4, figure 5.5 and figure 5.6 respectively. In each case, only the bis-adduct (two Fc groups per C_{60}) of the charge carrier was investigated. The charge carriers were tested in laboratory-scale flow cell assemblies to overcome the limitations of the coin cells i.e. high ohmic resistance and low electrolyte volume. We also aimed to better understand the instability of the C_{60}Fc charge carriers which were alluded to in the literature.[5]

5.2. Experimental

5.2.1 General experimental methods

C_{60} fullerene (>99.0%, TCI), ferrocene carboxaldehyde (Fluorochem) and glycine methyl ester (ACROS) were used as received. All other reagents were purchased from Aldrich and used without further purification. NMR spectra were obtained from Bruker AV3HD NMR spectrometer (9.4 T). MALDI ToF MS was recorded on an AXIMA Performance spectrometer.

Electrochemical investigations were carried out in an N_2-filled glove box (MBraun; <0.1 ppm H_2O; <0.1 ppm O_2) at room temperature, using a Bio-Logic SP-300 potentiostat/galvanostat with EC-Lab software. Glassware and equipment were dried in a vacuum oven at 60 °C for 16 hours prior to use. [TBA][BF_4], (≥ 99.0%) was dried at 100 °C under vacuum for a minimum of 1 day before being transferred to the glove box. Anhydrous oDCB solvent was degassed by purging with N_2 before use.

5.2.2 Synthesis of C_{60}Fc charge carriers

The methodology for the synthesis of C_{60}Fc1, C_{60}Fc2, and C_{60}Fc3 is provided. Step 1 was the synthesis of 2,2-dimethyl glycine methyl ester hydrochloride, a precursor for the synthesis of C_{60}Fc3. The synthesis of 2,2-dimethyl glycine methyl ester hydrochloride was carried out according to literature precedent.[16] Glycine methyl ester, the precursor for the synthesis of C_{60}Fc1 or C_{60}Fc2, was available commercially. Step 2 was the synthesis of 4-hexylbenzaldehyde, a precursor for the synthesis of C_{60}Fc2 and C_{60}Fc3. 4-hexylbenzaldehyde was synthesised according to a literature procedure[17] while 3,5-di-tert-butylbenzaldehyde (precursor for C_{60}Fc1) was purchased.

Steps 3-5 were necessary for the synthesis for all three charge carriers and have been generalised to account for their differing substituents. Step 3 was the synthesis of N-substituted glycine methyl esters and followed the methodology outlined in the literature.[18] Glycine methyl ester hydrochloride (2.96 mmol, 1 *equiv.*) and benzaldehyde (2.29 mmol, 0.77 *equiv.*) were dissolved in dichloromethane (DCM) (15 mL) and triethylamine (0.41 mL, 2.97 mmol, 1 *equiv.*) and degassed with N_2. The solution was stirred at room temperature for 17 hours in the presence of 4 Å

molecular sieves. The reaction mixture was filtered and $Na[B(OAc)_3H]$ (0.63 g, 2.97 mmol, 1 *equiv.*) and glacial acetic acid (2 mL) were added to the filtrate. The solution was stirred at room temperature for a further 17 hours under N_2. The solvent was removed *in vacuo* and methanol (5 mL) was added to the residue. The reaction mixture was cooled to 0 °C and $NaHCO_3$ (1 M) was used to adjust the pH to 7. The resulting mixture was extracted in DCM (4 x 15 mL), the organic layers were combined, washed with water (10 mL), and dried over $MgSO_4$. After removal of $MgSO_4$, further purification was carried out by column chromatography to yield a colourless oil as the product.

The N-substituted glycine methyl esters were then hydrolysed to amino acids using the following methodology (step 4). Firstly, N-substituted glycine methyl esters (1.68 mmol, 1 *equiv.*) was dissolved in methanol (10 mL). NaOH (3.75 mmol, 2.23 *equiv.*) was added and the resulting mixture was stirred at room temperature for 72 hours. Solvent was removed *in vacuo* and water (2 mL) was added to the residue. The pH was adjusted to 6.7 by addition of 1 M HCl. The resulting white precipitate was washed with water by centrifugation (40 mL x 3) and with chloroform (5 mL) to yield a white solid as product.

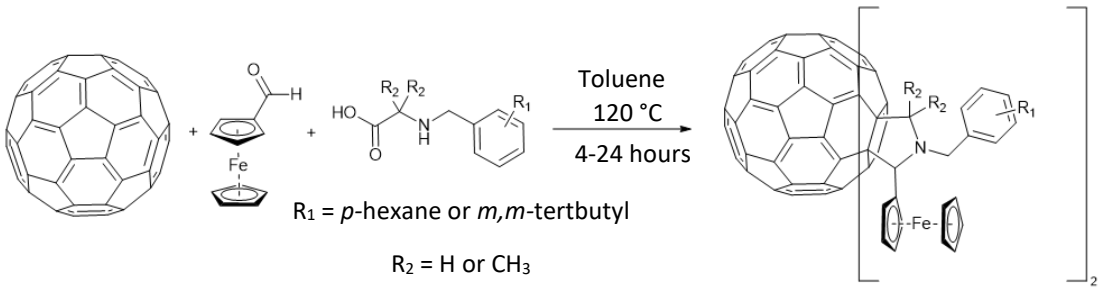

Figure 5.3. General schematic of $C_{60}Fc$ synthesis from C_{60}, ferrocene carboxaldehyde and amino acid (step 5).

Step 5 was the synthesis of $C_{60}Fc$ charge carriers based on the literature methodology and outlined in figure 5.3.[5] Each $C_{60}Fc$ charge carrier was synthesised following the same methodology with the exception of the substituents of the amino acid. C_{60} fullerene (150 mg, 0.21 mmol, 1 *equiv.*), ferrocene carboxaldehyde (64 mg, 0.252 mmol, 1.2 *equiv.*) and amino acid (0.42 mmol, 2 *equiv.*) were dissolved in anhydrous toluene (50 mL), sonicated for 15 minutes and thoroughly degassed with dry N_2. The

solution was refluxed at 120 °C for 4 hours (synthesis of C_{60}Fc3 required 24 hour reflux). Solvent was removed *in vacuo* and purified by column chromatography (silica gel, eluted with CS_2 to remove C_{60} starting material, then CS_2:toluene v:v 98:2 to isolate the product). The product was further purified by washing with excess methanol (50 mL) to yield a black solid.

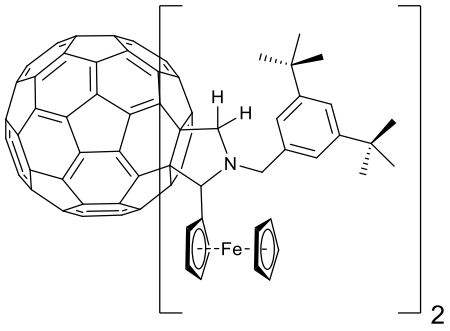

Figure 5.4. Structure of C_{60}Fc1. R_1 = *m,m*-tertbutyl and R_2 = H.

Yield (75 mg, 0.048 mM, 21%). ^{1}H NMR (400 MHz, $CDCl_3$, δ, ppm): 7.31-7.90 (m, 3H, ArH), 3.41-6.32 (m, 14H, Fc-H, CH_2 and pyrrolidine-H), 1.29-1.52 (m, 18H, (CH_3)C). MALDI ToF MS (DCTB/MeCN, m/z): 1577.84 $[M]^-$ (calculated mass: 1578.42).

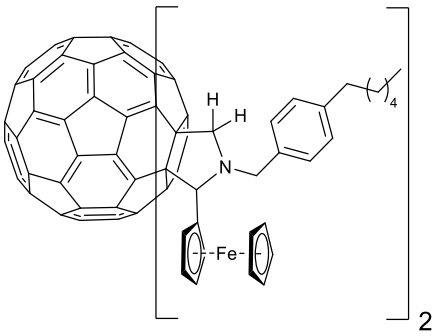

Figure 5.5. Structure of C_{60}Fc2. R_1 = *p*-hexane and R_2 = H.

Yield (80 mg, 0.053 mM, 23.6%). ^{1}H NMR (400 MHz, $CDCl_3$, δ, ppm): 7.22-7.88 (m, 4H, ArH), 3.32-6.34 (m, 14H, Fc-H, CH_2 and pyrrolidine-H), 0.85-2.87 (m, 13H, hexyl chain). MALDI ToF MS (DCTB/MeCN, m/z): 1522.29 $[M]^-$ (calculated mass: 1522.36).

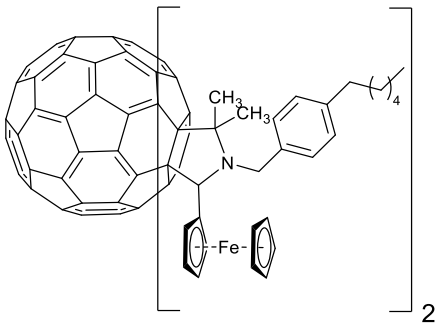

Figure 5.6. Structure of $C_{60}Fc3$. R_1 = *p*-hexane and R_2 = CH_3.

Yield (31 mg, 0.02 mM, 9.3%). ^{1}H NMR (400 MHz, $CDCl_3$, δ, ppm): 7.09-8.03 (m, 4H, ArH), 3.78-6.60 (m, 12H, Fc-H, CH_2 and pyrrolidine-H), 0.88-2.87 (m, 19H, hexyl and methyl chains). MALDI ToF MS (DCTB/MeCN, m/z): 1578.14 $[M]^-$ (calculated mass: 1578.42).

5.2.3 Cyclic voltammetry

CV was carried out using a three-electrode cell, containing a glassy carbon WE (0.071 cm^2 surface area) and Pt wire CE (>0.16 cm^2 surface area) and Ag wire QRE with Fc internal standard. The glassy carbon WE and Ag wire QRE were polished using aqueous alumina slurries of decreasing particle size (1 µm, 0.3 µm and 0.05 µm), and rinsed thoroughly with deionised water. The Pt wire CE was cleaned in a butane flame prior to use. CV was iR compensated at 85% using the ZIR tool included within the EC-Lab software.

5.2.4 Electrochemical impedance spectroscopy

EIS measurements were conducted over the frequency range of 100 kHz to 100 mHz at AC amplitude of 10 mV.

5.2.5 Redox flow battery

RFB charge-discharge cycling was carried out in a N_2-filled glove box with 5 cm^2 membrane surface area assembly (Scribner, Southern Pines, USA). Graphite felt electrodes (0.6 cm thickness, SGL carbon, Wiesbaden, Germany) were sandwiched between interdigitated graphite flow fields with PTFE flow frames and gaskets. Two sheets of polypropylene porous separator (Celgard) were used to separate the two half-cells. 0.5 M [TBA][BF_4] in oDCB was pumped through the RFB prior to charge-discharge cycling in order to wet the electrodes and membrane. An electrolyte

solution of 1 mM $C_{60}Fc$ in 0.5 M [TBA][BF_4] in oDCB was prepared and 10 mL of electrolyte was placed in each reservoir. A dual channel peristaltic pump (Masterflex L/S, Vernon Hills, USA) was used to pump electrolytes through the cell at a flow rate of 20 mL min^{-1} using Viton tubing (Masterflex, Vernon Hills, USA). Galvanostatic cycling was conducted at a current density of 0.1 mA cm^{-2} (±0.5 mA) unless stated otherwise. This equates to an approximate C-rate of 1C.

5.2.6 Electrolyte extraction

After galvanostatic cycling, electrolytes were removed from the battery and charge carrier was extracted using the following method. oDCB solvent was removed by rotary evaporation and methanol was added to the residue. The suspension was sonicated with 15 minutes before filtering through a PTFE membrane filter (pore size 0.4 µm). The resulting solid was dried and analysed by TLC, MALDI-ToF MS and ^1H NMR.

5.3. Results and Discussion

The synthesis of $C_{60}Fc$ charge carriers, determination of their saturation concentration in oDCB, and post cycling analysis of electrolyte extracts by TLC, MALDI ToF MS and ^{1}H NMR was carried out by Xiangyi Chen from the School of Chemistry, University of Leeds, UK.

5.3.1 Solubility of charge carriers

Table 5.1. Notation, structure and saturation concentration of $C_{60}Fc1$ - 3 in oDCB. *Average of two experiments. The error determined as $(S_{max} – S_{min})/2$.

Charge carrier notation	Charge carrier structure	Saturation concentration in oDCB* / M
$C_{60}Fc1$	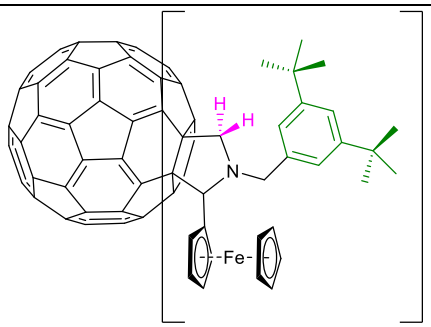	0.252 ± 0.007
$C_{60}Fc2$	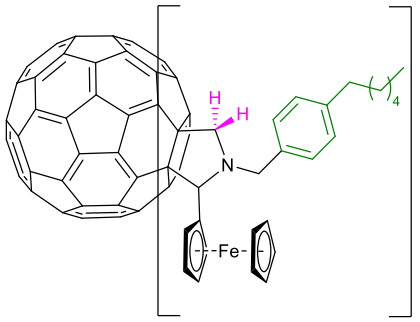	0.293 ± 0.002
$C_{60}Fc3$	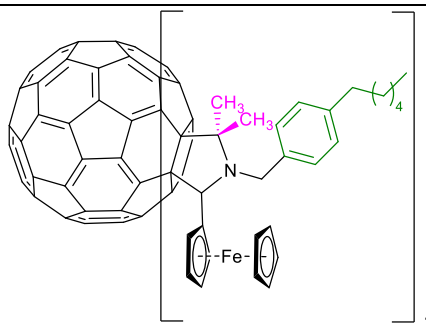	0.336 ± 0.011

Table 5.1 shows the three $C_{60}Fc$ charge carriers investigated in this study, their notation and saturation concentration in oDCB. Each bis-adduct has 8 possible isomers due to the numerous positions on the fullerene available for functionalisation.[19] The organic functionality surrounding the pyrrolidine (highlighted in green and pink) was varied for $C_{60}Fc1$ - 3.

Non-functionalised fullerene (C_{60}) is nonpolar and unable to partake in hydrogen bonding. Consequently, it is insoluble in polar solvents such as water, acetonitrile and methanol and is poorly soluble in many organic solvents.[20] Upon dissolution there is poor solvent-solute interactions meaning it is energetically unfavourable to break and rearrange the bonds between solvent molecules. Solubility is higher in aromatic solvents compared to aliphatic solvents due to the π-π interaction between solvent and solute. C_{60} has a saturation concentration of 0.037 M (27 g L^{-1}) in oDCB, one of the highest values of all solvents and is the justification for the choice of solvent in this study.[6]

The saturation concentration of $C_{60}Fc$ in oDCB was determined by preparing a saturated solution of charge carrier in oDCB and diluting to a concentration detectable by UV−visible absorption spectroscopy. The peak absorbance at 446 nm and 560 nm was compared to a pre-prepared calibration and back calculated to determine the saturation concentration of each $C_{60}Fc$.

The solubility of all $C_{60}Fc$ charge carriers in oDCB was increased by an order of magnitude compared to that of non-functionalised C_{60}. The functionalisation introduces a charged metal centre (Fe^{2+} within Fc) and slight dipole across the C-N bond of pyrrolidine. This heightened polarity enabled increased solvent-solute interaction and consequently enhanced solubility. In addition, the functionalisation introduced steric hinderance which was thought to prevent the agglomeration of C_{60} into clusters; a phenomenon known to occur in several solvents with low C_{60} solubility.[21]

The saturation concentration of the tris- and tetra-adduct analogues of $C_{60}Fc1$ were reported in the literature to be 0.107 M and 0.120 M respectively.[5] Here, the saturation concentration of the bis-adduct of $C_{60}Fc1$ was shown to be over double

that of the tris- and tetra-adducts at 0.252 M, which breaks the expected trend of increasing solubility with increasing number of Fc adducts. It is plausible that the tri- and tetra-adducts induce solute-solute interaction, causing agglomeration and reduced solubility of the charge carriers.

Substitution of the two meta substituted tert-butyl groups on the aromatic ring (C_{60}Fc1) for a single para substituted hexyl chain (C_{60}Fc2) increased the solubility from 0.252 to 0.293 M. The increased steric hinderance of the hydrocarbon chain is thought to further reduce the ability of C_{60}Fc to cluster together and therefore increase solubility. We also observed an increase in solubility from 0.293 M to 0.336 M when substituting the protons (C_{60}Fc2) in the α position of the pyrrolidine for methyl groups (C_{60}Fc3). The substantial increase in solubility from this minor change in structure is surprising.

5.3.2 Electrochemical analysis of C_{60}Fc charge carriers

5.3.2.a Electrochemical analysis of C_{60}Fc1

Figure 5.7 shows the CV of C_{60}Fc1 dissolved in oDCB with 0.5 M [TBA][BF_4] supporting electrolyte at a polished glassy carbon WE at v of 100 mV s^{-1}. The anodic peak (labelled I) is attributed to the oxidation of Fe^{2+} to Fe^{3+} in the Fc moieties of C_{60}Fc1. The corresponding cathodic peak (labelled I′) is attributed to the reduction of Fe^{3+} back to Fe^{2+}. Three cathodic and corresponding anodic peaks (labelled II/II′ to IV/IV′ from positive to negative potentials) are observed between −1 and −2.5 V and are attributed to the reversible reduction of C_{60}Fc1 centred at the fullerene.

The redox couples accessed during the voltametric experiment can be summarised as follows. The region of the charge carrier where the redox reaction is centred is highlighted in bold.

I/I': $C_{60}\mathbf{Fc}1 \rightleftharpoons C_{60}\mathbf{Fc}1^{2+} + 2e^-$ (5.1)

II/II': $\mathbf{C_{60}}Fc1 + e^- \rightleftharpoons \mathbf{C_{60}}Fc1^-$ (5.2)

III/III': $\mathbf{C_{60}}Fc1^- + e^- \rightleftharpoons \mathbf{C_{60}}Fc1^{2-}$ (5.3)

IV/IV': $\mathbf{C_{60}}Fc1^{2-} + e^- \rightleftharpoons \mathbf{C_{60}}Fc1^{3-}$ (5.4)

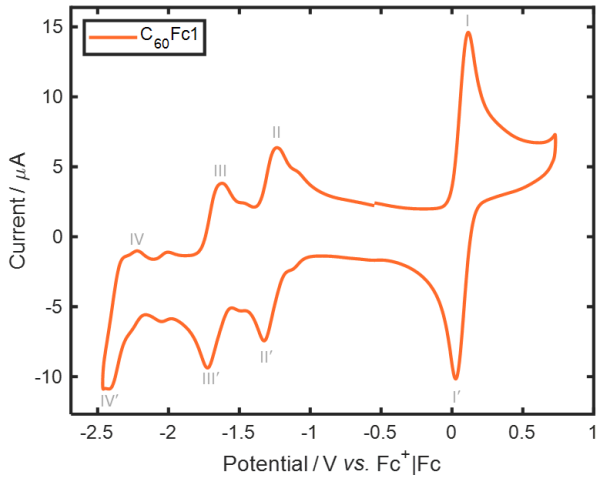

Figure 5.7. CV of 1 mM C_{60}Fc1 in 0.5 M [TBA][BF_4] in oDCB at a glassy carbon WE (0.071 cm^2) with Pt wire CE and referenced to $Fc^+|Fc$ at ν of 100 mV s^{-1} and iR compensation applied. Roman numerals denote the redox processes defined in Eq. 5.1 to 5.4.

Minor reduction and oxidation peaks in the region of –1.0 to –2.5 V are observed in addition to the primary peaks of processes II/II′ - IV/IV′. These 'shoulder' peaks are attributed to impurity of the C_{60}Fc1 analyte; most likely the mono-adduct analogue of C_{60}Fc1, as it is known to have equivalent C_{60}-centred redox couples at more positive potentials than the C_{60}Fc1 bis-adduct.[5]

From the molecular structure of C_{60}Fc1 it is anticipated that the fullerene-centred processes are one-electron redox couples, while the Fc-centred process is a two-electron reaction due to the two Fc moieties which are simultaneously oxidised/reduced. Differential pulse voltammetry (DPV) minimises capacitive current, allowing for a more accurate analysis of the faradaic process occurring. Figure 5.8 shows DPV of C_{60}Fc1 scanning positive of –0.8 V and scanning negative of –0.8 V. The Fc-centred oxidation and C_{60}-centred reduction peaks were integrated to estimate the charge passed. As anticipated, the charge of the Fc oxidation (9.9 μC) is approximately double that of each C_{60} reduction peaks (4.9 and 5.1 μC for II′ and III′ respectively). This confirmed that the bis-adduct is the dominant product in the sample.

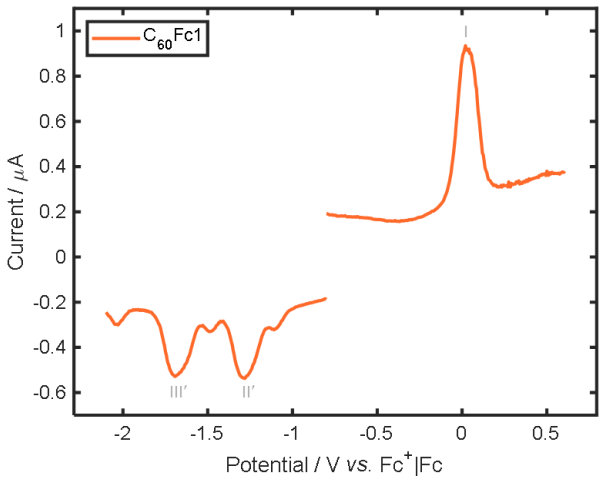

Figure 5.8. DPV of 1 mM C_{60}Fc1 in 0.5 M [TBA][BF_4] in oDCB at a glassy carbon WE (0.071 cm^2) with Pt wire CE and referenced to Fc^+|Fc and iR compensation applied. Roman numerals denote the redox processes defined in Eq. 5.1 to 5.4.

The third fullerene-centred reduction (labelled IV/IV') is only partially accessed as it occurs at the boundary of the electrolyte window of electrochemical stability. Chamberlain and co-workers investigated the voltammetry of C_{60}Fc1 in a lower concentration of supporting electrolyte (0.1 M [TBA][BF_4] in oDCB) and did not report the third one-electron fullerene-centred reduction.[22] Solution resistance is reduced by increasing the concentration of supporting electrolyte from 0.1 M to 0.5 M. The reduced ohmic resistance of the electrolyte used in this study allows for the observation of process IV/IV' within the electrolyte window of electrochemical stability. Process IV/IV' is not targeted in the flow battery charge-discharge reactions and is therefore not analysed further. To fully access process IV/IV', it would be necessary to analyse C_{60}Fc1 in a solvent with enhanced electrochemical stability at reducing potentials.

The mid-point potential, E_{mid}, and peak-to-peak separation, ΔE_p, of each redox couple are provided in table 5.2. The E_{mid} of the Fc-centred redox couple of C_{60}Fc1 is shifted positively by 60 mV compared to that of free Fc. A comparable shift in redox potential was observed in similar C_{60}Fc molecules studied by Wu and co-works,[23] and is attributed to the proximity of Fc to the highly electron-withdrawing C_{60} cage. Molecular tuning of this kind has been demonstrated previously for Fc-based charge carriers for RFBs. The addition of bromine[24] and acetyl[25] groups to the

cyclopentadienyl rings of Fc has been shown to positively shift the redox potential of the molecule and thereby enhance the V_{cell} of the RFB when applied as positive electrolyte. A >300 mV negative shift in redox potential is observed for the fullerene-centred reduction of C_{60}Fc1 compared to pristine fullerene(−0.98 to −0.95 V *vs.* $Fc^+|Fc$)[8,23] and is again attributed to the electronic properties of the nearby groups, in this case the electron-donating nature of the adduct. The increased difference in redox potential between the fullerene and Fc redox process of C_{60}Fc1 is beneficial for its application in a symmetric RFB as it enhances the V_{cell} of the resulting system. This demonstrates a secondary advantage of the bifunctional molecule over the individual charge carriers.

Table 5.2. E_{mid} and ΔE_p determined from the CV of C_{60}Fc1 recorded at ν of 100 mV s^{-1} with iR compensation applied. All potentials are reported versus that of an $Fc^+|Fc$ internal reference. $E_{mid} = (E_c + E_a)/2$, where E_c = cathodic peak potential and E_a = anodic peak potential.

C_{60}Fc1 Redox process	**E_{mid} / V *vs.* $Fc^+|Fc$**	**ΔE_p / mV**
Fc-centred (I/I')	0.06	108
C_{60}-centred (II/II')	−1.30	104
C_{60}-centred (III/III')	−1.69	111

Fast mass transport and electron transfer of charge carriers is key to enabling high power density RFBs. ΔE_p for each redox couple was greater than the value of 59 / 29 mV expected for the electrochemically reversible transfer of one / two electrons. Moreover, ΔE_p increased as ν increased. The ratio of cathodic to anodic peak currents, $i_{p,c}/i_{p,a}$ for the Fc-centred redox couple was 0.93. The equivalent values for C_{60}-centred redox couples are not provided due to the difficulty in attaining an accurate baseline in this region. These results indicate that each redox process was electrochemically quasi-reversible.

The diffusion coefficient, D, and heterogeneous electron transfer rate constant, k^0, of C_{60}Fc1 was determined by investigating the effect of ν on the voltametric response. As seen in figure 5.9, at ν > 200 mV s^{-1}, the plot of $i_{p,a}$ *vs.* $\nu^{1/2}$ for the oxidation of C_{60}Fc1 (process I) deviated from linearity, therefore the gradient in the region 10 mV

$s^{-1} < v < 200$ mV s^{-1} was used in conjunction with Eq. 3.5 from chapter 3 to estimate *D*. Our analysis reveals *D* of C_{60}Fc1 = 4.9×10^{-7} cm^2 s^{-1}. This value is an order of magnitude smaller than those reported in the literature for non-functionalised C_{60} (3.9×10^{-6} cm^2 s^{-1} in 0.1 M [TBA][BF_4] in oDCB[26] and 1.15×10^{-6} cm^2 s^{-1} in 0.5 M [TBA][Br] in oDCB).[27] The reduced value of *D* for C_{60}Fc1 could be as a result of the bulky ferrocene substituents hindering diffusion through the solvent.

The Nicholson method was used to estimate k^0 for the Fc-centred oxidation and C_{60}-centred reductions of C_{60}Fc1.[28] ΔE_p of each process was determined at various v . The

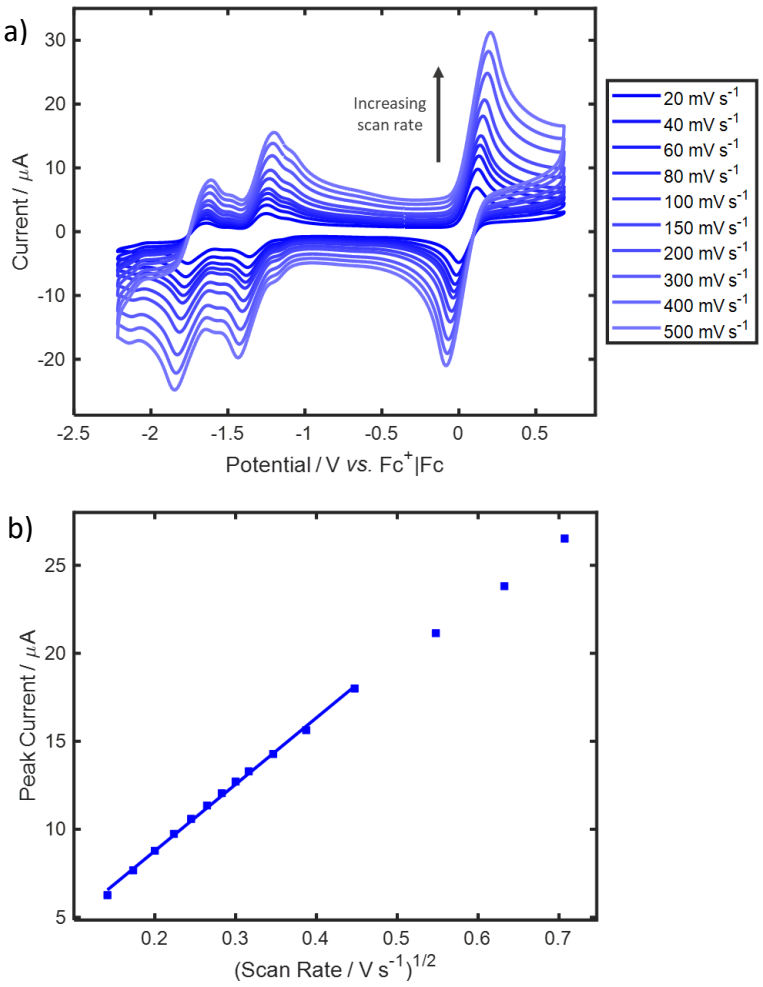

Figure 5.9. a) CV of 1 mM C_{60}Fc1 in 0.5 M [TBA][BF_4] in oDCB at a glassy carbon WE (0.071 cm^2) with Pt wire CE, referenced to $Fc^+|Fc$ at v of 20 to 500 mV s^{-1} and iR compensation applied. b) Peak current *vs.* $v^{1/2}$ for the oxidation of C_{60}Fc1 (process I). Data was attained from the second voltammetry sweep over the range of 10 to 500 mV s^{-1}.

corresponding dimensionless transfer parameter, Ψ, was obtained using Eq. 3.6 from chapter 3.[29] Eq. 3.7 was then used to calculate k^0 using the gradient of the slope from the plot of Ψ versus $[\pi \mathrm{DnF/RT}]^{-1/2} v^{-1/2}$. k^0 for the first and second C_{60}-centred reduction was calculated to be 7.52 x 10^{-4} cm s^{-1} and 4.48 x 10^{-4} cm s^{-1} respectively. This value is several orders of magnitude smaller than k^0 for the reduction of non-functionalised C_{60} which was determined by Bard and colleagues, by means of scanning electrochemical microscopy, to be 0.46 cm s^{-1}.[26] k^0 for the Fc-centred oxidation of C_{60}Fc1 to $C_{60}Fc1^{2+}$ was calculated to be 4.56 x 10^{-4} cm s^{-1}. The high solution resistance of the electrolyte is thought to prevent accurate calculation of k^0 by means of the Nicholson method. Future work should include analysis of k^0 by alternative means such as rotating disc electrode measurements. Chamberlain calculated k^0 of 0.34 cm s^{-1} for the Fc-centred oxidation of the mono-adduct analogue of C_{60}Fc1, using sampled current voltammetry.[5] However, similar C_{60}Fc molecules reported in the literature demonstrated ΔE_p for the Fc process of 180 to 200 mV at ν of 100 mV s^{-1}, which is in line with our assignment of redox couple as quasi-reversible.[23]

Successive CV cycling of the C_{60}Fc1 electrolyte across the potential window accessed in the flow battery, allows for an initial assessment of cycling stability. Over the course of 1000 CV cycles in the potential window of 0.7 V to −2.2 V, minimal change is observed in the current response of the C_{60}-centred redox couples (figure 5.10a). Conversely, changes to the Fc-centred couple are observed after 200 cycles. Both the anodic and cathodic peak currents reduce and ΔE_p increases with cycling, indicating that the redox couple becomes less electrochemically reversible with cycling and ultimately lost altogether.

Following 1000 cycles in C_{60}Fc1 electrolyte, the glassy carbon WE was removed and rinsed with 0.5 M [TBA][BF_4] in oDCB (termed blank electrolyte). CV of the cycled glassy carbon WE in blank electrolyte shows an enhanced capacitive current and oxidation peak at 0.63 V (figure 5.10b - brown trace) compared to the CV of a polished glassy carbon WE in the same electrolyte (figure 5.10b - grey dashes). CV analysis of a polished glassy carbon WE in the same blank electrolyte confirms that the

electrolyte was not contaminated with C_{60}Fc1 and that the current response observed was due to fouling of the electrode surface during cycling.

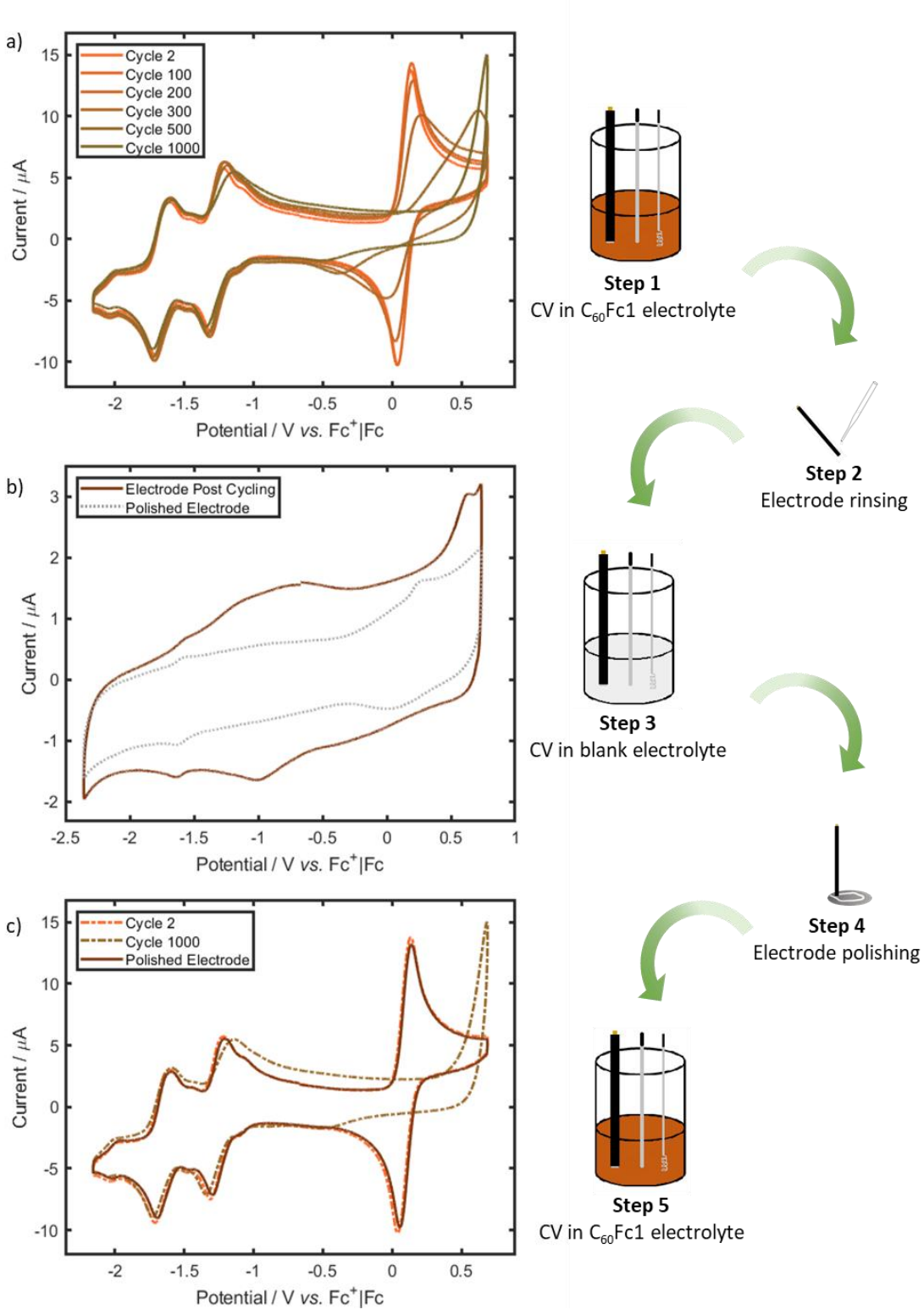

Figure 5.10. a) CV cycling of C_{60}Fc1 electrolyte at a glassy carbon WE (0.071 cm^2) with Pt wire CE and referenced to $Fc^+|Fc$ at ν of 100 mV s^{-1} and iR compensation applied (step 1). a) Cycle 2, 100, 200, 300, 500 and 1000 are overlaid b) CV of blank electrolyte at the cycled and polished glassy carbon WE (step 3). c) CV of C_{60}Fc1 electrolyte from step 1 at a polished glassy carbon WE (step 5).

Note that the redox couples observed in the CV of blank electrolyte at a polished glassy carbon WE (grey dotted line in figure 5.10b) at approximately 0.4 V and −1.6 V are attributed to a known contaminants of the supporting electrolyte and solvent respectively.

The glassy carbon WE was removed from the electrolyte, cleaned and polished with 1 µm, 0.3 µm and 0.05 µm alumina slurry. Once rinsed and dried the electrode was returned to the same C_{60}Fc1 electrolyte used in the CV cycling experiment. CV of the C_{60}Fc1 electrolyte with the polished electrode overlays well with the CV of C_{60}Fc1 electrolyte at the beginning of the cycling experiment i.e. cycle 2 (figure 5.10c). This indicates that the bulk electrolyte had not been degraded during the 1000 CV cycles.

In a separate experiment, successive CV cycling of C_{60}Fc1 electrolyte was conducted at a glassy carbon WE. After 300 cycles the CV cycling was stopped and the solution was agitated to mix the electrolyte. The CV cycling was continued and as indicated in figure 5.11, the voltammetry after electrolyte agitation is unchanged. This rules out the possibility that the change in voltametric response upon cycling was due to charge carrier degradation occurring within the diffusion layer at the electrode surface.

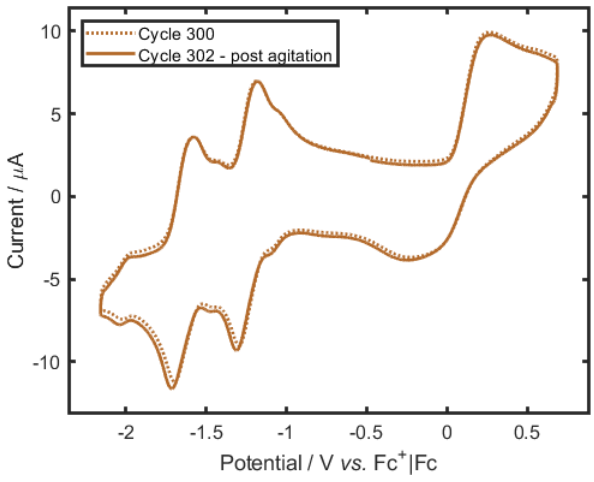

Figure 5.11. CV cycling study of C_{60}Fc1 electrolyte at a glassy carbon WE (0.071 cm^2) with Pt wire CE and referenced to $Fc^+|Fc$ at ν of 100 mV s^{-1} and iR compensation applied. After 300 cycles, the electrolyte was agitated to disperse the diffusion layer at the electrode surface. Cycle 300 and 302 (post agitation) are overlayed.

It is curious that the Fc-centred redox process is affected by the electrode fouling while the C_{60}-centred redox processes remain mostly unimpacted. We hypothesise that the Fc-centred redox process has an inner-sphere electron transfer mechanism which is severely impacted by the change in electrode surface while the C_{60}-centred redox process occurs by an outer-sphere electron transfer mechanism.

Similar fouling could be expected at the graphite felt electrodes upon cycling C_{60}Fc1 electrolyte in a RFB. In fact, the fouling could occur more quickly since the electrodes will be exposed to fully charged electrolyte solutions for prolonged periods compared to the CV cycling study. Electrode fouling would be expected to cause increased overpotentials and ultimately significant capacity fade as the charge and discharge redox reactions at the positive electrode become electrochemically irreversible and ultimately inhibited.

5.3.2.b Electrochemical analysis - comparison of C_{60}Fc1-3

Figures for the full electrochemical analysis of C_{60}Fc2 and C_{60}Fc3 can be found in appendix A, including CV, scan rate analysis and CV cycling studies (1000 cycles). The key electrochemical properties of C_{60}Fc1-3 are summarised and compared here.

Table 5.3. E_{mid} of processes I/I′, II/II′ and III/III′ for C_{60}Fc1-3. CVs were recorded at ν of 100 mV s^{-1} with iR compensation applied. All potentials are reported versus that of an $Fc^{+}|Fc$ internal reference.

Charge Carrier	E_{mid} Fc-centred (I/I′)/ V	E_{mid} 1st C_{60}-centred (II/II′) / V	E_{mid} 2nd C_{60}-centred (III/III′) / V
C_{60}Fc1	0.06	−1.30	−1.69
C_{60}Fc2	0.11	−1.23	−1.62
C_{60}Fc3	0.01	−1.36	−1.76

As seen in figure 5.12, the voltammetry of C_{60}Fc1, C_{60}Fc2 and C_{60}Fc3 are very similar. The difference in redox potential between the Fc-centred and first C_{60}-centred redox couple is 1.36 V ± 20 mV. The E_{mid} for the Fc-centred redox couple deviates by a maximum of 100 mV between the three charge carriers. The diffusion coefficient and k^0 for Fc oxidation and C_{60} reduction are also very similar for each charge carrier as

seen in table 5.4. These results indicate that while the molecular modification has a significant influence of solubility, the electrochemical properties of the charge carriers are mostly unchanged. Based on the CV, the performance of $C_{60}Fc2$ and $C_{60}Fc3$ in a RFB are expected to be comparable to $C_{60}Fc1$ but the theoretical E_v of the RFB to be enhanced due to their increased solubility in oDCB.

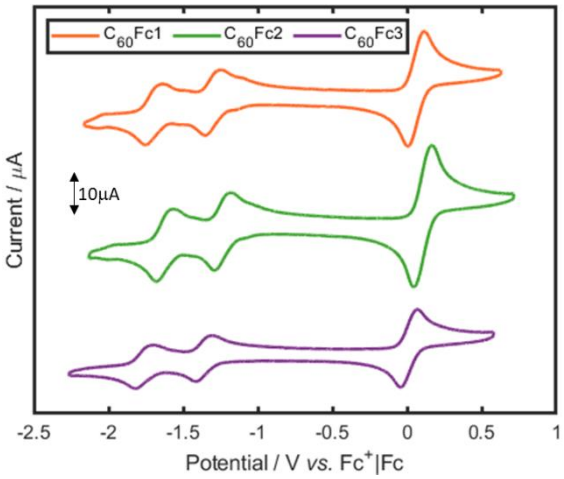

Figure 5.12. CV of $C_{60}Fc1$, $C_{60}Fc2$ and $C_{60}Fc3$ in 0.5 M [TBA][BF_4] in oDCB at a glassy carbon WE (0.071 cm^2) with Pt wire CE and referenced to $Fc^+|Fc$ at ν of 100 mV s^{-1} and with iR compensation applied.

Table 5.4. Diffusion coefficients, *D* and heterogeneous electron transfer coefficients, k^0 for process I/I′ - III/III′ for $C_{60}Fc1$-3. For each charge carrier, the gradient in the region 10 mV s^{-1} < ν < 200 mV s^{-1} was used in conjunction with Eq. 3.5 to estimate *D*. k^0 was calculated using the Nicholson method.

Charge Carrier	*D* / cm^2 s^{-1}	k^0 I/I′ / cm s^{-1}	k^0 II/II′ / cm s^{-1}	k^0 III/III′ / cm s^{-1}
$C_{60}Fc1$	4.9×10^{-7}	4.56×10^{-4}	7.52×10^{-4}	4.48×10^{-4}
$C_{60}Fc2$	9.2×10^{-7}	3.78×10^{-4}	8.88×10^{-3}	5.33×10^{-2}
$C_{60}Fc3$	2.9×10^{-7}	2.14×10^{-4}	4.43×10^{-4}	2.00×10^{-4}

5.3.3 Flow battery performance of $C_{60}Fc$ charge carriers

Several symmetric RFBs were assembled using $C_{60}Fc1$, $C_{60}Fc2$ and $C_{60}Fc3$ as charge carriers and their results are presented here. Initially, a detailed analysis of the $C_{60}Fc1$

RFB and its post cycling characterisation is provided. Later, the RFB performance of C_{60}Fc2 and C_{60}Fc3 are reported and compared to that of C_{60}Fc1.

5.3.3.a Flow battery Performance of C_{60}Fc1

A symmetric RFB was assembled in a N_2-filled glove box. Both the positive and negative electrolyte consisted of 10 mL of 1 mM C_{60}Fc1 in 0.5 M [TBA][BF_4] in oDCB. Two sheets of Celgard were used to separate the half-cells and electrolytes were pumped through the cell at a flow rate of 20 mL min^{-1}. Table 5.5 summarises the redox reactions expected to occur in the positive and negative electrolyte and the expected potential of charge/discharge plateaus upon cycling.

Table 5.5. Expected redox reactions (rxn.) of the positive and negative electrolytes in a symmetric C_{60}Fc1 RFB. The expected potential of plateaus have been calculated based of E_{mid} from CV of C_{60}Fc1.

Plateau	Positive electrolyte rxn. (E_{mid} *vs.* $Fc^+|Fc$ / V)	Negative electrolyte rxn. (E_{mid} *vs.* $Fc^+|Fc$ / V)	Plateau potential / V
1	½ C_{60}**Fc**1 ⇌ ½ C_{60}**Fc**1^{2+} + e^- (0. 06)	**C_{60}**Fc1 + e^- ⇌ **C_{60}**$Fc1^-$ (−1.30)	1.36
2	½ **C_{60}**Fc1 ⇌ ½ **C_{60}**$Fc1^{2+}$ + e^- (0. 06)	**C_{60}**$Fc1^-$ + e^- ⇌ **C_{60}**$Fc1^{2-}$ (−1.69)	1.75
3	½ **C_{60}**Fc1 ⇌ ½ **C_{60}**$Fc1^{2+}$ + e^- (0. 06)	**C_{60}**$Fc1^{2-}$ + e^- ⇌ **C_{60}**$Fc1^{3-}$ (approx. −2.30)	2.36

Blank electrolyte (0.5 M [TBA][BF_4] in oDCB) was pumped through the RFB in order to soak the separator and electrodes prior to the addition of charge carriers. Potentiostatic EIS was recorded across the assembled RFB after 30 minutes in order to measure the resistance across the flow cell. Measurements were recorded within the frequency range of 100 kHz to 100 mHz. R_{ohm} is the sum of ohmic resistance within the cell and includes contributions from the electrolyte, porous separators, graphite felt electrodes, and electrical leads between the cell and the potentiostat. R_{ohm} of the cell was measure to be 21 Ω which, given the electrode geometric surface area of 5 cm^2, corresponds to an area specific resistance (ASR) of 105 Ω cm^2.

Chamberlain *et al.* report R_{ohm} of 211 Ω for the coin cell assembly with 0.1 M [TBA][BF_4] in oDCB, which was the electrolyte used in testing $C_{60}Fc1$.[5] Assuming a geometric surface area of 1 cm^2 for the coin cell, this corresponds to a ASR of 211 Ω cm^2. The reduced ASR of the flow cell is expected to lead to reduced overpotentials and therefore improved VE compared to the coin cell.

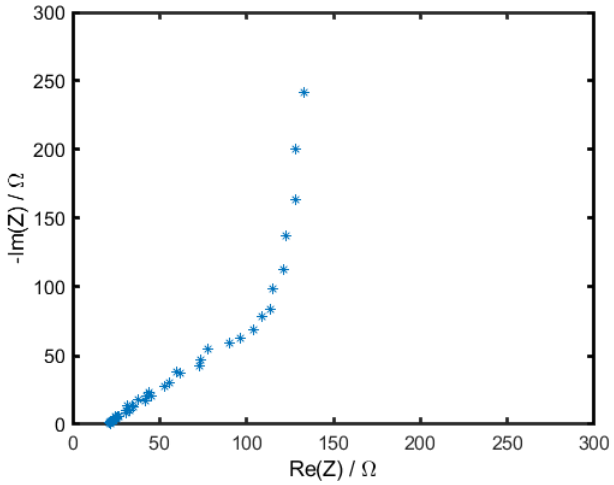

Figure 5.13. Nyquist plot of EIS measurement of full RFB assembly with 0.5 M [TBA][BF_4] in oDCB flowing through the cell at 20 mL min^{-1}.

Initially the RFB was cycled within the voltage window of 0 to 2.5 V in order to replicate conditions used in the literature.[5] Galvanostatic cycling was conducted at a current density of 0.1 mA cm^{-2} (±0.5 mA). Three charge plateaus were observed and are labelled charge 1-3 in figure 5.14. Charge plateaus 1-3 occur at potentials of 1.35 V, 1.80 V and 2.25 V respectively and correspond well to the reactions outlined in table 5.5.

Charge plateau 3 is thought to occur due to the C_{60}-centred reduction of $C_{60}Fc1^{2-}$ to $C_{60}Fc1^{3-}$ at the negative electrode and simultaneous Fc-centred oxidation of $C_{60}Fc1$ at the positive electrode. In an ideal system, the positive electrolyte would be fully oxidised to $C_{60}Fc1^{2+}$ once charge plateau 2 was complete. The presence of the third plateau indicates that $C_{60}Fc1$ and/or $C_{60}Fc1^{1+}$ were present in the positive electrolyte after charge plateau 2 was complete. This may be due to inaccuracy in distribution of electrolyte between reservoirs, the presence of impurities or due to crossover of charge carrier to the negative reservoir where it can be reduced and return to the

positive reservoir. While the third charge plateau is not explored further in this study, it demonstrates that there is promise in exploring the C_{60}Fc tris-adduct i.e. three Fc groups covalently bound to a fullerene centre. The tri-adduct could achieve enhanced E_v by enabling a three-electron charge/discharge redox reaction per molecule.

The voltage window was adjusted to 0 to 2.1 V and galvanostatic cycling was continued for 100 cycles over a duration of 150 hours. The initial charge cycle (when

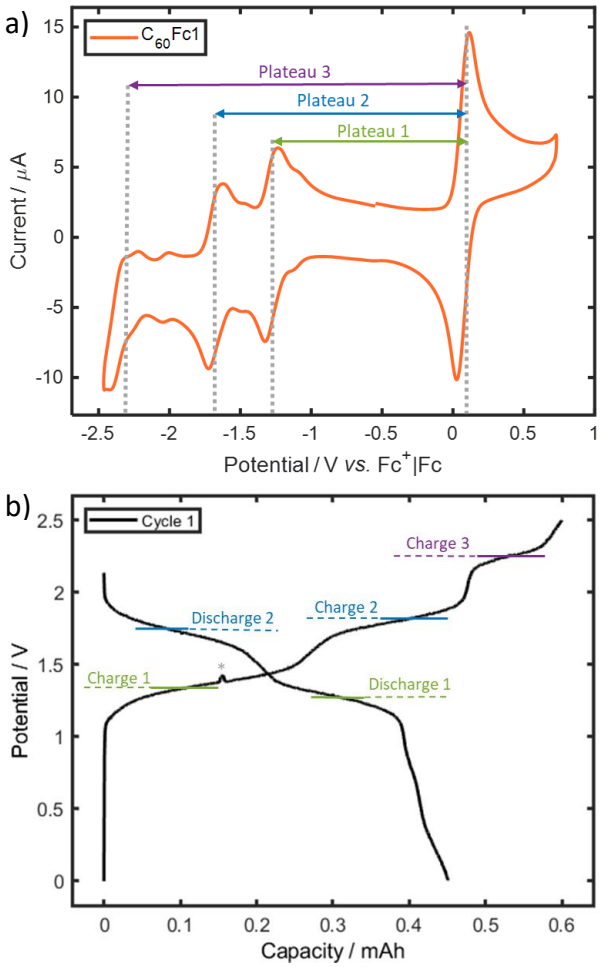

Figure 5.14. a) CV of 1 mM C_{60}Fc1 in 0.5 M [TBA][BF_4] in oDCB at a glassy carbon WE (0.071 cm^2) with Pt wire CE referenced to $Fc^+|Fc$ at ν of 100 mV s^{-1} and iR compensation applied. Dashed lines indicate E_{mid} of each redox couple and arrows indicate the expected potential of charge/discharge plateaus in a symmetric C_{60}Fc1 RFB. b) Charge-discharge profiles from cycle 1 of C_{60}Fc1 RFB. Voltage window of 0 to 2.5 V.* the minor variation in potential is due to electrolyte pumping briefly stopping.

capped at 2.1 V) realised an electrochemical yield of 89%. The RFB exhibited CE, VE and EE of 96%, 77% and 74% respectively over 100 cycles. The high CE indicates reversible electron transfer to and from C_{60}Fc1. VE is significantly improved in the flow cell compared to the equivalent system in a coin cell at the same current density.[5] This is attributed to the reduced ohmic resistance of the flow cell compared to the coin cell.

As seen in figure 5.15a, the shape of the charge and especially the discharge profiles change over the course of cycling. Most notable is the observation of an additional discharge plateau at approximately 0.8 V after 20+ cycles. A steady capacity fade of 0.33% per cycle over the course of 100 cycles (based of discharge capacities) is also observed. The capacity fade for the equivalent system in a coin cell was estimated at 0.4% per cycle over 100 cycles. The authors attributed capacity fade to several factors to include loss of available charge carrier due to electrolyte soaking into the absorbent glass-fibre separator. The use of a polypropylene separator and significantly larger volumes of electrolyte (20 mL for flow cell verses 400 μL for coin cell), means that this cause of capacity fade is avoided and could account for the lower rate of capacity fade observed in the flow cell.

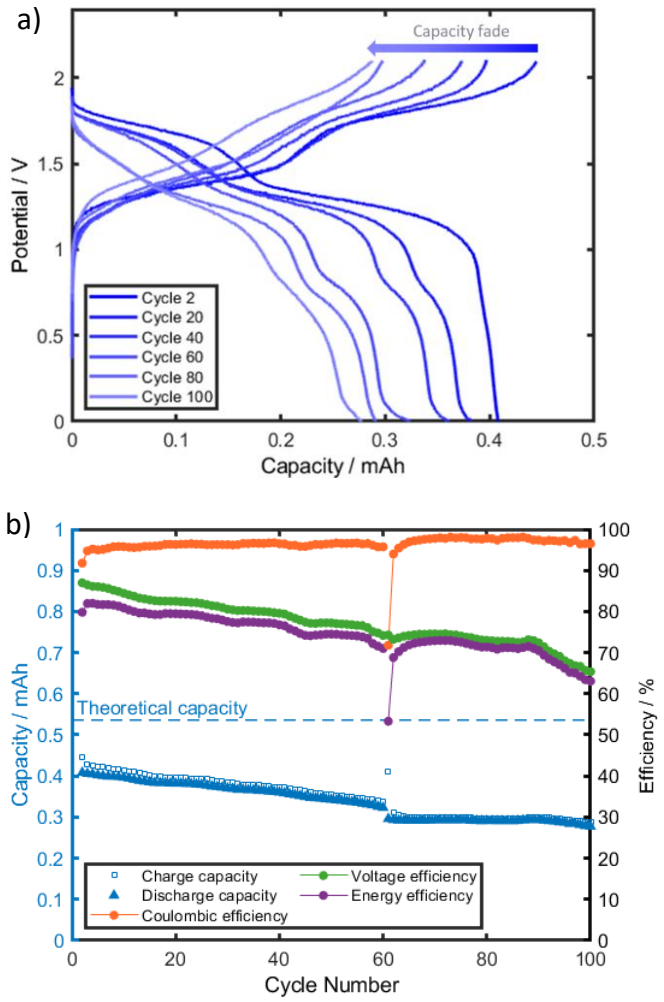

Figure 5.15. Symmetric C_{60}Fc1 RFB cycling within the voltage threshold of 0 to 2.1 V. Half-cells were separated by Celgard separator with current density of 0.1 mA cm^{-2} (C-rate of approximately 1C) and flow rate of 20 mL min^{-1}. a) Charge/discharge profiles of cycle 2 - 100 b) capacity and efficiency values per cycle.

After 60 cycles, the positive and negative electrolytes were mixed together and redistributed evenly between the electrolyte reservoirs (10 mL each). The electrolyte mixing did not regain lost capacity as seen by the charge and discharge capacity shown in figure 5.15b. This indicates that asymmetric membrane crossover (net migration of charge carrier to a single half-cell) is not a significant cause of capacity fade in this battery.[30]

To ascertain the cause of capacity fade in the symmetric C_{60}Fc1 RFB, the positive and negative electrolytes were removed after 100 charge-discharge cycles and were analysed by CV, TLC, MALDI ToF MS and ^{1}H NMR.

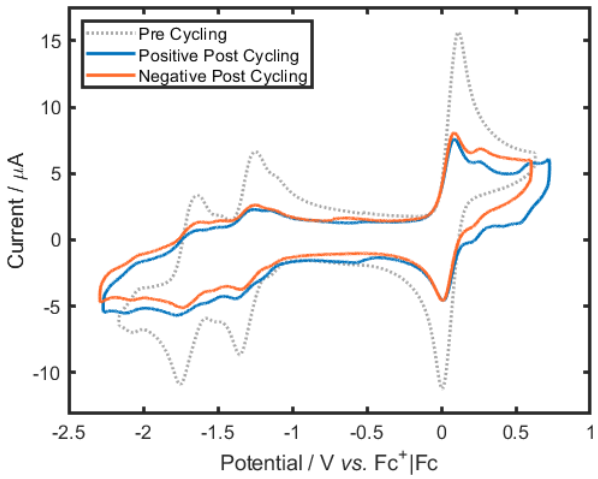

Figure 5.16. CV of electrolyte pre cycling (grey dashed) and of positive (blue) and negative (orange) electrolytes after 100 charge-discharge cycles in a C_{60}Fc1 RFB. CV was recorded at glassy carbon WE (0.071 cm^2) with Pt wire CE at ν of 100 mV s^{-1} and iR compensation applied. Ag wire QRE was used and voltammograms were referenced to the internal $Fc^+|Fc$ redox couple of C_{60}Fc1.

Figure 5.16 shows the CV of electrolytes pre cycling and following 100 charge-discharge cycles. Given the high boiling point of oDCB (178 °C), it can be assumed that minimal evaporation of solvent occurred during the flow battery cycling and therefore no change in charge carrier concentration is expected. Both the Fc- and C_{60}-centred redox process are present in the CV of electrolyte post 100 cycles but the current magnitude of the peaks is reduced. This indicates a reduction in the concentration of C_{60}Fc1 in the electrolyte and is likely the primary cause of capacity fade in the battery. A new redox couple is observed at ~0.2 V positive of the Fc-centred redox couple for both electrolytes. This additional redox couple is indicative of a new Fc environment. It can be speculated that the mono-adduct of C_{60}Fc1 and derivatives of free Fc could be present. In addition, a loss of definition and introduction of new redox couples are observed in the fullerene-centred redox region. These are hypothesised to be as a result of mono-adduct, non-functionalised fullerene and aggregates of C_{60}Fc1.

Charge carriers were extracted from the electrolytes for analysis by TLC, MALDI ToF MS and ^{1}H NMR. Solvent was removed by rotary evaporation and the residue was sonicated in methanol before being filtered to collect the solid. TLC was conducted with carbon disulfide mobile phase. Figure 5.17 shows the results of TLC of the extracted positive and negative electrolyte and pure C_{60}Fc1 for comparison. The retention factor, R_f, for C_{60}Fc1 bis-adduct is 0.25-0.55 and is observed for all three samples. Additional spots are observed for the positive and negative electrolyte extracts that are not observed for pure C_{60}Fc1. These occur at R_f of 0 and 0.85. The spot at R_f of 0.85 is attributed to the mono-adduct of C_{60}Fc1 (based on previous observations) while the spot at 0 is unidentified. This indicates that the mono-adduct of C_{60}Fc1 is a degradation product formed upon cycling of C_{60}Fc1 in a RFB.

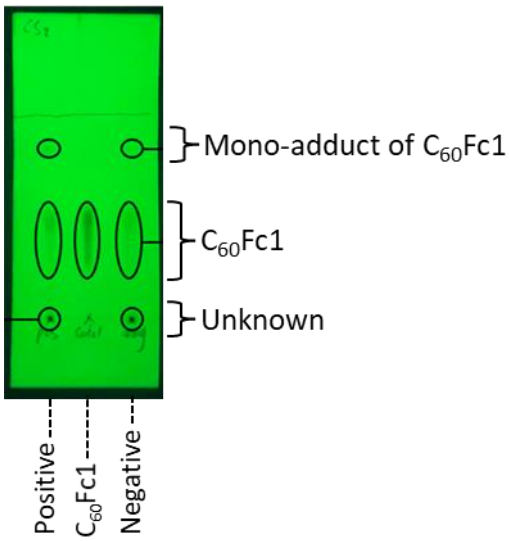

Figure 5.17. TLC of positive electrolyte extract (left), pure C_{60}Fc1 (middle) and negative electrolyte extract (right). The positive and negative electrolyte extracts were collected after 100 charge-dicscharge cycling in a RFB. Samples were extracted by solvent removal, sonication in methanol and collection of the residual solid by filtraton.

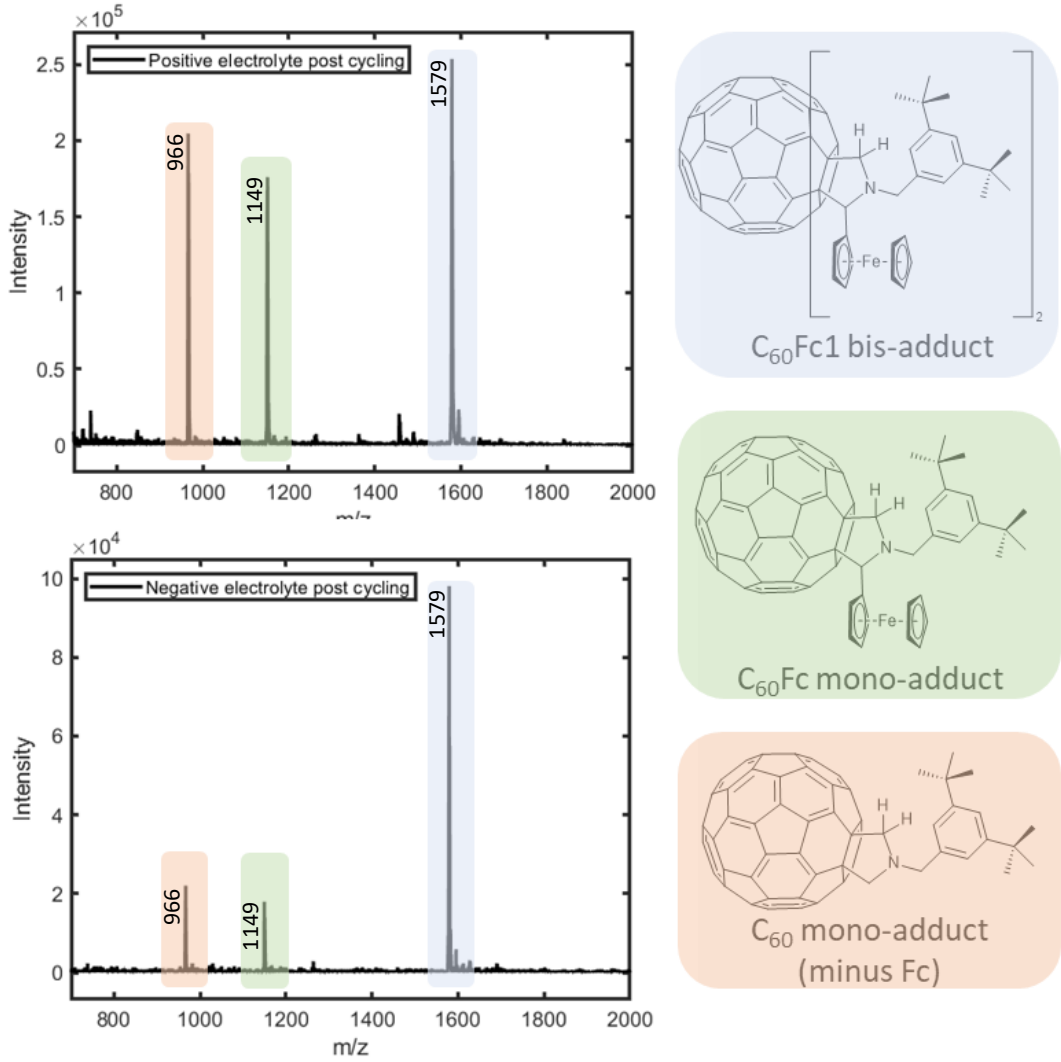

Figure 5.18. MALDI ToF MS of extracts from positive electrolyte (top) and negative electrolyte (bottom) following 100 charge-discharge cycles in a RFB. Samples were extracted by solvent removal, sonication in methanol and collection of the residual solid by filtraton.

The electrolyte extracts were also analysed by MALDI ToF MS and the results of which are shown in figure 5.18. The primary peak for both electrolytes occurs at m/z of 1579 and corresponds to C_{60}Fc1 bis-adduct (highlighted in blue). Two additional peaks are observed in both the positive and negative electrolyte. The peaks at m/z of 1149 and 966 correspond to the mono-adduct of C_{60}Fc1 (green) and the mono-adduct minus the Fc substituent (orange) respectively. Based on the peak height, the ratio of C_{60}Fc1 bis-adduct : C_{60}Fc mono-adduct : C_{60} mono-adduct (minus Fc) is 1 : 0.67 : 0.80 for the positive electrolyte and is 1 : 0.18 : 0.22 for the negative electrolyte. The positive electrolyte contains a higher proportion of degradation products compared to the

negative electrolyte. This may suggest that electrolyte degradation primarily occurs in the positive electrolyte and is perhaps accelerated by the oxidation of $C_{60}Fc1$ to $C_{60}Fc1^{2+}$. However, the selectivity of the separator to degradation products is thought to be poor and therefore the distribution of degradation products between electrolytes is not necessarily reflective of where they are formed.

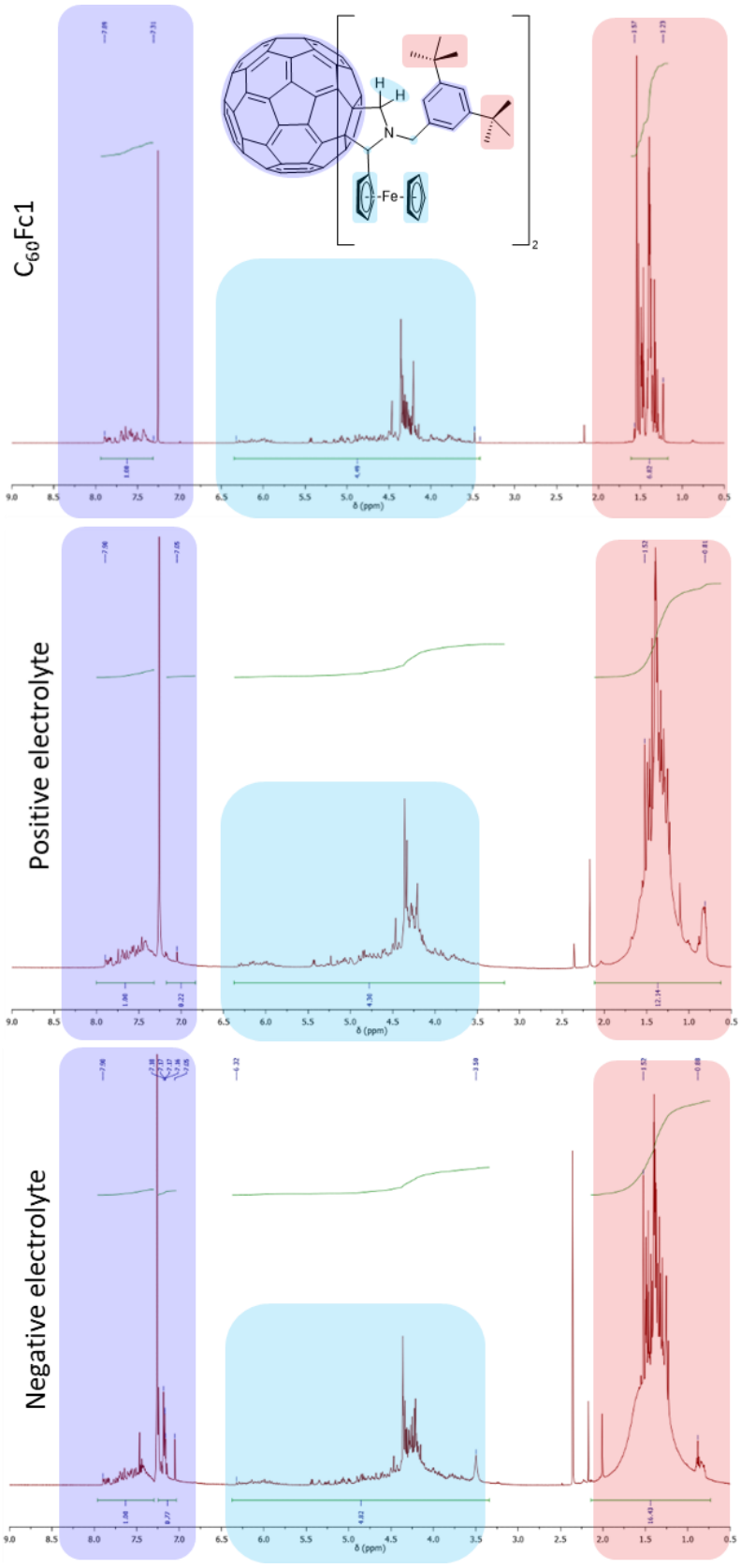

Figure 5.19. ^{1}H NMR spectra of positive and negative electrolyte extracts in $CDCl_3$. following 100 charge-discharge cycles in a RFB. Samples were extracted by solvent removal, sonication in methanol and collection of the residual solid by filtraton.

The positive and negative electrolytes were also analysed by ^{1}H NMR spectroscopy and results of which are shown in figure 5.19. The peaks in the region of 7-8 ppm (highlighted in purple) are attributed to the aromatic protons of the charge carrier. The peaks in the region of 3.5-6.5 ppm (highlighted in blue) are attributed to the protons of the pyrrolidine ring and cyclopentadiene rings of Fc. The broad multiplet in the region of 1-2 ppm (highlighted in red) is attributed to the protons of the tertbutyl groups $(CH_3)_3C$ of $C_{60}Fc1$. For the post cycling electrolyte extracts, each region is broadened and the peak pattern altered compared to the spectrum of pure $C_{60}Fc1$. While the complexity of the spectra prevents accurate structural determination, these results indicate the presence of degradation products in alignment with the CV, TLC and MALDI ToF MS results.

SEM was used to image the graphite felt electrodes following 100 cycles and the results are shown in figure 5.20. The electrodes were rinsed with oDCB to remove any residual electrolyte and dried in a vacuum oven at 40°C for a minimum of 72 hours before analysis. The samples were compared to an untreated electrode and a control electrode. The control was prepared by soaking graphite felt in a solution of $C_{60}Fc1$ electrolyte for 150 hours (equivalent to 100 cycles), before rinsing with oDCB and drying as described above. Deposits were observed on the graphite felt fibres for the control, positive and negative electrodes which were not seen to the same extent on untreated graphite felt. Energy dispersive x-ray (EDX) analysis was used to probe the elemental composition of the electrode surfaces. Carbon, nitrogen and fluorine were the primary elements observed and no iron was detected. The presence of nitrogen and fluorine on the electrode surface suggests that the deposits could be composed of $[TBA][BF_4]$. No substantial evidence of charge carrier deposition on the electrode surface is observed.

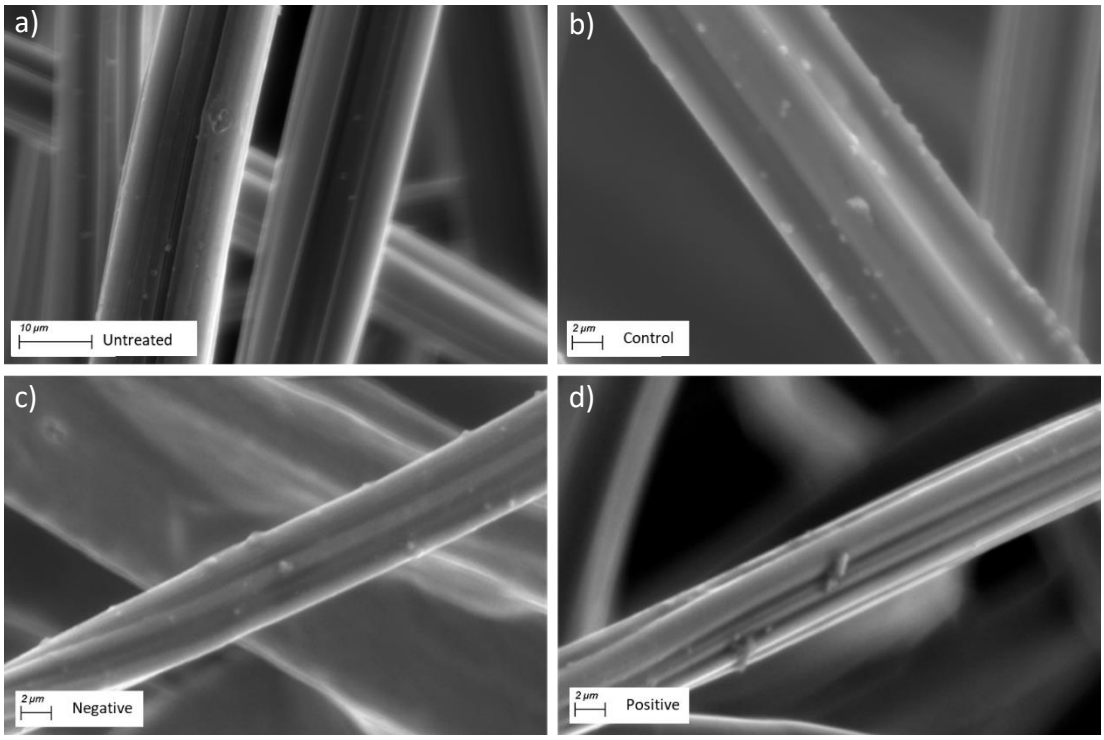

Figure 5.20. SEM images of a) pristine graphite felt electrode (untreated), b) control electrode (soaked in C_{60}Fc1 electrolyte for 150 hours), c) negative electrode post 100 cycles in C_{60}Fc1 RFB and d) positive electrode post 100 cycles in C_{60}Fc1 RFB. Electrodes b)-d) were rinsed with oDCB and dried in a vacuum oven at 40 °C for a minimum of 72 hours before analysis.

5.3.3.b Flow battery performance – comparison of C_{60}Fc1-3

The same conditions were used to investigate the performance of the more soluble charge carriers, C_{60}Fc2 and C_{60}Fc3, and to compare these results to those of C_{60}Fc1. The symmetric RFBs of C_{60}Fc2 and C_{60}Fc3 were successively cycled within the voltage threshold of 2.1 V an 0 V at a current density of 0.1 mA cm^{-2}. Charge and discharge plateaus were initially observed at the potentials expected from voltammetry. As in the C_{60}Fc1 RFB, the shape of the charge-discharge profiles changed over the course of cycling, concurrently with a reduction in the achieved charge and discharge capacities. Charge/discharge profiles and plots of capacity and efficiency per cycle for the C_{60}Fc2 and C_{60}Fc3 RFBs are available in figures A.7 and A.9 of appendix A.

The C_{60}Fc2 RFB showed a faster rate of capacity fade at 1.01% per cycle compared to the C_{60}Fc1 RFB at 0.33%. A large degree of asymmetric membrane crossover was observed in the C_{60}Fc2 RFB, as indicated by the unequal volume distribution between the two reservoirs after cycling. For the C_{60}Fc2 RFB, the volume distribution after 65 cycles was 0.5 mL and 19.5 mL in positive and negative electrolyte reservoir respectively. The discharge capacity for cycle 65 had reduced to 32% of the starting value (cycle 2). The electrolytes were mixed and redistributed evenly between reservoirs (10 mL each) and the discharge capacity of the following cycle increased to 78% of its original value. This is in contrast to the C_{60}Fc1 RFB which showed no significant increase in capacity following electrolyte mixing and redistribution (figure 5.15).

After 100 charge-discharge cycles, electrolytes of the symmetric C_{60}Fc2 RFB were analysed by CV, results of which are reported in figure A.8 of appendix A. A loss of current density in the Fc and fullerene potential regions was observed for both electrolytes, and is most pronounced for the positive electrolyte. Similarly to the post cycling analysis of C_{60}Fc1 electrolytes, additional peaks are observed in the Fc region, indicative of charge carrier degradation. Post cycling analysis in conjunction with the unequal distribution of electrolytes, indicates that two different causes of capacity fade are occurring for the C_{60}Fc2 RFB; (1) charge carrier degradation and (2) asymmetric membrane crossover.

The rate of capacity fade for the $C_{60}Fc3$ RFB was less severe than for the $C_{60}Fc2$, but an uneven volume distribution between electrolytes was observed which is indicative of asymmetric membrane crossover.

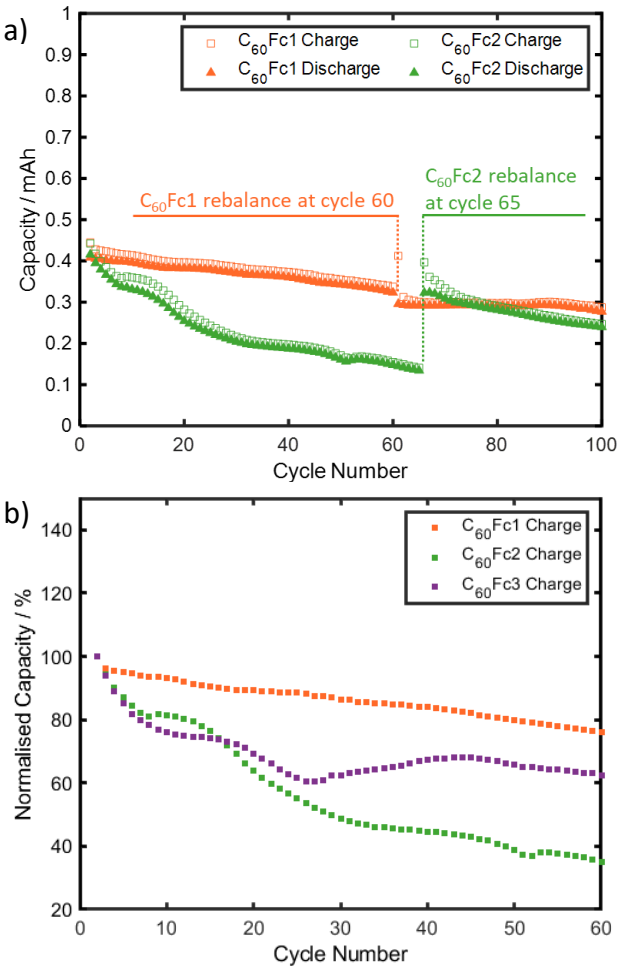

Figure 5.21. Performance comparison of symmetric RFBs containing $C_{60}Fc1$-3, cycling within the voltage threshold of 0 to 2.1 V. Half-cells were separated by Celgard separator with current density of 0.1 mA cm^{-2} (C-rate of approximately 1C) and flow rate of 20 mL min^{-1}. a) Charge and discharge capacities per cycle for the symmetric RFBs of $C_{60}Fc1$ (orange) and $C_{60}Fc2$ (green) over 100 cycles. Dashed lines represent the cycle at which the electrolytes were rebalanced by mixing the positive and negative electrolytes and evenly redistributing between the two reservoirs. b) Charge capacity (normalised to cycle 2) verses cycle number for RFBs containing $C_{60}Fc1$-3.

A comparison of the three RFBs is shown in figure 5.21b and table 5.6. Across all metrics, the $C_{60}Fc1$ RFB performed best and as previously discussed, displayed no

indication of asymmetric membrane crossover. Both the C_{60}Fc2 and C_{60}Fc3 RFBs experienced faster rates of capacity fade and inferior VE. Substantial asymmetric membrane crossover was observed after <100 cycles and capacity was recovered upon electrolyte rebalancing. The primary difference between C_{60}Fc1 and the latter two charge carriers, is the presence of a para substituted hexyl chain on the aromatic substituent as opposed to two meta substituted tert-butyl groups. Such variation in flow battery performance was unexpected given the minor tuning of the charge carrier structure.

Table 5.6. A comparison of performance metrics for RFBs containing C_{60}Fc1, C_{60}Fc2 and C_{60}Fc3. All values are averaged over cycles 2-60. *Capacity fade was calculated based on the gradient of the charge capacity-cycle number plot, divided by the initial capacity.[31]

Charge Carrier	Capacity fade* per cycle / %	CE / %	VE / %	EE / %
C_{60}Fc1	0.33	96	81	78
C_{60}Fc2	1.01	94	58	54
C_{60}Fc3	0.34	92	61	67

Transport phenomena across membranes in RFBs is complex and caused by several driving forces to include a concentration gradient (diffusion), electric field (migration) and pressure. In symmetric systems such as the C_{60}Fc RFBs studied here, a concentration gradient across the membrane is not present in the discharged state, where the charge carriers are in the same oxidation state in each half-cell. Upon charge, a concentration-gradient is induced as the charge carriers change oxidation state and degradation products are formed, leading to diffusion across the membrane. As the charge carriers are oxidised/reduced from neutral to cationic/anionic states, they become susceptible to transport by migration. Migrative transport is driven by the electric field and is therefore proportional to the applied current density. In each case, the transport of solvent (in the solvent shell) is coupled to that of the charge carriers in a phenomenon known as electroosmotic/solvent drag.[32,33]

Significant asymmetric membrane crossover was observed after <100 cycles in the case of the $C_{60}Fc2$ and $C_{60}Fc3$ RFBs. In each case, the volume of electrolyte in the negative electrolyte reservoir increased and the volume in the positive electrolyte reservoir decreased by the same amount. In addition, a significant proportion of lost capacity was regained by mixing electrolytes and evenly redistributing between reservoirs, which suggests that electrolyte imbalance is a key cause of capacity fade in these systems.

In order to scrutinise the engineering behind the RFB assembly, a series of experiments were conducted to measure the extent of electrolyte crossover under controlled conditions. A RFB was assembled under the same conditions as for the testing of $C_{60}Fc$ charge carriers, except for the absence of charge carrier in the electrolyte. The electrolytes were cycled at a flow rate of 20 mL min^{-1} for >100 hours, without the any application of charging currents. Over four repetitions of this experiment, the maximum volume deferential between electrolyte reservoirs was 4 mL after 100 hours. This was attributed to a small pressure difference between each half-cell and is thought to be due to a disparity in the compression of each electrode upon assembly of the RFB. The crossover observed in the $C_{60}Fc2$ RFB after <60 hours, far exceeds what is expected from pressure differential alone. Consequently, we can assume that asymmetric electroosmotic drag is responsible for the substantial asymmetric crossover that is observed.

We can speculate as to the reasoning for preferential membrane crossover in the direction of the negative electrolyte. Upon charge the charge carrier in the negative electrolyte is reduced to $C_{60}Fc^{2-}$ (dianionic state), and experiences electrical attraction towards the positive electrode in the opposite half-cell. The same but opposite phenomenon is true for the charge carrier in the positive electrolyte. We can speculate that the solvent-solute interaction of $C_{60}Fc^{2+}$ (charged positive electrolyte) is greater than for $C_{60}Fc^{2-}$ (charge negative electrolyte), due to the enhanced interaction of oDCB with the dication. This results in a net movement of solvent towards the negative electrolyte reservoir. However, it is perhaps unlikely that such a large degree of membrane crossover (10 mL of solvent) is facilitated by

electroosmotic drag from such a low concentration of charge carrier (1 mM). An alternative hypothesis is that TBA^+ cations of the supporting electrolyte facilitate transport of oDCB solvent through electroosmotic drag. Transport of supporting electrolyte ions across the membrane takes place to balance the charge generated upon charge/discharge of the cell. The reasons for this phenomenon occurring preferentially towards the negative electrolyte reservoir is unknow.

5.3.3.c Flow battery performance with alternating polarity

To minimise the impact of asymmetric membrane crossover, a second $C_{60}Fc2$ RFB was assembled and cycled in such a way that the polarity was alternated each cycle. The battery was alternately cycled between the voltage thresholds of 2.1 to 0 V and −2.1 to 0V. Figure 5.22 shows the charge and discharge profiles for cycle 1 and 2 of the $C_{60}Fc2$ RFB with alternating polarity. This has the impact of alternating which reservoir is the acting positive and negative electrolyte, in the aim of zeroing the net electroosmotic drag. This technique is applicable only for symmetric RFBs and specifically for those where both electrolytes discharge to the same oxidation state.[34]

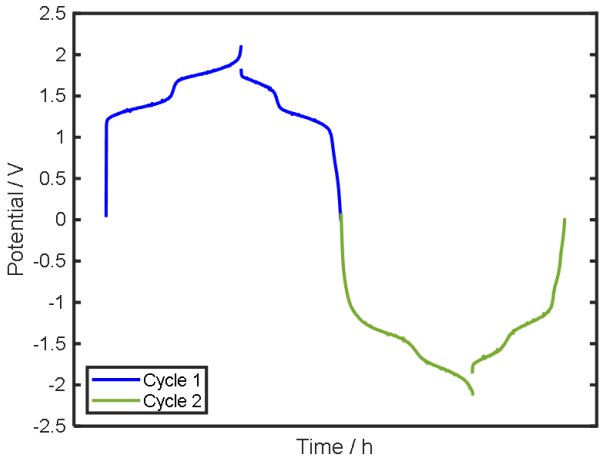

Figure 5.22. Charge-discharge profiles for cycle 1 and 2 of $C_{60}Fc2$ RFB with alternating polarity.

As seen in figure 5.23, the capacity fade observed for the $C_{60}Fc2$ RFB with alternating polity is reduced to 0.40% per cycle (measured over 60 cycles) which is a substantial reduction compared to the RFB with consistent polarity (1.01% per cycle). Following 100 charge-discharge cycles, no discrepancy in the volumes of electrolyte in the positive and negative reservoirs was observed. The remaining capacity fade is attributed to charge carrier degradation alone. This is supported by reduced current

density observed in the CV of electrolytes following 100 charge-discharge cycles, results of which are available in figure A.10 of appendix A. This supports our hypothesis that asymmetric electroosmotic drag has a significant and detrimental impact of capacity retention for C_{60}Fc2. Indeed, the charge capacity of the C_{60}Fc2 RFB with alternating polarity, matches well with that of the C_{60}Fc1 RFB.

It is somewhat surprising that the electroosmotic drag observed by C_{60}Fc2, unless compensated for by alternating the battery polarity, is much greater than for C_{60}Fc1. It can be assumed that the hexyl chain of C_{60}Fc2 plays a key role in enhancing the solvent-solute interaction, which results in not only an increase in solubility but also in an increase in solvent drag effect.

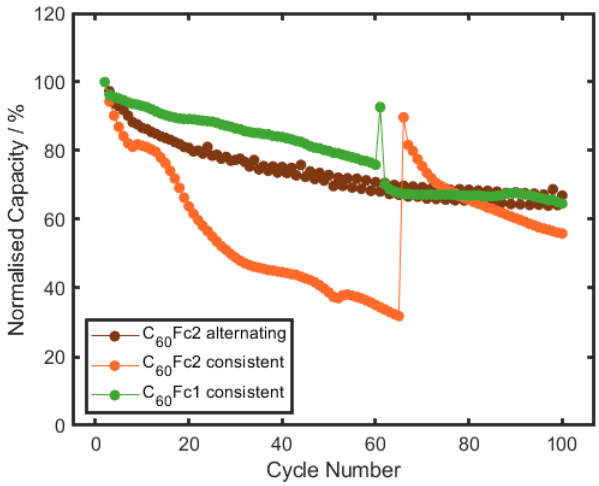

Figure 5.23. Normalised charge capacity verses cycle number for C_{60}Fc2 RFBs with alternating (brown) and consistent (orange) polarity and for the C_{60}Fc1 RFB (green). The electrolytes of the C_{60}Fc1 RFB and C_{60}Fc2 RFB with consistent polarity were regenerated by mixing and evenly distributing between reservoirs at cycle 60 and 65 respectively.

5.4. Conclusions

A series of C_{60}Fc bifunctional molecules were investigated as charge carriers in symmetric nonaqueous RFBs. Three different C_{60}Fc bis-adducts were synthesised, which differ in the structure of the substituents on the pyrrolidine linker which connects the fullerene core and Fc moieties. Substitution of two tertbutyl groups on the aromatic ring of the linker for a single hexane chain, showed an increase in solubility of the resulting charge carrier in oDCB from 0.25 M (C_{60}Fc1) to 0.29 M

(C_{60}Fc2). A further increase in solubility was observed from 0.29 M (C_{60}Fc2) to 0.34 M (C_{60}Fc3) when substituting the protons in the α position of the pyrrolidine for methyl groups. The effect of increasing the solubility of C_{60}Fc on the theoretical E_v of the RFB is shown in table 5.7. The theoretical E_v of a C_{60}Fc3 RFB was calculated to be 14.1 Wh L^{-1}.

CV and DPV were used to investigate the electrochemical properties of the charge carriers. A reversible two-electron oxidation, attributed to the two Fc substituents was observed at positive potentials. Two reversible one-electron reduction process were observed at negative potentials and were attributed to the consecutive one-electron reduction of the fullerene core. The multi-electron redox activity at both high and low potentials (separated by 1.36 V) enables the application of these charge carriers as both positive and negative electrolyte in symmetric RFBs.

A symmetric flow battery containing C_{60}Fc1 was cycled successfully for 100 cycles (>150 hours) with high CE of 96%. The results were compared with previously published results of the same charge carrier in a coin cell assembly. VE of the battery was greatly improved in the flow cell compared the coin cell and capacity fade due to absorption of electrolyte into the separator was mitigated. However, consistent capacity fade of 0.3% per cycle was observed. Post cycling analysis revealed that the principle cause of capacity fade was due to degradation of C_{60}Fc1. TLC and MALDI ToF MS revealed that C_{60}Fc1 mono-adduct and a C_{60} mono-adduct with no Fc moiety were present in the electrolyte post cycling. CV of electrolytes post cycling showed an additional redox couple at positive potentials which indicates the presence of a new Fc species, thought to be generated upon degradation of C_{60}Fc1.

Table 5.7. Key parameters of C_{60}Fc1-3 when applied as chare carrier in symmetric RFBs.

Charge Carrier	C_{active} **/ M**	V_{cell} **/ V**	***n***	**Theoretical E_v / Wh L^{-1}**	**Causes of capacity fade**
C_{60}Fc1	0.25	1.56	2	10.4	C_{60}Fc degradation
C_{60}Fc2	0.29	1.54	2	11.9	C_{60}Fc degradation Membrane crossover

C_{60}Fc3	0.34	1.57	2	14.1	C_{60}Fc degradation Membrane crossover

C_{60}Fc2 and C_{60}Fc3 (those featuring the hexyl chain substituent) were also tested in symmetric flow batteries, but showed significant asymmetric membrane crossover towards the negative electrolyte reservoir. The detrimental effect of asymmetric membrane crossover in the C_{60}Fc2 RFB, was shown to be avoidable by alternating the polarity of the battery each cycle. In this case, the rate of capacity fade was reduced from 1.01% per cycle to 0.40% per cycle.

The impact of molecular modification of the C_{60}Fc charge carriers on their membrane transport properties was a surprising observation. Future work should include a more detailed analysis of the membrane crossover trends observed in this study. Membrane crossover tests such as those described in section 2.1.2 (chapter 2) could quantify the rate of transport across the Celgard separator for each charge carrier and support the observations made here. Furthermore, molecular tuning of C_{60}Fc charge carriers to enhance their solubility in alternative organic solvent could be beneficial on two fronts. Firstly, substitution of oDCB for a more environmentally benign and less hazardous solvent would enhance the green credentials and commercial viability of the RFB. Secondly, substitution for a solvent with a wider window of electrochemical stability would allow for the oxidation and reduction of C_{60}Fc tris-adducts by three electrons per molecule, thereby increasing *n* from two to three and further enhancing the E_v of the resulting RFB.

5.5. References

1 G. Sikukuu Nambafu, Electrochem. commun., 2021, **127**, 107052.

2 K. Lourenssen, J. Williams, F. Ahmadpour, R. Clemmer and S. Tasnim, J. Energy Storage, 2019, **25**, 100844.

3 C. L. Peake, A. J. Kibler, G. N. Newton and D. A. Walsh, ACS Appl. Energy Mater., 2021, **4**, 8765–8773.

4 J. Winsberg, C. Stolze, S. Muench, F. Liedl, M. D. Hager and U. S. Schubert, ACS Energy Lett., 2016, **1**, 976–980.

5 J. Friedl, M. A. Lebedeva, K. Porfyrakis, U. Stimming and T. W. Chamberlain, J. Am. Chem. Soc., 2018, **140**, 401–405.

6 R. S. Ruoff, D. S. Tse, R. Malhotra and D. C. Lorents, J. Phys. Chem., 1993, **97**, 3379–3383.
7 H. W. Kroto, J. R. Heath, S. C. O'Brien, R. F. Curl and R. E. Smalley, Nature, 1985, **318**, 162–163.
8 L. Echegoyen and L. E. Echegoyen, Acc. Chem. Res., 1998, **31**, 593–601.
9 R. F. Curl, Angew. Chem. Int. Ed. Engl., 1997, **36**, 1566–1576.
10 H. W. Kroto, Angew. Chem. Int. Ed. Engl., 1997, **36**, 1578–1593.
11 R. E. Smalley, Angew. Chem. Int. Ed. Engl., 1997, **36**, 1594–1601.
12 R. Bakry, R. M. Vallant, M. Najam-ul-Haq, M. Rainer, Z. Szabo, C. W. Huck and G. K. Bonn, Int. J. Nanomedicine, 2007, **2**, 639–649.
13 S. Collavini and J. L. Delgado, Sustain. Energy Fuels, 2018, **2**, 2480–2493.
14 Y. Pan, X. Liu, W. Zhang, Z. Liu, G. Zeng, B. Shao, Q. Liang, Q. He, X. Yuan, D. Huang and M. Chen, Appl. Catal. B Environ., 2020, **265**, 118579.
15 Z. Jiang, Y. Zhao, X. Lu and J. Xie, J. Energy Chem., 2021, **55**, 70–79.
16 C. F. Da Costa, A. C. Pinheiro, M. V. De Almeida, M. C. S. Lourenço and M. V. N. De Souza, Chem. Biol. Drug Des., 2012, **79**, 216–222.
17 S. Choi, S. H. Chae, J. Shin, Y. Kim, S. J. Kim, D. H. Choi and S. J. Lee, Chem. Commun., 2013, **49**, 3994–3996.
18 M. A. Lebedeva, T. W. Chamberlain, P. A. Scattergood, M. Delor, I. V Sazanovich, E. S. Davies, M. Suyetin, E. Besley, M. Schröder, J. A. Weinstein and A. N. Khlobystov, Chem. Sci., 2016, **7**, 5908–5921.
19 S. B. Beil and M. von Delius, Org. Mater., 2021, **3**, 146–154.
20 N. Sivaraman, R. Dhamodaran, I. Kaliappan, T. G. Srinivasan, P. R. V. Rao and C. K. Mathews, J. Org. Chem., 1992, **57**, 6077–6079.
21 J. Brant, H. Lecoanet and M. R. Wiesner, J. Nanoparticle Res., 2005, **7**, 545–553.
22 J. Friedl, U. Stimming and E. Al, J. Am. Chem. Soc., 2018, **140**, 401–405.
23 Z. Y. Wu, R. Zhong and F. Z. Yang, J. Organomet. Chem., 2017, **840**, 75–81.
24 B. Hwang, M.-S. Park and K. Kim, ChemSusChem, 2015, **8**, 310–314.
25 H. S. Kim, T. Yoon, Y. Kim, S. Hwang, J. H. Ryu and S. M. Oh, Electrochem. commun., 2016, **69**, 72–75.
26 M. V. Mirkin, A. J. Bard and L. O. S. Bulhões, J. Am. Chem. Soc., 1993, **115**, 201–204.
27 B. Miller, J. M. Rosamilia, G. Dabbagh, A. J. Muller and R. C. Haddon, J. Electrochem. Soc., 1992, **139**, 1941–1945.
28 R. S. Nicholson, Anal. Chem., 1965, **37**, 1351–1355.
29 I. Lavagnini, R. Antiochia and F. Magno, Electroanalysis, 2004, **16**, 505–506.
30 C. G. Armstrong, R. W. Hogue and K. E. Toghill, J. Electroanal. Chem., 2020, **872**, 114241.
31 Y. Yao, J. Lei, Y. Shi, F. Ai and Y. C. Lu, Nat. Energy, 2021, **6**, 582–588.
32 L. Gubler, Curr. Opin. Electrochem., 2019, **18**, 31–36.

33 R. M. Darling, A. Z. Weber, M. C. Tucker and M. L. Perry, J. Electrochem. Soc., 2016, **163**, A5014–A5022.

34 R. A. Potash, J. R. McKone, S. Conte and H. D. Abruña, J. Electrochem. Soc., 2016, **163**, A338–A344.

Chapter 6: Conclusions and Outlook

The intermittent nature of renewable energy sources has fuelled a demand for low-cost and reliable grid-scale energy storage. RFBs offer a promising solution due to their long cycle life and scalability. However, widespread commercial uptake of RFBs requires a reduction in cost and increase in E_v compared to the archetypal VRFB. The work presented in this thesis focuses on the development of high E_v RFBs through the design of multi-electron charge carriers in nonaqueous electrolyte. Multi-electron charge carriers allow for multiple electrons to be transferred per molecule upon charge/discharge of the battery, while nonaqueous electrolytes offer a wide window of electrochemical stability which allows for high voltages to be achieved.

The rich electrochemistry of POMs and fullerene make them particularly promising charge carriers for high E_v batteries. We demonstrate how functionalisation of these species can enhance their solubility and redox properties to further increase E_v. In summary, this thesis comprises the design, synthesis, and characterisation of functionalised POMs and fullerenes, and investigates their performance in nonaqueous RFBs.

Organic-inorganic hybridisation of POMs was shown to be an effective method to increase their solubility in organic solvent. Hybridisation of the Keggin phosphotungstate POM, PW_{12}, with phenyl siloxane moieties (PW_{11}-SiPh), increased its saturation concentration in acetonitrile by two orders of magnitude. The four one-electron redox processes of PW_{11}-SiPh allowed for its application in symmetric RFBs (chapter 3) and as negative electrolyte in asymmetric RFBs (chapter 4). The asymmetric PW_{11}-SiPh|TEMPO RFB showed stable cycling for >400 hours with CE of 95% when the potential window was limited such that PW_{11}-SiPh was reduced by three electrons per molecules. The system has a theoretical E_v of 38.3 Wh L^{-1} which rivals that of the VRFB. Given that the system still requires substantial optimisation, this result shows the capability of hybrid POMs as charge carriers for high E_v RFBs. However, several challenges remain to be overcome for their successful application in RFBs.

It is evident that reduction of PW_{11}-SiPh by four electrons per molecules induces degradation of the POM. This was seen by the poor capacity retention of both the symmetric and asymmetric RFBs when PW_{11}-SiPh was reduced by four electrons. Future work should include an investigation into the nature of this instability as an understanding of the degradation mechanism will aid the design of more stable hybrid POMs in the future.

Given the vast structural diversity of organic-inorganic hybrid POMs, we have merely scratched the surface of this class of charge carrier. Future research should scope alternative hybrid POM structures by modifying the POM core, anchoring group and organic moiety, with the aim of enhancing the chare carrier stability. In addition, future work should include the exploration of hybrid POMs which possess rich electrochemistry at more positive potentials. For example, the hybridisation of a polyoxomolybdate with an electron-withdrawing linker group and organic moiety could realise a multi-electron redox molecule with highly positive redox potentials and high solubility in nonaqueous solvent, thereby achieving a promising charge carrier for the positive electrolyte. Paired with PW_{11}-SiPh in the negative electrolyte, this could yield a RFB with E_v far greater than VRFBs.

Functionalisation of fullerenes was shown to be an effective strategy to improve their properties as charge carriers for RFBs. Tethering of ferrocene moieties to the fullerene core (via pyrrolidine rings), not only generated a bifunctional charge carrier suitable for symmetric RFBs, it also increases the solubility of the resulting species in oDCB. The solubility of the C_{60}Fc charge carriers was further enhanced through substitution of two tertbutyl groups on the aromatic ring of the linker for a single hexane chain, thereby increasing the theoretical E_v from 10.4 to 14.1 Wh L^{-1}. C_{60}Fc charge carriers were investigated in flow cell assemblies for the first time and showed stable performance over 100 cycles. However, degradation of the charge carriers was shown to cause capacity fade in the RFBs. Furthermore, the molecular modification to enhance solubility had an unexpected impact on the charge carriers membrane crossover properties. As with the hybridisation of POMs, we have explored only a subsection of the available functionalisation strategies for fullerenes and future work

should look to improve the stability, solubility, and redox properties of the charge carriers further.

A challenge shared by each of the batteries investigated in this thesis is that of membrane crossover. While aqueous RFBs have benefitted from the substantial research into high performance membranes for fuel cells, nonaqueous RFBs are far less developed.[1] The membranes used in the nonaqueous electrolytes of LIBs are designed to be highly conductive but do not require high selectivity. Consequently, the choice of commercially available membranes for nonaqueous RFBs is limited to a) ion exchange membranes (moderate selectivity, poor conductivity), or b) porous separators (poor selectivity, high conductivity).

The detrimental effect of membrane crossover on capacity retention in asymmetric RFBs is well reported and is observed for the PW_{11}-SiPh|TEMPO RFB investigated in chapter 4. However, the detrimental effects of membrane crossover is also observed in the symmetric PW_{11}-SiPh RFBs (chapter 3) and symmetric C_{60}Fc RFBs (chapter 5). In these instances, the crossover is preferential towards a single half-cell causing an imbalance of charge carrier equivalents in each side. This is attributed to migration effects and/or electroosmotic drag. Mixing and redistribution of electrolytes is an effective strategy to regenerate the battery. Alternatively, operation of symmetric batteries with an alternating polarity such that the half-cells operating as the positive and negative side are alternated each cycle, greatly diminishes the capacity fade attributed to asymmetric membrane crossover.

Established RFB technologies such as the VRFB, benefit from the development of membranes designed to prevent crossover of that specific charge carrier ($V^{2+}/V^{3+}/VO^{2+}/VO_2^{+}$).[2] While it may be premature to develop membranes targeted for the novel charge carriers investigated in this thesis, there are some promising membrane for nonaqueous RFBs that are emerging.[1] The challenge of developing membranes for nonaqueous RFBs mirror that of the lithium-sulfur battery community, in that high conductivity and selectivity (preventing polysulfides crossover) are essential.[3] Polymers of intrinsic porosity (pore size <2 nm) have shown to be highly effective at blocking small organic charge carriers (and polysulfides too) without significant detriment to the conductivity.[4,5] The selectivity of these

nanoporous separators is expected to be particularly high for the bulky charge carriers investigated in this thesis.[5,6]

Assessment of the electrolyte cost, sustainability, safety, and practicality of synthesis is important for the development of commercially viable RFBs. The benefits of transitioning from aqueous to nonaqueous electrolytes must ultimately out way the cost, safety, and sustainability challenges that the nonaqueous electrolyte presents.[7] While a full techno-economic analysis is not presented here, we can recognise some of the strengths and weaknesses of the electrolytes investigated in this thesis. The application of POMs and fullerene charge carriers in nonaqueous electrolyte has been fundamental to their performance. The wide window of electrochemical stability of acetonitrile allowed access to the four, one-electron redox processes of PW_{11}-SiPh which would otherwise be inaccessible in aqueous electrolyte (without excessive hydrogen evolution). Furthermore, the poor solubility of fullerene in water prevents its application in aqueous solvents entirely. While nonaqueous electrolytes present several challenges (poor membrane selectivity, increased solution resistance, volatility etc), the benefits they offer (wide window of electrochemical stability, alternative solubilising properties) make them promising systems for high E_v RFBs and justifies further research in the area.

6.1. References

1 J. Yuan, Z. Z. Pan, Y. Jin, Q. Qiu, C. Zhang, Y. Zhao and Y. Li, *J. Power Sources*, 2021, **500**, 229983.

2 C. H. L. Tempelman, J. F. Jacobs, R. M. Balzer and V. Degirmenci, *J. Energy Storage*, 2020, **32**, 101754.

3 C. Li, A. L. Ward, S. E. Doris, T. A. Pascal, D. Prendergast and B. A. Helms, *Nano Lett.*, 2015, **15**, 5724–5729.

4 N. B. McKeown and P. M. Budd, *Macromolecules*, 2010, **43**, 5163–5176.

5 S. E. Doris, A. L. Ward, A. Baskin, P. D. Frischmann, N. Gavvalapalli, E. Chénard, C. S. Sevov, D. Prendergast, J. S. Moore and B. A. Helms, *Angew. Chemie*, 2017, **129**, 1617–1621.

6 S. on Tung, S. L. Fisher, N. A. Kotov and L. T. Thompson, *Nat. Commun.*, 2018, **9**, 4193.

7 R. M. Darling, K. G. Gallagher, J. A. Kowalski, S. Ha and F. R. Brushett, *Energy Environ. Sci.*, 2014, **7**, 3459–3477.

Appendix A: Supplementary Analysis of Fullerene-Ferrocene Charge Carriers

Appendix A contains data associated with chapter 5 including voltametric analysis and flow cell performance of two $C_{60}Fc$ charge carriers termed $C_{60}Fc2$ and $C_{60}Fc3$. The structure and notation of the charge carriers are shown in table A.1.

Table A.1. Structure and notation of $C_{60}Fc$ charge carriers investigated here.

Charge carrier notation	Charge carrier structure
$C_{60}Fc2$	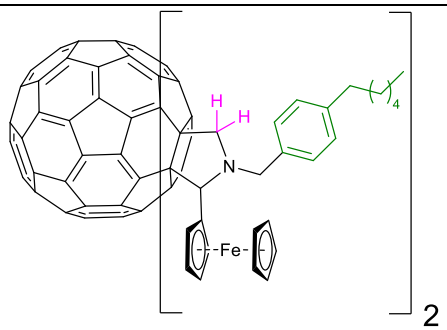
$C_{60}Fc3$	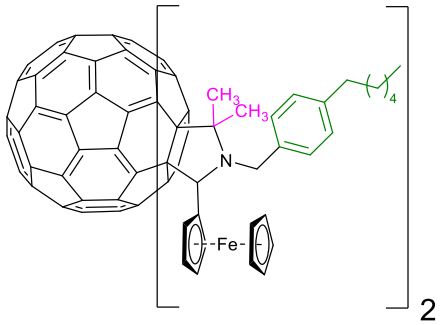

The roman numerals annotated in figure A.1 and figure A.4 refer to the redox processes defined in Eq. 5.1 to 5.4 of chapter 5. Figure A.2 and figure A.5 show the scan rate dependence of the redox processes and are used in the calculation of *D* using the Randles-Sevcik equation and k^0 using the Nicholson method.[1] Continuous CV of $C_{60}Fc2$ and $C_{60}Fc3$ over 1000 cycles is shown in figure A.3 and figure A.6 respectively. In each case, the effect of CV cycling on the electrode surface is evaluated by CV in blank electrolyte (0.5 M $[TBA][BF_4]$ in oDCB).

A.1. Electrochemical analysis of $C_{60}Fc2$

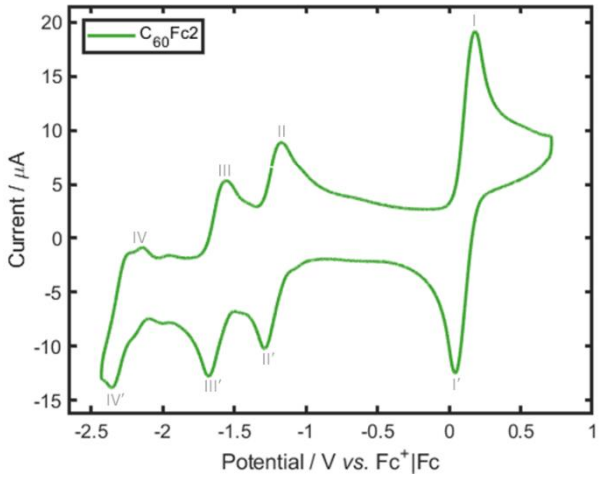

Figure A.1. CV of 1 mM $C_{60}Fc2$ in 0.5 M [TBA][BF_4] in oDCB at a glassy carbon WE (0.071 cm^2) with Pt wire CE and referenced to $Fc^+|Fc$ at ν of 100 mV s^{-1} and iR compensation applied.

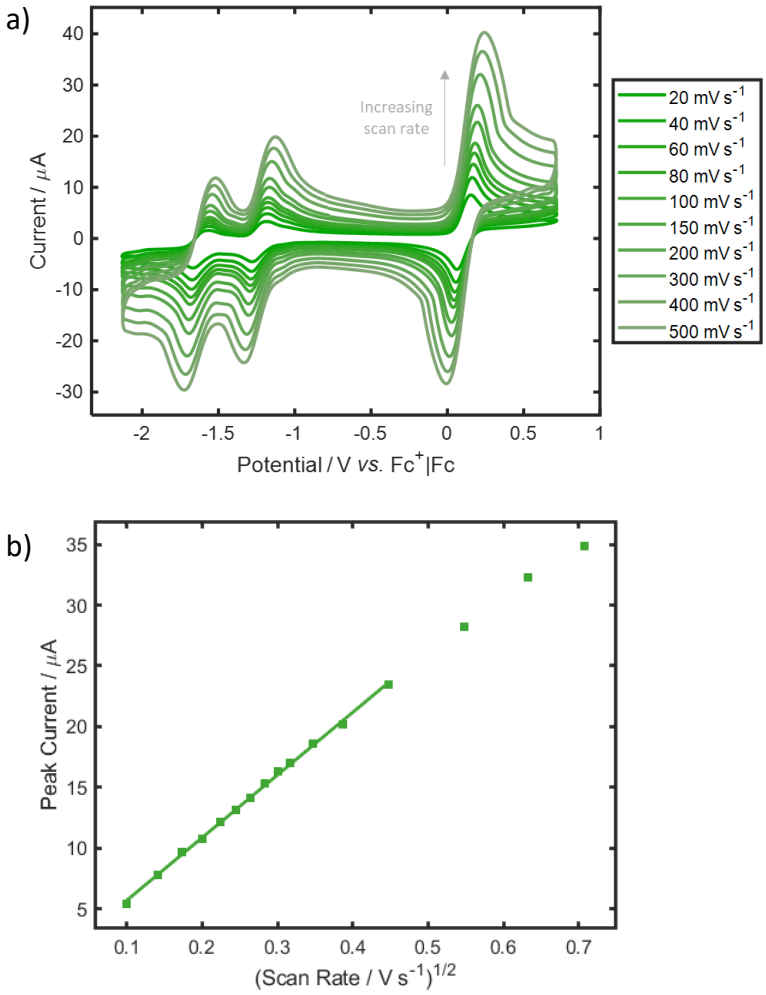

Figure A.2. a) CV of 1 mM $C_{60}Fc2$ in 0.5 M [TBA][BF_4] in oDCB at a glassy carbon WE (0.071 cm^2) with Pt wire CE and referenced to $Fc^+|Fc$ at ν of 20 to 500 mV s^{-1} and iR compensation applied. b) Peak *vs.* $\nu^{1/2}$ for the oxidation of $C_{60}Fc2$ (process I). Data was attained from the second voltammetry cycle over the range of 10 to 500 mV s^{-1}.

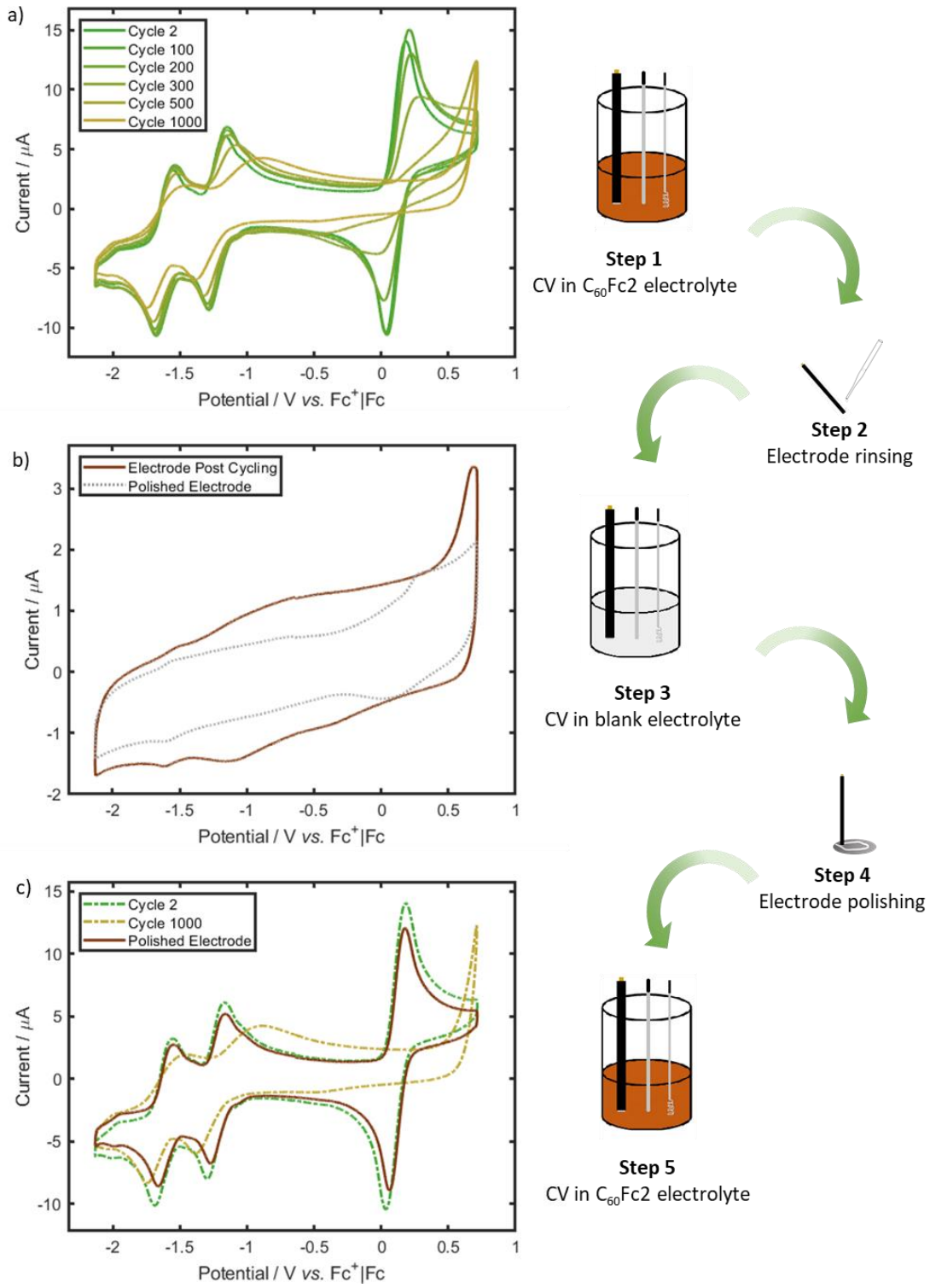

Figure A.3. a) CV cycling of $C_{60}Fc2$ electrolyte at a glassy carbon WE (0.071 cm^2) with Pt wire CE and referenced to $Fc^+|Fc$ at ν of 100 mV s^{-1} and iR compensation applied. a) Cycle 2, 100, 200, 300, 500 and 1000 are overlaid b) CV in blank electrolyte at the cycled and polished glassy carbon WE (step 3). c) CV of $C_{60}Fc2$ electrolyte from step 1 at a polished glassy carbon WE (step 5).

A.2. Electrochemical analysis of $C_{60}Fc3$

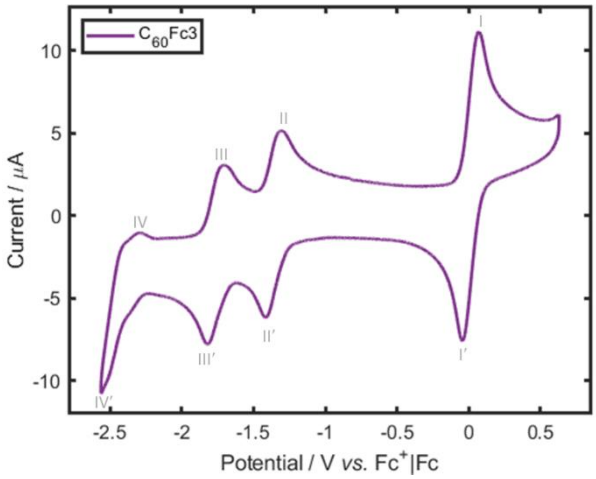

Figure A.4. CV of 1 mM $C_{60}Fc3$ in 0.5 M [TBA][BF_4] in oDCB at a glassy WE (0.071 cm^2) with Pt wire CE referenced to $Fc^+|Fc$ at ν of 100 mV s^{-1} and iR compensation applied.

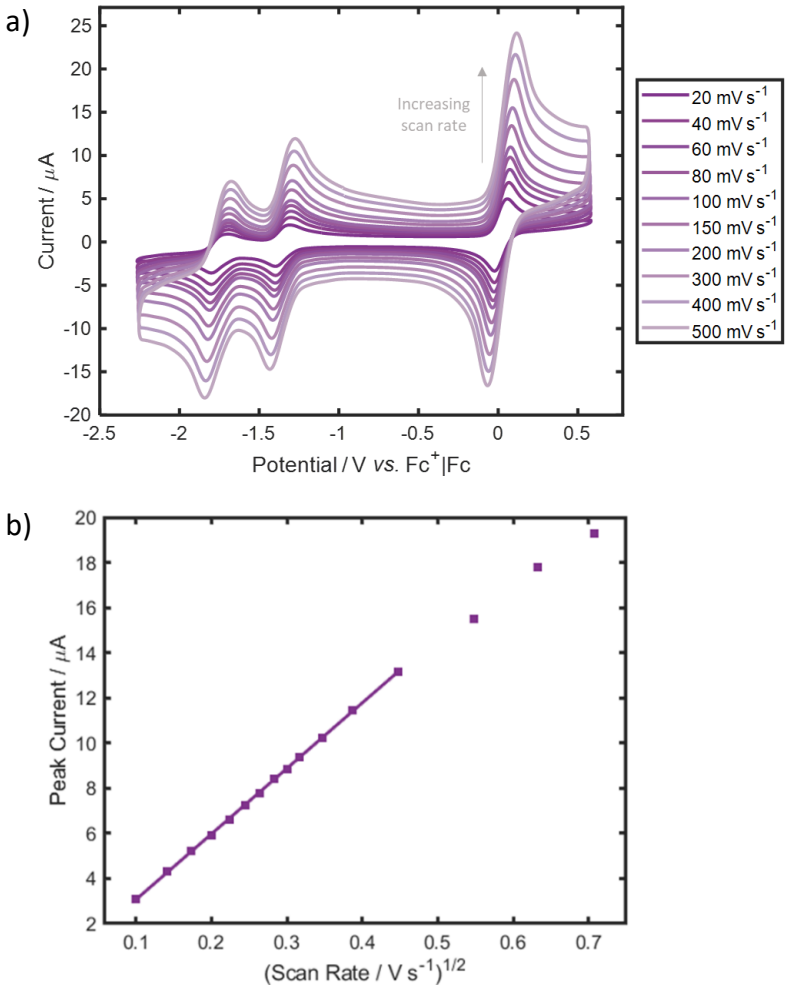

Figure A.5. a) CV of 1 mM C_{60}Fc3 in 0.5 M [TBA][BF_4] in oDCB at a glassy carbon WE (0.071 cm^2) with Pt wire CE referenced to $Fc^+|Fc$ at ν of 20 – 500 mV s^{-1} and iR compensation applied b) Peak current *vs.* $\nu^{1/2}$ for the oxidation of C_{60}Fc3 (process I). Data was attained from the second voltammetry cycle over the range of 10 to 500 mV s^{-1}.

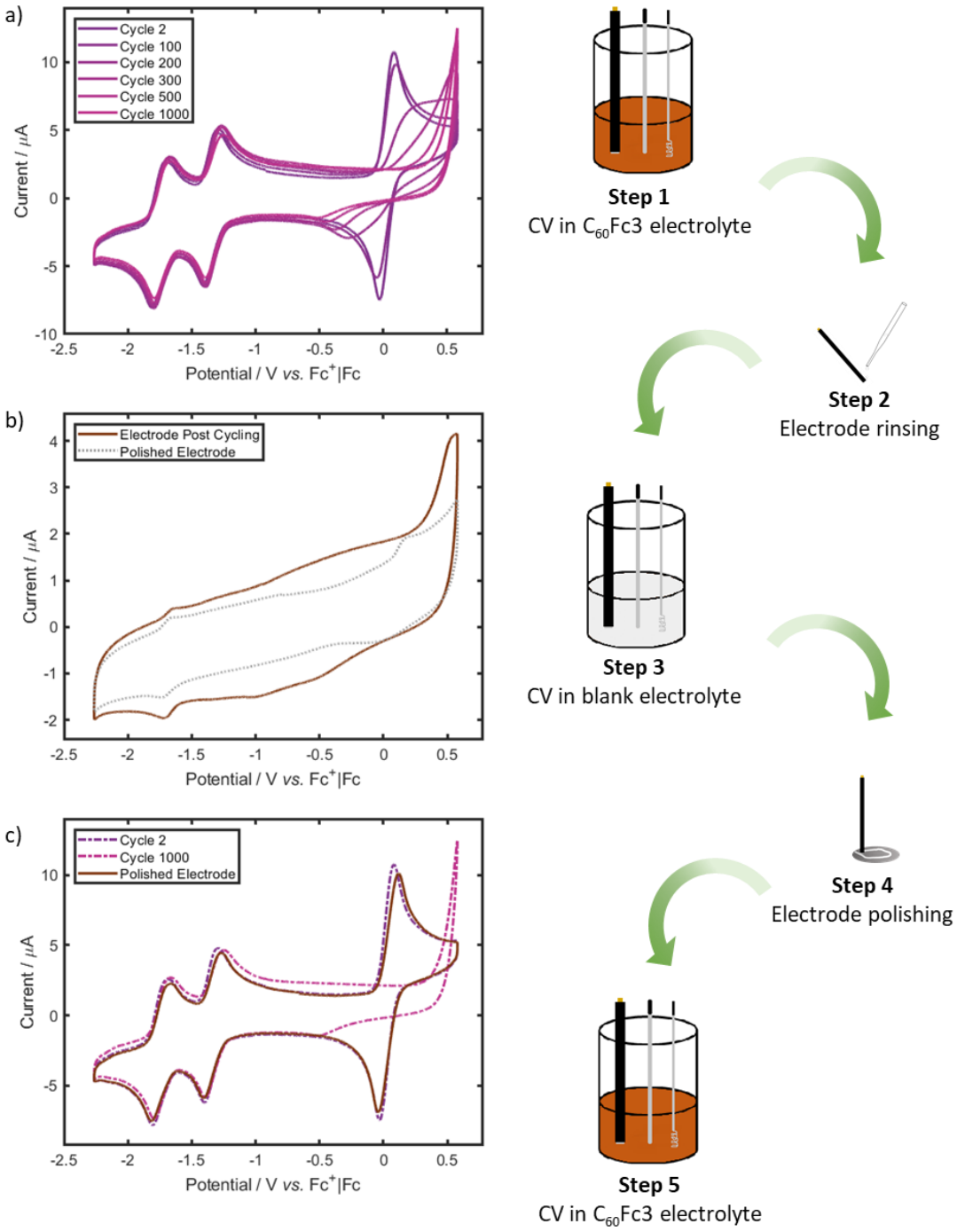

Figure A.6. a) CV cycling of $C_{60}Fc3$ electrolyte at a glassy carbon WE (0.071 cm^2) with Pt wire CE and $Fc^+|Fc$ internal reference at ν of 100 mV s^{-1} and iR compensation applied. a) Cycle 2, 100, 200, 300, 500 and 1000 are overlaid b) CV in blank electrolyte at the cycled and polished glassy carbon WE (step 3). c) CV of $C_{60}Fc3$ electrolyte from step 1 at a polished glassy carbon WE (step 5).

A.3. Flow battery performance of $C_{60}Fc2$ and $C_{60}Fc3$

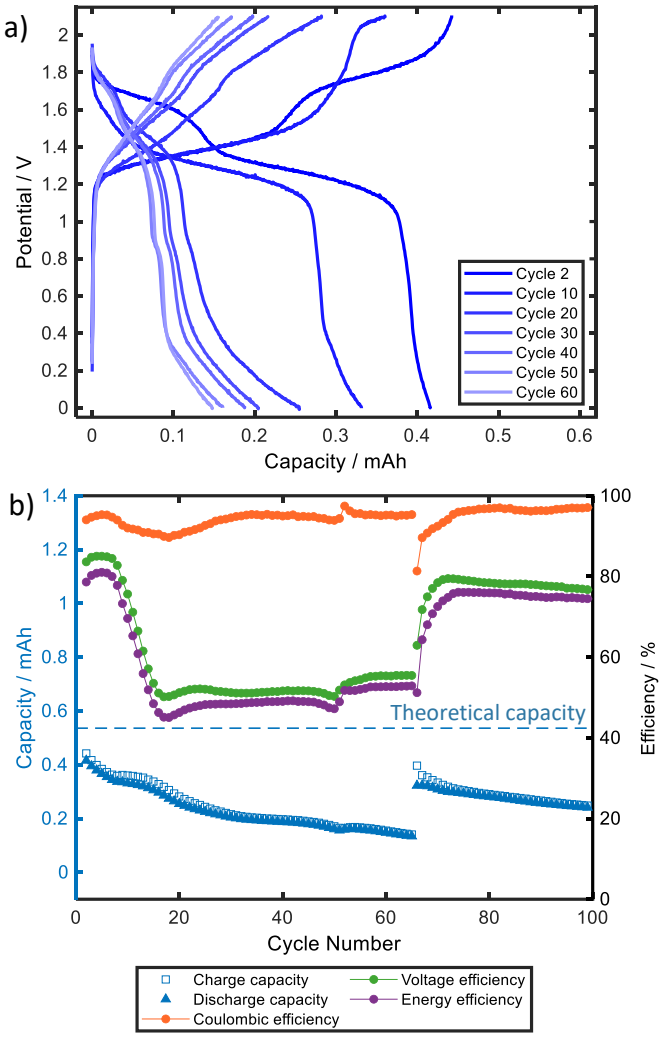

Figure A.7. Symmetric $C_{60}Fc2$ RFB cycling within the voltage threshold of 0 to 2.1 V. Half-cells were separated by Celgard separator with current density of 0.1 mA cm^{-2} (C-rate of approximately 1C) and flow rate of 20 mL min^{-1}. a) Charge/discharge profiles of cycle 2 - 100 b) capacity and efficiency values per cycle.

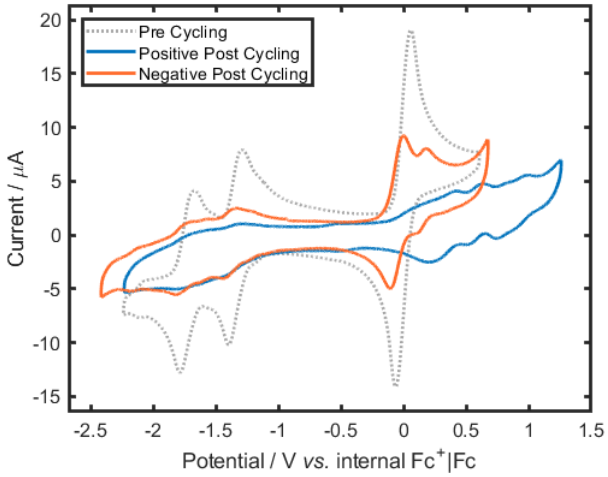

Figure A.8. CV of electrolyte pre cycling (grey dashed) and of positive (blue) and negative (orange) electrolytes after 100 charge-discharge cycles in a C_{60}Fc2 RFB with consistent polarity. CV was recorded at glassy carbon WE (0.071 cm^2) with Pt wire CE at ν of 100 mV s^{-1} and iR compensation applied. Ag wire QRE was used and voltammograms were referenced to the internal $Fc^+|Fc$ redox couple of C_{60}Fc2.

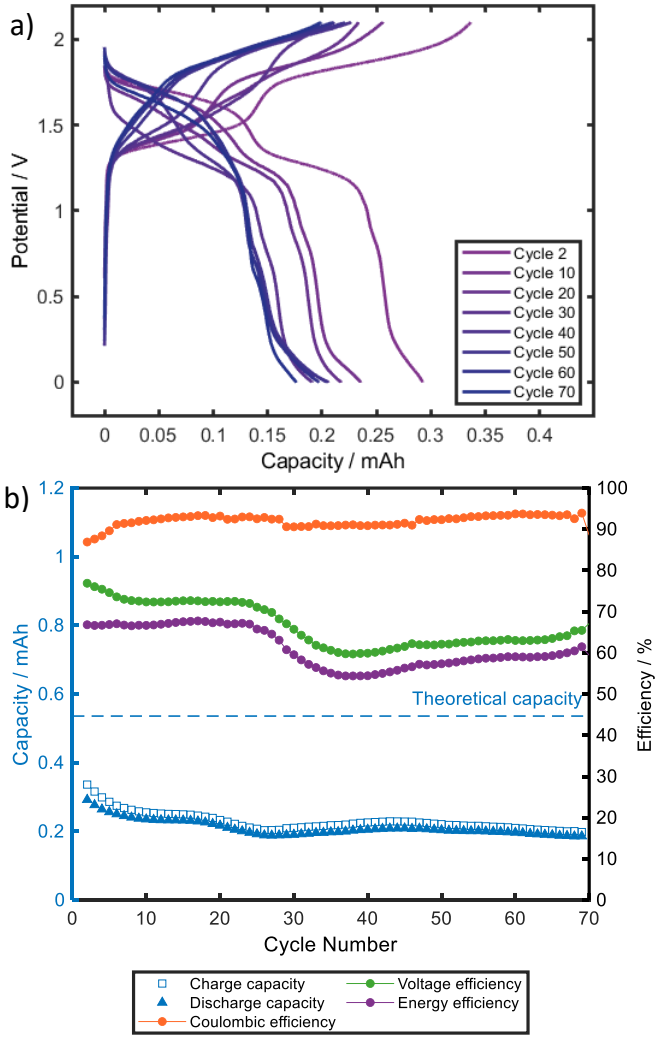

Figure A.9. Symmetric C_{60}Fc3 RFB cycling within the voltage threshold of 0 to 2.1 V. Half-cells were separated by Celgard separator with current density of 0.1 mA cm^{-2} (C-rate of approximately 1C) and flow rate of 20 mL min^{-1}. a) Charge/discharge profiles of cycle 2 - 70 b) capacity and efficiency values per cycle.

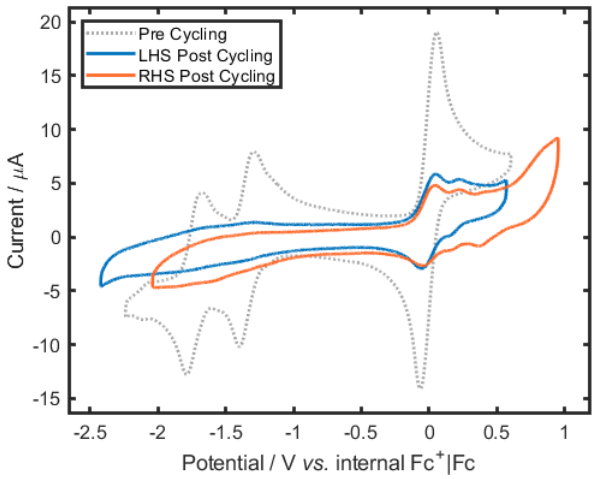

Figure A.10. CV of electrolyte pre cycling (grey dashed) and of LHS (blue) and RHS (orange) electrolytes after 100 charge-discharge cycles in a C_{60}Fc2 RFB with alternating polarity. CV was recorded at glassy carbon WE (0.071 cm^2) with Pt wire CE at ν of 100 mV s^{-1} and iR compensation applied. Ag wire QRE was used and voltammograms were referenced to the internal $Fc^+|Fc$ redox couple of C_{60}Fc2. The terms LHS and RHS have been used due to differentiate the reservoirs in alternating polarity experiments only.